

MECHANICS OF RIVER AVULSIONS
ON LOWLAND RIVER DELTAS

Thesis by
Austin John Chadwick

In Partial Fulfillment of the Requirements for the degree
of Doctor of Philosophy

The logo for the California Institute of Technology (Caltech), featuring the word "Caltech" in a bold, orange, sans-serif font.

CALIFORNIA INSTITUTE OF TECHNOLOGY
Pasadena, California

2020
(Defended October 21, 2019)

© 2020

Austin John Chadwick

ORCID: 0000-0002-2552-0083

ACKNOWLEDGEMENTS

This thesis would not have been possible without the support, guidance, and friendship of those around me. First and foremost, I would like to thank my advisor Mike Lamb. Thank you, Mike, for believing in me, and for pushing me to be a hard-working, thoughtful, and clear-headed scientist. I am immensely grateful for you taking me under your wing and teaching me the fundamentals of geomorphology, your approach to hypothesis-driven research, and your art of clear scientific communication. I deeply appreciate all the opportunities you have provided me to build experience and establish collaborations in our scientific community. I am also grateful for your respectful, professional, and hands-on approach to advising; thank you for always taking the time to chat with me amidst your busy schedule. Working with you has been challenging and deeply rewarding.

I also thank my many other mentors on my path to my PhD. In high school, I owe so much to Mr. Ikezi for inspiring me to pursue a career in science, and to Ms. Odes for helping me build confidence in my abilities in math and science. In college, Peter Bird inspired me to become a geophysicist, An Yin encouraged me to balance both geology and geophysics (to be a geolophysicist, in his words), and Jon Aurnou showed me the importance of a balanced theoretical and experimental approach. And of course, thank you to Gilles Peltzer for supporting me and encouraging me to apply to graduate school at Caltech. I am also so grateful for my many mentors, official and unofficial, during graduate school. In addition to my advisor Mike, I would like to thank Vamsi Ganti, Marisa Palucis, Brian Fuller, Tomas Ulizio, Victor Tsai, Woody Fischer, Andy Thompson, John Grotzinger, and Jean-Philippe Avouac. I would like to give a special thank you to Jean-Philippe, John, and Andy for serving on my thesis committee alongside my advisor; I am immensely grateful for your invaluable guidance and advice over the years.

Thank you to my colleagues, collaborators, and labmates who have continued to provide me with feedback, fresh perspectives, and friendship over the years: Hima Hassenruck-Gudipati, Alistair Hayden, Madison Douglas, Joel Scheingross, Jeff Prancevic, Luca Malatesta, Mathieu Lapotre, Ajay Limaye, Alex Beer, Jan de Leeuw, Lizzy Trower, Mark Torres, Isaac Larsen, Flavien Beaud, Gen Li, and Tien-Hao Liao. I would like to especially thank my undergraduate mentees Sarah Steele, Jose Silvestre, and Kirby Sikes: thank you for your contribution to this research, and for your

continued effort, patience, and feedback in helping me grow as a mentor. I would also like to thank Janice Grancich, Liz Boyd, Julie Lee, and the administrative staff within GPS and at Caltech as a whole.

Thank you to my friends, who have been instrumental in keeping me grounded and happy through the years. Thank you to Jonah Nakagawa, Tyler Overvold, and Stephen Mastrocola for your enduring friendship and loyalty. Thank you to my hausmates Kyle Metcalfe, Alistair Hayden, Mike Citrin, Dan Johnson, and Joseph Bowkett. Thank you Jen Buz, E.T.R., Elizabeth Bailey, Giuliana Viglione, Siobhan McArdle, Brenden Roberts, Olivia Quaglia, Monica Solis, Ryan Holmes, H.P. Arora, Soichi Hirokawa, Sarah Zeichner, Jan Aura, Cecilia Sanders, Zouk, Rhea, Misi, Koreqq, Bobo, Grove, and countless others. Thank you to Jim Barry, my friend and art teacher; you have reinvigorated my love for art, and I owe so much to your encouragement, guidance, open-mindedness, and generosity. Lastly, I give immeasurably huge thanks to Aida Behmard for your boundless love and emotional support.

Finally, I would not be here today without the love and support of my family. Mom, dad, Elizabeth (the-sis), Taylor (the-bro), and Frank: thanks for everything and more.

ABSTRACT

Lowland deltas are home to over 0.5 billion people and some of the most biodiverse ecosystems on Earth. Deltas are highly dynamic landscapes, and at the largest scale grow through repeated construction of depositional lobes punctuated by river avulsions – abrupt shifts in river course to the shoreline. River avulsions have been responsible for dangerous floods and civil unrest over human history, but also counter land loss due to sea-level rise and coastal subsidence by nourishing wetlands with sediment. Despite the central role avulsions play on lowland deltas, the processes controlling their location and frequency remain poorly understood compared to steeper environments such as alluvial fans. This thesis is focused on the mechanics of river avulsions on lowland deltas, and the factors controlling their location and frequency. Chapter 1 addresses the origin of a preferential avulsion site on river deltas, using a novel modeling framework that unites previous work to incorporate backwater hydrodynamics, river-mouth progradation, relative sea-level rise, variable flood regimes, and cycles of lobe construction, abandonment, and reoccupation. Chapter 2 focuses on changes to avulsion frequency caused by relative sea-level rise, incorporating a combination of theory, field data, and numerical modeling. Chapter 3 explores general model predictions for avulsion location and timing during climate change, including rising and falling sea level, imbalances in upstream water and sediment supply, and the magnitude and frequency of storm events. Finally, Chapter 4 presents a scaled laboratory experiment where models and theory for lowland delta avulsion mechanics were put to the test. The work presented in this thesis offers new tools to predict river avulsions on densely populated lowland deltas, and allows for comparison with existing models of coastal restoration that fail to account for river avulsion mechanics and the hydrodynamics of lowland rivers.

PUBLISHED CONTENT AND CONTRIBUTIONS

Chadwick, A. J., Lamb, M. P., Moodie, A. J., Parker, G., & Nittrouer, J. A. (2019). Origin of a preferential avulsion node on lowland river deltas. *Geophysical Research Letters*, 46(8), 4267-4277.

DOI: <https://doi.org/10.1029/2019GL082491>

A.J.C. participated in conception of the project, performed research and analyzed data, and wrote the paper.

TABLE OF CONTENTS

| | |
|--|-----|
| Acknowledgements..... | iii |
| Abstract | v |
| Published content and contributions | vi |
| Table of contents..... | vii |
| Introduction..... | 1 |
| | |
| Chapter 1: Origin of a preferential avulsion node on lowland river deltas | 11 |
| 1.0 Abstract | 12 |
| 1.1 Introduction | 12 |
| 1.2 Methods..... | 15 |
| 1.3 Avulsion nodes originating from initial conditions and flow variability | 18 |
| 1.4 Necessary degree of flow variability | 21 |
| 1.5 Avulsion nodes originating from relative sea-level rise..... | 23 |
| 1.6 Discussion and conclusions | 23 |
| 1.7 References | 26 |
| 1.8 Supplementary material | 30 |
| 1.8.1 Treatment of the river mouth and delta front | 30 |
| 1.8.2 Model workflow | 32 |
| 1.8.3 Flow variability parameters | 34 |
| 1.8.4 Non-dimensionalization | 36 |
| 1.8.5 Results for trunk-filling avulsion cycles | 39 |
| 1.8.6 Model sensitivity to other parameters | 40 |
| 1.9 References for supplementary material | 49 |
| | |
| Chapter 2: Accelerated river avulsion frequency on lowland deltas due to sea-level rise | 51 |
| 2.0 Abstract | 52 |
| 2.1 Introduction | 52 |
| 2.2 Morphodynamic model and field data compilation | 57 |
| 2.3 Results | 59 |
| 2.4 Discussion and conclusions | 63 |
| 2.5 References | 67 |
| 2.6 Supplementary material | 72 |
| 2.7 References for supplementary material | 84 |
| | |
| Chapter 3: Climate-change controls on river delta avulsion location and frequency | 87 |
| 3.0 Abstract | 88 |
| 3.1 Introduction | 88 |
| 3.2 Model derivation | 94 |

| | |
|---|-----|
| 3.3 Setup for model runs and climate-change scenarios | 99 |
| 3.3.1 Changes in sea level | 100 |
| 3.3.2 Changing sediment supply and transport capacity | 104 |
| 3.3.3 Changing flood regimes | 107 |
| 3.3.4 Base-case climate and climate-change model runs | 108 |
| 3.4 Results | 108 |
| 3.4.1 Avulsions under a base-case climate scenario | 108 |
| 3.4.2 Avulsions during changes in sea level | 110 |
| 3.4.3 Avulsions during changing sediment supply and transport capacity | 113 |
| 3.4.4 Avulsions during different flood regimes | 117 |
| 3.4.5 Inherent variability in avulsion dynamics across climate scenarios | 121 |
| 3.5 Discussion | 123 |
| 3.5.1 Comparison to avulsions during Holocene climate change | 123 |
| 3.7.2 Implications for avulsions during anthropogenic climate change | 124 |
| 3.7.3 Implications for interpreting ancient climates from avulsions in deltaic deposits | 125 |
| 3.6 Conclusions | 126 |
| 3.7 References | 128 |
| Chapter 4: Channel avulsions, land loss, and stratigraphy of an experimental backwater-scaled delta subjected to sea-level changes..... | |
| 4.0 Abstract | 135 |
| 4.1 Introduction | 136 |
| 4.2 Methods | 137 |
| 4.2.1 Experimental setup | 143 |
| 4.2.2 Data collection | 148 |
| 4.2.3 Data analysis | 149 |
| 4.2.3 Predictions from radially averaged and lobe-averaged models | 151 |
| 4.3 Results | 152 |
| 4.3.1 Phase A | 152 |
| 4.3.2 Phase B | 158 |
| 4.3.3 Phase C | 159 |
| 4.3.4 Phase D | 160 |
| 4.3.5 Phase E | 160 |
| 4.3.4 Phase F | 161 |
| 4.3.4 Predictions from radially averaged and lobe-averaged models | 162 |
| 4.4 Discussion | 164 |
| 4.4.1 Comparison to previous experiments and field observations | 164 |

| | |
|--|-----|
| 4.4.2 Comparison to existing models | 165 |
| 4.4.3 Implications for predicting avulsion hazards | 168 |
| 4.5 Conclusions | 169 |
| 4.6 References | 171 |

Introduction

Lowland deltas are highly dynamic, often fan-shaped depositional systems that form when a low-gradient river enters an ocean or lake. While comprising only ~1% of the land surface, lowland deltas are home to over 0.5 billion of the population and some of the most biodiverse ecosystems on Earth (Foufoula-Georgiou et al., 2011; Gleick, 2003; Olson & Dinerstein, 1998; Vörösmarty et al., 2009). Due to their low surface gradients, lowland deltas are susceptible to drowning due to sea-level rise and coastal subsidence associated with fluid extraction (Syvitski et al., 2009). At the same time, deltas are sensitive to upstream changes in water and sediment supplied to coastal rivers. Just over the past century, for example, shifting atmospheric circulation over the continental U.S. increased the magnitude of 20-year floods on the Mississippi River by 50% (Knox, 1993), and widespread dam construction has trapped nearly 80% of continental sediment yield upstream of deltas (Meade et al., 1990; Syvitski & Saito, 2007). Understanding how deltas function and respond to change is crucial for predicting future flooding hazards and sustaining coastal cities and ecosystems in the future, when anthropogenic greenhouse effects will induce unprecedented climate change (Pachauri et al., 2014). Furthermore, a better grasp of delta mechanics will also aid the stratigraphic interpretation of deltaic deposits, which are common on Earth and Mars and can record signatures of ancient sea levels and climates (DiBiase et al., 2013; Irwin et al., 2005; MacNaughton et al., 1997; McLennan et al., 2019; Pufahl et al., 2013).

At the largest scale, deltas grow through repeated construction of depositional lobes punctuated by river avulsions — abrupt shifts in river course to the shoreline (Fig. 0.1) (Jerolmack, 2009; Slingerland & Smith, 2004). Avulsions often occur around a persistent spatial node, giving deltas their characteristic planform-triangular shape and size. Lobe sizes can range from decimeters at a laboratory scale (Ganti, Chadwick, Hassenruck-Gudipati, Fuller, et al., 2016) to hundreds of kilometers at the scale of the Mississippi Delta (Fisk, 1944). Furthermore, avulsions tend to occur at a regular interval for a given delta, which can be as fast as once-per-decade on the Yellow River, China (Chunting Xue, 1993) or as slow as once-per-millennium on the Mississippi River, U.S.A (Fisk, 1944). River avulsions are natural hazards and have been associated with the deadliest floods in human history, amounting to millions of lives lost on the Yellow River alone (Kidder & Liu, 2017; Soong & Zhao, 1994). At the same time, avulsions counteract land lost due to relative sea-level rise

by nourishing wetlands with sediment (Edmonds et al., 2009; Richards et al., 2002). Engineered avulsions are now parts of billion-dollar coastal restoration plans worldwide, including on the Mississippi delta, to restore natural function to sinking land while mitigating flood hazards (Coastal Protection and Restoration Authority of Louisiana, 2007). Restoration efforts are hampered, however, because we lack a mechanistic understanding of what sets river avulsion location and frequency, and how their location and frequency will change in the next century with anticipated increased relative sea-level rise and human interference (Jerolmack, 2009; Kim et al., 2009; Paola et al., 2011; Syvitski & Saito, 2007).

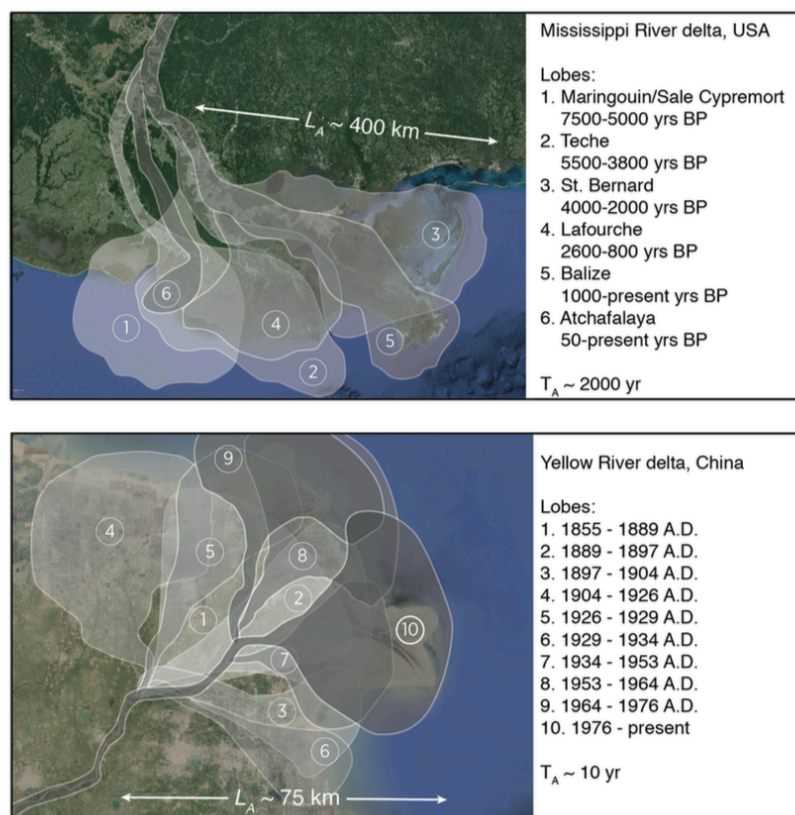


Fig. 0.1: Mapped delta lobes of the Mississippi River (top; after Coleman et al., 1998) and Yellow River (bottom; after Xue, 1993 and van Gelder et al., 1994) overlain on Google Earth imagery showing the characteristic lobe length, L_A , and avulsion timescale, T_A .

Previous research has tackled problems related to river avulsion location and frequency, but has focused on mechanics more applicable to steeper environments such as fan-deltas and alluvial fans. Alluvial fans and fan deltas are similar in shape to lowland deltas, but in their cases the fan apex is typically determined by a change in confinement, such as a canyon-fan transition, or a change in valley slope that can be tectonically controlled (Blair & McPherson, 1994; Ganti et al., 2014; Hartley et al., 2017). Topographic changes force sediment deposition at the fan apex, resulting in channel filling and repeated avulsion about that location (Reitz & Jerolmack, 2012; Reitz et al., 2010).

In contrast to steeper environments, lowland deltas are part of very low-relief landscapes, and avulsion nodes persist on unconfined plains. Recent work focused on lowland settings has identified sediment deposition and avulsion are linked to backwater hydrodynamics, the spatial acceleration of flow due to lateral spreading at the river mouth, which can extend for hundreds of kilometers upstream (Fig. 0.2) (Chatanantavet et al., 2012; Ganti, Chadwick, Hassenruck-Gudipati, Fuller, et al., 2016; Ganti, Chadwick, Hassenruck-Gudipati, & Lamb, 2016; Ganti et al., 2019; Jerolmack & Swenson, 2007; Paola & Mohrig, 1996; Trower et al., 2018). However, backwater hydrodynamics are not accounted for in the vast majority of models and laboratory experiments, and the effects of backwater on sediment transport and river avulsion remain critically unexplored. Furthermore, the few studies accounting for backwater effects have yielded conflicting results, leaving a number of outstanding questions (Chatanantavet et al., 2012; Lane et al., 2017; Moran et al., 2017; Ratliff et al., 2018). For example, it remains unclear if and how sea-level rise causes more frequent avulsions, less frequent avulsions, or no change in avulsion timing (Lane et al., 2017; Moran et al., 2017; Ratliff et al., 2018; Törnqvist, 1994). In addition, recent models disagree as to whether a persistent avulsion location originates from discharge variability or from geometric constraints associated with delta progradation (Chatanantavet et al., 2012; Ganti, Chadwick, Hassenruck-Gudipati, Fuller, et al., 2016; Hartley et al., 2017; Moran et al., 2017; Ratliff et al., 2018)

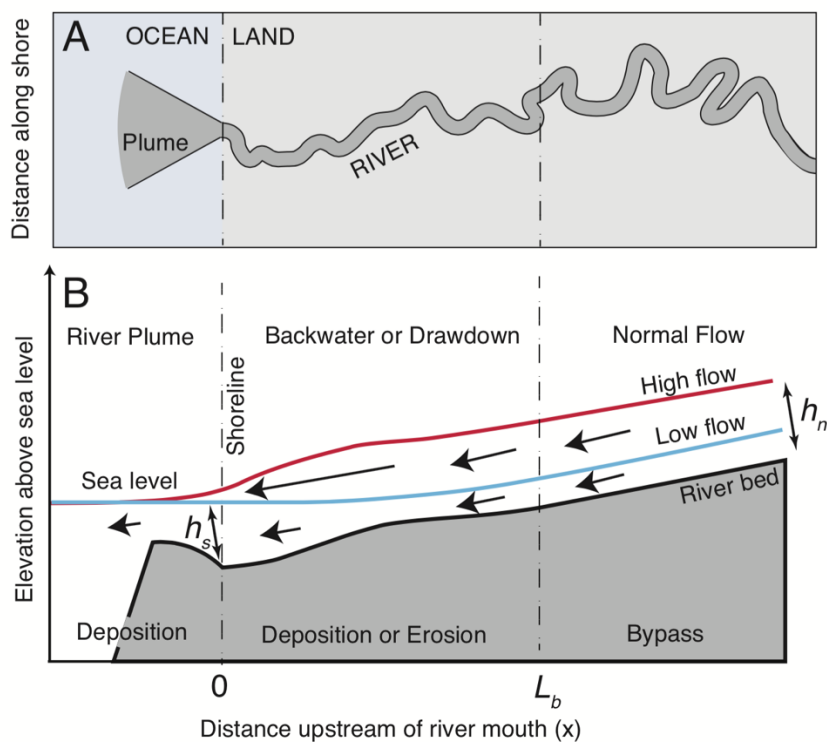


Fig. 0.2: Backwater hydrodynamics. Cartoon of the quasi-2D modeling framework of the backwater zone showing lateral spreading of the river plume at the shoreline in plan view that leads to adverse bedslopes (A) and non-uniform flows in cross section (B). Non-uniform flows drive a change from deposition during small floods to erosion during large floods that results in an upward convexity of the river profile. These patterns can be imprinted on trends of net aggradation from backfilling due to progradation or relative sea level rise, for example. After Lamb et al. (2012).

The goal of this thesis is to explore this gap in existing knowledge and tackle outstanding questions through detailed study of the mechanics of river avulsions on lowland river deltas. I begin with the development of a new modeling framework specifically geared towards lowland settings with backwater hydrodynamics, which I use to answer outstanding questions in the literature. I then broaden the scope, subjecting the model to a wide range of climate-change scenarios to predict changes in avulsion location and frequency. Finally, I test model predictions against an experimental backwater-scaled delta I grew in the laboratory, and explore the ramifications for land-loss patterns and delta stratigraphy.

Chapter 1 focuses on the origin of avulsion nodes on lowland river deltas, for which there exists a number of competing theories (Chatanantavet et al., 2012; Hartley et al., 2017; Ratliff et al.,

2018). Previous numerical models differ on the origin of backwater-scaled avulsion nodes, and their consistency with experimental data (Ganti, Chadwick, Hassenruck-Gudipati, Fuller, et al., 2016). To unify previous work, I developed a numerical model of lowland delta growth that includes backwater hydrodynamics, river-mouth progradation, relative sea-level rise, variable flow regimes, and cycles of lobe construction, abandonment, and reoccupation. For parameter space applicable to lowland deltas, I found that flow variability is the primary mechanism that causes persistent avulsion nodes by focusing sedimentation within the backwater zone.

Chapter 2 combines the numerical model, field observations, and analytical theory to address projected changes to avulsion frequency due to relative sea-level rise. The model provides a general solution that reconciles conflicting predictions between the two models commonly used among the scientific community and by the Intergovernmental Panel on Climate Change to predict coastal inundation (Giosan, 2014; Jerolmack, 2009; Pachauri et al., 2014; Paola et al., 2011; Reitz et al., 2010). I found most densely populated deltas have sufficiently low land-building rates such that modern sea-level rise will drive more frequent avulsions and flood hazards. Furthermore, with further increases in rise rates and reductions in sediment supply anticipated in the next century, I predict that shorelines and avulsion sites will shift inland, introducing major new hazards to upstream communities. Thus, there is a threshold condition beyond which coastal land will be lost and avulsion mitigation engineering needs to shift upstream.

While Chapters 1 and 2 target specific outstanding questions in the literature, in Chapter 3 I broaden the scope and explore generic model predictions across range of climatic forcings, including sea-level rise, imbalances in upstream water and sediment supply, and the magnitude and frequency of storm events. Results indicate that avulsion location is sensitive to upstream changes, with avulsions occurring farther upstream under stormier climates or higher sediment loads. Avulsion frequency, in contrast, is most affected by sea-level change. Minor changes in climate forcing are indistinguishable from inherent variability in the model arising from storms, avulsions between lateral lobes, and downstream shifts in the avulsion node in tandem with shoreline progradation. In contrast, extreme climate change can shift the delta to a transient state where avulsions become denodalized until the delta adjusts to new conditions.

Finally, Chapter 4 represents a controlled experiment wherein I grew the first ever experimental lowland delta scaled to incorporate backwater hydrodynamics and systematic changes in sea level. Consistent with modeling predictions from Chapters 1-3, river avulsions were more frequent under increasing rates of sea-level rise and occurred at a persistent spatial node that migrated downstream and upstream in tandem with delta progradation and retreat. Furthermore, I document results for land loss and deltaic stratigraphy from these experiments that challenge existing models that do not incorporate avulsion mechanics.

The work presented in this thesis offers new tools to predict river avulsion location and frequency on densely populated lowland deltas, and allows for comparison with existing models of delta restoration that fail to account for river avulsion mechanics and backwater hydrodynamics. For example, most coastal restoration models are based on radially-averaged response across the entire delta (Jerolmack, 2009; Kim et al., 2009; Paola et al., 2011; Swenson et al., 2000). However, deposition and land loss can vary spatially on a delta because channel avulsions periodically and abruptly shift the river course, changing the distribution of sediment. The model presented here is capable of resolving spatial patterns in deposition and land loss, unlike previous radially averaged models. This step forward will be critical for restoration efforts on deltas like the Mississippi, where the vast majority of land loss over the past century has been focused on abandoned delta lobes that are starved of sediment between avulsions (Coleman & Gagliano, 1964; Gagliano et al., 1981; Paola et al., 2011).

The progress made in this thesis highlights many opportunities for future research. The models and experiment presented here focus exclusively on the effect of river flow, sediment supply, and sea-level on river avulsion mechanics. For simplicity we neglected a number of other processes that can affect natural deltas, including: waves, tides, oceanic storms, water density gradients, strongly cohesive sediment, vegetation, and differential subsidence (Caldwell & Edmonds, 2014; Hoyal & Sheets, 2009; Jerolmack, 2009; Nienhuis et al., 2015; Reitz et al., 2015). Furthermore, the modeling framework is designed for deltas where one delta lobe is active at a given time. While this is the case for many large lowland deltas, other deltas grow through the proliferation of a widespread channel network, allowing for water and sediment exchange between lobes (Passalacqua, 2017;

Sendrowski & Passalacqua, 2017). Detailed theory on river avulsion occurrence that accounts for these factors does not yet exist, leaving important questions for future work.

REFERENCES

- Blair, T. C., & McPherson, J. G. (1994). Alluvial fans and their natural distinction from rivers based on morphology, hydraulic processes, sedimentary processes, and facies assemblages. *Journal of Sedimentary Research*, 64(3a), 450–489.
- Caldwell, R. L., & Edmonds, D. A. (2014). The effects of sediment properties on deltaic processes and morphologies: A numerical modeling study. *Journal of Geophysical Research: Earth Surface*, 961–982. <https://doi.org/10.1002/2013JF002965>. Received
- Chatanantavet, P., Lamb, M. P., & Nittrouer, J. a. (2012). Backwater controls of avulsion location on deltas. *Geophysical Research Letters*, 39(1). <https://doi.org/10.1029/2011GL050197>
- Coastal Protection and Restoration Authority of Louisiana. (2007). Integrated ecosystem restoration and hurricane protection: Louisiana’s comprehensive master plan for a sustainable coast.
- Coleman, J. M., & Gagliano, S. M. (1964). Cyclic sedimentation in the Mississippi River deltaic plain.
- Coleman, J. M., Roberts, H. H., & Stone, G. W. (1998). Mississippi River delta: an overview. *Journal of Coastal Research*, 14(3).
- DiBiase, R. a., Limaye, A. B., Scheingross, J. S., Fischer, W. W., & Lamb, M. P. (2013). Deltaic deposits at Aeolis Dorsa: Sedimentary evidence for a standing body of water on the northern plains of Mars. *Journal of Geophysical Research: Planets*, 118(6), 1285–1302. <https://doi.org/10.1002/jgre.20100>
- Edmonds, D. A., Hoyal, D. C. J. D., Sheets, B. A., & Slingerland, R. L. (2009). Predicting delta avulsions: Implications for coastal wetland restoration. *Geology*, 37(8), 759–762. <https://doi.org/10.1130/G25743A.1>
- Fisk, H. N. (1944). Geological investigations of the alluvial valley of the lower Mississippi River: US Army Corps of Engineers. *Mississippi River Commission, Vicksburg, Mississippi*.
- Foufoula-Georgiou, E., Syvitski, J., Paola, C., Hoanh, C. T., Tuong, P., Vörösmarty, C., et al. (2011). International year of deltas 2013: a proposal. *Eos, Transactions American Geophysical Union*, 92(40), 340–341.
- Gagliano, S. M., Meyer-Arendt, K. J., & Wicker, K. M. (1981). Land loss in the Mississippi River deltaic plain. *GCAGS Transactions*, 31, 295–300.
- Ganti, V., Chu, Z., Lamb, M. P., Nittrouer, J. A., & Parker, G. (2014). Testing morphodynamic controls on the location and frequency of river avulsions on fans versus deltas: Huanghe (Yellow River), China. *Geophysical Research Letters*, 41, 7882–7890. <https://doi.org/10.1002/2014GL061918>
- Ganti, V., Chadwick, A. J., Hassenruck-Gudipati, H. J., & Lamb, M. P. (2016). Avulsion cycles and their stratigraphic signature on an experimental backwater-controlled delta. *Journal of Geophysical Research: Earth Surface*, 121(9), 1651–1675.
- Ganti, V., Chadwick, A. J., Hassenruck-Gudipati, H. J., Fuller, B. M., & Lamb, M. P. (2016). Experimental river delta size set by multiple floods and backwater hydrodynamics. *Science Advances*, 2(5), e1501768.
- Ganti, V., Lamb, M. P., & Chadwick, A. J. (2019). Autogenic Erosional Surfaces in Fluvio-deltaic Stratigraphy from Floods, Avulsions, and Backwater Hydrodynamics. *Journal of Sedimentary Research*, 89(8), 815–832.
- van Gelder, A., van den Berg, J. H., Cheng, G., & Xue, C. (1994). Overbank and channelfill deposits of the modern Yellow River delta. *Sedimentary Geology*, 90(3–4), 293–305. [https://doi.org/10.1016/0037-0738\(94\)90044-2](https://doi.org/10.1016/0037-0738(94)90044-2)
- Giosan, L. (2014). Protect the world’s deltas. *Nature*, 516, 5–7.
- Gleick, P. H. (2003). Global freshwater resources: soft-path solutions for the 21st century. *Science (New York, N.Y.)*, 302(2003), 1524–1528. <https://doi.org/10.1126/science.1089967>
- Hartley, A. J., Weissmann, G. S., & Scuderi, L. (2017). Controls on the apex location of large deltas. *Journal of the Geological Society*, 174(1), 10–13.

- Hoyal, D., & Sheets, B. A. (2009). Morphodynamic evolution of experimental cohesive deltas. *Journal of Geophysical Research*, *114*(F2), F02009. <https://doi.org/10.1029/2007JF000882>
- Irwin, R. P., Howard, A. D., Craddock, R. a., & Moore, J. M. (2005). An intense terminal epoch of widespread fluvial activity on early Mars: 2. Increased runoff and paleolake development. *Journal of Geophysical Research E: Planets*, *110*, 1–38. <https://doi.org/10.1029/2005JE002460>
- Jerolmack, D. J. (2009). Conceptual framework for assessing the response of delta channel networks to Holocene sea level rise. *Quaternary Science Reviews*, *28*(17–18), 1786–1800. <https://doi.org/10.1016/j.quascirev.2009.02.015>
- Jerolmack, D. J., & Swenson, J. B. (2007). Scaling relationships and evolution of distributary networks on wave-influenced deltas. *Geophysical Research Letters*, *34*(23). <https://doi.org/10.1029/2007GL031823>
- Kidder, T. R., & Liu, H. (2017). Bridging theoretical gaps in geoarchaeology: archaeology, geoarchaeology, and history in the Yellow River valley, China. *Archaeological and Anthropological Sciences*, *9*(8), 1585–1602. <https://doi.org/10.1007/s12520-014-0184-5>
- Kim, W., Mohrig, D., Twilley, R. R., Paola, C., & Parker, G. (2009). Is it feasible to build new land in the Mississippi River delta? *Eos Transactions, AGU*, *90*(42), 373–374. Retrieved from http://www.agu.org/pubs/eos-news/supplements/2009/kim_90_42.shtml
- Knox, J. C. (1993). Large increases in flood magnitude in response to modest changes in climate. *Nature*, *361*(6411), 430.
- Lane, T. I., Nanson, R. A., Vakarelov, B. K., Ainsworth, R. B., & Dashtgard, S. E. (2017). Evolution and architectural styles of a forced-regressive Holocene delta and megafan, Mitchell River, Gulf of Carpentaria, Australia. *Geological Society, London, Special Publications*, *444*(1), 305–334.
- MacNaughton, R. B., Dalrymple, R. W., & Narbonne, G. M. (1997). Early Cambrian braid-delta deposits, MacKenzie Mountains, north-western Canada. *Sedimentology*, *44*(4), 587–609.
- McLennan, S. M., Grotzinger, J. P., Hurowitz, J. A., & Tosca, N. J. (2019). The sedimentary cycle on Early Mars. *Annual Review of Earth and Planetary Sciences*, *47*, 91–118.
- Meade, R. H., Yuzyk, T. R., & Day, T. J. (1990). Movement and storage of sediment in rivers of the United States and Canada. *IN: Surface Water Hydrology. Geological Society of America, Boulder, Colorado. 1990. p 255-280, 21 Fig, 3 Tab, 185 Ref.*
- Moran, K. E., Nittrouer, J. A., Perillo, M. M., Lorenzo-Trueba, J., & Anderson, J. B. (2017). Morphodynamic modeling of fluvial channel fill and avulsion time scales during early Holocene transgression, as substantiated by the incised valley stratigraphy of the Trinity River, Texas. *Journal of Geophysical Research: Earth Surface*, *122*(1), 215–234.
- Nienhuis, J. H., Ashton, A. D., & Giosan, L. (2015). What makes a delta wave-dominated? *Geology*, *43*(6), 511–514.
- Olson, D. M., & Dinerstein, E. (1998). The Global 200: a representation approach to conserving the Earth's most biologically valuable ecoregions. *Conservation Biology*, *12*(3), 502–515.
- Pachauri, R. K., Meyer, L., Plattner, G. K., & Stocker, T. (2014). IPCC, 2014: Climate Change 2014: Synthesis Report. *IPCC, Geneva, Switzerland.*
- Paola, C., & Mohrig, D. (1996). Palaeohydraulics revisited: Palaeoslope estimation in coarse-grained braided rivers. *Basin Research*, *8*(3), 243–254. <https://doi.org/10.1046/j.1365-2117.1996.00253.x>
- Paola, C., Twilley, R. R., Edmonds, D. a., Kim, W., Mohrig, D., Parker, G., et al. (2011). Natural Processes in Delta Restoration: Application to the Mississippi Delta. *Annual Review of Marine Science*, *3*(1), 67–91. <https://doi.org/10.1146/annurev-marine-120709-142856>
- Passalacqua, P. (2017). The Delta Connectome: A network-based framework for studying connectivity in river deltas. *Geomorphology*, *277*, 50–62.
- Pufahl, P. K., Pirajno, F., & Hiatt, E. E. (2013). Riverine mixing and fluvial iron formation: A new type of Precambrian biochemical sediment. *Geology*, *41*(12), 1235–1238.
- Ratliff, Katherine M., Hutton, E. H. W., & Murray, A. B. (2018). Exploring Wave and Sea-Level Rise Effects on Delta Morphodynamics With a Coupled River-Ocean Model. *Journal of Geophysical Research: Earth Surface*, *123*(11), 2887–2900. <https://doi.org/10.1029/2018JF004757>

- Reitz, M. D., & Jerolmack, D. J. (2012). Experimental alluvial fan evolution: Channel dynamics, slope controls, and shoreline growth. *Journal of Geophysical Research*, *117*(F2), F02021. <https://doi.org/10.1029/2011JF002261>
- Reitz, M. D., Jerolmack, D. J., & Swenson, J. B. (2010). Flooding and flow path selection on alluvial fans and deltas. *Geophysical Research Letters*, *37*(6). <https://doi.org/10.1029/2009GL041985>
- Reitz, M. D., Pickering, J. L., Goodbred, S. L., Paola, C., Steckler, M. S., Seeber, L., & Akhter, S. H. (2015). Effects of tectonic deformation and sea level on river path selection: theory and application to the Ganges-Brahmaputra-Meghna River Delta. *Journal of Geophysical Research: Earth Surface*. <https://doi.org/10.1002/2014JF003202>
- Richards, K., Brasington, J., & Hughes, F. (2002). Geomorphic dynamics of floodplains: ecological implications and a potential modelling strategy. *Freshwater Biology*, *47*(4), 559–579.
- Sendrowski, A., & Passalacqua, P. (2017). Process connectivity in a naturally prograding river delta. *Water Resources Research*, *53*(3), 1841–1863.
- Slingerland, R., & Smith, N. D. (2004). River Avulsions and Their Deposits. *Annual Review of Earth and Planetary Sciences*, *32*(1), 257–285. <https://doi.org/10.1146/annurev.earth.32.101802.120201>
- Soong, T. W., & Zhao, Y. (1994). The flood and sediment characteristics of the Lower Yellow River in China. *Water International*, *19*(3), 129–137.
- Swenson, J. B., Voller, V. R., Paola, C., Parker, G., & Marr, J. G. (2000). Fluvio-deltaic sedimentation: A generalized Stefan problem. *European Journal of Applied Mathematics*, *11*(5), 433–452.
- Syvitski, J. P. M., & Saito, Y. (2007). Morphodynamics of deltas under the influence of humans. *Global and Planetary Change*, *57*(3–4), 261–282. <https://doi.org/10.1016/j.gloplacha.2006.12.001>
- Syvitski, J. P. M., Kettner, A. J., Overeem, I., Hutton, E. W. H., Hannon, M. T., Brakenridge, G. R., et al. (2009). Sinking deltas due to human activities. *Nature Geoscience*, *2*(10), 681–686. <https://doi.org/10.1038/ngeo629>
- Trower, E. J., Ganti, V., Fischer, W. W., & Lamb, M. P. (2018). Erosional surfaces in the Upper Cretaceous Castlegate Sandstone (Utah, USA): Sequence boundaries or autogenic scour from backwater hydrodynamics? *Geology*, *46*(8), 707–710.
- Vörösmarty, C. J., Syvitski, J., Day, J., de Sherbinin, A., Giosan, L., & Paola, C. (2009). Battling to Save the World's River Deltas. *Bulletin of the Atomic Scientists*, *65*(2), 31–43. <https://doi.org/10.2968/065002005>
- Xue, C. (1993). Historical changes in the Yellow River delta, China. *Marine Geology*, *113*(3–4), 321–330. [https://doi.org/10.1016/0025-3227\(93\)90025-Q](https://doi.org/10.1016/0025-3227(93)90025-Q)

*Chapter 1***ORIGIN OF A PREFERENTIAL AVULSION NODE
ON LOWLAND RIVER DELTAS**

A. J. Chadwick^{1*}, M. P. Lamb¹, A.J. Moodie², G. Parker³, J.A. Nittrouer²

¹Division of Geological and Planetary Sciences, California Institute of Technology, 1200 E. California Boulevard, Pasadena, California 91125, USA

²Department of Earth, Environmental and Planetary Science, Rice University, Houston, Texas, USA

³Department of Civil and Environmental Engineering and Department of Geology, University of Illinois at Urbana-Champaign, Urbana, IL, USA

* Adapted from Chadwick, A. J., Lamb, M. P., Moodie, A. J., Parker, G., & Nittrouer, J. A. (2019). Origin of a preferential avulsion node on lowland river deltas. *Geophysical Research Letters*, 46(8), 4267-4277.

DOI: <https://doi.org/10.1029/2019GL082491>

1.0. ABSTRACT

River deltas are built by cycles of lobe growth and abrupt channel shifts, or avulsions, that occur within the backwater zone of coastal rivers. Previous numerical models differ on the origin of backwater-scaled avulsion nodes, and their consistency with experimental data. To unify previous work, we developed a numerical model of delta growth that includes backwater hydrodynamics, river-mouth progradation, relative sea-level rise, variable flow regimes, and cycles of lobe growth, abandonment, and reoccupation. For parameter space applicable to lowland deltas, we found that flow variability is the primary mechanism to cause persistent avulsion nodes by focusing aggradation within the backwater zone. Backwater-scaled avulsion nodes also occur under less likely scenarios of initially uniform bed slopes, or during rapid relative sea-level rise and marine transgression. Our findings suggest that flow variability is a fundamental control on long-term delta morphodynamics.

1.1. INTRODUCTION

Many deltas are built through the deposition of discrete lobes punctuated by river avulsions, or channel-switching events (Slingerland & Smith, 2004; Jerolmack, 2009). River avulsions pose a hazard to human life and property (Soong & Zhao, 1994; Kidder & Liu, 2017) and are fundamental for building new land and nourishing wetland ecosystems (Richards et al., 2002; Edmonds et al., 2009). We need to understand where avulsions occur on lowland deltas to improve predictions of flooding hazards and sustainability.

Deltaic avulsions tend to occur repeatedly at a similar location, termed the avulsion node, which sets the delta-apex location and determines delta size (Jerolmack, 2009; Ganti et al., 2016a). The avulsion node on some landforms, typically steeper fan-deltas and alluvial fans, is controlled by valley width and slope variations (Blair & McPherson, 1994; Ganti et al., 2014; Hartley et al., 2017), but on lowland deltas avulsion nodes persist on unconfined alluvial plains. The distance from the shoreline to the avulsion node, termed the avulsion length (L_A), typically scales with the backwater length-scale of the river (L_b), that is, the ratio of channel depth (H_c) to bed-slope (S) (i.e., $L_A \sim L_b = \frac{H_c}{S}$) (Figure 1.1a) (Paola & Mohrig, 1996; Jerolmack & Swenson, 2007; Chatanantavet et al., 2012).

The backwater length approximates the distance that sea level influences river flow upstream and can extend for hundreds of kilometers for low-sloping rivers (Lamb et al., 2012).

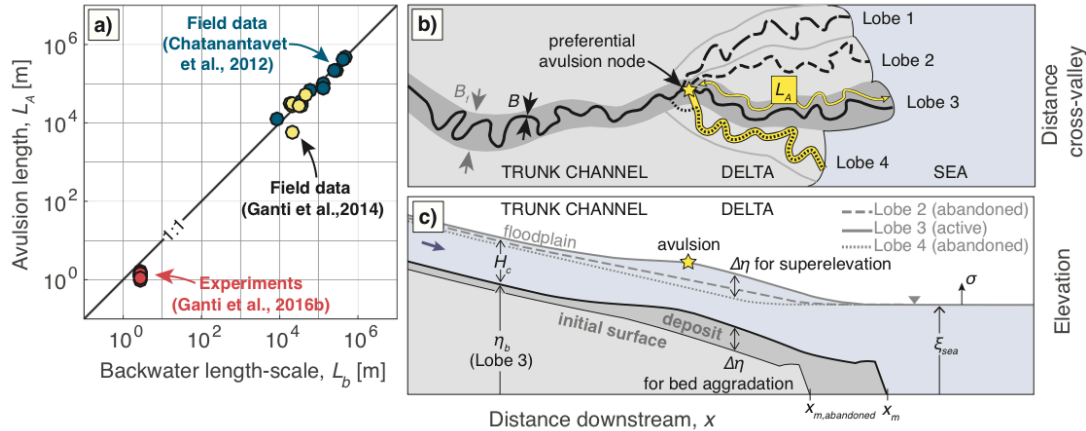


Figure 1.1: a) Correlation between avulsion length (L_A) and backwater length (L_b) from lowland river deltas and backwater-influenced experiments b) Planview schematic. Black solid lines are active channel of width B within a floodplain/lobe of width B_f (lobe 3). Broken lines are abandoned channels. After an avulsion, abandoned lobe 4 is reoccupied and its profile is joined with trunk channel at avulsion node (yellow star). c) Cross-section schematic, showing channel aggradation and floodplain superelevation of the active lobe (lobe 3) relative to the lowest abandoned lobe (lobe 4).

The Huanghe, China, provides an example where seven consecutive backwater-scaled avulsions occurred before major engineering (Ganti et al., 2014). In addition, abandoned lobes record six Holocene avulsions on the Mississippi that occurred within the backwater zone (Coleman et al., 1998; Chatanantavet et al., 2012), while two avulsions occurred farther upstream (Saucier, 1994; Chamberlain, 2018). Because river avulsions occur infrequently and are difficult to observe directly, flume experiments and numerical modeling have contributed substantially to our understanding. These modeling studies, however, differ in their explanation for the origin of persistent, backwater-scaled avulsion nodes.

Chatanantavet et al. (2012) hypothesized that avulsion nodes on lowland deltas originate from heightened channel-bed aggradation in the backwater zone that emerges due to flows of variable discharge. Using quasi-2D morphodynamic simulations, they showed that low flows deposit sediment in the upstream part of the backwater zone and high flows focus erosion and bypass farther downstream, resulting in a persistent peak in net aggradation in the middle of the backwater zone. Constant-discharge simulations, in contrast, yielded quasi-uniform flow and uniform bed-

aggradation rates. Chatanantavet et al. (2012) did not simulate avulsions and lobe switching, and the river mouth in their study was unrealistically fixed, which prevented riverbed aggradation due to progradation. Nonetheless, subsequent flume experiments that included progradation and natural lobe switching and reactivation supported their hypothesis by showing persistent avulsions about a preferential node at $L_A \sim 0.5L_b$, coinciding with a peak in channel-bed aggradation for an experiment with variable flows (Ganti et al., 2016a; 2016b). In contrast, a comparable constant-discharge experiment did not produce a persistent node, indicating that flow variability is the dominant mechanism to produce backwater-scaled avulsions.

Later numerical modeling studies by Moran et al. (2017) and Ratliff (2017), however, simulated delta growth with river-mouth progradation under a range of relative-sea-level-rise rates and constant-discharge conditions, and found backwater-scaled avulsion nodes despite the lack of flow variability. In their models, a wedge of sediment migrated downstream on a riverbed with an initially uniform slope, and eventually aggradation exceeded an imposed avulsion threshold. Thus, in contrast to experiments (Ganti et al., 2016a; 2016b) and earlier models (Chatanantavet et al., 2012), these studies suggest that backwater-scaled avulsions can be produced in models with constant water discharge. However, these models invoked a potentially unrealistic riverbed of uniform slope as an initial condition, and measured the potential for avulsion in terms of sediment accumulation thickness relative to the initial topography. In contrast, in natural environments, deltas tend to reoccupy lobes and build over previous fluvio-deltaic deposits. Thus, the assumed initial conditions in these numerical models might affect the emergence of an avulsion node.

Here we aim to elucidate the origin of a preferential avulsion node and unify the contradictory results of previous work. In particular, the model of Chatanantavet et al. (2012) requires flow variability to produce a persistent avulsion node, consistent with available experimental data, but the elimination of river-mouth progradation in their model might have biased their results. In contrast, more recent models (Moran et al., 2017; Ratliff, 2017) can produce persistent avulsion nodes with constant discharge, but they impose an unrealistic initial condition. To address these potentially problematic assumptions, we constructed a quasi-2D numerical model that allows for repeated lobe construction and avulsion such that lobes build on top of one another, thereby minimizing the role of initial topography as the delta evolves. The model also allows for river-mouth progradation. We

explored the model behavior over parameter space relevant to natural lowland deltas, including variable flow regimes and relative sea-level rise, to identify the conditions that cause a preferential backwater-scaled avulsion node.

1.2. METHODS

We aimed to isolate the cause of preferential avulsion nodes using a simplified model that captures delta-lobe construction, avulsion and reoccupation, and river-mouth progradation on lowland river deltas. The model does not represent a specific delta. Instead, the framework is generic and includes a deltaic plain with an imposed number of lobes (Figure 1.1b).

Following previous work, we modeled each lobe as a coupled river and floodplain of uniform floodplain width (B_f), channel sinuosity (Ω), wash-load ratio (Λ), and bed porosity (λ_p), which is well-described by a quasi-two-dimensional mass-balance framework (Parker, 2004; Parker et al., 2008a; 2008b; Chatanantavet et al. 2012). Sediment mass-balance also incorporates a floodplain representing the active delta lobe extent,

$$\frac{\partial \eta_b}{\partial t} + \sigma = - \frac{(1 + \Lambda)\Omega}{(1 - \lambda_p)B_f} \frac{\partial B q_t}{\partial x} \quad (1.1)$$

where η_b is channel bed elevation relative to sea level, t is time, σ is relative-sea-level-rise rate, x is downstream distance, and q_t is width-averaged flux of total bed-material load. Sediment is transported in a river of width B , and deposited uniformly over the floodplain width B_f (Parker, 2004). We routed water using a quasi-2D backwater equation for water mass and momentum conservation under quasi-steady flow conditions (Chatanantavet et al., 2012),

$$\frac{dH}{dx} = \frac{S - S_f}{1 - Fr^2} + \frac{Fr^2}{1 - Fr^2} \frac{H}{B} \frac{dB}{dx} \quad (1.2)$$

where H represents the channel depth, S is channel-bed slope, and $S_f = C_f Fr^2$ is friction slope with friction coefficient C_f and Froude number Fr . We assumed uniform channel width and a plume with constant spreading angle offshore (Lamb et al., 2012; Chatanantavet et al, 2012), but unlike previous

formulations the plume in our model advances and retreats in concert with the river mouth (Section 1.9.1). We routed sediment according to Engelund-Hansen (1967) for total bed-material load,

$$q_t = \sqrt{RgD^3} \frac{\alpha}{C_f} (\tau^*)^n \quad (1.3)$$

where R is submerged specific density of sediment, g is gravity, D is the median grain-size of bed material, τ^* is Shields number, and $\alpha = 0.05$ and $n = 2.5$ (Engelund & Hansen, 1967). Eqs. 1.2 and 1.3 adequately describe backwater hydrodynamics and sediment transport of sand-bedded rivers (Lamb et al., 2012; Nittrouer et al., 2012; Chatanantavet et al., 2014).

We approximated deltaic evolution over multiple cycles of lobe-switching using four one-dimensional profiles of predefined width, representing four distinct lobes (Figure 1.1b-c). Our choice of four lobes is arbitrary, but reasonable based on field observations (Roberts, 1997; Chu et al., 2006) and flume experiments (Reitz et al., 2010; Carlson et al., 2018). One delta lobe was active at a given time (Slingerland & Smith, 2004; Hajek & Edmonds, 2014), and the active lobe evolution was governed by Eqs. 1.1-3 and solved using finite differences (Section 1.9.2). We varied sediment supply at the upstream end with water discharge such that the normal-flow bed slope was held constant, and therefore erosion and deposition were not driven by changes in sediment-supply and water-discharge ratios (Paola, 2000). For the delta front, we used a moving-boundary formulation following Swenson et al. (2000) and others (Section 1.9.1). Inactive lobe shapes were unchanged when abandoned, approximating a river-dominated delta where reworking is minimal (Galloway, 1975); however abandoned lobes were partially drowned in cases due to relative sea-level rise.

We used an avulsion criterion given by a critical thickness of aggradation, which we refer to as superelevation ($\Delta\eta$):

$$\Delta\eta(x) \geq H^* H_c \quad (1.4)$$

in which H_c is the bankfull channel depth and H^* is the avulsion threshold, a dimensionless number that is of order unity (Jerolmack & Mohrig, 2007; Ganti et al., 2014), which we set to $H^* = 0.5$ consistent with field and experimental observations (Mohrig et al., 2000; Ganti et al., 2014; Ganti et al., 2016b). The critical superelevation $\Delta\eta$ may represent the local floodplain (or levee) elevation

relative to the distant floodplain or inactive lobes, or the bed aggradation thickness since the last avulsion (Figure 1.1c) (Mohrig et al., 2000; Hajek & Wolinsky, 2012; Ganti et al., 2014). In our model the floodplain (η_f) aggrades in concert with the channel bed ($\eta_f = \eta_b + H_c$; Section 1.9.1; Figure 1.1c) and inactive lobes remain unchanged once abandoned, so both explanations hold. We triggered an avulsion when and where the floodplain elevation of the active lobe exceeded the floodplain elevation of the lowest-elevation abandoned lobe ($\eta_{f,abandoned}$), evaluated at the same distance downstream from the trunk channel:

$$\Delta\eta(x) = \begin{cases} \eta_f(x) - \eta_{f,abandoned}(x) & \text{for } x \leq x_{m,abandoned} \\ \eta_f(x) - \xi_{sea} & \text{for } x > x_{m,abandoned} \end{cases} \quad (1.5)$$

where $x_{m,abandoned}$ is the stream-wise coordinate of the abandoned-lobe shoreline (Figure 1.1c). Seaward of the abandoned lobe, superlevation is measured relative to sea level (ξ_{sea}), consistent with assumptions in previous work (Ratliff, 2017). The occurrence of extreme floods and hydraulic connectivity with abandoned channels may also affect the location and timing of any one avulsion (Ganti et al., 2014; Nicholas et al., 2018), but following previous work these effects were neglected in our treatment of multiple avulsion cycles (Jerolmack & Paola, 2007; Hajek & Wolinsky, 2012).

After an avulsion, the river was routed to the lowest abandoned lobe by joining the bed profile of the active channel upstream of the avulsion site (the trunk channel) with the bed profile of the new flow path downstream (the daughter channel; Section 1.9.2). This process mimics the tendency of rivers to select steeper paths, fill in topographic lows (Slingerland & Smith, 2004; Straub et al., 2009), and to reoccupy previously abandoned channels (Reitz & Jerolmack, 2012). After establishing the new flow path, lobe construction (Eqs. 1.1-3) and avulsion setup (Eq. 1.4) began anew.

At the start of each model run, the initial state of the riverbed was assumed planar with a uniform downstream slope set to the transport slope for normal flow, similar to previous studies (Chatanantavet et al., 2012; Moran et al., 2017, Ratliff, 2017). However, due to the imposed number of lobes, after four avulsion cycles the river was forced to reoccupy lobes that were previously active. Thus, unlike previous work, the effect of the initial conditions was minimized after the fourth avulsion cycle.

For variable-discharge simulations, we implemented flow variability using a log-normal distribution of normal-flow depths (Section 1.9.3). The distribution is defined by the bankfull-exceedance probability F_{bf} , which describes the frequency of overbank flows relative to all possible flows, and the coefficient of variation CV , which describes the magnitude of low flows and high flows relative to the average flow. We randomly sampled the distribution with a characteristic flow-event duration (T_e) (Figure 1.S1). Gauge data of monthly-mean stage height ($T_e = 1$ month) from several lowland rivers show $F_{bf} \sim 5 - 20\%$ and $CV \sim 0.2 - 0.9$ (Table 1.S1; Ganti et al. 2014).

Our simulations explore how deltaic avulsion patterns respond to variable river discharge, relative sea-level rise, and initial topography by systematically varying the discharge and sea-level parameters for a base case characteristic of large, low-sloping deltas. We non-dimensionalized the model so that it can be applied to a wide range of river conditions (Section 1.9.4). The model is governed by nine input dimensionless parameters: bankfull Froude number in the normal-flow reach ($Fr_{n,bf}$), bankfull Shields number in the normal-flow reach ($\tau_{n,bf}^*$), friction factor (C_f), offshore basin floor depth normalized by bankfull depth (H_b^*), time normalized by the channel adjustment timescale ($t^* \sim \frac{tq_t}{L_b H_c}$), a dimensionless rate of relative sea-level rise ($\sigma^* \sim \frac{\sigma L_b}{qt}$), and the flow variability parameters (F_{bf}, CV, T_e^* ; Section 1.9.3), where $T_e^* = \frac{T_e q_t}{L_b H_c}$ is a dimensionless flow duration. In all simulations presented here, we assumed constant values typical of large sand-bedded rivers where $Fr_{n,bf} = 0.17$, $\tau_{n,bf}^* = 1$, $C_f = 0.005$, $H_b^* = 2$ (Table 1.S1), and changed only flow variability parameters (F_{bf} , CV , and T_e^*) and relative sea-level rise (σ^*). Model sensitivity to the other parameters is discussed in Section 1.9.6. For each set of dimensionless parameters, simulations proceeded until thirteen avulsions occurred, which was sufficient to capture trends in avulsion location (Section 1.9.4).

1.3. AVULSION NODES ORIGINATING FROM INITIAL CONDITIONS AND FLOW VARIABILITY

We first considered a scenario of constant river discharge equal to the bankfull condition and constant relative sea level ($F_{bf} = 1$, $CV = 0$, $\sigma^* = 0$), with other model parameters set to the base case. During the first four avulsion cycles, the delta built lobes on the initial surface, which

was a plane with a uniform seaward slope. The first avulsion occurred after 1.8 normalized time ($\Delta t^* = 1.8$), equivalent to 9-720 years for a range of parameters typical of natural deltas (Table 1.S1; Section 1.9.4), with an avulsion length equal to $0.78L_b$ ($L_A^* = 0.78$) (Figure 1.2a). Avulsion lengths were similar for the second, third, and fourth avulsions ($L_A^* = 0.74, 0.68, 0.98$, respectively). In contrast, after avulsion cycle four the constant-discharge delta built upon previously abandoned delta lobes and did not produce a backwater-scaled avulsion node. Normalized avulsion lengths varied considerably for these later avulsions ($L_A^* = 0.79 - 8.3$), and when avulsions occurred a reach of $3 - 5L_b$ was within 10% of the avulsion threshold, indicating no dominant avulsion location.

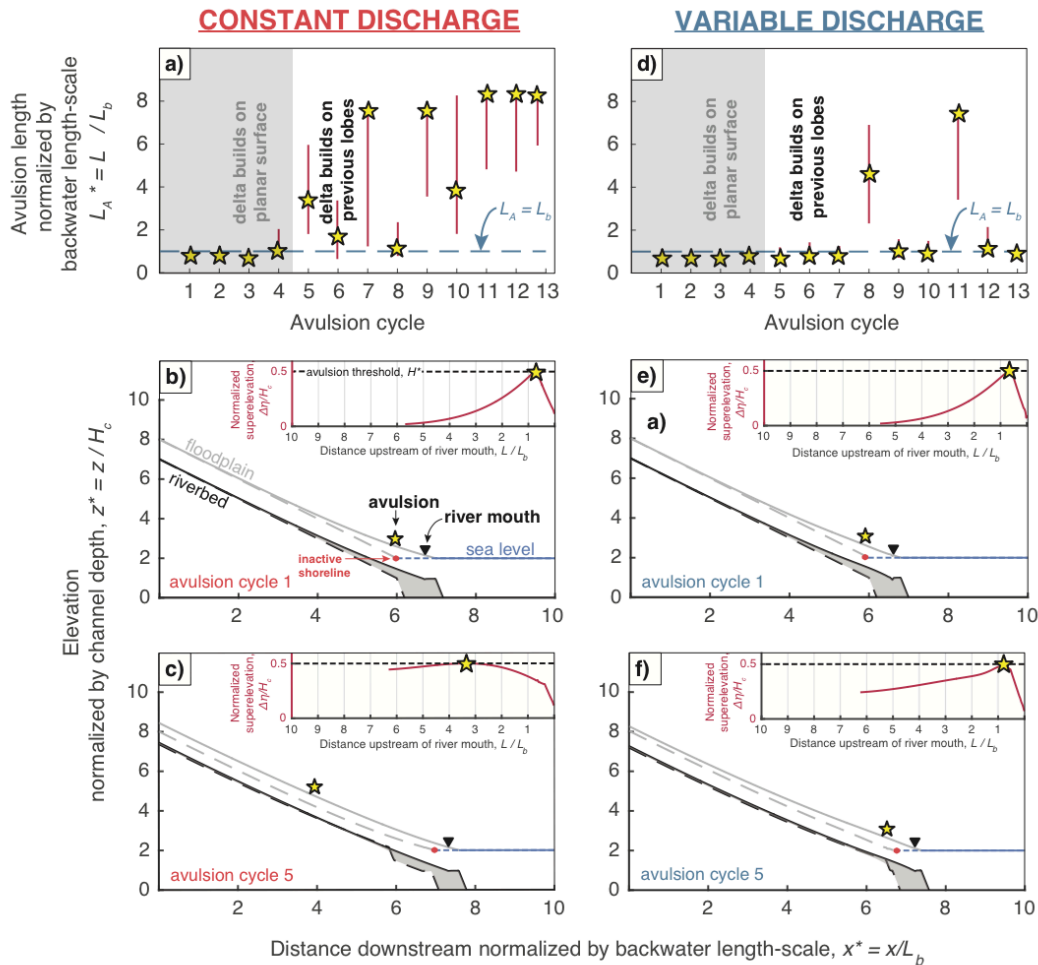


Figure 1.2: Model results for avulsion length through time over thirteen avulsion cycles under constant discharge (a) and variable discharge (d) with parameters set to base case ($Fr_{n,bf} = 0.17$, $\tau_{n,bf} = 1$, $C_f = 0.005$, $H_b^* = 2$). Red error bars indicate portion of reach within 10% of threshold superelevation

necessary for avulsion. Outliers in cycles 8 and 11 of the variable-discharge case are due to transient long-profile adjustment following major avulsions (cycles 7 and 10) that shift the avulsion node seaward and aggrade the trunk channel (Section 1.9.5). Results for channel long-profile under constant-discharge conditions (b-c) and variable flows (e-f) for two example avulsion cycles affected (cycle 1) and unaffected (cycle 5) by initial conditions. Black lines are riverbed profile at start (dashed) and end (solid) of an avulsion cycle. Floodplain profiles of active lobe (gray solid line) and lowest inactive lobe (gray dashed line) are used to calculate superelevation (see inset). Downstream of inactive-lobe shoreline location (red circle), floodplain superelevation is measured relative to sea level. Black triangles are river mouth at end of the avulsion cycle. Yellow stars show avulsion location. Delta progradation extended model domain length by $\sim 4L_b$ over thirteen cycles, leading to an increase in maximum possible avulsion length.

The consistent avulsion length during the first four avulsion cycles was a consequence of the assumed initial bed topography, and not due to backwater hydrodynamics. Delta front progradation led to channel aggradation and a quasi-steady concave-up bed elevation profile (Muto & Swenson, 2005; Bijkerk et al., 2016), in contrast to the uniform-slope bed profiles that were assumed for all lobes as initial conditions. Differencing the concave-up active lobe profile from the uniform-slope of the lowest inactive (and yet to be active) lobe profile resulted in a systematic downstream increase in superelevation (Figure 1.2b). Therefore, avulsions occurred at the farthest downstream location that was allowed, where superelevation was greatest, equivalent to the shoreline location on the inactive lobe of lowest elevation. Seaward of the inactive-lobe shoreline, avulsions did not occur because the active lobe elevation approached sea level and thus superelevation approached zero (Eq. 1.5). Avulsions that occurred at the shoreline of abandoned lobes necessarily scaled with the backwater length due to geometry; lobes prograded a unit fraction of the backwater length-scale before avulsing (i.e., the lobe progradation distance D scales as $D \approx H^*H_c/S \approx H^*L_b$; Ganti et al., 2014).

After avulsion cycles 1-4 in the constant-discharge model, the delta completely reworked its initial uniform slope and superelevation therefore was assessed by comparing the active lobe to previously occupied lobes, rather than to the planar initial surface. River profiles in these later avulsion cycles prograded with a quasi-steady and self-similar shape, causing nearly uniform deposition and a similar likelihood of avulsions everywhere, including far outside of the backwater zone (Figure 1.2c). Thus, avulsion locations and their apparent scaling with the backwater length in cycles 1-4 were a geometric artifact resulting from the assumed initial bed topography. Four

avulsions were required to rework the initial condition because four delta lobes were imposed (Figure 1.1A; Section 1.9.6). In absence of the uniform-slope initial condition, constant-discharge conditions did not produce a persistent backwater-scaled avulsion node.

Next, we considered a model run identical to the constant-discharge case but with variable discharge, using $CV = 0.53$, $F_{bf} = 0.05$, and $T_e^* = 0.001$, which is typical of lowland rivers (Table 1.S1). In this case, we observed a preferential avulsion node corresponding to an avulsion length nearly equal to the backwater length-scale, $L_A^* = L_A/L_b \sim 1$ (Figure 1.2d) which persisted through many avulsion cycles even after there was no longer an influence from the planar initial surface (Figure 1.2e-f). Consistent with previous studies (Lamb et al., 2012; Chatanantavet et al., 2012; Ganti et al., 2016a), periods of low flow had enhanced deposition due to spatial deceleration through the backwater zone and high flows eroded the downstream-most reach, resulting in a spatial peak in deposition rate midway through the backwater zone when averaged over many flow events. The avulsion node was coincident with the location of maximum deposition rate, and only a short reach ($< 0.4L_b$) was within 10% of the threshold at the time of an avulsion. Outliers are due to major avulsions that shifted the avulsion node downstream once the four lateral lobes were built, causing trunk channel aggradation and overall shoreline progradation (Section 1.9.5; Figure 1.S2).

1.4. NECESSARY DEGREE OF FLOW VARIABILITY

Given the importance of variable flows in controlling avulsion location for deltas that lack uniform bed slopes as initial conditions, we quantified how much flow variability is necessary to drive a preferential avulsion node. We ran 21 numerical experiments to systematically vary the coefficient of flow variation (CV), bankfull-exceedance probability (F_{bf}), and dimensionless flow duration (T_e^*) within a parameter space that represents many natural rivers (Table 1.S1). For each model run we changed one of these parameters and held all other parameters to base-case values. We focused our analysis on cycles 5-13 that were not affected by the initial uniform bed slope.

Isolation of the coefficient of variation (CV) reveals that there is an intermediate range $0.1 < CV < 0.6$ where modeled deltas preferentially avulsed within the upstream half of the backwater zone (Figure 1.3a). Similarly, avulsions occurred at a preferential node so long as less than 5% of

flows exceeded bankfull ($F_{bf} < 0.05$; Figure 1.3b) and that the duration of flow events was less than 10% of the reach-filling timescale ($T_e^* < 0.1$; Figure 1.3c). The conditions needed for a preferential avulsion node predicted by the model are common for natural lowland rivers (Table 1.S1) and correspond to a state of continuous riverbed adjustment, where the scours cut by large floods are partially filled during intervening low flows. Continuous riverbed adjustment is necessary for persistent backwater effects (Chatanantavet et al., 2014) and in our model resulted in broad convex-up portions of the long profile when averaged over many flood events (Figure 1.S3). Under milder flow regimes ($CV < 0.1$) and longer flow durations ($T_e^* > 0.1$) the riverbed fully adjusted to normal-flow conditions, resulting in uniform aggradation rates without a preferential avulsion location similar to the constant-discharge scenario. Flashier flow regimes ($CV > 0.6$) and high probabilities of bankfull exceedance ($F_{bf} > 0.05$) also lacked a preferred avulsion node, as the riverbed adjusted to normal-flow conditions associated with large floods.

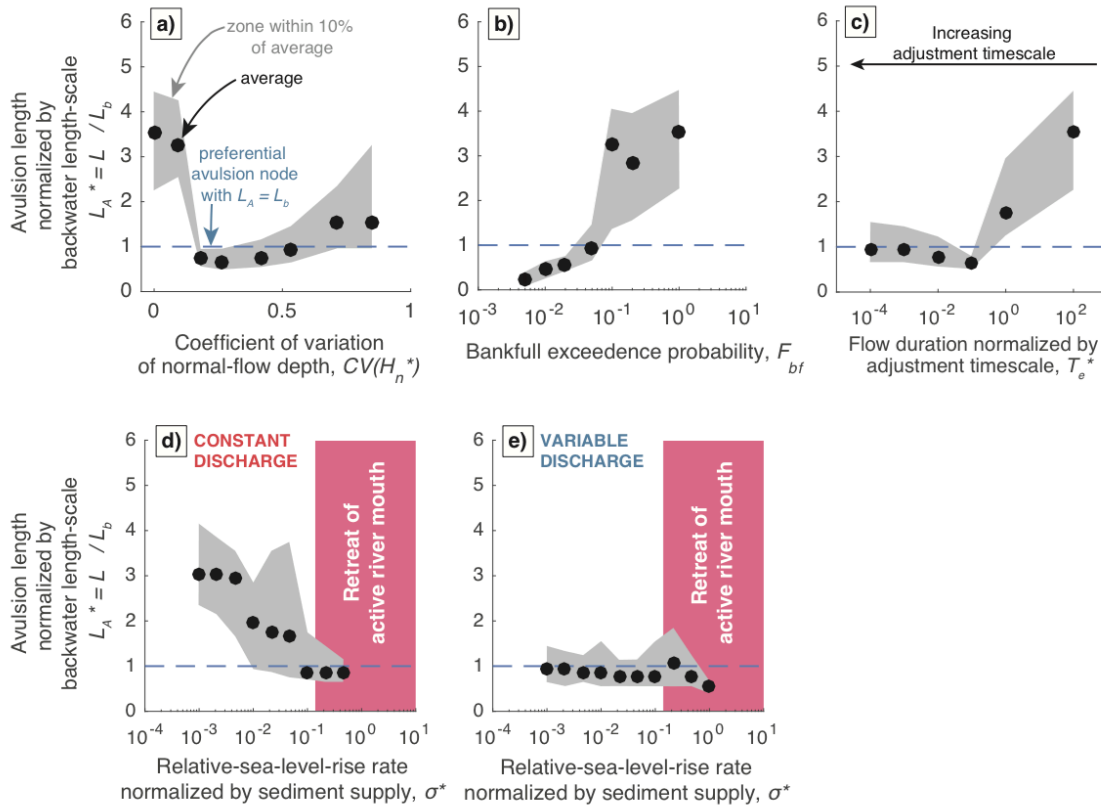


Figure 1.3: Model results for avulsion length with changing flow variability parameters: CV (a), F_{bf} (b), and T_e^* (c), as well as variation of relative-sea-level-rise rate σ^* under constant discharge (d) and variable discharge (e). Black circles show avulsion locations averaged over cycles not influenced by

initial conditions (cycles 5-13), and gray shaded areas denote the average reach within 10% of avulsion threshold at times of avulsion.

1.5. AVULSION NODES ORIGINATING FROM RELATIVE SEA-LEVEL RISE

In previous sections, the dimensionless relative-sea-level-rise rate was set to zero to isolate the initial conditions and flow variability. To relax this assumption, we varied the dimensionless relative-sea-level-rise rate across a range that encompasses many modern deltas ($\sigma^* = 10^{-3} - 10^0$) under constant-discharge (Figure 1.3d) and variable-discharge (Figure 1.3e) conditions, with other parameters identical to the base case (Table 1.S1). Similar to the scenario of $\sigma^* = 0$, constant-discharge deltas with $\sigma^* = 10^{-3} - 10^{-1}$ did not have a preferential node, whereas all variable-discharge cases had a preferential avulsion node with $L_A/L_b \sim 1$. Thus, relative sea-level rise at moderate rates common to modern deltas did not significantly affect avulsion node occurrence (Figure 1.3d-e). However, at very high rise rates ($\sigma^* > 10^{-1}$) the river mouth retreated upstream, forcing a strong downstream increase in deposition. Thus, for $\sigma^* > 10^{-1}$ the downstream increase in aggradation resulted in avulsion locations that coincided with the shoreline of the lowest-elevation inactive lobe, which scaled with the backwater length for the same geometric reasons as in the cases with planar initial conditions (Figure 1.S4).

1.6. DISCUSSION AND CONCLUSIONS

Our results reconcile previous work by showing that variable flow regimes are necessary to produce backwater-scaled avulsion nodes on lowland deltas. Our finding is consistent with experiments that isolated the role of flow variability (Ganti et al., 2016a) on deltas that experienced continuous lobe growth, abandonment and reoccupation. A certain amount of flow variability ($0.1 < CV < 0.6$, $F_{bf} < 0.05$, $T_e^* < 0.1$) is necessary to produce persistent backwater effects so that the riverbed is in a continual state of morphodynamic adjustment (Chatanantavet et al., 2014). These conditions are common to natural rivers (Table 1.1). Continual bed adjustment from floods in our model produced very broad, low-relief upward convexities in the riverbed in the backwater zone (Figure 1.2e-f; Figure 1.S3), consistent with the bed topography of the lower 200-700 km of the Mississippi (Harmar, 2004; Nittrouer et al., 2012; Figure 1.S5), which may be a topographic signature of backwater-mediated avulsions in other rivers.

In contrast, constant-discharge numerical experiments tend towards a graded state without strong backwater effects or a preferential node location. Our results suggest that previous numerical models that lacked variable discharges and produced backwater-scaled avulsions (Moran et al., 2017; Ratliff, 2017) were likely affected by initial conditions of uniformly sloped initial surfaces. A backwater-scaled avulsion node under these conditions is a geometric consequence of assessing superelevation of a prograding channel or lobe relative to a planar seaward-sloping landscape. For similar reasons, relative sea-level rise can also cause persistent avulsion nodes under constant discharge conditions, but only under high rise rates that cause marine transgression. In these cases, avulsions occur at the most downstream location allowed: near the inactive-lobe shoreline, which was $\sim L_b$ upstream of the active river mouth at the time of avulsion due to the geometry of lobe progradation. Although the simulations of Chatanantavet et al. (2012) also had an initial uniform bed slope and relative sea-level rise, they did not produce a persistent avulsion node under constant-discharge conditions because the model lacked river-mouth progradation.

In a sensitivity analysis, we found that changing other model parameters does not affect our results on the origin of preferred avulsion node (Section 1.9.6). Larger avulsion thresholds, H^* , cause avulsions to occur farther upstream, but do not change the overall results (Figure 1.S6). Likewise, the number of imposed delta lobes affects the number of avulsion cycles that are affected by the initial conditions, and the frequency of trunk-channel-filling avulsions (Section 1.9.5), but does not affect the origin of a preferential avulsion node.

Our variable-discharge simulations produced avulsion lengths within a factor of two of the backwater length-scale, similar to the distribution of avulsion lengths on the Huanghe (Ganti et al., 2014) and Mississippi (Coleman et al., 1998; Chatanantavet et al., 2012). Following four lateral avulsions that occupied the available prograding lobes, the avulsion node in our model shifted downstream in tandem with net shoreline progradation, as has been documented on the Huanghe (Ganti et al., 2014) and in flume experiments (Ganti et al., 2016a). Our model also produced outliers in the avulsion-length distribution, where deltas with a backwater-scaled avulsion node sometimes have avulsions much farther upstream, similar to the Mississippi (Chamberlain et al., 2018). These larger-scale avulsions occurred in our model near the time when the avulsion node shifted

downstream; once a full set of lateral avulsions occurred, the trunk channel upstream of the avulsion node must aggrade to allow continued net progradation (Section 1.9.5).

Avulsion node locations could be different when channels reoccupy topographically dissimilar lobes (e.g., the Danube; Giosan et al., 2005), cut new channels in the floodplain (Hajek & Edmonds, 2014), or where lobes have been modified by marine processes (e.g., the Red River; Mathers & Zalasiewicz, 1999). However, when channels build upon topographically similar abandoned delta-lobe topography, which is a common scenario, a backwater-scaled avulsion node emerges when flow variability is sufficient to cause a peak in aggradation within the backwater zone. Thus, changing flow regimes due to climate or built infrastructure may affect flood hazards and wetland sustainability by shifting the location of future avulsions.

1.7. REFERENCES

- Andrews, E. D. (1980). Effective and bankfull discharges of streams in the Yampa River basin, Colorado and Wyoming. *Journal of Hydrology*, 46(3-4), 311-330.
- Baumanis, C., & Kim, W. (2018). Reverse migration of lithofacies boundaries and shoreline in response to sea-level rise. *Basin Research*, 30, 89-100.
- Bijkerk, J. F., Eggenhuisen, J. T., Kane, I. A., Meijer, N., Waters, C. N., Wignall, P. B., & McCaffrey, W. D. (2016). Fluvio-marine sediment partitioning as a function of basin water depth. *Journal of Sedimentary Research*, 86(3), 217-235.
- Blair, T. C., & McPherson, J. G. (1994). Alluvial fans and their natural distinction from rivers based on morphology, hydraulic processes, sedimentary processes, and facies assemblages. *Journal of sedimentary research*, 64(3a), 450-489.
- Borland, W. M. (1971). Reservoir sedimentation. *River mechanics*, 2, 29-1.
- Carlson, B., Piliouras, A., Muto, T., & Kim, W. (2018). Control of Basin Water Depth On Channel Morphology and Autogenic Timescales in Deltaic Systems. *Journal of Sedimentary Research*, 88(9), 1026-1039.
- Chamberlain, E. L., Törnqvist, T. E., Shen, Z., Mauz, B., & Wallinga, J. (2018). Anatomy of Mississippi Delta growth and its implications for coastal restoration. *Science advances*, 4(4), eaar4740.
- Chatanantavet, P., Lamb, M. P., & Nittrouer, J. A. (2012). Backwater controls of avulsion location on deltas. *Geophysical Research Letters*, 39(1).
- Chatanantavet, P., & Lamb, M. P. (2014). Sediment transport and topographic evolution of a coupled river and river plume system: An experimental and numerical study. *Journal of Geophysical Research: Earth Surface*, 119(6), 1263-1282.
- Chu, Z. X., Sun, X. G., Zhai, S. K., & Xu, K. H. (2006). Changing pattern of accretion/erosion of the modern Yellow River (Huanghe) subaerial delta, China: Based on remote sensing images. *Marine Geology*, 227(1-2), 13-30.
- Church, M. (2006). Bed material transport and the morphology of alluvial river channels. *Annu. Rev. Earth Planet. Sci.*, 34, 325-354.
- Coleman, J. M., Roberts, H. H., & Stone, G. W. (1998). Mississippi River delta: an overview. *Journal of Coastal Research*, 14(3).
- Dade, W. B., & Friend, P. F. (1998). Grain-size, sediment-transport regime, and channel slope in alluvial rivers. *The Journal of Geology*, 106(6), 661-676.
- Edmonds, D. A., Hoyal, D. C., Sheets, B. A., & Slingerland, R. L. (2009). Predicting delta avulsions: Implications for coastal wetland restoration. *Geology*, 37(8), 759-762.
- Einstein, H. A. (1950), The bed-load function for sediment transportation in open channel flows, Technical Bulletin 1026, U.S. Dept. of the Army, Soil Conservation Service.
- Engelund, F., & Hansen, E. (1967). A monograph on sediment transport in alluvial streams. *Technical University of Denmark Østervoldgade 10, Copenhagen K.*
- Fernandes, A. M., Törnqvist, T. E., Straub, K. M., & Mohrig, D. (2016). Connecting the backwater hydraulics of coastal rivers to fluvio-deltaic sedimentology and stratigraphy. *Geology*, 44(12), 979-982.
- Galloway, W. (1975). Process framework for describing the morphologic and stratigraphic evolution of deltaic depositional systems. *Deltas: Models for Exploration*.
- Galloway, W. E. (1989). Genetic stratigraphic sequences in basin analysis I: architecture and genesis of flooding-surface bounded depositional units. *AAPG bulletin*, 73(2), 125-142.
- Ganti, V., Chu, Z., Lamb, M. P., Nittrouer, J. A., & Parker, G. (2014). Testing morphodynamic controls on the location and frequency of river avulsions on fans versus deltas: Huanghe (Yellow River), China. *Geophysical Research Letters*, 41(22), 7882-7890.

- Ganti, V., Chadwick, A. J., Hassenruck-Gudipati, H. J., Fuller, B. M., & Lamb, M. P. (2016). Experimental river delta size set by multiple floods and backwater hydrodynamics. *Science advances*, 2(5), e1501768.
- Ganti, V., Chadwick, A. J., Hassenruck-Gudipati, H. J., & Lamb, M. P. (2016). Avulsion cycles and their stratigraphic signature on an experimental backwater-controlled delta. *Journal of Geophysical Research: Earth Surface*, 121(9), 1651-1675.
- Giosan, L., Donnelly, J. P., Vespremeanu, E., Bhattacharya, J. P., Olariu, C., & Buonaiuto, F. S. (2005). River delta morphodynamics: Examples from the Danube delta.
- Hajek, E. A., & Edmonds, D. A. (2014). Is river avulsion style controlled by floodplain morphodynamics?. *Geology*, 42(3), 199-202.
- Hajek, E. A., & Wolinsky, M. A. (2012). Simplified process modeling of river avulsion and alluvial architecture: connecting models and field data. *Sedimentary Geology*, 257, 1-30.
- Harmar, O. P. (2004). *Morphological and process dynamics of the Lower Mississippi River* (Doctoral dissertation, University of Nottingham).
- Hartley, A. J., Weissmann, G. S., & Scuderi, L. (2017). Controls on the apex location of large deltas. *Journal of the Geological Society*, 174(1), 10-13.
- Hotchkiss, R. H., & Parker, G. (1991). Shock fitting of aggradational profiles due to backwater. *Journal of Hydraulic Engineering*, 117(9), 1129-1144.
- Jerolmack, D. J., & Mohrig, D. (2007). Conditions for branching in depositional rivers. *Geology*, 35(5), 463-466.
- Jerolmack, D. J., & Paola, C. (2007). Complexity in a cellular model of river avulsion. *Geomorphology*, 91(3-4), 259-270.
- Jerolmack, D. J., & Swenson, J. B. (2007). Scaling relationships and evolution of distributary networks on wave-influenced deltas. *Geophysical Research Letters*, 34(23).
- Jerolmack, D. J. (2009). Conceptual framework for assessing the response of delta channel networks to Holocene sea level rise. *Quaternary Science Reviews*, 28(17), 1786-1800.
- Kidder, T. R., & Liu, H. (2017). Bridging theoretical gaps in geoarchaeology: Archaeology, geoarchaeology, and history in the Yellow River valley, China. *Archaeological and Anthropological Sciences*, 9(8), 1585-1602.
- Kim, W., Paola, C., Voller, V. R., & Swenson, J. B. (2006). Experimental measurement of the relative importance of controls on shoreline migration. *Journal of Sedimentary Research*, 76(2), 270-283.
- Kostic, S., & Parker, G. (2003). Progradational sand-mud deltas in lakes and reservoirs. Part 1. Theory and numerical modeling. *Journal of Hydraulic Research*, 41(2), 127-140.
- Lague, D., Hovius, N., & Davy, P. (2005). Discharge, discharge variability, and the bedrock channel profile. *Journal of Geophysical Research: Earth Surface*, 110(F4).
- Lamb, M. P., Nittrouer, J. A., Mohrig, D., & Shaw, J. (2012). Backwater and river plume controls on scour upstream of river mouths: Implications for fluvio-deltaic morphodynamics. *Journal of Geophysical Research: Earth Surface*, 117(F1).
- Langbein, W. B., & Leopold, L. B. (1964). Quasi-equilibrium states in channel morphology. *American Journal of Science*, 262(6), 782-794.
- LeBoutillier, D. W., & Waylen, P. R. (1993). A stochastic model of flow duration curves. *Water Resources Research*, 29(10), 3535-3541.
- Liang, M., Van Dyk, C., & Passalacqua, P. (2016). Quantifying the patterns and dynamics of river deltas under conditions of steady forcing and relative sea level rise. *Journal of Geophysical Research: Earth Surface*, 121(2), 465-496.
- Maselli, V., Pellegrini, C., Del Bianco, F., Mercorella, A., Nones, M., Crose, L., Guerrero, M., & Nittrouer, J. A. (2018). River Morphodynamic Evolution Under Dam-Induced Backwater: An Example from the Po River (Italy). *Journal of Sedimentary Research*, 88(10), 1190-1204.
- Mathers, S., & Zalasiewicz, J. (1999). Holocene sedimentary architecture of the Red River delta, Vietnam. *Journal of Coastal Research*, 314-325.

- Milliman, J. D., & Syvitski, J. P. (1992). Geomorphic/tectonic control of sediment discharge to the ocean: the importance of small mountainous rivers. *The Journal of Geology*, 100(5), 525-544.
- Mohrig, D., Heller, P. L., Paola, C., & Lyons, W. J. (2000). Interpreting avulsion process from ancient alluvial sequences: Guadalupe-Matarranya system (northern Spain) and Wasatch Formation (western Colorado). *Geological Society of America Bulletin*, 112(12), 1787-1803.
- Moran, K. E., Nittrouer, J. A., Perillo, M. M., Lorenzo-Trueba, J., & Anderson, J. B. (2017). Morphodynamic modeling of fluvial channel fill and avulsion time scales during early Holocene transgression, as substantiated by the incised valley stratigraphy of the Trinity River, Texas. *Journal of Geophysical Research: Earth Surface*, 122(1), 215-234.
- Muto, T., & Steel, R. J. (1997). Principles of regression and transgression: the nature of the interplay between accommodation and sediment supply: perspectives. *Journal of Sedimentary Research*, 67(6).
- Muto, T., & Steel, R. J. (2002). Role of autoretreat and A/S changes in the understanding of deltaic shoreline trajectory: a semi-quantitative approach. *Basin Research*, 14(3), 303-318.
- Muto, T., & Swenson, J. B. (2005). Large-scale fluvial grade as a nonequilibrium state in linked depositional systems: Theory and experiment. *Journal of Geophysical Research: Earth Surface*, 110(F3).
- Nicholas, A. P., Aalto, R. E., Sambrook Smith, G. H., & Schwendel, A. C. (2018). Hydrodynamic controls on alluvial ridge construction and avulsion likelihood in meandering river floodplains. *Geology*.
- Nittrouer, J. A., Mohrig, D., Allison, M. A., & Peyret, A. P. B. (2011). The lowermost Mississippi River: a mixed bedrock-alluvial channel. *Sedimentology*, 58(7), 1914-1934.
- Nittrouer, J. A., Shaw, J., Lamb, M. P., & Mohrig, D. (2012). Spatial and temporal trends for water-flow velocity and bed-material sediment transport in the lower Mississippi River. *Bulletin*, 124(3-4), 400-414.
- Pang, J. Z., & Si, S. H. (1979). Evolution of the Yellow River mouth: I. Historical shifts. *Oceanologia et Limnologia Sinica*, 10(2), 136-141.
- Paola, C. (2000). Quantitative models of sedimentary basin filling. *Sedimentology*, 47(s1), 121-178.
- Paola, C., & Mohrig, D. (1996). Palaeohydraulics revisited: palaeoslope estimation in coarse-grained braided rivers. *Basin Research*, 8(3), 243-254.
- Paola, C., Twilley, R. R., Edmonds, D. A., Kim, W., Mohrig, D., Parker, G., Viparelli, E., & Voller, V. R. (2011). Natural processes in delta restoration: Application to the Mississippi Delta. *Annual Review of Marine Science*, 3, 67-91.
- Parker, G. (1979). Hydraulic geometry of active gravel rivers, *J. Hydraul. Eng.*, 105(9), 1185-1201.
- Parker, G. (2004). 1D sediment transport morphodynamics with applications to rivers and turbidity currents. *E-book available at Gary Parker's Morphodynamics Web Page, last update April, 13, 2006.*
- Parker, G., Muto, T., Akamatsu, Y., Dietrich, W. E., & Lauer, J. (2008). Unravelling the conundrum of river response to rising sea-level from laboratory to field. Part I: Laboratory experiments. *Sedimentology*, 55(6), 1643-1655.
- Parker, G., Muto, T., Akamatsu, Y., Dietrich, W. E., & Wesley Lauer, J. (2008). Unravelling the conundrum of river response to rising sea-level from laboratory to field. Part II. The Fly-Strickland River system, Papua New Guinea. *Sedimentology*, 55(6), 1657-1686.
- Parker, G., Wilcock, P. R., Paola, C., Dietrich, W. E., & Pitlick, J. (2007). Physical basis for quasi-universal relations describing bankfull hydraulic geometry of single-thread gravel bed rivers. *Journal of Geophysical Research: Earth Surface*, 112(F4).
- Ratliff, K. M. (2017). *From the River to the Sea: Modeling Coastal River, Wetland, and Shoreline Dynamics* (Doctoral dissertation).
- Reitz, M. D., Jerolmack, D. J., & Swenson, J. B. (2010). Flooding and flow path selection on alluvial fans and deltas. *Geophysical Research Letters*, 37(6).
- Reitz, M. D., & Jerolmack, D. J. (2012). Experimental alluvial fan evolution: Channel dynamics, slope controls, and shoreline growth. *Journal of Geophysical Research: Earth Surface*, 117(F2).

- Richards, K., Brasington, J., & Hughes, F. (2002). Geomorphic dynamics of floodplains: ecological implications and a potential modelling strategy. *Freshwater Biology*, 47(4), 559-579.
- Richards, K., Brasington, J., & Hughes, F. (2002). Geomorphic dynamics of floodplains: ecological implications and a potential modelling strategy. *Freshwater Biology*, 47(4), 559-579.
- Roberts, H. H. (1997). Dynamic changes of the Holocene Mississippi River delta plain: the delta cycle. *Journal of Coastal Research*, 605-627.
- Saucier, R. T. (1994). Geomorphology and quaternary geologic history of the Lower Mississippi Valley (Vol. 1). US Army Engineer Waterways Experiment Station.
- Slingerland, R., & Smith, N. D. (2004). River avulsions and their deposits. *Annu. Rev. Earth Planet. Sci.*, 32, 257-285.
- Soong, T. W., & Zhao, Y. (1994). The flood and sediment characteristics of the Lower Yellow River in China. *Water International*, 19(3), 129-137.
- Stedinger, J. R., Vogel, R. M., & Foufoula-Georgiou, E. (1993). Frequency analysis of extreme events, Chapter 18 in Handbook of Hydrology, edited by DR Maidment.
- Straub, K. M., Paola, C., Mohrig, D., Wolinsky, M. A., & George, T. (2009). Compensational stacking of channelized sedimentary deposits. *Journal of Sedimentary Research*, 79(9), 673-688.
- Sturm, T. W. (2010). *Open channel hydraulics*. New York: McGraw-Hill.
- Swenson, J. B., Voller, V. R., Paola, C., Parker, G., & Marr, J. G. (2000). Fluvio-deltaic sedimentation: A generalized Stefan problem. *European Journal of Applied Mathematics*, 11(5), 433-452.
- Syvitski, J. P., Kettner, A. J., Overeem, I., Hutton, E. W., Hannon, M. T., Brakenridge, G. R., ... & Nicholls, R. J. (2009). Sinking deltas due to human activities. *Nature Geoscience*, 2(10), 681.
- Syvitski, J. P., & Saito, Y. (2007). Morphodynamics of deltas under the influence of humans. *Global and Planetary Change*, 57(3-4), 261-282.
- Venditti, J. G., & Church, M. (2014). Morphology and controls on the position of a gravel-sand transition: Fraser River, British Columbia. *Journal of Geophysical Research: Earth Surface*, 119(9), 1959-1976.
- Wolman, M. G., and J. P. Miller (1960), Magnitude and frequency of forces in geomorphic processes, *J. Geol.*, 68, 54-74, doi:10.1086/626637

1.8. SUPPLEMENTARY MATERIAL

1.8.1. Treatment of the river mouth and delta front

The river mouth and plume set the downstream end of the backwater zone. Previous models of backwater hydrodynamics have considered a fixed river mouth position, resulting in a constant flow-width profile and fixed backwater zone (Lamb et al., 2012; Chatanantavet et al., 2012; Chatanantavet et al., 2014). This is a good approximation over the timescales of flow events considered by these studies, where the degree of sea-level and land-surface change is small compared to the channel depth. However, the timescales of river avulsion are sufficiently long to drive lobe aggradation and drowning on the order of the channel depth, which could drive significant river mouth advance and retreat respectively, resulting in changes to the flow-width profile.

In this study we develop a new approach to modeling backwater zones that may translate over the timescales of river avulsion. The spatio-temporal evolution of flow width is driven by the emergence and submergence of the land surface. At a given time, the location of the river mouth (x_m) is set by the intersection of the floodplain profile η_f with sea-level ξ_o ,

$$x_m = x|_{\eta_f(x) = \xi_o} \quad (1. S1)$$

where the floodplain elevation is defined as the sum of the bed elevation and channel depth,

$$\eta_f = \eta_b + H_c \quad (1. S2)$$

The flow-width profile is a piecewise function of the channel width, assumed constant and uniform upstream of the river mouth, and a linearly spreading plume downstream

$$B = \begin{cases} B_0 & x < x_m \\ B_0 \frac{H_c}{H_{nf}} + B_{flare} \frac{H_{nf} - H_c}{H_{nf}} & x \geq x_m \end{cases} \quad (1. S3)$$

where B is the flow width, B_0 is the channel width, B_{flare} is the width of the flare, and $H_{nf} = \xi_o - \eta$ is the no-flow depth. Upstream of the river mouth ($x < x_m$), flow is confined by the channel and the flow width is set by the channel width (B_0). Downstream of the mouth ($x \geq x_m$), the unconfined portion of the flow expands laterally to form the river plume. In this setting, B is the depth-averaged width of a submerged channel and a linearly expanding flare,

$$B_{flare} = B_c + 2 \tan \theta (x_m - x) \quad (1. S4)$$

where θ is the plume spreading angle, here set to fifteen degrees (Lamb et al., 2012; Chatanantavet et al., 2014). When the river mouth progrades into an empty basin with flat topography, $H_c = 0$ and the flow width in Eq. 1.S3 reduces to the flare width ($B = B_{flare}$). When the land is drowned, the river mouth retreats and a portion of the flow is confined to the submerged channel. The terms $\frac{H_c}{H_{nf}}$ and $\frac{H_{nf}-H_c}{H_{nf}}$ in Eq. 1.S3 represent the fraction of the no-flow depth that is of width B_0 and width B_{flare} respectively to yield a depth-averaged width of B . This scheme leads to dynamic backwater profiles that advance with river mouth progradation (i.e., increasing x_m) and back-step during shoreline retreat (i.e., decreasing x_m), and conveniently facilitates numerical stability in our simulations by producing a gradient in width (dB/dx) that is everywhere differentiable.

At the river mouth lateral flow expansion drives an abrupt deceleration of flow, resulting in a mound of sediment that accumulates and steepens. At sufficiently steep slopes, fluvial sediment transport gives way to gravity flows and avalanching to form a delta front, or foreset. We model the development of delta fronts in terms of a threshold slope condition following Hotchkiss and Parker (1991). A delta front develops at position x_s if the bed steepens to the threshold slope S_a associated with gravity flows and sediment avalanching.

$$x_s = x|_{S \geq S_a} \quad (1. S5)$$

Once a delta front initiates, the slope of the front is fixed at S_a and deposition drives progradation of the new delta front and delta toe according to shock-capturing conditions (Kostic & Parker, 2003; Parker et al., 2004; Kim et al., 2006; Parker et al., 2008a; Chatanantavet et al., 2014).

Previous work has focused on conditions where the delta front is sufficiently far downstream such that the water velocity is approximately zero. Over longer timescales, however, we find that lobe-switching over antecedent topography can drive the creation of shallow foreset wedges farther upstream, with significant flow velocities at their toes. The foreset wedges pose an order of magnitude discontinuity in bed slope that violates the gradually-varied flow assumption in the backwater equation (Parker, 2004). Across the shallow foreset wedge, we reason the water surface is more accurately described by the Borda-Carnot relationship for flow encountering a sudden expansion (Sturm, 2010).

$$\left(\xi + \frac{U^2}{2g}\right)_u = \left(\xi + \frac{U^2}{2g}\right)_d + \frac{1}{2g}(U_u - U_d)^2 \quad (1. S6)$$

where ξ is the water surface elevation, U is flow velocity, g is acceleration due to gravity, and subscripts u and d denote conditions upstream and downstream of the shallow foreset respectively. We can rearrange to find that this describes a “jump” in the water surface at the lip of the foreset.

$$\frac{\Delta\xi}{H_u} = Fr_u^2(1 - r_A) \quad (1. S7)$$

where $\Delta\xi$ is the increase in water surface elevation from the upstream to downstream end and r_A is the ratio of the upstream to downstream cross-sectional areas of the flow. For the low Froude number scenarios considered in our study, water surface deflections are limited to 1-5% of the flow depth measured upstream of the foreset. Nevertheless, this treatment is important for avoiding erroneous and unstable application of the backwater formula to reaches with a steep, thin delta front. Downstream of the foreset, the flow can again be adequately described in terms of quasi-steady, gradually varied flow.

1.8.2. Model workflow

Our simplified modeling scenario consists of an initial planar delta surface with a topset slope equal to the normal flow bankfull transport slope (S_0), a delta foreset slope equal to five times the topset slope ($S_a = 5S_0$) (Borland, 1971; Hotchkiss & Parker, 1991), and a horizontal basin floor. We vary water discharge at the upstream end, and co-vary sediment supply such that

all discharges have the same equilibrium transport slope, simulating an alluvial river profile that is always at transport capacity and isolating backwater effects from long-term adjustment in riverbed slope due to changes in sediment-supply and water-discharge ratios (Dade & Friend, 1998; Paola, 2000; Parker et al., 2004; Church, 2006; Ganti et al., 2016b). For each timestep, the river mouth is identified according to S1 and any developing shock fronts are detected using Eq. 1.S5. The backwater equation is solved using an upwind predictor-corrector scheme applied to Eq. 1.2, except across foreset wedges where Eq. 1.S7 is locally applied. Next, sediment is routed upstream of the foreset wedge with Eq. 1.3 utilizing a “ghost node” at the upstream end (Parker 2004). After routing water and sediment, the delta foreset and riverbed profile η_b for the next timestep are calculated using a finite-difference approximation of Eq. 1.1 in a moving-boundary formulation that is explicit, centered in space, and forward in time (Kostic & Parker, 2003; Parker et al., 2004). We update the floodplain elevation profile using Eq. 1.S2, assuming the channel depth profile is equal to the flow depth profile (Eq. 1.2) under bankfull discharge conditions. The updated floodplain profile is used to determine the super-elevation using Eq. 1.5, and also determines the river mouth for the next timestep via Eq. 1.S1. We repeat this numerical scheme, stepping through time until the avulsion threshold is exceeded somewhere along the long-profile according to Eq. 1.4. At this point an avulsion occurs, and avulsion length is measured by the stream-wise distance along the parent channel between the avulsion location and the river mouth.

We find that stable numerical simulation requires an especially small timestep when large floods erode the bed near the river mouth and drive progradation of the delta front. For computational expedience, we employ a discharge-dependent CFL condition based on rates of change of bed topography near the river mouth, maintaining numerical stability during high flows and vastly speeding up model simulation during low flow periods where smaller timesteps are not necessary. This is in contrast to previous users of this technique, who have employed a constant river discharge (Kostic & Parker, 2003) or abandoned the moving-boundary framework during high flow events (Chatanantavet et al. 2012). Because the floodplain profile is set by the bankfull-water-surface profile (Eq. 1.S15), changes in the bankfull flow depth over time violate Eq. 1.1. However, we found that changes in the bankfull flow depth over time were so small that the error in mass-balance incurred is acceptable – it is less than the $\sim 3\%$ truncation error introduced by our

numerical scheme, which is a common value for similar morphodynamic models (Parker, 2004) – and should not significantly affect modeled avulsions.

In our simulations we have imposed four delta lobes, represented by four one-dimensional stream-wise long profiles in parallel. At a given time, a single lobe is actively routing flow, and the other three lobes are abandoned. When the active lobe experiences avulsion, flow finds a new path downstream of the avulsion location along one of the abandoned lobes, and the flow path upstream remains unchanged,

$$\eta_{b,new}(x) = \begin{cases} \text{MIN}(\eta_{b,abandoned1}(x), \eta_{b,abandoned2}(x), \eta_{b,abandoned3}(x)) & x > x_A \\ \eta_b(x) & x \leq x_A \end{cases} \quad (1. S8)$$

where x is distance downstream, x_A is the avulsion location, $\eta_{b,new}$ is the new riverbed profile after avulsion, η_b is the riverbed profile before avulsion, and $\eta_{b,abandoned1}$, $\eta_{b,abandoned2}$, and $\eta_{b,abandoned3}$ are the three abandoned lobe long profiles. The MIN operator here selects the abandoned profile that has the minimum mean elevation, $\bar{\eta}_b$, downstream of the avulsion node,

$$\bar{\eta}_b = \frac{1}{x_m - x_A} \int_{x_A}^{x_m} \eta_b(x) dx \quad (1. S9)$$

where x_m is the downstream coordinate of the river mouth. For example, if $\eta_{b,abandoned2}(x)$ yields a lower value of $\bar{\eta}_b$ than both $\eta_{b,abandoned1}(x)$ and $\eta_{b,abandoned3}(x)$ yield, then $\eta_{b,abandoned2}(x)$ is selected as the path downstream of the avulsion location. This simple selection scheme mirrors the tendency of river deltas to fill in topographic lows when avulsing (Straub et al., 2009).

1.8.3. Flow variability parameters

In this study, we explore how deltaic avulsion patterns respond to upstream flow regimes and downstream changes in relative-sea-level through the systematic variation of these variables on a base case of the model that is characteristic of large, low-sloping deltas. Flow variability is parameterized in terms of a distribution of flow events with varying frequency, magnitude, and

duration. Table 1.S1 provides field examples of the relevant parameters, and summarizes the range of parameter space explored in this study.

The water discharge of alluvial rivers can fluctuate across a range of timescales, but generally stage height will fill the channel banks on a recurrence interval of ~ 2 years (Wolman & Miller, 1960). Many have argued that the morphodynamics of alluvial rivers can be well-approximated using an intermittency factor and a constant discharge that is equal to this bankfull condition, on the grounds that the bankfull flood represents a balance of frequency and magnitude that has the maximum impact on alluvial form (Wolman & Miller, 1960; Andrews, 1980; Parker et al., 2007). However, this approximation should break down for rivers in their backwater zone, where the downstream boundary enhances deposition during lower-than-bankfull flows and drives erosion during larger floods (Lamb et al., 2012). We explicitly model variable flows using a log-normal distribution of stage height upstream in the normal-flow reach. A log-normal distribution of stage height sufficiently describes flow in many river systems measured on a monthly-mean basis (Stedinger et al., 1993; Leboutillier & Waylen, 1993; Lague et al., 2005), and is uniquely defined by a bankfull-exceedence probability and a coefficient of variation (Figure 1.S1). The bankfull exceedence probability F_{bf} describes the frequency of overbank flows relative to all possible flows, and can range from zero to unity. On many low-gradient alluvial rivers, monthly-averaged flows will exceed bankfull between 1-10% of the time, corresponding roughly to a 1-2 year recurrence flood (Langbein & Leopold, 1964). The coefficient of variation (CV) describes the magnitude of low flows and high flows relative to the average flow, and is defined by the standard deviation of the stage height divided by the mean. Among the lowland deltas considered in Table 1.S1, the coefficient of variation ranges from 0.18-0.91.

In our numerical model, we discretize the distribution into twenty logarithmically spaced bins that span from low flow (less than bankfull) to high flow (greater than bankfull) conditions. Over time, each bin is randomly sampled at a defined event timescale, T_e . In our scaled framework the normalized event timescale ($T_e^* = T_e/T_{adj}$) describes how long flow events persist relative to channel adjustment timescale, the time required for those flows to transport enough sediment to aggrade the backwater reach by one channel depth. Based on previous work (Chatanantavet et al. 2014), we expect flow regimes to maintain bed disequilibrium and a persistent backwater zone

when the normalized event timescale is much less than unity. This condition is satisfied for many deltaic rivers, where we calculate $T_e^* = 10^{-4} - 10^{-1}$. If $T_e^* > 1$, individual flow events may persist long enough to mute backwater effects through aggradation or degradation of the river profile to quasi-uniform flow conditions.

1.8.4. Non-dimensionalization

Our simulations explore how deltaic avulsion patterns respond to river flow regime, relative sea-level rise, and initial topography by systematically varying the discharge and sea-level parameters. We non-dimensionalize the model to develop a framework that can be applied to a wide range of river conditions, reduce the number of model inputs, and identify key controls on model behavior. Channel-bed elevation (η_b) is scaled in terms of bankfull channel depth in the normal-flow reach, flow width (B) is scaled in terms of the channel width in the normal-flow reach, and stream-wise distance (x) is scaled in terms of the backwater length-scale,

$$\eta_b = \eta_b^* H_0 \quad (1. S10)$$

$$B = B^* B_0 \quad (1. S11)$$

$$x = x^* L_b = x^* \left(\frac{H_0}{S_0} \right) \quad (1. S12)$$

where η^* is dimensionless channel-bed elevation, B^* is dimensionless flow width, x^* is dimensionless distance downstream, and H_0 , B_0 , and S_0 are the channel depth, width, and slope in the normal-flow reach upstream. We also scale time (t) in terms of the time required to fill a backwater reach with the sediment supply. Here, we modify the bed-adjustment timescale to apply to a sinuous channel that exchanges sediment with its nearby floodplain, making the simplifying assumption that floodplain width (B_f), channel sinuosity (Ω), deposit porosity (λ_p), and the ratio of wash load to bed-material load (Λ) are constant and uniform,

$$t = t^* T_0 = \frac{t^* H_0 B_f L_b (1 - \lambda_p)}{\Omega \bar{q}_t (1 + \Lambda)} \quad (1. S13)$$

where t^* is dimensionless time, T_0 is the reach-filling timescale, and \bar{q}_t is the time-averaged sediment supply per unit width. It should be noted that previous authors have hypothesized that backwater effects may drive downstream fining trends (Nittrouer et al., 2011; Nittrouer et al., 2012; Venditti & Church, 2014; Maselli et al., 2018) and downstream reductions in floodplain and channel-belt width (Fernandes et al., 2016) in some systems, which could alter the bed-adjustment timescale. For example, narrow floodplains will aggrade faster than wide floodplains for the same amount of sediment-flux convergence (Eq. 1.1), and therefore backwater reaches with narrow floodplains adjust more quickly after flood events and may avulse more frequently compared to wider floodplains upstream.

We non-dimensionalize Eqs. 1.1-3 in the main text by inserting Eqs. 1.S10-S13 and simplifying,

$$\frac{\partial \eta^*}{\partial t^*} + \sigma^* = -\frac{1}{\bar{q}_t^*} \frac{\partial B^* q_t^*}{\partial x^*} \quad (1. S14)$$

$$\frac{\partial H^*}{\partial x^*} = \frac{S^* - S_f^*}{1 - Fr^2} + \frac{Fr^2}{1 - Fr^2} \frac{H^*}{B^*} \frac{dB^*}{dx^*} \quad (1. S15)$$

$$C_f q_t^* = \alpha (\tau^*)^n \quad (1. S16)$$

where $H^* = H/H_0$ is the dimensionless flow depth, $S^* = S/(H_0/L_b)$ is the normalized bed slope, $S_f^* = Fr^2 C_f/S_0$ is the normalized friction slope, q_t^* is the Einstein number representing dimensionless bed-material transport (Einstein, 1950; Parker, 1979) and \bar{q}_t^* is the time-averaged Einstein number. We note that η^* in Eq. 1.S14 is defined as elevation relative to sea level, not relative to the basin floor (as it is defined in some previous work, e.g. Baumanis & Kim, 2018). We prefer this reference frame because it condenses relative sea-level rise into the single parameter σ^* , illustrating that sea-level rise and subsidence have the same effect on sediment mass-balance. While Fr and τ^* are commonly defined in terms of gravity (g) and grain-size (D), we can reduce

the number of model inputs by casting them in terms of their counterparts in the normal-flow reach upstream during bankfull conditions.

$$Fr^2 = \frac{U^2}{gH} = Fr_{bf}^2 \frac{C_{f,bf}}{C_f} \left(\frac{1}{B^*}\right)^2 \left(\frac{1}{H^*}\right)^3 \quad (1.S17)$$

$$\tau^* = \frac{C_f U^2}{RgD} = \tau_{bf}^* H^* \frac{C_f}{C_{f,bf}} \left(\frac{Fr}{Fr_{bf}}\right)^2 \quad (1.S18)$$

where the subscript *bf* denotes bankfull conditions in the normal-flow reach. Another important parameter is the dimensionless relative sea-level rise (or basin subsidence) rate,

$$\sigma^* = \frac{\sigma L_b}{\bar{q}_t} \frac{B_f}{\Omega B} \frac{(1 - \lambda_p)}{(1 + \Lambda)}. \quad (1.S19)$$

where σ^* describes the balance of accommodation space created by relative sea-level rise over the active floodplain, as compared to the sediment supply to the backwater reach. When $\sigma^* \ll 1$, sediment supply far outpaces the rate of sea-level rise and we expect lobe growth and avulsion similar to steady sea-level scenarios. As σ^* approaches unity, we expect that sea level will cause intermittent or permanent drowning of delta lobes and potentially affect the location of avulsions. This parameterization is similar to the ‘‘A/S’’ ratio concept’’ of Muto and Steel (1997, 2002) and similar theories for radially averaged deltas (Galloway, 1989; Paola et al., 2011; Liang et al., 2016) but is here applied to avulsion cycles and discrete deltaic lobes.

Inserting Eq. 1.S10 into Eq. 1.4, we find the equation for normalized avulsion setup,

$$\Delta\eta^* \geq H^* H_c^* \quad (1.S20)$$

where $\Delta\eta^* = \Delta\eta/H_0$ is normalized superelevation and $H_c^* = H_c/H_0$ is the dimensionless channel depth. The avulsion threshold H^* is equal to fifty percent of the channel depth ($H^* = 0.5$) for all our simulations presented here, representing a value that is consistent with field and laboratory observations (Mohrig et al., 2000; Ganti et al., 2016b). However, field evidence suggests that the avulsion threshold is systematically reduced under flashier discharge regimes in the range of $H^* =$

0.2 – 1 (Ganti et al., 2014). At each model timestep, normalized superelevation $\Delta\eta^*$ is calculated by inserting Eq. 1.S10 into Eq. 1.5,

$$\Delta\eta^*(x) = \begin{cases} \eta_f^*(x) - \eta_{f,abandoned}^*(x) & \text{for } x^* \leq x_{m,abandoned}^* \\ \eta_f^*(x) - \xi_{sea}^* & \text{for } x^* > x_{m,abandoned}^* \end{cases} \quad (1.S21)$$

where $\eta_f^* = \eta_f/H_0$ is dimensionless floodplain elevation, $x_m^* = x_m/L_b$ is dimensionless river mouth location, $\xi_{sea}^* = \xi_{sea}/H_0$ is dimensionless sea-level elevation, and subscript “abandoned” indicates quantities on the abandoned delta lobe with lowest elevation. The dimensionless avulsion length (L_A^*) is the ratio of the avulsion length (L_A) to the backwater length-scale (L_b),

$$L_A^* = \frac{L_A}{L_b} = \frac{L_A}{H_0/S_0}. \quad (1.S22)$$

For lowland deltas with a preferential avulsion length set by the backwater length, we expect that $L_A^* \sim 1$. We ran our simulations for a total of 13 avulsion cycles, which we found sufficient to capture trends in avulsion location between our different model runs. Running the model for many more avulsion cycles yields similar results but is computationally expensive given the broad parameter space considered in our study.

1.8.5. Results for trunk-filling avulsion cycles

Most simulated avulsion cycles feature focused deposition within one backwater length-scale of the river mouth (Figure 2b-c, e-f). However, we also observed occasional avulsion cycles with significant deposition farther upstream in the trunk channel. These trunk-filling avulsion cycles occur when the initial floodplain profile η_f is significantly lower than all other inactive lobes, for example during avulsion cycle 4 (Figure S2). Consequently, the active lobe begins construction with substantially lower superelevation compared to other avulsion cycles, requiring greater aggradation along the entire river long-profile before reaching the avulsion threshold.

Trunk-filling avulsion cycles occurred periodically in all our simulations, usually during cycle number 4, 7, 10, and 13. In simulations with a preferential avulsion node, we observed that trunk-filling avulsion cycles were also associated with downstream translation of the avulsion node

(Figure S2b). The avulsion node translated downstream with major shoreline progradation, as a result of greater aggradation of the river long-profile with a constant transport slope. Similar behavior involving a periodic shift in the avulsion node has been documented for the Yellow River in China (Ganti et al., 2014).

During avulsion cycles 8 and 11 in the variable-discharge case, avulsions occurred far upstream of the backwater zone, but without a prominent peak in superelevation. These avulsions were similar to those in the constant-discharge case and were due to a transient period of nearly uniform deposition rate as the trunk channel adjusted to a new profile immediately following trunk-filling avulsion cycles. Occasional avulsions far upstream of a backwater-mediated node have been interpreted from Mississippi River deposits (Chamberlain et al., 2018).

1.8.6. Model sensitivity to other parameters

In the main text, we present three conditions that can produce a backwater-scaled avulsion node in our model: 1) a uniformly downstream-sloping initial condition, 2) flow variability, and 3) rapid sea-level rise. During the course of our analyses, we also explored how, and to what extent, changing other model parameters impacts our main results. Here we discuss the avulsion threshold parameter H^* and the number of imposed delta lobes N which, after the important roles of flow variability, the initial condition, and sea-level rise, we found to have a notable effect on model behavior.

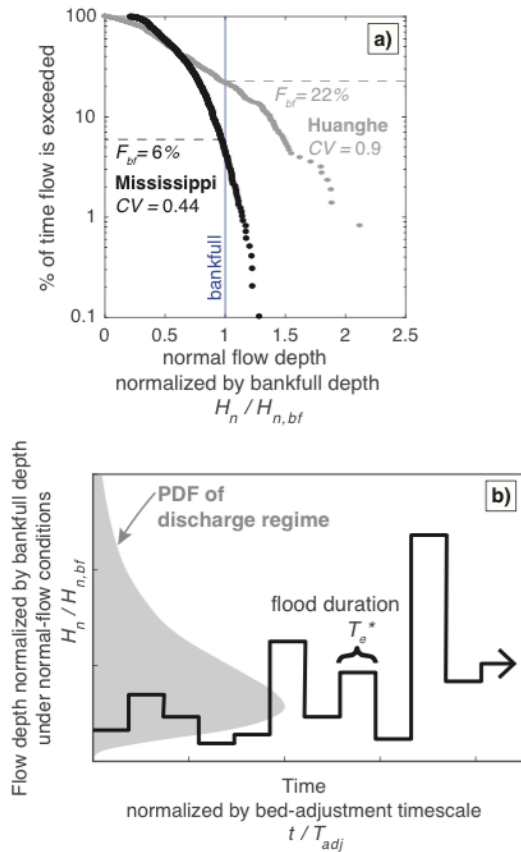
In previous simulations the avulsion threshold was set to $H^* = 0.5$. To relax this assumption, we varied the avulsion threshold across a range comparable to modern deltas ($0.2 \leq H^* \leq 1$, Ganti et al., 2014) under constant-discharge conditions and under variable-discharge conditions, with all other parameters set to the base case (Figure S6). Similar to the scenario of $H^* = 0.5$, a preferential avulsion node emerges only in simulations with flow variability. When avulsions occurred in constant-discharge simulations, a reach of ~ 2 backwater lengths was within 10% of the avulsion threshold, indicating no dominant avulsion location regardless of the value of H^* . In both constant- and variable-discharge scenarios, increasing the avulsion threshold leads to an increase in the observed avulsion lengths. This is because, at higher values of H^* , lobes prograde farther seaward of the inactive-lobe shoreline, where avulsions are unlikely to occur.

Thus, the avulsion threshold influences the location of the avulsion node in our model, but it does not control the occurrence of a preferential avulsion node itself, which still depends on flow variability, initial conditions, or sea-level rise.

The avulsion threshold was set to a constant value during all simulations for simplicity. However, avulsion threshold may not be a constant in reality and may in fact depend on flow variability at different sites, as argued by Ganti et al. (2014). Nonetheless, the sensitivity analysis shows that changing the threshold does not change our main conclusion that flow variability is necessary for emergence of a persistent node. Varying H^* under variable-discharge conditions only shifted avulsion lengths between $0.5L_b$ to $2L_b$ (Figure S5b), which was minor compared to spread in avulsion lengths resulting from a constant discharge (Figure S5a), and also within the scatter of backwater-mediated avulsion lengths observed in the field (Figure 1a).

In previous simulations, we also imposed a fixed number of 4 delta lobes. This was an arbitrary but reasonable choice based on field observations (Pang & Si, 1979; Roberts, 1997; Coleman et al., 1998; Chu et al., 2006) and flume experiments (Reitz et al., 2010; Carlson et al., 2018). We found that changing the number of delta lobes alters the timing of an avulsion node's behavior, but does not affect the occurrence of the avulsion node. For example, the shift from preferential to non-preferential avulsions in the constant-discharge scenario occurs after 4 avulsion cycles in our model (Figure 2A) because we impose four delta lobes, and so it takes 4 avulsions for the delta to bury its initial conditions. On a delta with N discrete lobes, this same behavior occurs after burying the initial conditions, but it requires N avulsion cycles. Other examples include outlier avulsions far upstream of the backwater zone, and downstream translation of the avulsion node, both of which occur every $N - 1$ avulsion cycles in our simulations. Both outlier avulsions and translation of the avulsion node are a consequence of trunk-filling avulsion cycles in our model (Section 1.9.5), which occur when all lateral space has been filled and the new lobe is forced to prograde farther seaward than previous lobes, corresponding to every $N - 1$ avulsion cycles after the delta has buried its initial conditions. Thus, simulated deltas with 4 lobes filled their trunk channels every 3 avulsion cycles (usually cycles 4, 7, 10, and 13) and experienced a shift in the avulsion node and then an outlier avulsion. A delta with fewer lobes has less lateral space to fill

before advancing seaward, and therefore experiences more frequent filling of its trunk channel, a more mobile avulsion node, and more common outlying avulsion sites.



Figure

1.S1: a) Exceedence probability of normal-flow depth normalized by bankfull depth for the Mississippi and Huanghe (Ganti et al., 2014), illustrating how bankfull exceedence probability (F_{bf}) and the coefficient of variation (CV) were estimated in Table 1.S1. Steeper trends of exceedence probability correspond to lower values of CV . b) Schematic time-series of modelled normal-flow depth in after non-dimensionalization, showing how input flow depth is determined by randomly sampling a log-normal distribution for fixed flow events of duration T_e^* .

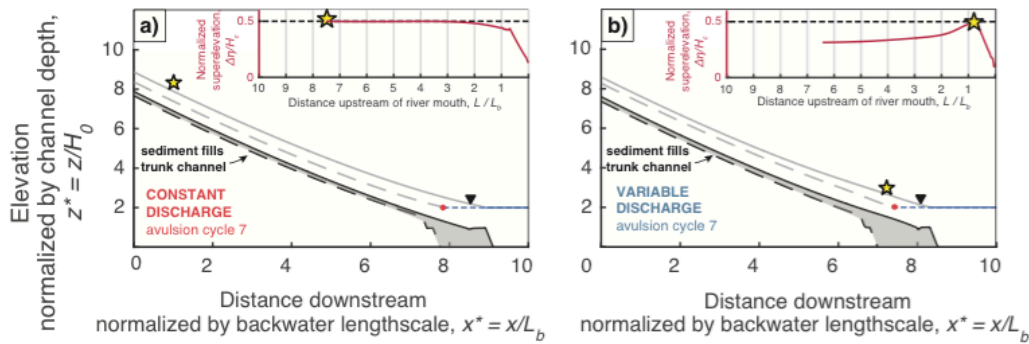


Figure 1.S2: Long profile evolution of avulsion cycle 7 under constant discharge (a) and variable flows (b). Avulsion cycle 7 is an example of a major avulsion cycle where sediment fills the trunk channel and, under variable flows, the avulsion node migrates downstream with shoreline progradation. Black lines are the riverbed profile at the start (dashed) and end (solid) of an avulsion cycle, the floodplain profiles of the active lobe (gray solid line) and the lowest inactive lobe (gray dashed line) are used to calculate super-elevation (see insert). Downstream of the inactive-lobe shoreline location (red circle), levee super-elevation is measured relative to sea level. Black triangles are the river mouth at the end of the avulsion cycle. Yellow stars show the avulsion location.

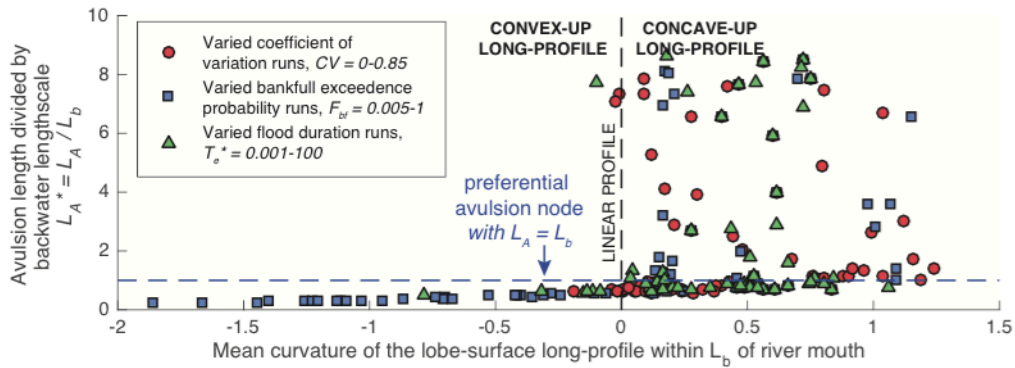


Figure 1.S3: Normalized avulsion length as a function of mean lobe-surface curvature for all simulated avulsion cycles, showing that there is a preferential avulsion node when flow regimes are sufficiently variable to produce a convex-up long profile in the backwater zone. The mean curvature of lobe-surface long profiles (i.e., the x-axis) was calculated by taking the mean of the second spatial derivative of bed elevation within one backwater length-scale of the river mouth (i.e., $\frac{1}{L_b} \int_{x_m-L_b}^{x_m} \frac{\partial^2 \eta}{\partial x^2} dx$) using centered finite differences.

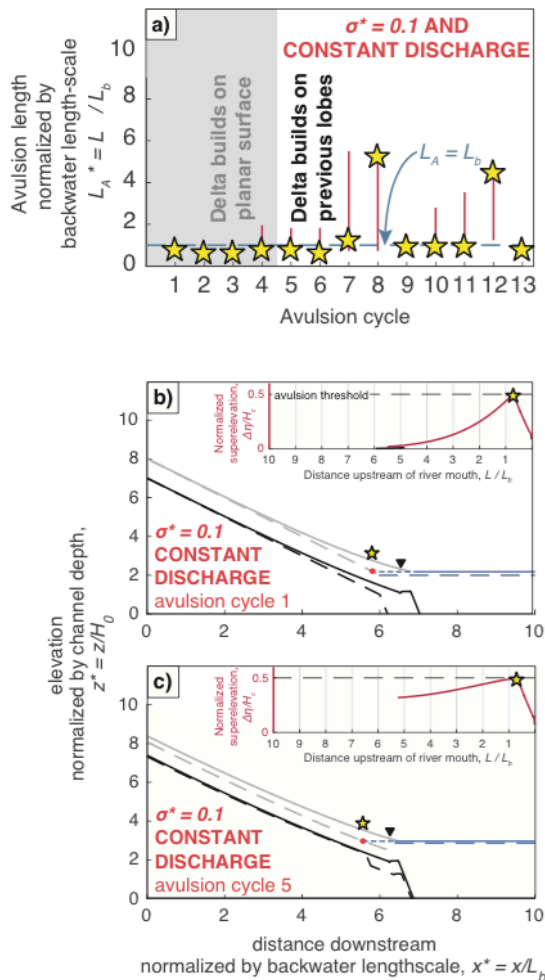


Figure 1.S4: Avulsion length through time (a) and long-profile results (b-c) for constant-discharge conditions and a rapid relative-sea-level-rise rate ($\sigma^* = 0.1$). Rapid relative sea-level rise induces a persistent downstream increase in deposition rate, leading to avulsions near the inactive-lobe shoreline in the absence of backwater effects. Downstream of the inactive-lobe shoreline location (red circle), floodplain superelevation is measured relative to sea level and so the superelevation is reduced despite high aggradation rates. In a), red error bars indicate the portion of the reach within 10% of the threshold superelevation necessary for avulsion. In b-c), black lines are the riverbed profile at the start (dashed) and end (solid) of an avulsion cycle. The floodplain profiles of the active lobe (gray solid line) and the lowest inactive lobe (gray dashed line) are used to calculate superelevation (see insert). Black triangles are the river mouth at the end of the avulsion cycle. Yellow stars show the avulsion location.

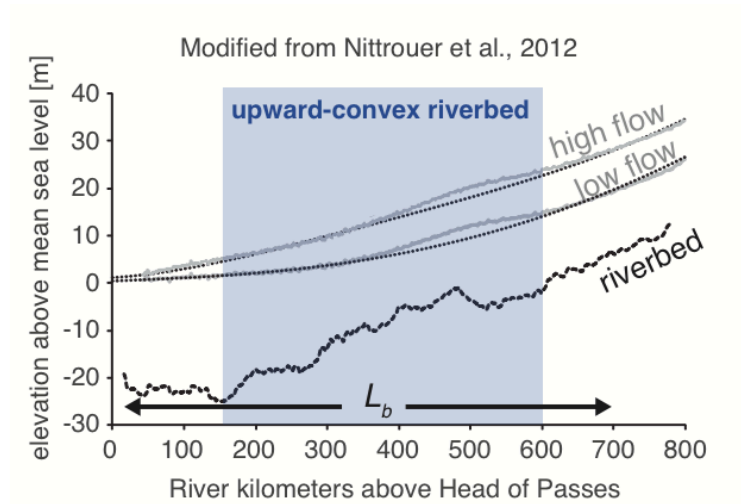


Figure 1.S5: Elevation long profile of the lower Mississippi River's backwater zone, modified from Nittrouer et al., (2012). The riverbed is shown in a black dashed line, and water surfaces during a low flow discharge ($7500 \text{ m}^3/\text{sec}$) and a high flow discharge ($40,000 \text{ m}^3/\text{sec}$) are shown based on stage measurements (black dotted lines) and based on a backwater hydrodynamic model (gray lines). The blue shaded region highlights the reach of broad upward-convexity in the riverbed that bears resemblance to riverbed curvature in our variable-discharge simulations, which in our model resulted from transient riverbed adjustment and co-occurred with a backwater-mediated avulsion node.

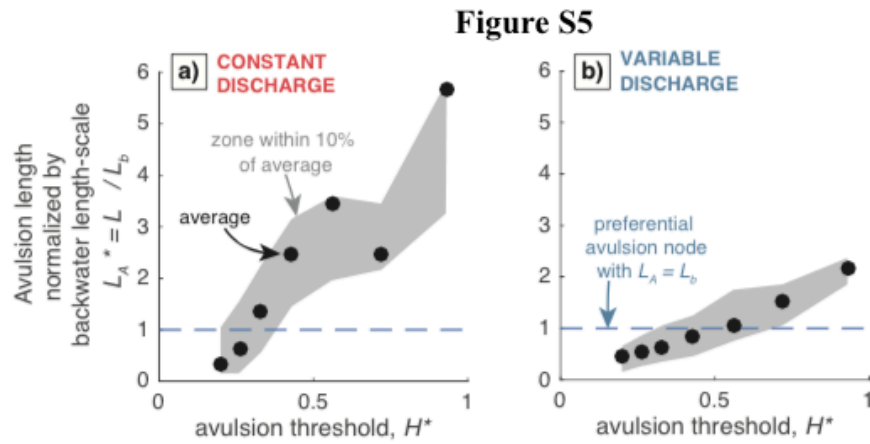


Figure 1.S6: Model results for avulsion length with changing avulsion threshold H^* under constant discharge (a) and variable discharge (b). Each black circle shows the avulsion locations averaged over cycles not influenced by the initial conditions (cycles 5-13), and the gray shaded areas denote the average reach within 10% of the avulsion threshold at times of avulsion. For all model runs, $Fr_{n,bf} = 0.17$, $\tau_{n,bf}^* = 1$, $C_f = 0.005$, and $H_b^* = 2$.

| | FLOW VARIABILITY PARAMETERS | | | BASIN PARAMETERS | | NORMAL FLOW PARAMETERS AT BANKFULL | | | |
|----------------------|--|-------------|----------------|-------------------|------------------|------------------------------------|--------------------|------------------------|------|
| | F_{bf} [-] | CV [-] | T_e^* [-] | σ^* [-] | H_b^* [-] | C_f [-] | $Fr_{n,bf}$ [-] | $\tau_{n,bf}^*$ [-] | |
| NUMERICAL MODEL RUNS | Constant-discharge model run | 1 | 0 | N/A | 0.0E+00 | 2.0 | 0.005 | 0.17 | 1.00 |
| | Variable-discharge model run (base case) | 0.05 | 0.53 | 1.0E-03 | 0.0E+00 | 2.0 | 0.005 | 0.17 | 1.00 |
| | Flood-frequency model runs | 0.005 - 1 | 0.53 | 1.0E-03 | 0.0E+00 | 2.0 | 0.005 | 0.17 | 1.00 |
| | Flood-magnitude model runs | 0.05 | 0 - 0.85 | 1.0E-03 | 0.0E+00 | 2.0 | 0.005 | 0.17 | 1.00 |
| | Flow-duration model runs | 0.05 | 0.53 | 1.0E-03 - 1.0E02 | 0.0E+00 | 2.0 | 0.005 | 0.17 | 1.00 |
| | Relative-sea-level-rise model runs | 0.05 | 0.53 | 1.0E-03 | 1.0E-03 - 1.0E01 | 2.0 | 0.005 | 0.17 | 1.00 |
| NATURAL DELTAS | Ganges-Brahmaputra, Bangladesh | 0.08 | 0.68 | 3.73E-03 | 7.14E-02 | 11.4 | 0.005 | 0.22 | 0.88 |
| | Danube River, Romania | 0.10 | 0.27 | 2.95E-03 | 7.85E-02 | 11.1 | 0.005 | 0.16 | 0.66 |
| | Yellow River, China | 0.22 | 0.91 | 3.77E-01 | 9.11E-03 | 8.6 | 0.005 | 0.22 | 2.19 |
| | Mississippi River, USA | 0.06 | 0.44 | 1.80E-03 | 1.70E-01 | 3.8 | 0.005 | 0.15 | 1.88 |
| | Orinoco River, Venezuela | 0.43 | 0.61 | 7.37E-04 | 6.08E-02 | 13.8 | 0.005 | 0.17 | 1.00 |
| | Nile River, Egypt | 0.05 | 0.65 | 6.39E-02 | 2.46E-02 | 7.4 | 0.005 | 0.18 | 1.62 |
| | Parana River, Argentina | 0.12 | 0.18 | 1.87E-04 | 1.70E-01 | 3.4 | 0.005 | 0.14 | 0.98 |

Table 1.S1: Flow variability parameters, basin parameters and bankfull flow parameters in numerically simulated and natural deltas. F_{bf} is bankfull exceedence probability, CV is the coefficient of variation of normal-flow depth upstream, T_e^* is the dimensionless flow event duration, σ^* is the dimensionless relative-sea-level-rise parameter, H_b^* is dimensionless basin depth, C_f is the friction coefficient, $Fr_{n,bf}$ is the bankfull Froude number in the normal-flow reach, and $\tau_{n,bf}^*$ is the bankfull Shields number in the normal-flow reach. For natural deltas, parameters were calculated using bankfull characteristics reported in Jerolmack and Mohrig (2007) and Chatanantavet et al. (2012), discharge time-series from Ganti et al. (2014), relative-sea-level-rise rates reported in Syvitski et al., (2009), basin depths reported in Syvitski and Saito (2007), and sediment supplies reported in Milliman and Syvitski (1992).

1.9 REFERENCES FOR SUPPLEMENTARY MATERIAL

- Andrews, E. D. (1980). Effective and bankfull discharges of streams in the Yampa River basin, Colorado and Wyoming. *Journal of Hydrology*, 46(3–4), 311–330. [https://doi.org/10.1016/0022-1694\(80\)90084-0](https://doi.org/10.1016/0022-1694(80)90084-0)
- Baumanis, C., & Kim, W. (2018). Reverse migration of lithofacies boundaries and shoreline in response to sea-level rise. *Basin Research*, 30, 89–100. <https://doi.org/10.1111/bre.12209>
- Borland, W. M. (1971). Reservoir sedimentation. In *River mechanics* (Vol. 2, pp. 29–21). Church, M. (2006). Bed material transport and the morphology of alluvial river channels. *Annual Review of Earth and Planetary Sciences*, 34(1), 325–354. <https://doi.org/10.1146/annurev.earth.33.092203.122721>
- Dade, W. B., & Friend, P. F. (1998). Grain-size, sediment-transport regime, and channel slope in alluvial rivers. *The Journal of Geology*, 106(6), 661–676. <https://doi.org/10.1086/516052>
- Einstein, H. A. (1950). The bed-load function for sediment transportation in open channel flows. In *Technical bulletin 1026* (p. 34). Washington, DC: U.S. Dept. of the Army, Soil Conservation Service.
- Fernandes, A. M., Törnqvist, T. E., Straub, K. M., & Mohrig, D. (2016). Connecting the backwater hydraulics of coastal rivers to fluvio-deltaic sedimentology and stratigraphy. *Geology*, 44(12), 979–982. <https://doi.org/10.1130/G37965.1>
- Galloway, W. E. (1989). Genetic stratigraphic sequences in basin analysis I: Architecture and genesis of flooding-surface bounded depositional units. *AAPG Bulletin*, 73(2), 125–142.
- Kim, W., Paola, C., Voller, V. R., & Swenson, J. B. (2006). Experimental measurement of the relative importance of controls on shoreline migration. *Journal of Sedimentary Research*, 76(2), 270–283. <https://doi.org/10.2110/jsr.2006.019>
- Kostic, S., & Parker, G. (2003). Progradational sand-mud deltas in lakes and reservoirs. Part 1. Theory and numerical modeling. *Journal of Hydraulic Research*, 41(2), 127–140. <https://doi.org/10.1080/00221680309499956>
- Lague, D., Hovius, N., & Davy, P. (2005). Discharge, discharge variability, and the bedrock channel profile. *Journal of Geophysical Research*, 110, F04006. <https://doi.org/10.1029/2004JF000259>
- Langbein, W. B., & Leopold, L. B. (1964). Quasi-equilibrium states in channel morphology. *American Journal of Science*, 262(6), 782–794. <https://doi.org/10.2475/ajs.262.6.782>
- LeBoutillier, D. W., & Waylen, P. R. (1993). A stochastic model of flow duration curves. *Water Resources Research*, 29(10), 3535–3541. <https://doi.org/10.1029/93WR01409>
- Liang, M., Van Dyk, C., & Passalacqua, P. (2016). Quantifying the patterns and dynamics of river deltas under conditions of steady forcing and relative sea level rise. *Journal of Geophysical Research: Earth Surface*, 121, 465–496.
- Maselli, V., Pellegrini, C., Del Bianco, F., Mercorella, A., Nones, M., Crose, L., et al. (2018). River morphodynamic evolution under dam-induced backwater: An example from the Po River (Italy). *Journal of Sedimentary Research*, 88(10), 1190–1204. <https://doi.org/10.2110/jsr.2018.61>
- Milliman, J. D., & Syvitski, J. P. (1992). Geomorphic/tectonic control of sediment discharge to the ocean: The importance of small mountainous rivers. *The Journal of Geology*, 100(5), 525–544. <https://doi.org/10.1086/629606>
- Muto, T., & Steel, R. J. (1997). Principles of regression and transgression: the nature of the interplay between accommodation and sediment supply: Perspectives. *Journal of Sedimentary Research*, 67(6), 994–1000. <https://doi.org/10.1306/D42686A8-2B26-11D7-8648000102C1865D>
- Muto, T., & Steel, R. J. (2002). Role of autoretreat and A/S changes in the understanding of deltaic shoreline trajectory: A semi-quantitative approach. *Basin Research*, 14(3), 303–318. <https://doi.org/10.1046/j.1365-2117.2002.00179.x>

- Nittrouer, J. A., Mohrig, D., Allison, M. A., & Peyret, A. P. B. (2011). The lowermost Mississippi River: A mixed bedrock-alluvial channel. *Sedimentology*, 58(7), 1914–1934. <https://doi.org/10.1111/j.1365-3091.2011.01245.x>
- Pang, J. Z., & Si, S. H. (1979). Evolution of the Yellow River mouth: I. Historical shifts. *Oceanologia et Limnologia Sinica*, 10(2), 136–141.
- Paola, C., Twilley, R. R., Edmonds, D. A., Kim, W., Mohrig, D., Parker, G., et al. (2011). Natural processes in delta restoration: Application to the Mississippi Delta. *Annual Review of Marine Science*, 3(1), 67–91. <https://doi.org/10.1146/annurev-marine-120709-142856>
- Parker, G. (1979). Hydraulic geometry of active gravel rivers. *Journal of Hydraulic Engineering*, 105(9), 1185–1201.
- Parker, G., Wilcock, P. R., Paola, C., Dietrich, W. E., & Pitlick, J. (2007). Physical basis for quasi-universal relations describing bankfull hydraulic geometry of single-thread gravel bed rivers. *Journal of Geophysical Research*, 112, F04005. <https://doi.org/10.1029/2006JF000549>
- Stedinger, J. R., Vogel, R. M., & Foufoula-Georgiou, E. (1993). Frequency analysis of extreme events, Chapter 18. In D. R. Maidment (Ed.), *Handbook of hydrology* (pp. 18.1–18.66). New York: McGraw-Hill.
- Sturm, T. W. (2010). *Open channel hydraulics*. New York: McGraw-Hill.
- Syvitski, J. P., & Saito, Y. (2007). Morphodynamics of deltas under the influence of humans. *Global and Planetary Change*, 57(3–4), 261–282. <https://doi.org/10.1016/j.gloplacha.2006.12.001>
- Venditti, J. G., & Church, M. (2014). Morphology and controls on the position of a gravel-sand transition: Fraser River, British Columbia. *Journal of Geophysical Research: Earth Surface*, 119, 1959–1976. <https://doi.org/10.1002/2014JF003147>
- Wolman, M. G., & Miller, J. P. (1960). Magnitude and frequency of forces in geomorphic processes. *Journal of Geology*, 68(1), 54–74. <https://doi.org/10.1086/626637>

*Chapter 2***ACCELERATED RIVER AVULSION FREQUENCY
ON LOWLAND DELTAS DUE TO SEA-LEVEL RISE**A.J. Chadwick^a, M.P. Lamb^a, and V. Ganti^{b,c}^aDivision of Geological and Planetary Sciences, California Institute of Technology, Pasadena, CA
91125^bDepartment of Geography, University of California, Santa Barbara, CA 93106^cDepartment of Earth Science, University of California, Santa Barbara, CA 93106

* Adapted from Chadwick, A.J., Lamb M.P., Ganti, V. “Accelerated river avulsion frequency on lowland deltas due to sea-level rise.” Proceedings of the National Academy of Sciences, *In review*.

2.0. ABSTRACT

Sea level rise, subsidence and reduced fluvial sediment supply are drowning river deltas worldwide, affecting ecosystems and billions of people. Delta plains are nourished with water and sediment primarily through abrupt shifts in river course, or avulsions, which are a land-building process that also creates catastrophic flood hazards. Existing observations and models conflict on whether the occurrence of avulsions will change due to relative sea-level rise, hampering the ability to forecast delta response to global climate change. We combined theory, numerical modeling and field observations to develop a unified, mechanistic framework to predict avulsion frequency on river deltas. Similar to natural deltas, our model has multiple self-formed delta lobes that maintain a near constant size set by backwater hydrodynamics. Results show that avulsion frequency is controlled by the competition between relative sea-level rise and sediment supply that drives lobe progradation. We find that most large deltas have sufficiently low progradation rates such that modern relative sea-level rise enhances delta-top sedimentation, accelerating avulsion frequency and associated hazards. However, avulsion frequency can become insensitive to relative sea-level rise with the anticipated increase in rise rates over the next century. In this case, sea-level rise can outpace delta-top aggradation, causing delta plains to drown and avulsion nodes to retreat inland, posing new hazards to upstream communities. Results indicate that managed deltas can support more frequent engineered avulsions to recover sinking land; however, there is a threshold beyond which coastal land loss will occur, and mitigation efforts should shift upstream.

2.1. INTRODUCTION

Coastal cities and wetlands are drowning due to global sea-level rise, accelerated subsidence from fluid extraction, and reduced fluvial sediment supply (Darby et al., 2016; Michener et al., 1997; Nicholls & Cazenave, 2010), with significant implications for the global economy, carbon cycle, and diverse ecosystems (Gleick, 2003; Hopkinson et al., 2012; Syvitski, 2008). Most estimates of coastal inundation for the next century do not consider the land-building potential of riverine sedimentation (W. Kim et al., 2009; Louisiana Coastal Wetlands Conservation and Restoration Task Force and the Wetlands Conservation and Restoration Authority, 1998; Paola et al., 2011). Rivers naturally distribute sediment across deltaic plains through avulsions—catastrophic shifts in the river course—

which tend to occur every 10 to 1000 years on different deltas worldwide (Fig. 2.1A-B) (Jerolmack, 2009; Slingerland & Smith, 2004). However, it is unknown what sets avulsion timescales and how avulsion occurrence will change with ongoing and projected increases in relative sea-level rise rate, caused by changes in climate and land use (Erban et al., 2014; Rignot et al., 2004). River avulsions counter land loss by nourishing wetlands with sediment (Edmonds et al., 2009b) but also have caused some of the deadliest floods in human history (Kidder & Liu, 2017; Sinha, 2009; Slingerland & Smith, 2004). On densely populated fluvial systems, dammed reservoirs trap sediment and engineered levees prevent avulsions, with the unintended consequence of heightened land loss (W. Kim et al., 2009; Paola et al., 2011). Engineered river diversions are now important parts of future billion-dollar coastal restoration plans (Coastal Protection and Restoration Authority of Louisiana, 2007). Despite their global importance, we lack a predictive framework for the controls on avulsion reoccurrence, which is imperative to mitigate catastrophic hazards on deltas and design effective diversions on engineered deltas (W. Kim et al., 2009; Paola et al., 2011).

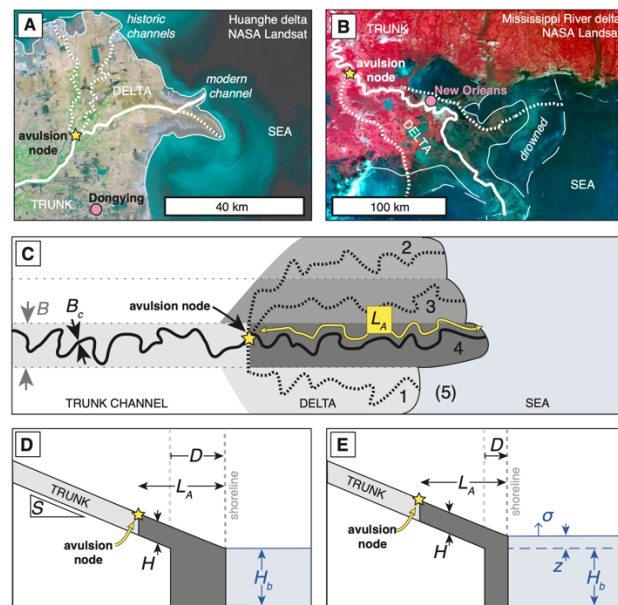


Figure 2.1: Natural and modeled deltas composed of discrete lobes. A) A) Huanghe delta, China, illustrating modern (solid line) and abandoned (dotted line) channel pathways and avulsion node (yellow star). Pink circle denotes city of Dongying. B) Mississippi River delta, USA. Thin dashed line indicates approximate shoreline before human management (72). Pink circle denotes New Orleans. C) Conceptual model, showing channels of width B_c in a floodplain/lobe of width B (shaded regions), and lobes with constant size L_A (yellow line). Shaded regions are deposits created during avulsion cycles 1-4. Once the channel avulses from the active lobe 4 to the space 5, all lateral accommodation is filled, and the avulsion node moves downstream in tandem with progradation. D-E) Long profile schematics

for constant relative sea level and rising sea level scenarios. Dark shaded region indicates sediment deposited during a single avulsion cycle.

Existing observations and models produce conflicting results as to whether avulsions will become more or less frequent with relative sea-level rise. The Rhine-Meuse delta provides an example of how avulsion frequency increased as a result of sea-level rise during the late Holocene (Törnqvist, 1994), a trend also observed in fan-delta experiments (Martin et al., 2009). The Mitchell River delta provides a counterexample, where river avulsions were less frequent during Holocene sea-level rise (Lane et al., 2017). Numerical modeling studies of the Mississippi and Trinity rivers also differed on whether avulsions were more or less frequent over the Holocene (Chatanantavet et al., 2012; Moran et al., 2017b) despite their shared sea-level history along the Gulf Coast (Anderson et al., 2014). Sequence stratigraphic models (Van Wagoner, 1998) and physical experiments (Tetsuji Muto & Steel, 2004) predict sea-level fall causes valley incision preventing avulsion, whereas the Goose River delta (Nijhuis et al., 2015) represents an example where avulsions persisted during sea-level fall.

Previous work documented that the characteristic avulsion frequency, f_A , scales with the rate that the riverbed aggrades to a height comparable to its channel depth,

$$f_A = \frac{v_a}{H} \quad (2.1)$$

where v_a is the in-channel aggradation rate and $H = H^*H_c$ is the aggradation thickness necessary for avulsion, where H_c is the bankfull channel depth and H^* is the avulsion threshold (Jerolmack & Mohrig, 2007; Mohrig et al., 2000). The avulsion threshold is a dimensionless number between 0.2 – 1.1 on modern lowland deltas (Ganti et al., 2019). Aggradation rates on lowland deltas, in contrast, span orders of magnitude ($v_a = 0.5 - 100$ mm/yr) (Jerolmack & Mohrig, 2007). Thus, river avulsions may occur as frequently as every decade (e.g., the Huanghe; Fig. 2.1A; 30) or as rarely as each millennium (e.g., the Mississippi; Fig. 2.1B; 31), and Eq. (2.2.1) is only useful insofar as aggradation rate can be predicted.

Analytical models are commonly used to approximate v_a through spatial averaging of sediment mass balance. A common approach to estimate v_a relies on the assumption of radial

symmetry in the delta planform (Jerolmack, 2009; Wonsuck Kim et al., 2006; T Muto & Steel, 1997; Tetsuji Muto & Steel, 2002b; Paola et al., 2011; Parker, Muto, Akamatsu, Dietrich, & Lauer, 2008a; Parker, Muto, Akamatsu, Dietrich, & Wesley Lauer, 2008; Swenson et al., 2005). Central to this radially averaged model is the premise that the delta apex is geographically fixed, and so relative sea-level rise causes the delta radius to shrink until sediment supply is sufficient to keep pace with sea level. At steady state, the delta land area is given by $A_{\Delta} = \frac{Q_s}{\sigma}$, where Q_s is the volumetric sediment supply flux and σ is the relative sea-level rise rate (Jerolmack, 2009; Paola et al., 2011), such that

$$v_a = \frac{Q_s}{A_{\Delta}} = \sigma \quad (2.2)$$

Thus, in radially averaged models, aggradation is enhanced during marine transgression because, with a fixed delta apex, the delta land area is reduced (T Muto & Steel, 1997; Tetsuji Muto, 2001). Eq. (2.2) shows agreement with steep experimental deltas where the delta apex was geographically fixed, for example by a canyon-fan transition or flume inlet (Wonsuck Kim et al., 2006; Martin et al., 2009). However, in contrast to steep fan deltas, lowland deltas have an apex that is not geographically fixed, but instead is found at a characteristic distance upstream of the shoreline where avulsions preferentially occur due to backwater hydrodynamics (Chatanantavet et al., 2012; Ganti, Chadwick, Hassenruck-Gudipati, Fuller, et al., 2016; Ganti et al., 2014; Jerolmack & Swenson, 2007). It is unknown if lowland deltas will change their area to equilibrate with sediment supply and sea-level rise as indicated by Eq. (2.2.2), or if delta response will differ because backwater hydrodynamics set a constant lobe size (Ganti, Chadwick, Hassenruck-Gudipati, Fuller, et al., 2016; Ganti, Chadwick, Hassenruck-Gudipati, & Lamb, 2016).

A second analytical approach, referred to as the channel-averaged model, is to constrain aggradation rate using sediment mass balance for a channel. For example, Reitz et al. (Reitz et al., 2010) found avulsions occurred in a fan-delta experiment at the rate the sediment supply could fill the channel: $Q_s T_A = H B_c L_A$, where T_A is the time between avulsions, B_c is channel width, and L_A is the avulsion length defined as the length of the delta lobe. Combined with Eq. (2.2.1) and using $1/f_A \equiv T_A$, aggradation rate is given by

$$v_a = \frac{Q_s}{L_A B_c} \quad (2.3)$$

The channel-width term in Eq. (2.3) can be substituted by an effective delta-lobe width B to approximate lateral distribution of sediment across a delta lobe, for example, due to bifurcations (Edmonds & Slingerland, 2007; Parker, Muto, Akamatsu, Dietrich, & Lauer, 2008a; Reitz & Jerolmack, 2012; Reitz et al., 2015; Salter et al., 2018; Tejedor et al., 2015). While this approach considers sedimentation within a discrete channel or lobe, it does not account for backwater hydrodynamics, multiple lobes, or sediment partitioning between lobe aggradation and progradation (Törnqvist et al., 2004).

More complex 2-D morphodynamic models, designed to study delta bifurcations and channelization (Caldwell & Edmonds, 2014; Edmonds et al., 2009a, 2010; Gao et al., 2019; Liang, Kim, et al., 2016; Liang, Van Dyk, et al., 2016; Nijhuis et al., 2015), are often computationally expensive and have yet to be run systematically to explore backwater-scaled avulsions. While simpler 1-D morphodynamic models that include backwater hydrodynamics exist, these models are tuned to specific case studies (Chatanantavet et al., 2012; Moran et al., 2017a) and yielded opposite trends for avulsion frequency response to relative sea-level rise. A 2-D reduced complexity model found that avulsion frequency was insensitive to sea-level rise for small rise rates due to progradation (Katherine M Ratliff et al., 2018). However, this model did not include backwater hydrodynamics and a model spin-up phase that is needed to avoid bias associated with the assumed initial river profile shape (Chadwick et al., 2019). More recent models for backwater-influenced avulsions have included quasi-2D non-uniform flow, lobe aggradation and progradation, multiple cycles of lobe growth and abandonment, and a spin-up phase to avoid issues with the choice of initial conditions (Chadwick et al., 2019; Moodie et al., 2019). These models provided new insight into the controls on avulsion location on deltas (Chadwick et al., 2019), and were validated against field observations from the Huanghe delta (Moodie et al., 2019); however, they have yet to be used to explore how relative sea-level rise affects avulsion frequency.

Here we built on the model of Chadwick et al. (2019) to develop a generic, dimensionless framework to predict the response of avulsion frequency on deltas to different rates of relative sea-level rise and fall, which reconciles conflicting results in previous work. We also derived an

analytical approximation to the model that can be directly compared to the commonly used radially averaged and channel-averaged approximations.

2.2. MORPHODYNAMIC MODEL AND FIELD DATA COMPILATION

The numerical morphodynamic model consists of a delta with an imposed number of lobes that are assumed to form a branching pattern, with only one lobe active at a given time (Fig. 2.1C) (Chadwick et al., 2019; Ganti et al., 2019) (*SI Appendix*). Each lobe is represented by a separate long profile and a shared trunk channel, governed by quasi-2-dimensional, non-uniform hydrodynamics (Chatanantavet et al., 2012), sediment transport (Engelund & Hansen, 1967), and sediment partitioning between lobe topset and foreset. Lobes are abandoned and reoccupied during avulsion cycles; avulsions occur when and where the active lobe first aggrades to the avulsion threshold H^* , set to 50% of the channel depth (H_c), relative to the lowest neighboring lobe (Chatanantavet et al., 2012; Ganti, Chadwick, Hassenruck-Gudipati, Fuller, et al., 2016; Mohrig et al., 2000; Katherine M Ratliff et al., 2018). After an avulsion, the active channel consists of the old channel upstream of the avulsion location concatenated with the new (lowest elevation) channel downstream (*SI Appendix*). We focused on river-dominated deltas and neglected shoreline erosion from waves or currents (Moodie et al., 2019; Katherine M Ratliff et al., 2018).

We non-dimensionalized the numerical model to explore the model results in a generic framework that allows direct comparison to a wide range of natural deltas. The aggradation rate was normalized by a maximum possible aggradation rate dictated by sediment supply, $\hat{v}_a = \frac{Q_s}{L_b B_c}$, where $L_b = H_c/S$ is the backwater length-scale and S is channel bed slope. Normalized avulsion frequency $f_A^* = \frac{f_A}{\hat{v}_a/H_c}$ depends on ten parameters: normalized rate of relative sea-level rise (σ^*), offshore basin floor depth normalized by channel depth (H_b^*), lobe width normalized by channel width (B^*), the avulsion threshold (H^*), and six additional parameters that describe river flow hydraulics and sediment transport (*SI Appendix*). Importantly, the dimensionless relative sea-level rise rate $\sigma^* = \frac{\sigma}{Q_s/nL_b B}$ describes the ratio of sea-level rise to the sediment supplied to the delta as a whole (where $n = (N + 1)/2$ and N is the number of delta lobes; *SI Appendix*). When $\sigma^* < 1$ the delta is expected to prograde seaward, whereas $\sigma^* > 1$ should correspond to delta drowning and shoreline retreat. For

each model delta, we measured the average time T_A between avulsions over 13 cycles and calculated $f_A \equiv 1/T_A$ under different scenarios of relative sea-level rise (σ^*), with all other dimensionless parameters held constant at values representative of typical lowland deltas (Table 2.1).

Table 2.1: Non-dimensional model input parameters

| Model run | σ^* | H_b^* | H^* | L_A^* | B^* |
|---|------------|---------|---------|---------|-------|
| | [-] | [-] | [-] | [-] | [-] |
| Numerical model, base case | -1-10 | 3 | 0.5 | - | 40 |
| Analytical solution, base case | -1-10 | 3 | 0.5 | 1 | 40 |
| Analytical solution, field example envelope | -1-10 | 3-14 | 0.2-0.7 | 0.5-2 | 40 |

$\sigma^* = \sigma n L_b B / Q_s$ is dimensionless relative sea-level rise rate, $H_b^* = H_b / H_c$ is dimensionless basin depth, H^* is avulsion threshold, $L_A^* = L_A / L_b$ is dimensionless avulsion length, $B^* = B / B_c$ is dimensionless lobe width. The numerical model requires an additional six input parameters describing flow hydraulics and sediment transport (Table S2).

We also derived an independent analytical model for lobe-averaged aggradation rate by constraining lobes to a fixed size scaled by backwater hydrodynamics (Chatanantavet et al., 2012; Jerolmack & Swenson, 2007), and averaging sediment mass balance over an avulsion timescale T_A for a river channel of constant slope S , thereby avoiding the need to solve the nonlinear equations for water and sediment transport (*SI Appendix*). The result is

$$f_A^* = \begin{cases} \frac{\sigma^* / B^*}{-\left(\frac{1}{\sigma^*} + H_b^* - H^*\right) + \sqrt{\left(\frac{1}{\sigma^*} + H_b^* - H^*\right)^2 + 2H^* \left(L_A^* + H_b^* - \frac{H^*}{2}\right)}}, & \text{if } D^* > 0 \\ \frac{1}{L_A^* B^* H^*}, & \text{if } D^* \leq 0 \end{cases} \quad (4)$$

where $D^* = \frac{D}{L_b}$ is the normalized lobe progradation distance just before an avulsion (Fig. 2.1D-E) and $L_A^* = \frac{L_A}{L_b}$ is user-specified normalized lobe size after avulsion, which typically varies between 0.5 to 2 for large, coastal rivers (Chadwick et al., 2019; Ganti et al., 2019). We compared the analytical solution to the numerical model, and performed a sensitivity analysis of f_A^* for a range of relative sea-level rise rates with systematic variation of the dimensionless basin depth, avulsion length, avulsion threshold, and floodplain width.

We also compared the numerical and analytical models to a compilation of Holocene data from fifteen natural deltas spanning a wide range of avulsion frequencies ($f_A = 0.5 - 140 \text{ ky}^{-1}$) and lobe sizes ($L_A = 30 - 490 \text{ km}$; Tables S1 and S2). Consistent with our model assumptions, these deltas feature a single major channel and avulsion node at the scale of the backwater length (Chatanantavet et al., 2012; Salter et al., 2018). Relative sea-level rise was determined by the sum of eustatic sea-level rise rate (σ_{eu}) and coastal subsidence rate (σ_{subs}) for each delta over the Holocene ($\sigma = \sigma_{eu} + \sigma_{subs}$). We used the data compilation to define dimensionless parameter combinations for model inputs (Table 2.1) and to test the model predictions against six of those deltas where all parameters could be constrained. We also computed next-century model predictions for avulsion frequency using modern values of relative sea-level rise reported for each delta (Syvitski et al., 2009). In our analysis we assumed a characteristic lobe width of $40B_c$, a reasonable estimate consistent with field data (Coleman et al., 1998; Hayden et al., 2019; Pang & Si, 1979; Parker, Muto, Akamatsu, Dietrich, & Lauer, 2008b).

2.3. RESULTS

Our numerical model results and lobe-averaged solution show that avulsion frequency responds nonlinearly to relative sea-level rise rate, falling within three regimes depending on the competition between relative sea-level rise and the sediment supply as described by σ^* (Fig. 2.2). In the regime $10^{-4} < \sigma^* \lesssim 10^{-1}$, which we term progradation-dominated, relative sea-level rise does not significantly contribute to aggradation rate (Fig. 2.S1). Instead, shoreline progradation causes channel aggradation because the channel adjusts to maintain a transport slope as the river mouth and avulsion node advance seaward (Ganti et al., 2014). Because avulsion frequency scales with

aggradation rate (Eq. (2.2.1)), f_A is insensitive to relative sea-level rise rate in this regime (Fig. 2.2), similar to previous reduced-complexity model results (Katherine M Ratliff et al., 2018).

If rise rate is the same order of magnitude as the maximum potential aggradation rate ($10^{-1} \lesssim \sigma^* < 10^0$), channel aggradation increases with relative sea-level rise rate (Fig. 2.2; Fig. 2.S1). In this regime, termed rise-dominated, relative sea-level rise controls channel aggradation because more sediment is partitioned into the lobe's channel and floodplain relative to the foreset, in a process similar to radially averaged theory (Wonsuck Kim et al., 2006; Paola et al., 2011; Swenson et al., 2005, 2000a) but here manifesting at the scale of delta lobes. Consequently, v_a is enhanced at the avulsion node and avulsion frequency accelerates as relative sea-level rise rate increases (Fig. 2.2).

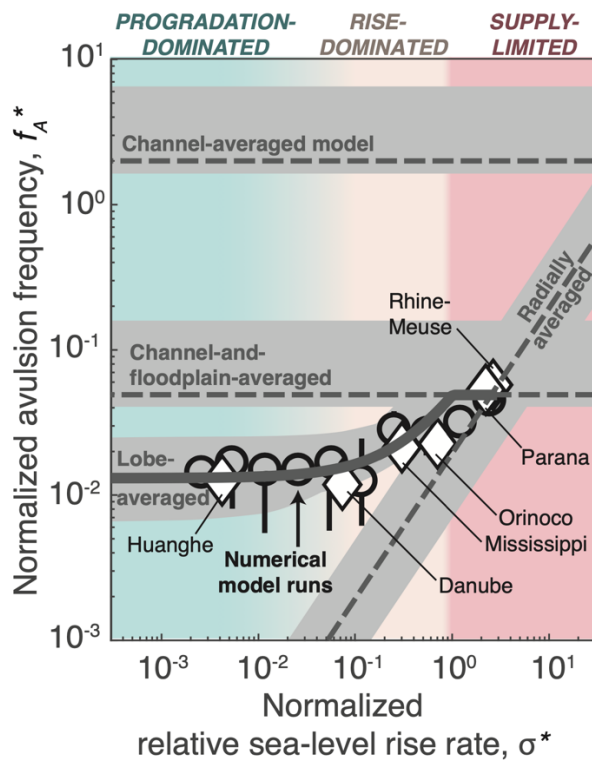


Figure 2.2: Avulsion frequency f_A^* as a function of normalized relative-sea level rise σ^* . Black circles and error bars show the median, minimum, and maximum of avulsion frequency distributions from numerical model runs, gray solid line is lobe-averaged model solution (Eq. (2.4)), and dashed lines are radially averaged and channel-averaged or lobe-width averaged model solutions for $H^* = 0.5, L_A^* = 1, H_b^* = 2, N = 4$, and $B^* = 40$ (*SI Appendix*). White diamonds are natural deltas where all parameters could be constrained, and gray shaded regions are lobe-averaged model-solution envelopes encompassing natural delta input parameters (Table 2.S2).

For $\sigma^* > 10^0$, relative sea-level rise outpaces the rate at which the sediment supply can aggrade the reach downstream of the avulsion node, inducing landward retreat of the shoreline and avulsion node. In this regime, termed supply-limited, v_a no longer increases with rise rate. Instead, aggradation rate is limited by the sediment supply divided by the fixed lobe land area (i.e., the product of lobe length L_A and width B), and avulsion frequency reaches a maximum value (Fig. 2.2).

A sensitivity analysis of the analytical model revealed that relative sea-level rise is a primary control on delta-lobe aggradation, universally increasing avulsion frequency in the rise-dominated regime ($0.1 \lesssim \sigma^* < 1$) by creating accommodation at a rate commensurate with the volumetric sediment input (Fig. 2.3). Smaller basin depths also increase avulsion frequency (Fig. 2.3A), but only for low rise rates. Small basin depths allow for more rapid progradation when $\sigma^* \lesssim 0.1$, driving high aggradation rates on the topset to maintain a transport slope. Results show avulsions are more frequent on deltas with lower avulsion thresholds and shorter avulsion lengths (Fig. 2.3B-C) because less sediment is needed on the delta top to trigger an avulsion. Avulsion frequency decreases with lobe width in our model (Fig. 2.3D), consistent with the recent finding that wider distributary networks are more resilient to environmental change (Tejedor et al., 2015). Lobe geometry (H^* , L_A^* , B^*) is the primary control on avulsion frequency when rapid relative sea-level rise causes marine transgression ($D \leq 0$) because the entire sediment load is sequestered on the delta top, and f_A^* is maximized to a value set by lobe area and the avulsion threshold (Eq. (2.4)). For cases with shallow basins and $L_A^* \gg 1$, such as steep fan deltas (Ganti et al., 2014), avulsion frequency is insensitive to σ^* because a large delta topset can transition from progradation-dominated to supply-limited conditions at relatively low rise rates (Fig. 2.3C). For $\sigma^* \gtrsim 2.5$ the avulsion node is drowned before an avulsion can occur.

Model results also indicate that avulsions can occur during relative sea-level fall, so long as the channel is aggradational (Fig. 2.3E) (Tetsuji Muto & Swenson, 2005; Nijhuis et al., 2015). Basin depth is the fundamental control on avulsion frequency during sea-level fall because topset aggradation is driven primarily by lobe progradation, similar to the case of slow relative sea-level rise.

In contrast to the radially averaged models that impose a fixed avulsion node location, our model incorporates the crucial component of a backwater-scaled avulsion node that fixes the lobe size, consistent with natural lowland deltas (Fig. 2.2; Fig. 2.S2). For a geographically fixed avulsion node, shoreline progradation and retreat cause adjustment of delta top area, which scales inversely with the topset aggradation and avulsion frequency ($f_A^* \propto \sigma^*$; Eq. (2.2); Fig. 2.2). In contrast, the backwater-scaled avulsion node in our model can move seaward and landward in tandem with the shoreline progradation and retreat, respectively, consistent with field observations (Ganti et al., 2014; Moodie et al., 2019). As a result, lobe area remains constant, and the competition between shoreline progradation, relative sea-level rise, and sediment supply control avulsion frequency. The radially averaged model and our model produce qualitatively similar trends only in the rise-dominated regime ($10^{-1} \lesssim \sigma^* < 10^0$); our model predicts more frequent avulsions in this regime due to additional topset aggradation from progradation that is not included in the radially averaged model.

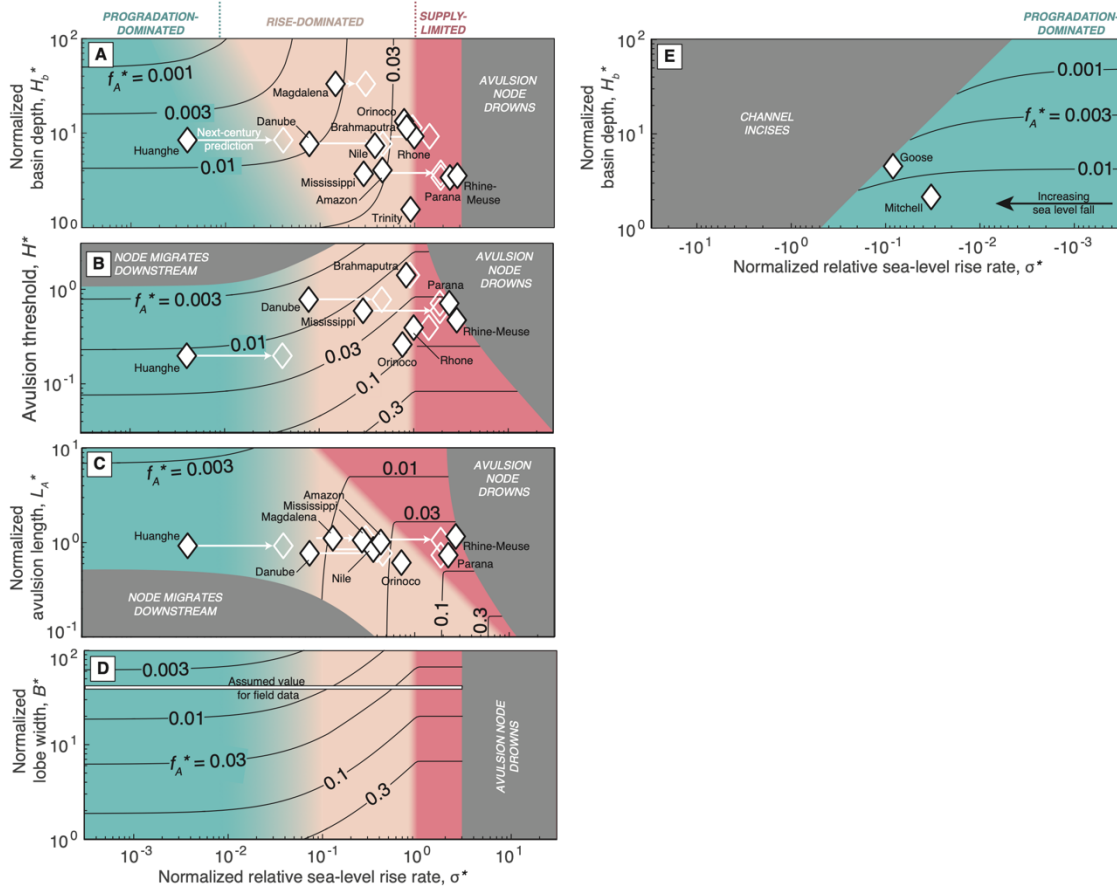


Figure 2.3: Analytical model results for normalized avulsion frequency under rising sea level. Panels show systematic variation of A) basin depth, B) avulsion threshold, C) avulsion length, and D) lobe width with other model parameters set to constant values typical of large lowland deltas ($H^* = 0.5$, $L_A^* = 1$, $H_b^* = 2$, $B^* = 40$; Table 2.S2). E) Solutions for falling sea level and basin depth. Gray zones indicate areas where the analytical model is not applicable due to migration of the avulsion node or channel incision (*SI Appendix*). White diamonds are field data for modern conditions (filled markers) and predictions for the next century (unfilled markers) (Tables S1 and S2).

Channel-averaged mass balance models, on the other hand, predict $f_A^* = 2$ regardless of rise rate as all sediment is sequestered in the channel. Our model predicts far fewer avulsions than the channel-averaged model because it incorporates sediment distribution onto the delta foreset and floodplain which reduces the channel aggradation rates. Incorporating lobe width into Eq. (2.3) yields predictions similar to our model, but only in the supply-limited regime ($\sigma^* \geq 1$).

Holocene field data for the Huanghe, Danube, Mississippi, Rhine-Meuse, Orinoco, and Parana deltas all fall within the prediction envelope of our model (Fig. 2.2). The high sediment load of the Huanghe yields $\sigma^* \cong 0.004$, placing it in the regime where f_A^* is controlled by shoreline progradation and is insensitive to relative sea-level rise. The Danube, Mississippi and Orinoco appear most vulnerable to changes in relative sea-level rise rate because they reside in the rise-dominated regime ($\sigma^* \cong 0.1, 0.3$ and 0.77 , respectively). Relative sea-level rise outpaces sediment supply on the Parana and Rhine-Meuse ($\sigma^* \cong 2.3$ and 2.6 , respectively), and their shorelines are expected to retreat and avulsion frequency should be sensitive to sediment supply and delta size, not relative sea-level rise rate. While sufficient data to test the model was unavailable for the other nine deltas in our compilation (Table 2.S2), they can be placed within the model parameter space (Fig. 2.3). Model comparison suggests that the Nile, Magdalena, Amazon, Rhone, Brahmaputra, and Trinity deltas likely reside in the rise-dominated regime (Fig. 2.3A-D), whereas the Goose and Mitchell deltas are in the progradation-dominated regime, where avulsions can occur despite sea level fall (Fig 3E), consistent with observations (Lane et al., 2017; Nijhuis et al., 2015).

2.4. DISCUSSION AND CONCLUSIONS

Our model shows lowland delta avulsion frequency depends on the dominant cause of channel aggradation: whether due to progradation, relative sea-level rise, or limited by sediment

supply (Fig. 2.4A-D). Depending on the dominant cause, avulsion frequency can vary by over an order of magnitude, and may or may not be sensitive to changes in relative sea-level rise rate. Our lobe-averaged analytical model, despite its simplicity, accurately predicts avulsion frequencies observed in the physics-based numerical model (Fig. 2.2). Minor differences in mass balance arose because we assumed $L_A = L_b$ in the analytical model, whereas L_A in the numerical model emerged autogenically and varied between $0.5L_b - 2L_b$. Consistency between our model and the analytical approximation (Fig. 2.2) suggests that the sediment mass partitioning between foreset progradation and aggradation of the backwater-scaled delta top exerts the primary control on avulsion frequency. Thus, beyond accounting for a backwater-scaled lobe area, modeling hydrodynamics and transient bed adjustment are not necessary to predict f_A^* to first order.

The parameter σ^* distinguishes between avulsion-frequency regimes because it compares the relative sea-level rise rate to the maximum possible aggradation rate dictated by sediment supply (Fig. 2.4A-D). Deltas with a backwater-scaled avulsion node ($L_A^* \sim 1$) feature a transition between the rise-dominated and supply-limited regimes at $\sigma^* = 1$, where delta tops can only barely keep pace with sea-level rise. Similarly, $\sigma^* \approx 0.1$ marks a transition between the rise-dominated and progradation-dominated regimes. Our model indicates deltas may also transition between aggradational regimes due to increasing basin depth (H_b^*) and delta size (L_A^*) associated with shoreline autoretreat (Fig. 2.3A,C) (T Muto & Steel, 1997; Tetsuji Muto, 2001).

Our results have important implications for delta flood hazards and morphodynamics that depend on σ^* and basin depth. Basin depth plays a significant role in the progradation-dominated regime ($\sigma^* \lesssim 0.1$) (Fig. 2.3A; Fig. 2.4) because less sediment is required for a given amount of progradation to occur in shallow basins (Bijkerk et al., 2016; Tetsuji Muto et al., 2016; Paola, 2000). Thus, lowland deltas building into shallow epicontinental seas likely reside in the progradation-dominated regime and their avulsion frequency may be insensitive to sea-level rise. This model prediction can explain the puzzling observations of decreased avulsion frequency during Holocene sea-level rise on the Mitchell River delta (Lane et al., 2017), which builds into a shallow basin ($H_b = 15\text{m}$, compared to the channel depth $H_c = 7\text{m}$, i.e. $H_b^* = 2.1$). We reason that progradation rates may have decreased on the Mitchell delta as its basin deepened over the Holocene, causing less frequent avulsions. In contrast, on deltas with deep offshore basins, such as shelf-edge deltas during

sea-level lowstands (Tetsuji Muto & Steel, 2002a), progradation is slow and so avulsion frequency should be more responsive to sea level change.

Our model also shows that high progradation rates can drive channel aggradation and avulsion even during sea level fall (Fig. 2.3E), which is typically thought to cause channel incision and prevent avulsion. This finding complicates sequence-stratigraphic interpretations of deltas building into shallow seas, such as the Cretaceous Interior Seaway (Van Wagoner, 1998), where unconformities interpreted as sequence boundaries reflecting sea-level fall could instead form intrinsically due to flood variability and avulsions (Ganti et al., 2019; Trower et al., 2018).

Large lowland deltas host a disproportionate fraction of the world population (Giosan, 2014; Syvitski, 2008), and are experiencing accelerated relative rise rates due to hydrocarbon extraction and eustatic sea-level rise. Our model predicts relative sea-level rise in the next century will drive more frequent avulsions farther upstream (Fig. 2.3; Table 2.S3). We expect most deltas on continental shelves to lie in the rise-dominated regime ($0.1 \lesssim \sigma^* < 1$; Fig. 2.3), in which higher rise rates cause more frequent avulsions. More frequent avulsions increase the potential for catastrophic flooding hazards (Kidder & Liu, 2017), but also represent an opportunity to mimic natural processes on managed deltas by using engineered diversions to build land (Coastal Protection and Restoration Authority of Louisiana, 2007; Ganti et al., 2014; W. Kim et al., 2009; Paola et al., 2011). Our results also point to distinct hazards associated with the supply-limited regime ($\sigma^* > 1$). Unlike radially averaged models with geographically fixed avulsion node locations (Fig. 2.4F), avulsion nodes in our model migrate upstream when $\sigma^* > 1$ in order to keep pace with shoreline retreat and maintain a constant, backwater-scaled lobe size (Fig. 2.4E). Notably, the Mississippi and Rhone are predicted to transition to supply-limited conditions, similar to the Rhine-Meuse and Parana (Fig. 2.3). As a result, we expect coastal land will drown and node migration will introduce new flood hazards upstream of historical avulsion sites. While the Huanghe has experienced a drastic increase in σ^* due to fluid extraction (Syvitski et al., 2009), our model indicates negligible change to natural avulsion frequency because aggradation is still predominantly induced by progradation.

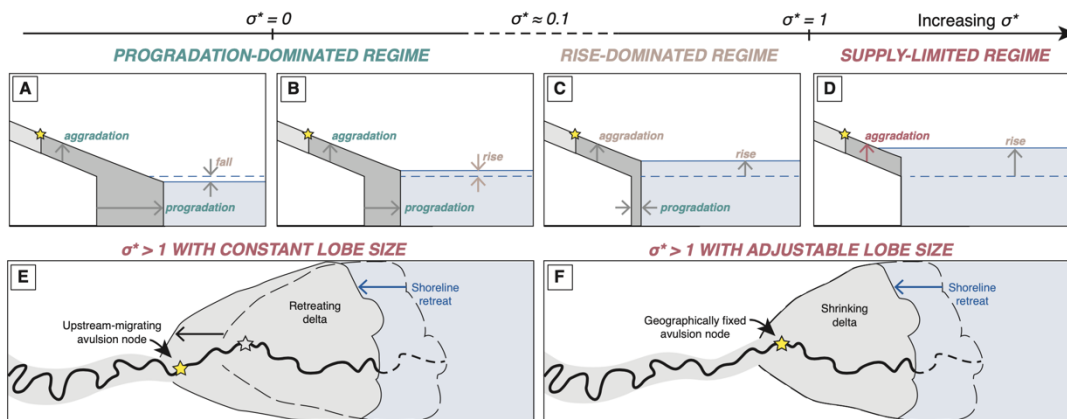


Figure 2.4: Schematics of delta response to sea level rise. Topographic profiles show locations of sediment deposition at the onset of avulsion under progradation-dominated (A-B), rise-dominated (C), and supply-limited (D) regimes, corresponding to increasing rates of relative sea-level rise. Planview schematics highlight different delta responses to rapid relative sea-level rise for E) our model where deltas have a constant lobe size and F) the radially averaged model where avulsion locations are fixed and delta lobes shrink in size.

Overall our results indicate lowland deltas will not passively drown but instead will respond to relative sea-level rise through more frequent natural cycles of sedimentation and river avulsion (Fig. 2.4). While this response acts to mitigate land loss in coastal wetlands, it increases the natural hazards associated with accelerated avulsion frequency and avulsions that occur farther upstream. Engineered diversions that mimic rivers' natural tendency of more frequent avulsions during relative sea-level rise may offset land loss, but our model suggests there is a threshold beyond which sediment supply cannot keep pace with increasing rise rates.

2.5. REFERENCES

- Anderson, J. B., Wallace, D. J., Simms, A. R., Rodriguez, A. B., & Milliken, K. T. (2014). Variable response of coastal environments of the northwestern Gulf of Mexico to sea-level rise and climate change: Implications for future change. *Marine Geology*, 352, 348–366.
- Bijkerk, J. F., Eggenhuisen, J. T., Kane, I. A., Meijer, N., Waters, C. N., Wignall, P. B., & McCaffrey, W. D. (2016). Fluvio-marine sediment partitioning as a function of basin water depth. *Journal of Sedimentary Research*, 86(3), 217–235.
- Bintanja, R., van de Wal, R. S. W., & Oerlemans, J. (2005). Modelled atmospheric temperatures and global sea levels over the past million years. *Nature*, 437(7055), 125.
- Caldwell, R. L., & Edmonds, D. A. (2014). The effects of sediment properties on deltaic processes and morphologies: A numerical modeling study. *Journal of Geophysical Research: Earth Surface*, 961–982. <https://doi.org/10.1002/2013JF002965>. Received
- Chadwick, A. J., Lamb, M. P., Moodie, A. J., Parker, G., & Nittrouer, J. A. (2019). Origin of a preferential avulsion node on lowland river deltas. *Geophysical Research Letters*, 46(8), 4267–4277.
- Chatanantavet, P., Lamb, M. P., & Nittrouer, J. A. (2012). Backwater controls of avulsion location on deltas. *Geophysical Research Letters*, 39(1). <https://doi.org/10.1029/2011GL050197>
- Coastal Protection and Restoration Authority of Louisiana. (2007). *Integrated ecosystem restoration and hurricane protection: Louisiana's comprehensive master plan for a sustainable coast*.
- Coleman, J. M., Roberts, H. H., & Stone, G. W. (1998). Mississippi River delta: an overview. *Journal of Coastal Research*, 14(3).
- Darby, S. E., Hackney, C. R., Leyland, J., Kummu, M., Lauri, H., Parsons, D. R., Best, J. L., Nicholas, A. P., & Aalto, R. (2016). Fluvial sediment supply to a mega-delta reduced by shifting tropical-cyclone activity. *Nature*, 539(7628), 276.
- Edmonds, D. A., Hoyal, D. C. J. D., Sheets, B. A., & Slingerland, R. L. (2009a). Predicting delta avulsions: Implications for coastal wetland restoration. *Geology*, 37(8), 759–762. <https://doi.org/10.1130/G25743A.1>
- Edmonds, D. A., Hoyal, D. C., Sheets, B. A., & Slingerland, R. L. (2009b). Predicting delta avulsions: Implications for coastal wetland restoration. *Geology*, 37(8), 759–762. <https://doi.org/10.1130/G25743A.1>
- Edmonds, D. A., & Slingerland, R. L. (2007). Mechanics of river mouth bar formation: Implications for the morphodynamics of delta distributary networks. *Journal of Geophysical Research: Earth Surface*, 112(F2).
- Edmonds, D. A., Slingerland, R. L., Best, J., Parsons, D., & Smith, N. (2010). Response of river-dominated delta channel networks to permanent changes in river discharge. *Geophysical Research Letters*, 37(12). <https://doi.org/10.1029/2010GL043269>
- Einstein, H. A. (1950). The bed-load function for sediment transportation. In *Open channel flow technical bulletin* (p. 1026). U.S. Department of Agriculture, Washington, D.C.
- Engelund, F., & Hansen, E. (1967). A monograph on sediment transport in alluvial streams. *Technical University of Denmark Ostervoldgade 10, Copenhagen K*.
- Erban, L. E., Gorelick, S. M., & Zebker, H. A. (2014). Groundwater extraction, land subsidence, and sea-level rise in the Mekong Delta, Vietnam. *Environmental Research Letters*, 9(8), 84010.
- Gagliano, S. M., Meyer-Arendt, K. J., & Wicker, K. M. (1981). Land loss in the Mississippi River deltaic plain. *GCAGS Transactions*, 31, 295–300.
- Galloway, W. E. (1975). *Process framework for describing the morphologic and stratigraphic evolution of deltaic depositional systems*.
- Ganti, V., Chadwick, A. J., Hassenruck-Gudipati, H. J., Fuller, B. M., & Lamb, M. P. (2016). Experimental river delta size set by multiple floods and backwater hydrodynamics. *Science Advances*, 2(5), e1501768.

- Ganti, V., Chadwick, A. J., Hassenruck-Gudipati, H. J., & Lamb, M. P. (2016). Avulsion cycles and their stratigraphic signature on an experimental backwater-controlled delta. *Journal of Geophysical Research: Earth Surface*, *121*(9), 1651–1675.
- Ganti, V., Chu, Z., Lamb, M. P., Nittrouer, J. A., & Parker, G. (2014). Testing morphodynamic controls on the location and frequency of river avulsions on fans versus deltas: Huanghe (Yellow River), China. *Geophysical Research Letters*, *41*, 7882–7890. <https://doi.org/10.1002/2014GL061918>
- Ganti, V., Lamb, M. P., & Chadwick, A. J. (2019). Autogenic erosional surfaces in fluvio-deltaic stratigraphy from floods, avulsions, and backwater hydrodynamics. *Journal of Sedimentary Research*.
- Gao, W., Shao, D., Wang, Z. B., Nardin, W., Rajput, P., Yang, W., Sun, T., & Cui, B. (2019). Long-Term Cumulative Effects of Intra-Annual Variability of Unsteady River Discharge on the Progradation of Delta Lobes: A Modeling Perspective. *Journal of Geophysical Research: Earth Surface*, *124*(4), 960–973.
- Giosan, L. (2014). Protect the world's deltas. *Nature*, *516*, 5–7.
- Gleick, P. H. (2003). Global freshwater resources: soft-path solutions for the 21st century. *Science (New York, N.Y.)*, *302*(2003), 1524–1528. <https://doi.org/10.1126/science.1089967>
- Hajek, E.A., & Edmonds, D. A. (2014). Is river avulsion style controlled by floodplain morphodynamics? *Geology*, *42*(3), 199–202. <https://doi.org/10.1130/G35045.1>
- Hajek, Elizabeth A., & Wolinsky, M. A. (2012). Simplified process modeling of river avulsion and alluvial architecture: Connecting models and field data. *Sedimentary Geology*, *257–260*, 1–30. <https://doi.org/10.1016/j.sedgeo.2011.09.005>
- Hayden, A. T., Lamb, M. P., Fischer, W. W., Ewing, R. C., McElroy, B. J., & Williams, R. M. E. (2019). Formation of sinuous ridges by inversion of river-channel belts in Utah, USA, with implications for Mars. *Icarus*.
- Hopkinson, C. S., Cai, W.-J., & Hu, X. (2012). Carbon sequestration in wetland dominated coastal systems—a global sink of rapidly diminishing magnitude. *Current Opinion in Environmental Sustainability*, *4*(2), 186–194.
- Jerolmack, D. J. (2009). Conceptual framework for assessing the response of delta channel networks to Holocene sea level rise. *Quaternary Science Reviews*, *28*(17–18), 1786–1800. <https://doi.org/10.1016/j.quascirev.2009.02.015>
- Jerolmack, D. J., & Mohrig, D. (2007). Conditions for branching in depositional rivers. *Geology*, *35*(5), 463. <https://doi.org/10.1130/G23308A.1>
- Jerolmack, D. J., & Paola, C. (2007). Complexity in a cellular model of river avulsion. *Geomorphology*, *91*(3–4), 259–270.
- Jerolmack, D. J., & Swenson, J. B. (2007). Scaling relationships and evolution of distributary networks on wave-influenced deltas. *Geophysical Research Letters*, *34*(23). <https://doi.org/10.1029/2007GL031823>
- Kidder, T. R., & Liu, H. (2017). Bridging theoretical gaps in geoarchaeology: archaeology, geoarchaeology, and history in the Yellow River valley, China. *Archaeological and Anthropological Sciences*, *9*(8), 1585–1602. <https://doi.org/10.1007/s12520-014-0184-5>
- Kim, W., Mohrig, D., Twilley, R. R., Paola, C., & Parker, G. (2009). Is it feasible to build new land in the Mississippi River delta? *Eos Transactions, AGU*, *90*(42), 373–374. http://www.agu.org/pubs/eos-news/supplements/2009/kim_90_42.shtml
- Kim, Wonsuck, Paola, C., Voller, V. R., & Swenson, J. B. (2006). Experimental measurement of the relative importance of controls on shoreline migration. *Journal of Sedimentary Research*, *76*(2), 270–283.
- Kostic, S., & Parker, G. (2003). Progradational sand-mud deltas in lakes and reservoirs. Part 1. Theory and numerical modeling. *Journal of Hydraulic Research*, *41*(2), 127–140.
- Lamb, M. P., Nittrouer, J. a., Mohrig, D., & Shaw, J. (2012). Backwater and river plume controls on scour upstream of river mouths: Implications for fluvio-deltaic morphodynamics. *Journal of Geophysical Research*, *117*(F1), F01002. <https://doi.org/10.1029/2011JF002079>

- Lane, T. I., Nanson, R. A., Vakarelov, B. K., Ainsworth, R. B., & Dashtgard, S. E. (2017). Evolution and architectural styles of a forced-regressive Holocene delta and megafan, Mitchell River, Gulf of Carpentaria, Australia. *Geological Society, London, Special Publications*, 444(1), 305–334.
- LeBoutillier, D. W., & Waylen, P. R. (1993). A stochastic model of flow duration curves. *Water Resources Research*, 29(10), 3535–3541.
- Liang, M., Kim, W., & Passalacqua, P. (2016). How much subsidence is enough to change the morphology of river deltas? *Geophysical Research Letters*, 43(19), 10–266.
- Liang, M., Van Dyk, C., & Passalacqua, P. (2016). Quantifying the patterns and dynamics of river deltas under conditions of steady forcing and relative sea level rise. *Journal of Geophysical Research: Earth Surface*, 121(2), 465–496.
- Louisiana Coastal Wetlands Conservation and Restoration Task Force and the Wetlands Conservation and Restoration Authority. (1998). Coast 2050: Toward a sustainable coastal Louisiana. *Louisiana Department of Natural Resources, Baton Rouge, Louisiana*.
- Martin, J., Sheets, B., Paola, C., & Hoyal, D. (2009). Influence of steady base-level rise on channel mobility, shoreline migration, and scaling properties of a cohesive experimental delta. *Journal of Geophysical Research*, 114(F3), F03017. <https://doi.org/10.1029/2008JF001142>
- Michener, W. K., Blood, E. R., Bildstein, K. L., Brinson, M. M., & Gardner, L. R. (1997). Climate change, hurricanes and tropical storms, and rising sea level in coastal wetlands. *Ecological Applications*, 7(3), 770–801.
- Milliman, J. D., & Syvitski, J. P. M. (1992). Geomorphic/Tectonic Control of Sediment Discharge to the Ocean: The Importance of Small Mountainous Rivers. *The Journal of Geology*, 100(5), 525–544. <https://doi.org/10.1086/629606>
- Mohrig, D., Heller, P. L., & Lyons, W. J. (2000). *Interpreting avulsion process from ancient alluvial sequences: Guadalope-Matarranya system (northern Spain) and Wasatch Formation (western Colorado)*. 12, 1787–1803.
- Moodie, A. J., Nittrouer, J. A., Ma, H., Carlson, B. N., Chadwick, A. J., Lamb, M. P., & Parker, G. (2019). Modeling Deltaic Lobe-Building Cycles and Channel Avulsions for the Yellow River Delta, China. *Journal of Geophysical Research: Earth Surface*. <https://doi.org/10.1029/2019JF005220>
- Moran, K. E., Nittrouer, J. a., Perillo, M. M., Lorenzo-Trueba, J., & Anderson, J. B. (2017a). Morphodynamic modeling of fluvial channel fill and avulsion time scales during early Holocene transgression, as substantiated by the incised valley stratigraphy of the Trinity River, Texas. *Journal of Geophysical Research: Earth Surface*, 122(1), 215–234. <https://doi.org/10.1002/2015JF003778>
- Moran, K. E., Nittrouer, J. A., Perillo, M. M., Lorenzo-Trueba, J., & Anderson, J. B. (2017b). Morphodynamic modeling of fluvial channel fill and avulsion time scales during early Holocene transgression, as substantiated by the incised valley stratigraphy of the Trinity River, Texas. *Journal of Geophysical Research: Earth Surface*, 122(1), 215–234.
- Muto, T., & Steel, R. J. (1997). Principles of regression and transgression: The nature of the interplay between accommodation and sediment supply. *Journal of Sedimentary Research*, 67(6, B), 994–1000. <https://doi.org/10.1306/D42686A8-2B26-11D7-8648000102C1865D>
- Muto, Tetsuji. (2001). Shoreline autoretreat substantiated in flume experiments. *Journal of Sedimentary Research*, 71(2), 246–254.
- Muto, Tetsuji, Furubayashi, R., Tomer, A., Sato, T., Kim, W., Naruse, H., & Parker, G. (2016). Planform evolution of deltas with graded alluvial topsets: Insights from three-dimensional tank experiments, geometric considerations and field applications. *Sedimentology*, 63(7), 2158–2189.
- Muto, Tetsuji, & Steel, R. J. (2002a). In Defense of Shelf-Edge Delta Development during Falling and Lowstand of Relative Sea Level. *The Journal of Geology*, 110(4), 421–436. <https://doi.org/10.1086/340631>
- Muto, Tetsuji, & Steel, R. J. (2002b). Role of autoretreat and A/S changes in the understanding of deltaic shoreline trajectory: A semi-quantitative approach. *Basin Research*, 14, 303–318. <https://doi.org/10.1046/j.1365-2117.2002.00179.x>

- Muto, Tetsuji, & Steel, R. J. (2004). Autogenic response of fluvial deltas to steady sea-level fall: Implications from flume-tank experiments. *Geology*, 32(5), 401–404. <https://doi.org/10.1130/G20269.1>
- Muto, Tetsuji, & Swenson, J. B. (2005). Large-scale fluvial grade as a nonequilibrium state in linked depositional systems: Theory and experiment. *Journal of Geophysical Research: Earth Surface*, 110(F3).
- Nicholas, A. P., Aalto, R. E., Smith, G. H. S., & Schwendel, A. C. (2018). Hydrodynamic controls on alluvial ridge construction and avulsion likelihood in meandering river floodplains. *Geology*, 46(7), 639–642.
- Nicholls, R. J., & Cazenave, A. (2010). Sea-level rise and its impact on coastal zones. *Science*, 328(5985), 1517–1520.
- Nijhuis, A. G., Edmonds, D. A., Caldwell, R. L., Cederberg, J. A., Slingerland, R. L., Best, J. L., Parsons, D. R., & Robinson, R. A. J. (2015). Fluvio-deltaic avulsions during relative sea-level fall. *Geology*, 43(8), 719–722.
- Pang, J., & Si, S. (1979). The Estuary Changes of Huanghe River I. Changes in modern time [J]. *Oceanologia Et Limnologia Sinica*, 2.
- Paola, C. (2000). Quantitative models of sedimentary basin filling. *Sedimentology*, 47, 121–178.
- Paola, C., Twilley, R. R., Edmonds, D. a., Kim, W., Mohrig, D., Parker, G., Viparelli, E., & Voller, V. R. (2011). Natural Processes in Delta Restoration: Application to the Mississippi Delta. *Annual Review of Marine Science*, 3(1), 67–91. <https://doi.org/10.1146/annurev-marine-120709-142856>
- Parker, G. (1979). Hydraulic geometry of active gravel rivers. *ASCE J Hydraul Div*, 105(9), 1185–1201.
- Parker, G., Muto, T., Akamatsu, Y., Dietrich, W. E., & Lauer, J. W. (2008a). Unravelling the conundrum of river response to rising sea-level from laboratory to field. Part I: Laboratory experiments. *Sedimentology*, 55(6), 1643–1655. <https://doi.org/10.1111/j.1365-3091.2008.00961.x>
- Parker, G., Muto, T., Akamatsu, Y., Dietrich, W. E., & Lauer, J. W. (2008b). Unravelling the conundrum of river response to rising sea-level from laboratory to field. Part II. The Fly-Strickland River system, Papua New Guinea. *Sedimentology*, 55(6), 1657–1686. <https://doi.org/10.1111/j.1365-3091.2008.00962.x>
- Parker, G., Muto, T., Akamatsu, Y., Dietrich, W. E., & Wesley Lauer, J. (2008). Unravelling the conundrum of river response to rising sea-level from laboratory to field. Part II. The Fly--Strickland River system, Papua New Guinea. *Sedimentology*, 55(6), 1657–1686.
- Ratliff, Katherine M, Hutton, E. H. W., & Murray, A. B. (2018). Exploring Wave and Sea-Level Rise Effects on Delta Morphodynamics With a Coupled River-Ocean Model. *Journal of Geophysical Research: Earth Surface*, 123(11), 2887–2900.
- Ratliff, Katherine Murray. (2017). *From the River to the Sea: Modeling Coastal River, Wetland, and Shoreline Dynamics*. Duke University.
- Reitz, M. D., & Jerolmack, D. J. (2012). Experimental alluvial fan evolution: Channel dynamics, slope controls, and shoreline growth. *Journal of Geophysical Research*, 117(F2), F02021. <https://doi.org/10.1029/2011JF002261>
- Reitz, M. D., Jerolmack, D. J., & Swenson, J. B. (2010). Flooding and flow path selection on alluvial fans and deltas. *Geophysical Research Letters*, 37(6). <https://doi.org/10.1029/2009GL041985>
- Reitz, M. D., Pickering, J. L., Goodbred, S. L., Paola, C., Steckler, M. S., Seeber, L., & Akhter, S. H. (2015). Effects of tectonic deformation and sea level on river path selection: theory and application to the Ganges-Brahmaputra-Meghna River Delta. *Journal of Geophysical Research: Earth Surface*. <https://doi.org/10.1002/2014JF003202>
- Rignot, E., Casassa, G., Gogineni, P., Krabill, W., Rivera, a., & Thomas, R. (2004). Accelerated ice discharge from the Antarctic Peninsula following the collapse of Larsen B ice shelf. *Geophysical Research Letters*, 31(August), 2–5. <https://doi.org/10.1029/2004GL020697>
- Salter, G., Paola, C., & Voller, V. R. (2018). Control of delta avulsion by downstream sediment sinks. *Journal of Geophysical Research: Earth Surface*, 123(1), 142–166.
- Sinha, R. (2009). The great avulsion of Kosi on 18 August 2008. *Current Science*, 429–433.
- Slingerland, R., & Smith, N. D. (2004). River Avulsions and Their Deposits. *Annual Review of Earth and Planetary Sciences*, 32(1), 257–285. <https://doi.org/10.1146/annurev.earth.32.101802.120201>

- Stedinger, J. R. (1993). Frequency analysis of extreme events. *In Handbook of Hydrology*.
- Straub, K. M., Paola, C., Mohrig, D., Wolinsky, M. A., & George, T. (2009). Compensational Stacking of Channelized Sedimentary Deposits. *Journal of Sedimentary Research*, 79(9), 673–688. <https://doi.org/10.2110/jsr.2009.070>
- Swenson, J. B., Paola, C., Pratson, L., Voller, V. R., & Murray, B. A. (2005). Fluvial and marine controls on combined subaerial and subaqueous delta progradation: Morphodynamic modeling of compound-clinoform development. *Journal of Geophysical Research: Earth Surface*, 110(F2).
- Swenson, J. B., Voller, V. R., Paola, C., Parker, G., & Marr, J. G. (2000a). Fluvio-deltaic sedimentation: A generalized Stefan problem. *European Journal of Applied Mathematics*, 11(5), 433–452.
- Swenson, J. B., Voller, V. R., Paola, C., Parker, G., & Marr, J. G. (2000b). Fluvio-deltaic sedimentation: A generalized Stefan problem. *European Journal of Applied Mathematics*, 11(5), 433–452.
- Syvitski, J. P. M. (2008). Deltas at risk. *Sustainability Science*, 3(1), 23–32.
- Syvitski, J. P. M., Kettner, A. J., Overeem, I., Hutton, E. W. H., Hannon, M. T., Brakenridge, G. R., Day, J., Vörösmarty, C., Saito, Y., Giosan, L., & Nicholls, R. J. (2009). Sinking deltas due to human activities. *Nature Geoscience*, 2(10), 681–686. <https://doi.org/10.1038/ngeo629>
- Syvitski, J. P. M., & Saito, Y. (2007). Morphodynamics of deltas under the influence of humans. *Global and Planetary Change*, 57(3–4), 261–282. <https://doi.org/10.1016/j.gloplacha.2006.12.001>
- Tejedor, A., Longjas, A., Zaliapin, I., & Foufoula-Georgiou, E. (2015). Delta channel networks: 2. Metrics of topologic and dynamic complexity for delta comparison, physical inference, and vulnerability assessment. *Water Resources Research*, 51(6), 4019–4045.
- Törnqvist, T. E. (1994). Middle and late Holocene avulsion history of the River Rhine (Rhine-Meuse delta, Netherlands). *Geology*, 22(8), 711–714.
- Törnqvist, T. E., González, J. L., Newsom, L. A., der Borg, K., De Jong, A. F. M., & Kurnik, C. W. (2004). Deciphering Holocene sea-level history on the US Gulf Coast: A high-resolution record from the Mississippi Delta. *Geological Society of America Bulletin*, 116(7–8), 1026–1039.
- Trower, E. J., Ganti, V., Fischer, W. W., & Lamb, M. P. (2018). Erosional surfaces in the Upper Cretaceous Castlegate Sandstone (Utah, USA): Sequence boundaries or autogenic scour from backwater hydrodynamics? *Geology*, 46(8), 707–710.
- Van Wagoner, J. C. (1998). Sequence stratigraphy and marine to nonmarine facies architecture of foreland basin strata, Book Cliffs, Utah, USA: Reply. *AAPG Bulletin*, 82(8), 1607–1618.

2.6. SUPPLEMENTARY MATERIAL

2.6.1 Numerical model derivation

The numerical model builds on (1); authors explored controls on avulsion location on lowland deltas, but did not analyze avulsion frequency and its dependency on relative sea level rise. The model consists of a delta with an imposed number of lobes that are assumed to form a branching pattern, with only one lobe active at a given time (Fig. 2.1C) (1, 2). Each delta lobe is modeled as a coupled river and floodplain in a quasi-two-dimensional mass balance framework (3, 4),

$$\frac{\partial \eta}{\partial t} + \sigma = -\frac{1}{(1 - \lambda_p)B} \frac{\partial Q_t}{\partial x} \quad (2. S5)$$

where η is channel bed elevation relative to sea level, t is time, σ is relative sea-level rise rate, x is downstream distance, and Q_t is the volumetric sediment transport capacity at position x . Sediment is deposited uniformly over floodplain width B with porosity λ_p . At the delta front, fluvial sediment transport gives way to gravity flow and avalanching, and deposition drives foreset progradation. We approximate progradation using a moving-boundary formulation, with a foreset of constant slope S_a set to five times the transport slope (5, 6).

We used the backwater equation to constrain water mass and momentum under quasi-steady flow conditions (3),

$$\frac{dH_w}{dx} = \frac{S - S_f}{1 - Fr^2} + \frac{Fr^2}{1 - Fr^2} \frac{H}{B_w} \frac{dB_w}{dx} \quad (2. S6)$$

where H_w is flow depth, S is channel bed slope, $S_f = C_f Fr^2$ is friction slope, C_f is friction coefficient, Fr is Froude number, and B_w is the width of flow. We assumed flow width was contained by the channel upstream of the river mouth, and expanded at a constant spreading angle offshore (3, 7), here set to 15 degrees. Following recent work (1), the location of the river mouth x_m is set by the intersection of the floodplain profile η_f with sea level ξ_o ,

$$x_m = x|_{\eta_f(x) = \xi_o} \quad (2. S7)$$

where the floodplain elevation is defined as the sum of the bed elevation and channel depth H_c ,

$$\eta_f(x) = \eta(x) + H_c \quad (2. S8)$$

Over time, the floodplain in our model aggrades in concert with the channel bed, driving river mouth advancement. A mobile river mouth is necessary for foreset progradation to drive topset aggradation (1).

We routed sediment in the river according to Engelund-Hansen (8) for total bed-material load,

$$Q_t = B_c \sqrt{RgD^3} \frac{\alpha}{C_f} (\tau^*)^n \quad (2. S9)$$

where R is submerged specific density of sediment, g is gravity, D is the median grain-size of bed material, τ^* is Shields number, and $\alpha = 0.05$ and $n = 2.5$. All sediment delivered to the delta front is captured in the foreset (6, 9).

Following recent work (1), we approximate deltaic evolution using four separate quasi-2-dimensional profiles of predefined width that represent four distinct lobes. At a given time, one delta lobe was active (10, 11) and was governed by Eqs. (2.S1 – S5). We varied sediment supply at the upstream end with water discharge such that the normal-flow bed slope was held constant, and therefore erosion and deposition were not driven by changes in the ratio of sediment supply to water discharge (12). Inactive lobe shapes were unchanged when abandoned (13) but were partially drowned in cases due to relative sea-level rise.

We used an avulsion criterion given by a critical thickness of aggradation, which we refer to as superelevation ($\Delta\eta$):

$$\Delta\eta(x) \geq H^* H_c \quad (2. S10)$$

in which H_c is the bankfull channel depth and H^* is the avulsion threshold, a dimensionless number that is of order unity, which we set to $H^* = 0.5$ consistent with field and experimental observations

(14–16). We triggered an avulsion when and where the floodplain elevation of the active lobe exceeded the floodplain elevation of the lowest-elevation abandoned lobe ($\eta_{f,abandoned}$), evaluated at the same distance downstream from the trunk channel:

$$\Delta\eta(x) = \begin{cases} \eta_f(x) - \eta_{f,abandoned}(x) & \text{for } x \leq x_{m,abandoned} \\ \eta_f(x) - \xi_{sea} & \text{for } x > x_{m,abandoned} \end{cases} \quad (2.S11)$$

where $x_{m,abandoned}$ is the stream-wise coordinate of the abandoned-lobe shoreline. Seaward of the abandoned lobe, superelevation is measured relative to sea level (ξ_{sea}) (1, 17). Extreme floods may also affect the timing of any one avulsion (15, 18), but these factors were neglected for simplicity following previous work (1, 19, 20). For simplicity we neglected the river reach laterally spanning lobes because lobes are much longer than they are wide (21, 22).

After avulsion, the river was rerouted to the lowest abandoned lobe by joining the bed profile of the active channel upstream of the avulsion site with the bed profile of the new flow path downstream,

$$\eta_{new}(x) = \begin{cases} \text{MIN}(\eta_{abandoned1}(x), \eta_{abandoned2}(x), \eta_{abandoned3}(x)) & x > x_A \\ \eta(x) & x \leq x_A \end{cases} \quad (2.S12)$$

where x is distance downstream, x_A is the avulsion location, $\eta_{b,new}$ is the new riverbed profile after avulsion, η_b is the riverbed profile before avulsion, and $\eta_{b,abandoned1}$, $\eta_{b,abandoned2}$, and $\eta_{b,abandoned3}$ are the three abandoned-lobe long profiles. The MIN operator here selects the abandoned profile that has the minimum mean elevation, $\bar{\eta}_b$, downstream of the avulsion node,

$$\bar{\eta} = \frac{1}{x_m - x_A} \int_{x_A}^{x_m} \eta(x) dx \quad (2.S13)$$

where x_m is the downstream coordinate of the river mouth. For example, if $\eta_{b,abandoned2}(x)$ yields a lower value of $\bar{\eta}_b$ than both $\eta_{b,abandoned1}(x)$ and $\eta_{b,abandoned3}(x)$ yield, then $\eta_{b,abandoned2}(x)$ is selected as the path downstream of the avulsion location. This process mimics the tendency of rivers to select steeper paths, fill in topographic lows (10, 23), and to reoccupy previously abandoned

channels (24). After establishing the new flow path, lobe construction (Eqs. S1 – S5) and avulsion setup (Eqs. S6 and S7) began anew.

At the start of each model run, the initial state of the riverbed was assumed planar with a uniform downstream slope set to the transport slope for normal flow, similar to previous studies (3, 17, 25). Due to the imposed number of lobes, after four avulsion cycles the river was forced to reoccupy lobes that were previously active, and thus the effect of initial conditions was minimized (1). Here we focus on results after the fourth avulsion cycle, and consider the first four avulsions a model spin-up period.

Simulations incorporate a variable discharge, which is necessary to reproduce a backwater-scaled avulsion node in most scenarios (1). We approximate variability using a log-normal distribution of flow depths (26, 27). The distribution is defined by the bankfull-exceedance probability F_{bf} , which describes the frequency of overbank flows relative to all flows, and the coefficient of variation CV , which describes the magnitude of low flows and high flows relative to the average flow. We randomly sampled the distribution with a characteristic flow-event duration (T_e).

To enable applicability across a wide range of river conditions, the model was non-dimensionalized using the maximum possible aggradation rate of the backwater zone, $\hat{v}_a = \frac{Q_s}{B_c L_b}$. Non-dimensionalizing Eqs. (2.S1 – S9) yields

$$\frac{\partial \eta^*}{\partial t^*} + \sigma^* = -\frac{1}{B^* \bar{q}_t^*} \frac{\partial q_t^*}{\partial x^*} \quad (2.S14)$$

$$x_m^* = x^* |_{\eta_f^*(x^*) = \xi_o^*} \quad (2.S15)$$

$$\eta_f^*(x^*) = \eta^*(x^*) + 1 \quad (2.S16)$$

$$\frac{\partial H_w^*}{\partial x^*} = \frac{S^* - S_f^*}{1 - Fr^2} + \frac{Fr^2}{1 - Fr^2} \frac{H^*}{B_w^*} \frac{dB_w^*}{dx^*} \quad (2.S17)$$

$$C_f q_t^* = \alpha(\tau^*)^n \quad (2.S18)$$

$$\Delta\eta^* \geq H^* \quad (2.S19)$$

$$\Delta\eta^*(x^*) = \begin{cases} \eta_f^*(x^*) - \eta_{f,abandoned}^*(x^*) & \text{for } x^* \leq x_{m,abandoned}^* \\ \eta_f^*(x^*) - \xi_{sea}^* & \text{for } x^* > x_{m,abandoned}^* \end{cases} \quad (2.S20)$$

$$\eta_{,new}^*(x^*) = \begin{cases} \text{MIN}(\eta_{abandoned1}^*(x^*), \eta_{abandoned2}^*(x^*), \eta_{abandoned3}^*(x^*)) & x^* > x_A^* \\ \eta^*(x^*) & x^* \leq x_A^* \end{cases} \quad (2.S21)$$

$$\bar{\eta}_b^* = \frac{1}{x_m^* - x_A^*} \int_{x_A^*}^{x_m^*} \eta_b^*(x^*) dx^* \quad (2.S22)$$

where $x^* = x/L_b$ is dimensionless distance downstream, $t^* = t\bar{Q}_s/B_c L_b(1 - \lambda_p)$ is dimensionless time and \bar{Q}_s is time-averaged volumetric sediment supply, $B^* = B/B_c$ is dimensionless lobe width, $H_w^* = H_w/H_c$ is the dimensionless depth of flow, $B_w^* = B_w/B_c$ is dimensionless width of flow, $S^* = S/(H_c/L_b)$ is the normalized bed slope, $S_f^* = Fr^2 C_f/(H_c/L_b)$ is the normalized friction slope, q_t^* is the Einstein number representing dimensionless bed-material transport (28, 29) and \bar{q}_t^* is the time-averaged Einstein number. All elevation variables are normalized relative to channel depth (e.g., $\xi_{sea}^* = \xi_{sea}/H_c$, $\eta^* = \eta/H_c$).

The model is governed by ten input dimensionless parameters quantifying hydrology, sediment transport, and channel morphology, which can be measured easily using existing data. The parameters are: bankfull Froude number in the normal-flow reach ($Fr_{n,bf}$), bankfull Shields number in the normal-flow reach ($\tau_{n,bf}^*$), friction factor (C_f), offshore basin floor depth normalized by bankfull depth (H_b^*), lobe width normalized by channel width (B^*), the avulsion threshold (H^*), a dimensionless rate of relative sea-level rise ($\sigma^* = \frac{\sigma n L_b B}{\bar{Q}_s}$), bankfull exceedance probability (F_{bf}), coefficient of variation of stage height (CV), and flood duration normalized by the channel adjustment timescale ($T_e^* = \frac{T_e \bar{Q}_s}{L_b H_c B_c}$, where $T_e \sim 1$ month is the dimensional flood duration).

During most numerical simulations, avulsion cycles featured focused deposition downstream of the avulsion node (Fig. 2.1D-E). However, during cycle numbers 4, 7, 10, and 13, we observed significant deposition farther upstream in the trunk channel. These trunk-filling avulsion cycles occur when the initial lobe's floodplain profile (η_f) is significantly lower than all other inactive lobes. Consequently, the active lobe begins construction with substantially lower superelevation (Eq. (2.S7)) compared to other avulsion cycles, requiring greater aggradation along the entire river long profile before reaching the avulsion threshold. We observed that trunk-filling avulsion cycles were also associated with downstream translation on of the avulsion node, similar to behavior documented on the Yellow River, China (15, 30). For model results presented here, we neglected trunk-filling avulsions and focused on lateral avulsions, because lateral avulsions constitute 70% of total avulsions in our model, and because sediment mass balance is constrained to downstream of the avulsion node in agreement with our analytical solution (Fig. 2.1D-E).

2.7.2 Analytical model derivation

Our analytical solution averages mass balance over an avulsion cycle where lobes are assumed to build at a fixed length L_A set by backwater hydrodynamics (3, 31, 32), and the river aggrades to thickness H before an avulsion occurs (2, 14, 15). The trunk channel upstream of the avulsion node aggrades during construction of the first lobe (Fig. 2.1C), such that aggradation occurs only downstream of the avulsion node for subsequent avulsion cycles. We assume a uniform riverbed slope, S , and a vertical delta foreset. These assumptions are relaxed in the full numerical solution, but here allow for an analytical approximation:

$$\frac{Q_s T_A}{(1 - \lambda_p)} = \begin{cases} (L_A - D)BH + DB \left(H_b + z + \frac{1}{2}DS \right) & \text{if } D > 0 \\ L_A BH & \text{if } D \leq 0 \end{cases} \quad (2.S19)$$

where Q_s is volumetric sediment supply at the upstream end, H_b is initial basin depth, D is lobe progradation distance just prior to avulsion, and z is the height of sea-level rise over an avulsion cycle. For $D > 0$, the first two terms on the right-hand side account for deposition on the delta topset and progradation of the foreset (Fig. 2.1B-C). For $D < 0$, sedimentation is only on the topset.

Geometric constraints (15) dictate that shoreline progradation is:

$$D = L_b \left(H^* - \frac{z}{H_c} \right) \quad (2.S20)$$

The magnitude of sea-level rise during an avulsion cycle can be rewritten as

$$z = n\sigma T_A \quad (2.S21)$$

where n is the number of avulsions that occur before lobe reoccupation, which —for random switching amongst topographic low areas— is

$$n = \frac{N + 1}{2} \quad (2.S22)$$

where N is the total number of lobes (2). Combining Eq. (2.1), Eqs. (2.S19 – S22) and $f_A \equiv 1/T_A$, and non-dimensionalizing results in the solution given by Eq. (2.4).

Some parameter combinations can violate model assumptions, and so we impose three constraints. Marine transgression between avulsions must not drown the avulsion node,

$$D > -L_A \quad (2.S23)$$

and lobes must not prograde greater than an avulsion length between avulsions,

$$D < L_A \quad (2.S24)$$

If Eqs. (2.S23) or (2.S24) are unsatisfied, then the avulsion node is forced to migrate upstream or downstream respectively, and our mass balance framework is not applicable, but the numerical solution still holds. Lastly, sea level fall cannot drop below the basin floor,

$$z > -H_b \quad (2.S25)$$

or else the channel is predicted to incise and avulsions do not occur.

The analytical model, Eq. (2.4), is a general solution that encompasses the channel-averaged model (Eq. (2.3)), which can be recovered by assuming no shoreline progradation ($D^* = 0$) and no floodplain ($B^* = 1$), and the radially averaged model, with a further assumption that lobe size is in equilibrium with sediment supply and sea level rise ($L_A^* = \sigma^* = 1$). In dimensionless form, the radially averaged mass balance model (Eq. (2.2)) is

$$f_A^* = \frac{\sigma^*}{nB^*H^*} \quad (2.S26)$$

Similarly, the dimensionless channel-averaged sediment mass balance model (Eq. (2.3)) is

$$f_A^* = \frac{1}{L_A^*H^*B^*} \quad (2.S27)$$

where $B^* = 1$ if sedimentation is confined to a channel and $B^* > 1$ if sedimentation is distributed across the channel and floodplain.

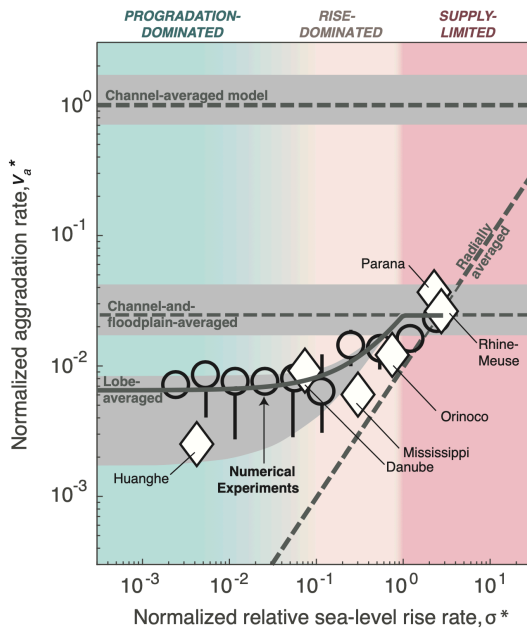


Fig. 2.S1. Model results for normalized aggradation rate v_a^* as a function of normalized relative sea-level rise σ^* , showing progradation-dominated, sea-level-rise-dominated, and supply-limited regimes. Black circles and error bars show the median, minimum, and maximum of avulsion frequency distributions from numerical model runs that encompass input parameters of field data. Gray solid line is lobe-averaged analytical solution (Eq. (2.4)), and dashed lines are radially averaged (Eq. (2.S26)) and channel-averaged (Eq. (2.S27)) model predictions using $H^* = 0.5$, $L_A^* = 1$, $H_b^* = 2$, $N = 4$, and $B^* = 40$ and a dimensionless version of equation 1:

$f_A^* = v_a^*/H^*$. White diamonds are field data (33) (Table 2.S1), and shaded regions are envelopes of model predictions for parameter combinations corresponding to the six field sites (Table 2.S2).

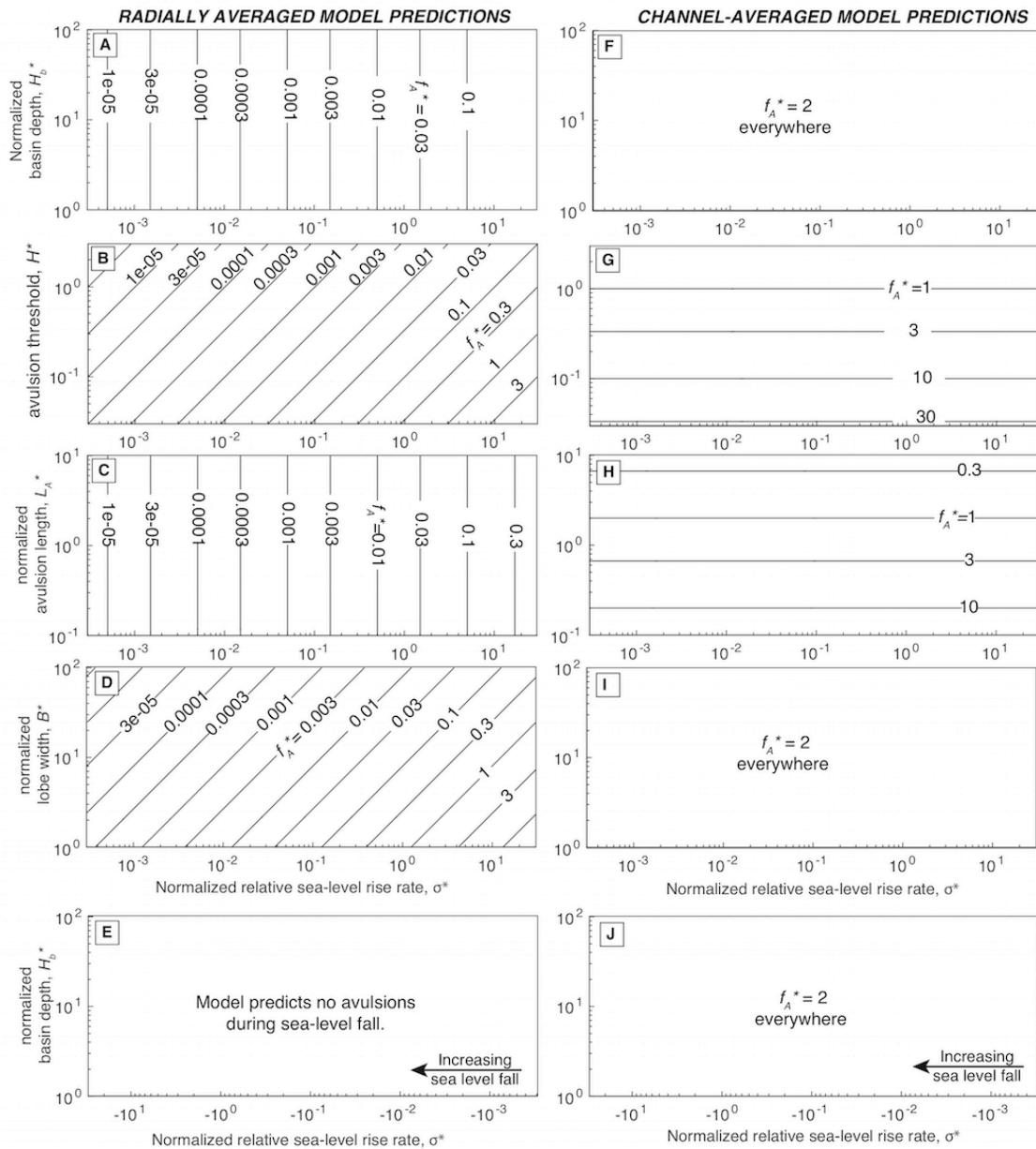


Fig. 2.S2. Normalized avulsion frequency predictions according to the radially averaged model (A-E) and channel-averaged model (F-J), with systematic variation of basin depth, avulsion threshold, avulsion length, and lobe width. Other model parameters were set to constant values typical of large lowland deltas ($H^* =$

0.5, $L_A^* = 1$, $H_b^* = 2$, $B^* = 40$; Table 2.S2). Predictions for falling sea level and basin depth are shown in

| River | H_c | B_c | L_b | Q_s | H_b | L_A | σ_{eu} | σ_{sub} | σ | B | v_a | T_A | f_A |
|-------------|-------|-------|-------|-----------|-------|-------|---------------|----------------|----------|-------|---------|-------|---------|
| | [m] | [m] | [km] | [Mt/year] | [m] | [km] | [mm/yr] | [mm/yr] | [mm/yr] | [km] | [mm/yr] | [yr] | [1/kyr] |
| Parana | 11.8 | 1270 | 295.0 | 79.0 | 40 | 210 | 1.6 | 1.4 | 3.0 | 50.8 | 5 | 1633 | 0.6 |
| Danube | 6.3 | 1250 | 125.0 | 67.0 | 50 | 95 | – | – | 0.2 | 50 | 2.5 | 1991 | 0.5 |
| Nile | 16.2 | 240 | 254.0 | 120.0 | 120 | 210 | 1.5 | 3 | 4.5 | 9.6 | – | – | – |
| Mississippi | 21.0 | 650 | 480.0 | 400.0 | 80 | 490 | 1.3 | 1 | 2.3 | 26 | 10 | 1250 | 0.8 |
| Assiniboine | 4.2 | 100 | 8.4 | 0.9 | 7 | 12 | – | – | – | 4 | 1.4 | 1000 | 1.0 |
| Rhine-Meuse | 5.0 | 700 | 45.5 | 3.1 | 18 | 51 | 1.5 | 0.1 | 1.6 | 28 | 1.6 | 1450 | 0.7 |
| Magdalena | 6.0 | 1100 | 63.2 | 220.0 | 200 | 67 | 1.5 | 1.4 | 2.9 | 44 | 3.8 | – | – |
| Orinoco | 8.0 | 2000 | 133.3 | 150.0 | 110 | 78 | 1.3 | 1.4 | 2.7 | 80 | 2.1 | 1000 | 1.0 |
| Mid-Amazon | 12.0 | 3000 | 400.0 | 1200.0 | 50 | 404 | 1.5 | 1.4 | 2.9 | 120 | 5 | – | – |
| Upper Rhone | 5.4 | 377 | 135.2 | 31.0 | 70 | – | 1.5 | 1.4 | 2.9 | 15.08 | 2 | 1450 | 0.7 |
| Huanghe | 3.5 | 500 | 35.0 | 1100.0 | 30 | 31 | 0.3 | 1.4 | 1.7 | 20 | 100 | 7 | 142.9 |
| Brahmaputra | 7.0 | 3300 | 70.0 | 540.0 | 80 | – | 1.4 | 10 | 11.4 | 132 | 20 | 500 | 2.0 |
| Goose | 2.0 | 100 | 0.9 | 0.3 | 10 | – | – | – | -3 | 4 | 1.98 | 333 | 3.0 |
| Mitchell | 7.0 | 100 | 23.3 | 2.9 | 15 | – | – | – | -0.25 | 4 | – | 63 | 16.0 |
| Trinity | 5.0 | 200 | 31.3 | 6.2 | 8 | – | – | – | 4.2 | 8 | 1.1 | – | – |

panels E and J. Lobe-averaged model predictions for the same parameter space are shown in Figure 3.

Table 2.S1. Field data used in this study

Bankfull channel depth (H_c), channel width (B_c), aggradation rates (v_a), and avulsion frequencies (f_A) are reported in (33), and avulsion lengths (L_A) and backwater lengths (L_b) are reported in (3, 15). Basin depths (H_b) are reported in (34) and sediment supplies (Q_s) are reported in (35). The avulsion threshold for each site was estimated using $H^* = v_a/(f_A H_c)$ (15). Eustatic sea-level rise (σ_{sus}) was estimated from (36) using the average rate during the period that avulsion frequency was measured. Coastal subsidence rates (σ_{sub}) are reported in (37–41), and for sites where data were unavailable we assumed an average value for deltas (1.4 mm/yr) (42). Relative sea-level rise (σ) was calculated as the sum of eustatic sea level rise and coastal subsidence ($\sigma = \sigma_{eu} + \sigma_{subs}$). Data for the Danube, Goose, Mitchell, and Trinity were compiled from recent studies (25, 43–45).

Table 2.S2. Dimensionless model input parameters

| River or model run | σ^* | H_b^* | H^* | L_A^* | B^* | $Fr_{n,bf}$ | $\tau_{n,bf}^*$ | C_f | F_{bf} | CV | T_e^* |
|-----------------------------------|------------|---------|-----------|---------|-------|-------------|-----------------|-------|----------|------|---------|
| | [-] | [-] | [-] | [-] | [-] | [-] | [-] | [-] | [-] | [-] | [-] |
| Parana | 2.3 | 3.4 | 0.69 | 0.7 | 40 | 0.09 | 0.98 | 0.005 | 0.12 | 0.18 | 1.9E-04 |
| Danube | 0.076 | 7.9 | 0.79 | 0.8 | 40 | 0.10 | 0.66 | 0.005 | 0.10 | 0.27 | 3.0E-03 |
| Nile | 3.7 | 7.4 | – | 0.8 | 40 | 0.11 | 1.62 | 0.005 | 0.05 | 0.65 | 6.4E-02 |
| Mississippi | 0.29 | 3.8 | 0.60 | 1.0 | 40 | 0.09 | 1.88 | 0.005 | 0.06 | 0.44 | 1.8E-03 |
| Assiniboine | – | 1.7 | 0.33 | 1.4 | 40 | 0.32 | 2.63 | 0.005 | – | – | 2.8E-03 |
| Rhine-Meuse | 2.6 | 3.6 | 0.46 | 1.1 | 40 | 0.15 | 0.69 | 0.005 | – | – | 2.0E-04 |
| Magdalena | 0.15 | 33.3 | – | 1.1 | 40 | 0.14 | 1.02 | 0.005 | – | – | 5.5E-03 |
| Orinoco | 0.77 | 13.8 | 0.26 | 0.6 | 40 | 0.11 | 1.00 | 0.005 | 0.43 | 0.61 | 7.4E-04 |
| Mid-Amazon | 0.47 | 4.2 | – | 1.0 | 40 | 0.08 | 0.90 | 0.005 | – | – | 8.7E-04 |
| Upper Rhone | 1.0 | 12.9 | 0.54 | – | 40 | 0.09 | 0.61 | 0.005 | – | – | 6.4E-04 |
| Huanghe | 0.0043 | 8.6 | 0.20 | 0.9 | 40 | 0.14 | 2.19 | 0.005 | 0.22 | 0.91 | 3.8E-01 |
| Brahmaputra | 0.80 | 11.4 | 1.43 | – | 40 | 0.14 | 0.88 | 0.005 | 0.08 | 0.68 | 3.7E-03 |
| Goose | -0.13 | 5.0 | 0.33 | – | 40 | 0.68 | 8.46 | 0.005 | – | – | 2.0E-02 |
| Mitchell | -0.033 | 2.1 | – | – | 40 | 0.24 | – | 0.005 | – | – | 1.9E-03 |
| Trinity | 0.69 | 1.6 | – | – | 40 | 0.18 | 2.00 | 0.005 | – | – | 2.1E-03 |
| Numerical model, base case | -1 – 10 | 3 | 0.5 | – | 40 | 0.17 | 1.00 | 0.005 | 0.05 | 0.53 | 1.0E-03 |
| Analytical solution, base case | -1 – 10 | 3 | 0.5 | 1 | 40 | – | – | – | – | – | – |
| Analytical solution, envelope | -1 – 10 | 3 – 14 | 0.2 – 0.7 | 0.5 – 2 | 40 | – | – | – | – | – | – |

All values were calculated using field data in Table 2.1 and discharge time series in Ganti et al. (15). $\sigma^* = \sigma n L_b B / Q_s$ is dimensionless relative sea level rise rate, $H_b^* = H_b / H_c$ is dimensionless basin depth, H^* is avulsion threshold, $L_A^* = L_A / L_b$ is dimensionless avulsion length, $B^* = B / B_c$ is dimensionless lobe width, $Fr_{n,bf}$ is bankfull Froude number in the normal flow reach, $\tau_{n,bf}^*$ is bankfull Shields number in the normal

flow reach, C_f is friction coefficient, F_{bf} is bankfull exceedance probability, CV is coefficient of variation of stage height, and $T_e^* = T_e Q_s / H_c B_c L_b$ is dimensionless flood duration where $T_e = 1$ month.

Table 2.S3. Next-century predictions of the lobe-averaged model

| River | σ [mm/yr] | σ^* [-] | T_A [yr] | f_A [1/kyr] |
|--------------|---------------------------------------|-------------------------------------|---------------------------------|------------------------------------|
| Parana | 2–3 | 1.5–2.3 | 1797 | 0.6 |
| Danube | 1.2 | 0.46 | 1423 | 0.7 |
| Nile | 4.8 | 0.40 | – | – |
| Mississippi | 5–25 | 0.64–3.2 | 897 | 1.1 |
| Assiniboine | – | – | – | – |
| Rhine-Meuse | – | – | – | – |
| Magdalena | 5.3–6.6 | 0.27–0.34 | – | – |
| Orinoco | 0.8–3 | 0.23–0.87 | 269–833 | 1.2–3.7 |
| Mid-Amazon | – | – | – | – |
| Upper Rhone | 2–6 | 0.73–2.2 | – | – |
| Huanghe | 8–23 | 0.02–0.06 | 5–6 | 170–220 |
| Brahmaputra | 8–18 | 0.56–1.3 | – | – |
| Goose | – | – | – | – |
| Mitchell | – | – | – | – |
| Trinity | – | – | – | – |

Relative sea-level rise rate (σ), Normalized relative sea-level rise (σ^*), avulsion timescale (T_A), and avulsion frequency ($f_A \equiv 1/T_A$), using the lobe-averaged model. Predictions were made using modern estimates of relative sea-level rise rates reported by Syvitski et al. (2009) and available field data (Table 2.S1) assuming no change in other model parameters (Table 2.S2).

2.8. REFERENCES FOR SUPPLEMENTARY MATERIAL

1. A. J. Chadwick, M. P. Lamb, A. J. Moodie, G. Parker, J. A. Nittrouer, Origin of a preferential avulsion node on lowland river deltas. *Geophys. Res. Lett.* **46**, 4267–4277 (2019).
2. V. Ganti, M. P. Lamb, A. J. Chadwick, Autogenic erosional surfaces in fluvio-deltaic stratigraphy from floods, avulsions, and backwater hydrodynamics. *J. Sediment. Res.* (2019).
3. P. Chatanantavet, M. P. Lamb, J. A. Nittrouer, Backwater controls of avulsion location on deltas. *Geophys. Res. Lett.* **39** (2012).
4. G. Parker, T. Muto, Y. Akamatsu, W. E. Dietrich, J. W. Lauer, Unravelling the conundrum of river response to rising sea-level from laboratory to field. Part II. The Fly-Strickland River system, Papua New Guinea. *Sedimentology* **55**, 1657–1686 (2008).
5. J. B. Swenson, V. R. Voller, C. Paola, G. Parker, J. G. Marr, Fluvio-deltaic sedimentation: A generalized Stefan problem. *Eur. J. Appl. Math.* **11**, 433–452 (2000).
6. S. Kostic, G. Parker, Progradational sand-mud deltas in lakes and reservoirs. Part 1. Theory and numerical modeling. *J. Hydraul. Res.* **41**, 127–140 (2003).
7. M. P. Lamb, J. a. Nittrouer, D. Mohrig, J. Shaw, Backwater and river plume controls on scour upstream of river mouths: Implications for fluvio-deltaic morphodynamics. *J. Geophys. Res.* **117**, F01002 (2012).
8. F. Engelund, E. Hansen, A monograph on sediment transport in alluvial streams. *Tech. Univ. Denmark Ostervoldgade 10, Copenhagen K.* (1967).
9. J. B. Swenson, V. R. Voller, C. Paola, G. Parker, J. G. Marr, Fluvio-deltaic sedimentation: A generalized Stefan problem. *Eur. J. Appl. Math.* **11**, 433–452 (2000).
10. R. Slingerland, N. D. Smith, River Avulsions and Their Deposits. *Annu. Rev. Earth Planet. Sci.* **32**, 257–285 (2004).
11. E. A. Hajek, D. A. Edmonds, Is river avulsion style controlled by floodplain morphodynamics? *Geology* **42**, 199–202 (2014).
12. C. Paola, Quantitative models of sedimentary basin filling. *Sedimentology* **47**, 121–178 (2000).
13. W. E. Galloway, Process framework for describing the morphologic and stratigraphic evolution of deltaic depositional systems (1975).
14. D. Mohrig, P. L. Heller, W. J. Lyons, Interpreting avulsion process from ancient alluvial sequences : Guadalope-Matarranya system (northern Spain) and Wasatch Formation (western Colorado). 1787–1803 (2000).
15. V. Ganti, Z. Chu, M. P. Lamb, J. A. Nittrouer, G. Parker, Testing morphodynamic controls on the location and frequency of river avulsions on fans versus deltas: Huanghe (Yellow River), China. *Geophys. Res. Lett.* **41**, 7882–7890 (2014).
16. V. Ganti, A. J. Chadwick, H. J. Hassenruck-Gudipati, M. P. Lamb, Avulsion cycles and their stratigraphic signature on an experimental backwater-controlled delta. *J. Geophys. Res. Earth Surf.* **121**, 1651–1675 (2016).
17. K. M. Ratliff, E. H. W. Hutton, A. B. Murray, Exploring Wave and Sea-Level Rise Effects on Delta Morphodynamics With a Coupled River-Ocean Model. *J. Geophys. Res. Earth Surf.* **123**, 2887–2900 (2018).
18. A. P. Nicholas, R. E. Aalto, G. H. S. Smith, A. C. Schwendel, Hydrodynamic controls on alluvial ridge construction and avulsion likelihood in meandering river floodplains. *Geology* **46**, 639–642 (2018).
19. D. J. Jerolmack, C. Paola, Complexity in a cellular model of river avulsion. *Geomorphology* **91**, 259–270 (2007).
20. E. A. Hajek, M. A. Wolinsky, Simplified process modeling of river avulsion and alluvial architecture: Connecting models and field data. *Sediment. Geol.* **257–260**, 1–30 (2012).

21. J. Pang, S. Si, The Estuary Changes of Huanghe River I. Changes in modern time [J]. *Oceanol. Limnol. Sin.* **2** (1979).
22. J. M. Coleman, H. H. Roberts, G. W. Stone, Mississippi River delta: an overview. *J. Coast. Res.* **14** (1998).
23. K. M. Straub, C. Paola, D. Mohrig, M. A. Wolinsky, T. George, Compensational Stacking of Channelized Sedimentary Deposits. *J. Sediment. Res.* **79**, 673–688 (2009).
24. M. D. Reitz, D. J. Jerolmack, Experimental alluvial fan evolution: Channel dynamics, slope controls, and shoreline growth. *J. Geophys. Res.* **117**, F02021 (2012).
25. K. E. Moran, J. A. Nittrouer, M. M. Perillo, J. Lorenzo-Trueba, J. B. Anderson, Morphodynamic modeling of fluvial channel fill and avulsion time scales during early Holocene transgression, as substantiated by the incised valley stratigraphy of the Trinity River, Texas. *J. Geophys. Res. Earth Surf.* **122**, 215–234 (2017).
26. J. R. Stedinger, Frequency analysis of extreme events. *Handb. Hydrol.* (1993).
27. D. W. LeBoutillier, P. R. Waylen, A stochastic model of flow duration curves. *Water Resour. Res.* **29**, 3535–3541 (1993).
28. H. A. Einstein, “The bed-load function for sediment transportation” in *Open Channel Flow Technical Bulletin*, (U.S. Department of Agriculture, Washington, D.C, 1950), p. 1026.
29. G. Parker, Hydraulic geometry of active gravel rivers in *ASCE J Hydraul Div*, (1979), pp. 1185–1201.
30. A. J. Moodie, *et al.*, Modeling Deltaic Lobe-Building Cycles and Channel Avulsions for the Yellow River Delta, China. *J. Geophys. Res. Earth Surf.* (2019)
<https://doi.org/10.1029/2019JF005220>.
31. V. Ganti, A. J. Chadwick, H. J. Hassenruck-Gudipati, B. M. Fuller, M. P. Lamb, Experimental river delta size set by multiple floods and backwater hydrodynamics. *Sci. Adv.* **2**, e1501768 (2016).
32. D. J. Jerolmack, J. B. Swenson, Scaling relationships and evolution of distributary networks on wave-influenced deltas. *Geophys. Res. Lett.* **34** (2007).
33. D. J. Jerolmack, D. Mohrig, Conditions for branching in depositional rivers. *Geology* **35**, 463 (2007).
34. J. P. M. Syvitski, Y. Saito, Morphodynamics of deltas under the influence of humans. *Glob. Planet. Change* **57**, 261–282 (2007).
35. J. D. Milliman, J. P. M. Syvitski, Geomorphic/Tectonic Control of Sediment Discharge to the Ocean: The Importance of Small Mountainous Rivers. *J. Geol.* **100**, 525–544 (1992).
36. R. Bintanja, R. S. W. van de Wal, J. Oerlemans, Modelled atmospheric temperatures and global sea levels over the past million years. *Nature* **437**, 125 (2005).
37. S. Jelgersma, “Land subsidence in coastal lowlands” in *Sea-Level Rise and Coastal Subsidence*, (Springer, 1996), pp. 47–62.
38. T. E. Törnqvist, *et al.*, Mississippi Delta subsidence primarily caused by compaction of Holocene strata. *Nat. Geosci.* **1**, 173 (2008).
39. S.-Y. Yu, T. E. Törnqvist, P. Hu, Quantifying Holocene lithospheric subsidence rates underneath the Mississippi Delta. *Earth Planet. Sci. Lett.* **331**, 21–30 (2012).
40. J. P. M. Syvitski, Deltas at risk. *Sustain. Sci.* **3**, 23–32 (2008).
41. J. D. Milliman, J. M. Broadus, F. Gable, Environmental and economic implications of rising sea level and subsiding deltas: the Nile and Bengal examples. *Ambio*, 340–345 (1989).
42. J. P. Ericson, C. J. Vörösmarty, S. L. Dingman, L. G. Ward, M. Meybeck, Effective sea-level rise and deltas: causes of change and human dimension implications. *Glob. Planet. Change* **50**, 63–82 (2006).
43. A. G. Nijhuis, *et al.*, Fluvio-deltaic avulsions during relative sea-level fall. *Geology* **43**, 719–722 (2015).

44. T. I. Lane, R. A. Nanson, B. K. Vakarelov, R. B. Ainsworth, S. E. Dashtgard, Evolution and architectural styles of a forced-regressive Holocene delta and megafan, Mitchell River, Gulf of Carpentaria, Australia. *Geol. Soc. London, Spec. Publ.* **444**, 305–334 (2017).
45. L. Giosan, *et al.*, Young Danube delta documents stable Black Sea level since the middle Holocene: Morphodynamic, paleogeographic, and archaeological implications. *Geology* **34**, 757–760 (2006).

*Chapter 3***CLIMATE-CHANGE CONTROLS ON RIVER DELTA AVULSION
LOCATION AND FREQUENCY**

A.J. Chadwick, M.P. Lamb

Division of Geological and Planetary Sciences, California Institute of Technology, Pasadena, CA
91125

3.0. ABSTRACT

Climate change affects the water discharge, sediment supply, and base level of coastal rivers. Coastal rivers that build deltas undergo repeated avulsion events, that is, catastrophic changes in river course, which may be affected by climate change. Understanding avulsions is necessary for predicting land-building potential and flood hazards on modern deltas, and for understanding sedimentary archives of ancient deltas. Here we present results from quasi-2D morphodynamic simulations of repeated delta lobe construction and avulsion to explore how avulsion location and frequency are affected by changes in relative sea level, sediment supply and transport capacity, and flood regime. Model results indicate relative sea-level rise drives more frequent avulsions at a constant avulsion length set by backwater hydrodynamics. Reducing the sediment supply relative to transport capacity in our simulations had little impact on avulsions in the backwater zone, because despite upstream incision the delta continued to aggrade as a result of progradation. However, increasing the sediment supply relative to transport capacity was capable of driving avulsions far upstream of the backwater zone, so long as aggradation during upstream slope adjustment outpaced backwater sedimentation. Across different climates, backwater-scaled avulsions required a variable flood regime, but avulsion location and frequency were relatively insensitive to the degree of flow variability. Results imply that climate and anthropogenic changes in the coming century will provoke avulsions farther upstream with greater frequency, and that anomalous avulsion sites observed in Holocene may record pulses in sediment supply.

3.1. INTRODUCTION

River deltas are densely populated, ecologically diverse, and socioeconomically valuable landscapes (Olson and Dinerstein 1998; Vörösmarty et al. 2009; Gleick 2003) that are sensitive to changes in climate (Livio Giosan 2014; Syvitski 2008; Bianchi and Allison 2009). At their downstream boundary, sea-level fluctuations are responsible for global trends in delta growth and destruction (Daniel Jean Stanley and Warne 1994), with the most recent phase of growth linked to the development of agriculture on deltaic plains (Zong et al. 2012; Daniel J Stanley and Warne 1997). At their upstream boundary, changing climate and weather patterns alter runoff and sediment yield to river deltas (Langbein and Schumm 1958; Walling and Webb 1996; Members 1988; Hallet,

Hunter, and Bogen 1996). Over just the last century, shifting atmospheric circulation over the continental US has increased the magnitude of 20-year floods on the Mississippi by over 50% (Knox 1993). Anthropogenic greenhouse emissions are linked to unprecedented climate change (Pachauri et al. 2014), and we need to understand how deltas respond to climate change to predict flood hazards and to sustain land for coastal cities and ecosystems. Furthermore, understanding how climate is recorded in deltaic stratigraphy provides an opportunity to unravel paleoclimatic conditions on ancient Earth and Mars, where deltaic deposits are common (McLennan et al. 2019; Howard, Moore, and Irwin III 2005; DiBiase et al. 2013; Pufahl, Pirajno, and Hiatt 2013; MacNaughton, Dalrymple, and Narbonne 1997).

Over decades to millenia, river deltas undergo repeated avulsion events — catastrophic changes in river course — which may be affected by climate change (Fig. 3.1). Avulsions tend to occur at a characteristic location and frequency (Chatanantavet, Lamb, and Nittrouer 2012; Jerolmack and Swenson 2007; Jerolmack and Mohrig 2007), corresponding to when and where the river has aggraded to a critical height that renders its course gravitationally unstable (Slingerland and Smith 2004; Mohrig, Heller, and Lyons 2000; Ganti et al. 2014). Thus, over glacio-eustatic cycles, avulsions are susceptible to spatiotemporal changes in aggradation rate driven by climate. Previous work has identified three primary influences of climate on delta aggradation, namely 1) changes in sea level, 2) changes in sediment supply and transport capacity, and 3) changes in flood regime (Blum and Törnqvist 2000a).

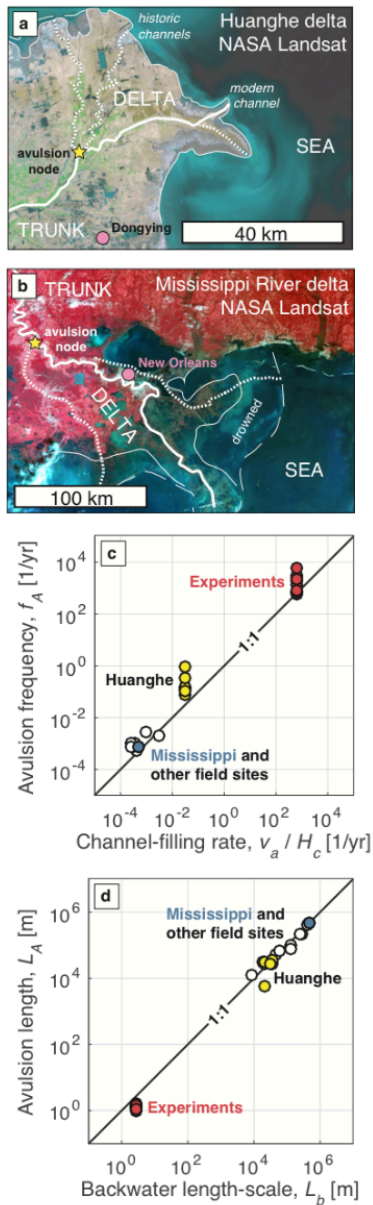


Fig. 3.1: a) Huanghe delta, China, illustrating modern (solid line) and abandoned (dotted line) channel pathways and avulsion node (yellow star). Pink circle denotes city of Dongying. b) Mississippi River delta, USA. Thin dashed line indicates approximate shoreline before human management (Gagliano, Meyer-Arendt, and Wicker 1981). Pink circle denotes New Orleans. c) Correlation between measured avulsion frequency and the rate at which riverbed aggradation fills the channel-depth (Jerolmack and Mohrig 2007; Ganti et al. 2014; Ganti, Chadwick, Hassenruck-Gudipati, Fuller, et al. 2016). d) Correlation between measured avulsion length and computed backwater length-scale, which approximates the distance upstream of the shoreline where sea-level causes gradually-varied flow (Chatanantavet, Lamb, and Nittrouer 2012; Ganti et al. 2014; Ganti, Chadwick, Hassenruck-Gudipati, Fuller, et al. 2016).

Global radiation balance drives periodic glaciation of continents and associated rise and fall of global sea levels (Oeschger et al. 1983; Sellers 1969; Lambeck and Chappell 2001). Field observations show climatic sea-level rise causes aggradation in the lower reaches of deltaic rivers (Fisk and others 1945; Powell 1875; Davis 1902; Schumm 1993), a trend supported by laboratory experiments (Martin et al. 2009; W. Kim et al. 2006) and numerical models (Parker, Muto, Akamatsu, Dietrich, and Wesley Lauer 2008; J.B. Swenson et al. 2005). This aggradation has been linked to more frequent avulsions on the Rhine-Meuse delta (Törnqvist 1994; Stouthamer and Berendsen 2001) and in experiments (Martin et al. 2009). However, the Mitchell River delta provides a counterexample where avulsions were less frequent during Holocene sea-level rise (Lane et al. 2017). Numerical modeling studies have produced both trends, even for deltas with shared sea-level histories (Moran et al. 2017; Chatanantavet, Lamb, and Nittrouer 2012), and have shown avulsion response is dampened by progradation and wave action along the shoreline (Katherine M Ratliff, Hutton, and Murray 2018; John B Swenson 2005). Extensive work by Muto and others has shown constant sea-level rise inevitably reduces aggradation rates, causing deltas to drown in a process termed autoretreat (Parker, Muto, Akamatsu, Dietrich, and Lauer 2008b; Tetsuji Muto and Steel 1992; T Muto and Steel 1997; Tetsuji Muto and Steel 2002), with unclear consequences for river avulsion. With regards to avulsion location, experiments and models of delta response are often based on the premise that avulsion location is geographically fixed regardless of sea-level rise and shoreline migration rate (T Muto and Steel 1997; Tetsuji Muto and Steel 2002; Parker, Muto, Akamatsu, Dietrich, and Lauer 2008a; Parker, Muto, Akamatsu, Dietrich, and Wesley Lauer 2008; W. Kim et al. 2006; J.B. Swenson et al. 2005; Jerolmack 2009; Paola et al. 2011). Other models based on probabilistic, slope-driven avulsion found downstream aggradation due to sea-level rise caused avulsion sites to occur closer to the shoreline (Mackey and Bridge 1995).

Over climate cycles, continental glaciation is also associated with reduced runoff and increased sediment supplied to alluvial rivers (Blum and Törnqvist 2000a). Changes in water and sediment supply cause waves of aggradation and incision that can propagate downstream to affect deltas (Blum and Törnqvist 2000b; Schumm 1993). Early experimental efforts showed higher sediment supplies were associated with enhanced aggradation and higher avulsion frequency (Bryant, Falk, and Paola 1995), to a degree that depends on water discharge and riverbed slope, i.e., the river's sediment transport capacity (Ashworth, Best, and Jones 2004). Consistent with this

framework, field observations on the Rhine-Meuse delta show more frequent avulsions during a period of increased sediment supply in the Holocene (Stouthamer and Berendsen 2001). Avulsion location is also influenced by sediment supply, with pulses in sediment supply historically being linked to avulsion sites far upstream of deltas, for example on the Tacquari megafan (Makaske et al. 2012) and in New Zealand (Korup 2004). Notwithstanding, field data linking deltaic avulsions and upstream conditions are limited, and the problem remains critically unexplored from a numerical modeling perspective.

Climatic changes in glaciation, atmospheric and oceanic circulation, and soil and vegetation cover influence the magnitude and frequency of large flood events on river deltas (Knox 2000; Members 1988). Flood regimes control the aggradation and morphology of both channel and floodplain (Leopold and Maddock 1953; Naito and Parker 2019), with consequences for river avulsion (Nicholas et al. 2018; Brizga and Finlayson 1990; E.A. Hajek and Edmonds 2014). For example, on deltas with flashier flood regimes, field evidence indicates that less in-channel aggradation is necessary to trigger an avulsion, resulting in more frequent avulsions on average (Ganti et al. 2014). Flood regimes also affect avulsion location: in models and laboratory experiments, a constant discharge regime results in avulsion sites that are tied to initial and boundary conditions (Mackey and Bridge 1995; Katherine M Ratliff, Hutton, and Murray 2018; Y. Kim et al. 2013), whereas variable flood regimes can result in backwater-scaled avulsion sites consistent with field observations (Chatanantavet and Lamb 2014; Ganti, Chadwick, Hassenruck-Gudipati, Fuller, et al. 2016; Chadwick et al. 2019; Moodie et al. 2019). Despite the importance of variable flood regimes, it remains unclear to what extent climatic variability affects avulsion location and frequency.

Previous work highlighted important ways climate change can affect deltas, but major questions remain: how are avulsion location and frequency affected by different climate forcings? This knowledge gap is not easily addressed using existing models, which describe radially averaged or channel-averaged aggradation and are not designed to resolve avulsions among multiple delta lobes. More complex 2-D morphodynamic models, designed to study delta bifurcations and channelization (Edmonds et al. 2010; Nijhuis et al. 2015; Edmonds et al. 2009; Caldwell and Edmonds 2014; Gao et al. 2019; Liang, Van Dyk, and Passalacqua 2016a; Liang, Kim, and

Passalacqua 2016), are often computationally expensive and have yet to be run systematically to explore lobe-scale avulsions. Furthermore, previous models do not investigate backwater hydrodynamics, which have been shown to play an important role mediating aggradation and avulsion on lowland deltas (Chatanantavet, Lamb, and Nittrouer 2012; Nittrouer et al. 2012; Lamb et al. 2012).

Coastal rivers are characterized by backwater hydrodynamics, non-uniform flows forced by standing water beyond the shoreline that produce spatial deceleration and deposition during low flows, and spatial acceleration and deposition during high flows (Chow 1959; Lamb et al. 2012; Nittrouer et al. 2012; Chatanantavet, Lamb, and Nittrouer 2012). Backwater effects extend hundreds of kilometers upstream of the river mouth for large, low-sloping rivers, to a distance that is well-approximated by the ratio of river depth to slope, the so-called backwater length-scale L_b (Paola and Mohrig 1996; Paola, Heller, and Angevine 1992). Many lowland deltas feature a preferential avulsion location, or avulsion node, located in the backwater zone (i.e., $L_A \sim L_b$, where L_A is the distance upstream of the river mouth where avulsions occur) (Fig. 3.1) (Jerolmack and Swenson 2007; Chatanantavet, Lamb, and Nittrouer 2012). Using a numerical model of the Mississippi River, Chatanantavet et al. (2012) hypothesized that variable flood discharges in the backwater zone cause a spatial maximum in long-term aggradation rate that determines the preferential avulsion node. Scaled physical experiments supported this hypothesis, showing laboratory-scale deltas produced a backwater-scaled avulsion node when subjected to variable flood regimes (Ganti, Chadwick, Hassenruck-Gudipati, Fuller, et al. 2016; Ganti, Chadwick, Hassenruck-Gudipati, and Lamb 2016). Building on this work, Chadwick et al. (2019) developed a model incorporating backwater hydrodynamics and multiple delta lobes. Results indicated that avulsion nodes arise in the backwater zone under a wide range of realistic flood regimes, but not under constant discharges or extremely flashy regimes. Chadwick et al. (*in review*) used the same model to show avulsion frequency response to sea-level rise falls into three regimes depending on the competition between the rise rate and the sediment supply that drives lobe progradation. Results reconciled existing field data, showing sea-level rise at rates commensurate to the sediment supply can drive a ten-fold increase in avulsion frequency, but that the effect is less important on deltas with lower rise rates, where avulsion frequency is set by progradation rate, or on deltas with much higher rise rates where avulsion frequency is limited by the sediment supply. Importantly, previous studies did not address the effects

of sea-level rise on avulsion location, or the effect of flood regimes on avulsion frequency, or any influences upstream changes in sediment supply and transport capacity.

Here, we use the model of Chadwick et al. (2019) to address this knowledge gap. First, we briefly review the model's function and parameterization of climate forcings. We then present results from numerical simulations with systematic variation of climate forcing parameters, exploring inherent variability and systematic change in avulsion location and frequency. Finally, we discuss implications for avulsion dynamics over glacial-interglacial cycles, during modern anthropogenic climate change, and for preservation of climate change signatures in avulsive stratigraphic architecture.

3.2. MODEL DERIVATION

The numerical model presented here was first developed by Chadwick et al. (Chadwick et al. 2019) and here we summarize the essential details of their model setup. The framework consists of a generic deltaic plain with an imposed number of lobes (Fig. 3.2) Each lobe was modeled as a coupled river and floodplain, which is well-described by a quasi-two-dimensional mass-balance framework (Parker 2004; Parker, Muto, Akamatsu, Dietrich, and Lauer 2008a; 2008b; Chatanantavet, Lamb, and Nittrouer 2012). Sediment mass is balanced by the equation

$$\frac{\partial \eta}{\partial t} + \sigma = - \frac{1}{(1 - \lambda_p)B} \frac{\partial Q_t}{\partial x} \quad (3.1)$$

where η is channel bed elevation relative to sea level, t is time, σ is relative sea-level rise rate, x is downstream distance, and Q_t is the volumetric sediment transport capacity at position x . Sediment is deposited uniformly over floodplain width B with porosity λ_p . At the delta front, fluvial sediment transport gives way to gravity flow and avalanching, and deposition drives foreset progradation. We approximate progradation using a moving-boundary formulation, with a foreset of constant slope S_a set to five times the transport slope (J B Swenson et al. 2000; Kostic and Parker 2003).

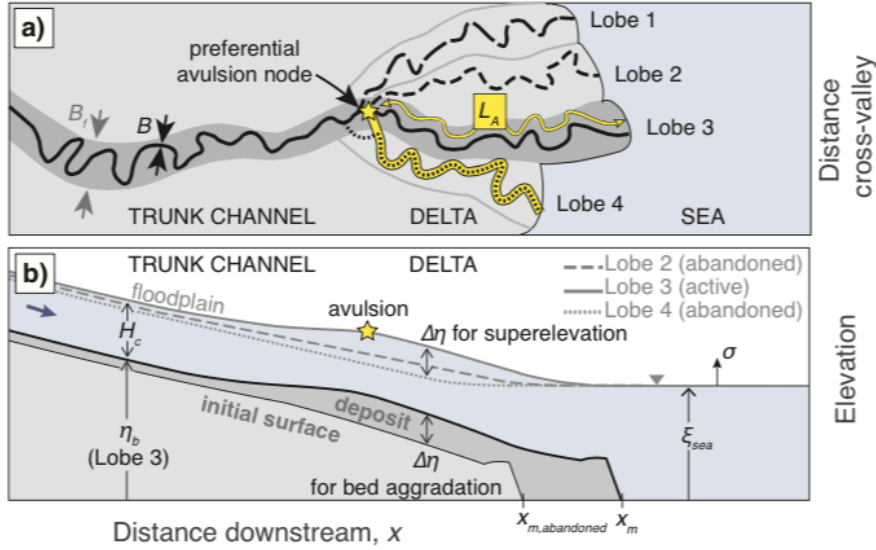


Fig. 3.2: a) Conceptual model in plan view. Black solid lines are active channel of width B_c in a floodplain/lobe of width B (Lobe 3). Broken lines are abandoned channels. After an avulsion, abandoned lobe 4 is reoccupied and its profile is joined with trunk channel at avulsion node (yellow star). b) Conceptual model in long profile, showing channel aggradation and floodplain super-elevation of the active lobe (lobe 3) relative to the lowest abandoned lobe (lobe 4).

We used the backwater equation to constrain water mass and momentum under quasi-steady flow conditions (Chatanantavet, Lamb, and Nittrouer 2012),

$$\frac{dH_w}{dx} = \frac{S - S_f}{1 - Fr^2} + \frac{Fr^2}{1 - Fr^2} \frac{H_w}{B_w} \frac{dB_w}{dx} \quad (3.2)$$

where H_w is flow depth, S is channel bed slope, $S_f = C_f Fr^2$ is friction slope, C_f is friction coefficient, Fr is Froude number, and B_w is the width of water flow. We assumed flow width was contained by the channel upstream of the river mouth, and expanded at a constant spreading angle offshore (Lamb et al. 2012; Chatanantavet, Lamb, and Nittrouer 2012), here set to 15 degrees. Following recent work (Chadwick et al. 2019), the location of the river mouth x_m is set by the intersection of the floodplain profile η_f with sea level ξ_o ,

$$x_m = x |_{\eta_f(x) = \xi_o} \quad (3.3)$$

where the floodplain elevation is defined as the sum of the bed elevation and channel depth H_c ,

$$\eta_f(x) = \eta(x) + H_c \quad (3.4)$$

Over time, the floodplain in our model aggrades in concert with the channel bed, driving river mouth advancement. A mobile river mouth is necessary for foreset progradation to drive topset aggradation (Chadwick et al. 2019).

Sediment was routed according to Engelund and Hansen (Engelund and Hansen 1967) for total bed-material load, similar to previous studies (Lamb et al. 2012; Nittrouer et al. 2012; Chatanantavet, Lamb, and Nittrouer 2012),

$$Q_t = B_c \sqrt{RgD^3} \frac{\alpha}{C_f} (\tau^*)^n \quad (3.5)$$

where R is submerged specific density of sediment, g is gravity, D is the median grain-size of bed material, τ^* is Shields number, and $\alpha = 0.05$ and $n = 2.5$ (Engelund and Hansen 1967). All sediment delivered to the delta front is captured in the foreset (Kostic and Parker 2003; J.B. Swenson et al. 2000).

The numerical morphodynamic model consists of a delta with an imposed number of lobes that are assumed to form a branching pattern, with only one lobe active at a given time (Fig. 3.2) (Ganti, Lamb, and Chadwick 2019; Chadwick et al. 2019). Avulsions occurred when the active lobe aggraded to a critical height H at some point in the model domain, corresponding to the spatial maximum in aggradation rate (Mohrig, Heller, and Lyons 2000; Ganti, Chadwick, Hassenruck-Gudipati, Fuller, et al. 2016; Chatanantavet, Lamb, and Nittrouer 2012) (Fig 1b). We used an avulsion criterion given by a critical thickness of aggradation, which we refer to as superelevation ($\Delta\eta$):

$$\Delta\eta(x) \geq H^* H_c \quad (3.6)$$

in which H_c is the bankfull channel depth and H^* is the avulsion threshold, a dimensionless number that is of order unity describing the necessary amount of aggradation before an avulsion takes place (Mohrig, Heller, and Lyons 2000; Ganti et al. 2014; Ganti, Chadwick, Hassenruck-Gudipati, and Lamb 2016). We triggered an avulsion when and where the floodplain elevation of the active lobe

exceeded the floodplain elevation of the lowest-elevation abandoned lobe ($\eta_{f,abandoned}$), evaluated at the same distance downstream from the trunk channel:

$$\Delta\eta(x) = \begin{cases} \eta_f(x) - \eta_{f,abandoned}(x) & \text{for } x \leq x_{m,abandoned} \\ \eta_f(x) - \xi_{sea} & \text{for } x > x_{m,abandoned} \end{cases} \quad (3.7)$$

where $x_{m,abandoned}$ is the stream-wise coordinate of the abandoned-lobe shoreline. Seaward of the abandoned lobe, superelevation is measured relative to sea level (ξ_{sea}) (Chadwick et al. 2019; Katherine M Ratliff, Hutton, and Murray 2018). Extreme floods may also affect the timing of any one avulsion (Nicholas et al. 2018; Ganti et al. 2014), but these factors were neglected for simplicity following previous work (Jerolmack and Paola 2007; Elizabeth A. Hajek and Wolinsky 2012; Chadwick et al. 2019).

After avulsion, the river was rerouted to the lowest abandoned lobe by joining the bed profile of the active channel upstream of the avulsion site with the bed profile of the new flow path downstream,

$$\eta_{new}(x) = \begin{cases} \text{MIN}(\eta_{abandoned1}(x), \eta_{abandoned2}(x), \eta_{abandoned3}(x)) & x > x_A \\ \eta(x) & x \leq x_A \end{cases} \quad (3.8)$$

where x is distance downstream, x_A is the avulsion location, $\eta_{b,new}$ is the new riverbed profile after avulsion, η_b is the riverbed profile before avulsion, and $\eta_{b,abandoned1}$, $\eta_{b,abandoned2}$, and $\eta_{b,abandoned3}$ are the three abandoned-lobe long profiles. The MIN operator here selects the abandoned profile that has the minimum mean elevation, $\bar{\eta}_b$, downstream of the avulsion node,

$$\bar{\eta} = \frac{1}{x_m - x_A} \int_{x_A}^{x_m} \eta(x) dx \quad (3.9)$$

where x_m is the downstream coordinate of the river mouth. For example, if $\eta_{b,abandoned2}(x)$ yields a lower value of $\bar{\eta}_b$ than both $\eta_{b,abandoned1}(x)$ and $\eta_{b,abandoned3}(x)$ yield, then $\eta_{b,abandoned2}(x)$ is selected as the path downstream of the avulsion location. This process mimics the tendency of rivers to select steeper paths, fill in topographic lows (Slingerland and Smith 2004; Straub et al. 2009), and to reoccupy previously abandoned channels (Reitz and Jerolmack 2012). Inactive lobe

shapes were unchanged when abandoned (Galloway 1975) but were partially drowned in cases due to relative sea-level rise. After establishing the new flow path, lobe construction (Eqs. (3.1 – 5)) and avulsion setup (Eq. (3.6)) began anew.

To enable applicability across a wide range of river conditions, the model was non-dimensionalized using bankfull normal-flow channel depth (H_c), width (B_c), riverbed transport slope (S), and flow-averaged sediment supply (\bar{Q}_s) at the start of the model run. Non-dimensionalizing Eqs. (3.1 – 9) yields

$$\frac{\partial \eta^*}{\partial t^*} + \frac{\sigma^*}{NB^*} = -\frac{1}{B^* \bar{q}_t^*} \frac{\partial q_t^*}{\partial x^*} \quad (3.10)$$

$$x_m^* = x^* |_{\eta_f^*(x^*) = \xi_o^*} \quad (3.11)$$

$$\eta_f^*(x^*) = \eta^*(x^*) + H_c^* \quad (3.12)$$

$$\frac{\partial H_w^*}{\partial x^*} = \frac{S^* - S_f^*}{1 - Fr^2} + \frac{Fr^2}{1 - Fr^2} \frac{H^*}{B_w^*} \frac{dB_w^*}{dx^*} \quad (3.13)$$

$$C_f q_t^* = \alpha (\tau^*)^n \quad (3.14)$$

$$\Delta \eta^* \geq H^* H_c^* \quad (3.15)$$

$$\Delta \eta^*(x^*) = \begin{cases} \eta_f^*(x^*) - \eta_{f,abandoned}^*(x^*) & \text{for } x^* \leq x_{m,abandoned}^* \\ \eta_f^*(x^*) - \xi_{sea}^* & \text{for } x^* > x_{m,abandoned}^* \end{cases} \quad (3.236)$$

$$\eta_{,new}^*(x^*) = \begin{cases} \text{MIN}(\eta_{abandoned1}^*(x^*), \eta_{abandoned2}^*(x^*), \eta_{abandoned3}^*(x^*)) & x^* > x_A^* \\ \eta^*(x^*) & x^* \leq x_A^* \end{cases} \quad (3.17)$$

$$\bar{\eta}^* = \frac{1}{x_m^* - x_A^*} \int_{x_A^*}^{x_m^*} \eta_b^*(x^*) dx^* \quad (3.18)$$

where $x^* = x/L_b$ is dimensionless distance downstream, $\eta^* = \eta/H_c$ is dimensionless channel-bed elevation, $t^* = t\bar{Q}_s/B_c L_b (1 - \lambda_p)$ is dimensionless time and \bar{Q}_s is time-averaged volumetric

sediment supply, and $\sigma^* = \sigma / (\bar{Q}_s / nBL_b(1 - \lambda_p))$ is dimensionless sea-level rise rate averaged over N delta lobes of normalized width $B^* = B/B_c$. $H_w^* = H_w/H_c$ is the dimensionless flow depth, $B_w^* = B_w/B_c$ is dimensionless flow width, $S^* = S/(H_c/L_b)$ is the normalized bed slope, $S_f^* = Fr^2 C_f / S$ is the normalized friction slope, q_t^* is the Einstein number representing dimensionless bed-material transport (Einstein 1950; Parker 1979) and \bar{q}_t^* is the time-averaged Einstein number. All elevation variables are normalized relative to channel depth (e.g. $\eta_f^* = \eta_f/H_c$) and all horizontal distance variables are normalized relative to the backwater length (e.g., $x_m^* = x_m/L_b$). For simplicity channel depth and width are assumed constant in our model, but flow-averaged sediment supply and transport slope are allowed to change due to upstream climate controls. For all simulations considered here, we assume typical values for bankfull Froude number in the normal-flow reach ($Fr_{n,bf} = 0.17$), bankfull Shields number in the normal-flow reach ($\tau_{n,bf}^* = 1$), friction factor ($C_f = 0.005$), offshore basin floor depth normalized by bankfull depth ($H_b^* = 3$), lobe width normalized by channel width ($B^* = 40$), and vary only parameters that are associated with climate change.

3.3. SETUP FOR MODEL RUNS AND CLIMATE-CHANGE SCENARIOS

At the start of each model run, the initial state of the riverbed was assumed planar with a uniform downstream slope set to the transport slope for normal flow, similar to previous studies (Chatanantavet, Lamb, and Nittrouer 2012; Moran et al. 2017; Katherine Murray Ratliff 2017). Due to the imposed number of lobes, after four avulsion cycles the river was forced to reoccupy lobes that were previously active, and thus the effect of initial conditions on avulsion location was minimized (Chadwick et al. 2019). Here we focus on results after the fourth avulsion cycle, and consider the first four avulsions a model spin-up period.

Climate change affects model behavior through dynamic boundary conditions that describe through 1) changes in sea level, 2) changes in sediment supply and transport capacity, and 3) changes in flood regime (Blum and Törnqvist 2000a). We parameterized climate change in terms of these three effects, for a total of six input parameters: normalized relative sea-level rise rate (σ^*), fractional change in equilibrium transport slope (δS), coefficient of variation of stage height (CV), bankfull exceedance probability (F_{bf}), normalized flood duration (T_e^*), and the avulsion threshold (H^*). These

parameters are user-specified for simplicity, as their connection to global radiation balance and atmospheric and oceanic circulation is site-specific and scale-dependent in nature (Langbein and Schumm 1958; Knox and Wright 1983; Probst 1989).

3.3.1 Changes in sea level

Following previous work, we parameterized sea-level rise in terms of its competition with sediment supply (T Muto and Steel 1997; Liang, Van Dyk, and Passalacqua 2016b; Ganti, Lamb, and Chadwick 2019), which we term the normalized relative sea-level rise rate σ^* , defined as

$$\sigma^* = \frac{\sigma}{\bar{v}_a} = \frac{\sigma}{\bar{Q}_s/nL_bB} \quad (3.19)$$

where σ is relative sea-level rise rate and $\bar{v}_a = \bar{Q}_s/nL_bB$ is the characteristic rate of aggradation assuming the time-averaged sediment supply \bar{Q}_s is deposited evenly across n delta lobes of length L_b and lobe width B . The condition $0 < \sigma^* < 1$ corresponds to when sea level rises slowly compared to aggradation rates, and deltas can prograde. Conversely, $\sigma^* > 1$ when sea level rises quickly compared to aggradation rates, corresponding to delta shoreline retreat. The condition $\sigma^* = 1$ represents a threshold where sea-level and sediment supply are in approximate balance and the delta shoreline is relatively stable. Sea level fall corresponds to $\sigma^* < 0$. Using characteristic rise and fall rates (Bintanja, van de Wal, and Oerlemans 2005) and sediment supply records (Milliman and Syvitski 1992), we estimate σ^* ranges from -1 to 5 for a number of large, modern deltas under climate change (Table 1, Table 2). Because sea-level rise rate is relatively constant over the 10-1000-yr timescales of avulsion (Fig. 3.3), we adopted a single value of σ^* in each sea-level change simulation. To avoid premature drowning of the model domain, during the spin-up period of model simulations we enforced $\sigma = 0$.

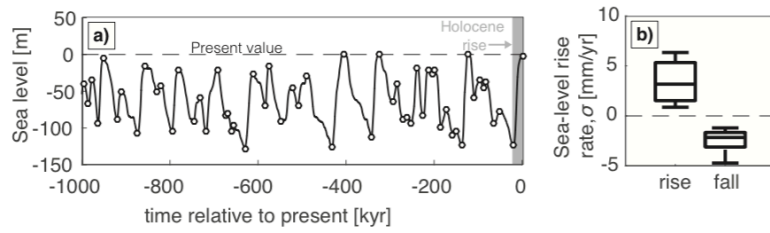


Fig. 3.3: a) Globally averaged eustatic sea-level curve over the past million years (Bintanja, van de Wal, and Oerlemans 2005). Black dashed line shows present sea-level, and gray shaded region indicates Holocene sea-level rise. White circles indicate still-stands (local extreme) in sea-level. b) Box plots of average eustatic sea-level rise rate between still-stands in panel (a). Data are grouped by whether sea level was rising or falling between still-stands.

| River or model run | σ^* | δS | F_{bj} | CV | T_e^* | H^* |
|---------------------------------|------------|------------|-----------|-------|---------------------|-----------|
| | [-] | [-] | [-] | [-] | [-] | [-] |
| Parana | 2.3 | - | 0.12 | 0.18 | 1.9E-04 | 0.69 |
| Danube | 0.1 | - | 0.10 | 0.27 | 3.0E-03 | 0.79 |
| Nile | 0.2 | - | 0.05 | 0.65 | 6.4E-02 | - |
| Mississippi | 0.4 | - | 0.06 | 0.44 | 1.8E-03 | 0.60 |
| Assiniboine | - | - | - | - | 2.8E-03 | 0.33 |
| Rhine-Meuse | 5.0 | - | - | - | 2.0E-04 | 0.46 |
| Magdalena | 0.2 | - | - | - | 5.5E-03 | - |
| Orinoco | 0.9 | - | 0.43 | 0.61 | 7.4E-04 | 0.26 |
| Mid-Amazon | 0.5 | - | - | - | 8.7E-04 | - |
| Upper Rhone | 0.8 | - | - | - | 6.4E-04 | 0.54 |
| Huanghe | 0.0 | - | 0.22 | 0.91 | 3.8E-01 | 0.20 |
| Brahmaputra | 0.2 | - | 0.08 | 0.68 | 3.7E-03 | 1.43 |
| Goose | -0.1 | - | - | - | 2.0E-02 | 0.33 |
| Mitchell | 0.0 | - | - | - | 1.9E-03 | - |
| Trinity | 0.7 | - | - | - | 2.1E-03 | - |
| Base-case model run | 0 | 0 | 0.05 | 0.53 | 1.0E-03 | 0.5 |
| Scale-level-change runs | -1-10 | 0 | 0.05 | 0.53 | 1.0E-03 | 0.5 |
| Sediment supply & capacity runs | 0 | -0.4 - 0.4 | 0.05 | 0.53 | 1.0E-03 | 0.5 |
| Flow-regime runs (F_{bj}) | 0 | 0 | 0.001 - 1 | 0.53 | 1.0E-03 | 0.5 |
| Flow-regime runs (CV) | 0 | 0 | 0.05 | 0-0.9 | 1.0E-03 | 0.5 |
| Flow-regime runs (T_e^*) | 0 | 0 | 0.05 | 0.53 | 1.0E-06 - 1.0E02 | 0.5 |
| Flow-regime runs (H^*) | 0 | 0 | 0.05 | 0.53 | 1.0E-03 | 0.2 - 2.5 |

Table 2) Non-dimensionalized model input parameters corresponding to field data in Table 1 and discharge time series (Ganti et al 2014), and values used for model runs. σ^* = $\sigma n L_b B / Q_s$ is dimensionless relative sea level rise rate, $\delta S = (S_{eq} - S_{eq0}) / S_{eq0}$ is fractional change in equilibrium transport slope, F_{bj} is bankfull exceedance probability, CV is coefficient of variation of stage height, T_e^* = $T_e Q_s / H_c B_c L_b$ is dimensionless flood duration where $T_e = 1$ month, and H^* is avulsion threshold.

| River | H_c [m] | B_c [m] | L_b [km] | Q_s [M/year] | v_a [mm/yr] | σ [mm/yr] | T_A [yr] | f_A [1/kyr] | L_A [km] |
|-------------|--------------|--------------|---------------|-------------------|------------------|---------------------|---------------|------------------|---------------|
| Parana | 11.8 | 1270 | 295.0 | 79.0 | 5 | 3 | 1633 | 0.6 | 210 |
| Danube | 6.3 | 1250 | 125.0 | 67.0 | 2.5 | 0.2 | 1991 | 0.5 | 95 |
| Nile | 16.2 | 240 | 254.0 | 120.0 | – | 3 | – | – | 210 |
| Mississippi | 21.0 | 650 | 480.0 | 400.0 | 10 | 3 | 1250 | 0.8 | 490 |
| Assinboine | 4.2 | 100 | 8.4 | 0.9 | 1.4 | – | 1000 | 1.0 | 12 |
| Rhine-Meuse | 5.0 | 700 | 45.5 | 3.1 | 1.6 | 3 | 1450 | 0.7 | 51 |
| Magdalena | 6.0 | 1100 | 63.2 | 220.0 | 3.8 | 3 | – | – | 67 |
| Orinoco | 8.0 | 2000 | 133.3 | 150.0 | 2.1 | 3 | 1000 | 1.0 | 78 |
| Mid-Amazon | 12.0 | 3000 | 400.0 | 1200.0 | 5 | 3 | – | – | 404 |
| Upper Rhone | 5.4 | 377 | 135.2 | 31.0 | 2 | 3 | 1450 | 0.7 | – |
| Huanghe | 3.5 | 500 | 35.0 | 1100.0 | 100 | 0.3 | 7 | 142.9 | 31 |
| Brahmaputra | 7.0 | 3300 | 70.0 | 540.0 | 20 | 3 | 500 | 2.0 | – |
| Goose | 2.0 | 100 | 0.9 | 0.3 | 1.98 | -3 | 333 | 3.0 | – |
| Mitchell | 7.0 | 100 | 23.3 | 2.9 | – | -0.25 | 63 | 16.0 | – |
| Trinity | 5.0 | 200 | 31.3 | 6.2 | 1.1 | 4.2 | – | – | – |

Table S1) Field data used in this study. Bankfull channel depth (H_c), channel width (B_c), aggradation rates (v_a), and avulsion frequencies (f_A) are reported in Jerolmack and Mohrig (Jerolmack and Mohrig 2007), and avulsion lengths (L_A) and backwater lengths (L_b) are reported in Chatanantavej et al. (Chatanantavej, Lamb, and Nitrouer 2012) and Ganti et al. (Ganti et al. 2014). Sediment supplies (Q_s) are reported in Milliman and Syvitski (Milliman and Syvitski 1992). The avulsion threshold for each site was estimated using $H^* = v_a / (f_A H_c)$ (Ganti et al. 2014). Sea level rise (σ) was estimated using the 10,000-year-averaged rate from Bintanja et al. (Bintanja, van de Wal, and Oerlemans 2005), except for the Huanghe where avulsions are more recent and the 100-year-averaged rise rate was used. Values for the Goose, Mitchell, and Trinity were compiled from recent studies (Nijhuis et al. 2015; Lane et al. 2017; Moran et al. 2017).

3.3.2 Changing sediment supply and transport capacity

Changing climate upsets the balance between supply and transport capacity, resulting in riverbed adjustment via aggradation or degradation (Fig. 3.4). When supply exceeds capacity, channels aggrade in a downstream-propagating diffusional wave pattern, until the slope steepens and transport capacity increases to match supply (termed ‘downfilling’) (Schumm 1993). When capacity exceeds supply, channels degrade in a mechanically similar wave of degradation until the slope decreases and transport capacity decreases to match supply. In our model, sediment supply enters the model using a ghost-node at the upstream end, where the river is assumed to have reached grade (Kostic and Parker 2003). For each flow event, we varied upstream sediment supply ($Q_{f,i}$) using Engelund Hansen (1967) such that normal-flow transport slope was always equal to S_{eq} ,

$$Q_{f,i} = B_c \sqrt{RgD^3} \frac{\alpha}{C_f} \left(\frac{H_n S_{eq}}{RD} \right)^n = B_c \sqrt{RgD^3} \frac{\alpha}{C_f} \left(\tau_{bf}^* H_n^* (\delta S + 1) \right)^n \quad (3.20)$$

where H_n is normal flow depth, τ_{bf}^* is Shields number under normal flow bankfull conditions, and $H_n^* = H_n/H_{bf}$ is normal flow depth normalized by bankfull depth. By fixing the transport slope across flood events, we were able to explore the effects of changing flood regimes and changing sediment supplies and transport capacities independently. The time-averaged sediment supply for each model run (\bar{Q}_f) is the linear combination of sediment supply and occurrence probability for each flow bin,

$$\bar{Q}_f = \sum_i Q_{f,i} F_i \quad (3.21)$$

In our analysis, we quantified changes in sediment supply and transport capacity in terms of a fractional change in equilibrium transport slope, which we define as δS ,

$$\delta S = \frac{S_{eq} - S_{eq0}}{S_{eq0}} \quad (3.22)$$

where S_{eq} is the equilibrium transport slope resulting from upstream climate change, and S_{eq0} is the initial equilibrium transport slope before climate change took place. The condition $\delta S > 0$ results from increasing sediment supply, decreasing runoff, and/or increasing sediment grain size. Conversely, $\delta S < 0$ describes decreasing sediment supply, increasing runoff, and/or fining of upstream grain size (Fig. 3.4). $\delta S = 0$ represents a scenario where the equilibrium transport slope remains unchanged. Variations in runoff, sediment supply, and grain size can influence the equilibrium transport slope over a wide range of timescales (Paola, Heller, and Angevine 1992). Understanding the interplay of these variables is beyond the scope of this study. For simplicity, we implemented instantaneous step-wise changes in δS in our model runs, simulating abrupt changes in upstream conditions. However, we reason that delta response to gradual climate change can be inferred from model runs with low-magnitude δS , to the extent that long-term changes in equilibrium slope can be approximated by a series of small step-wise changes (Fig. 3.4). We held $\delta S = 0$ during the spin-up period so that river adjustment from initial conditions was not convoluted with adjustment due to imbalances between sediment supply and transport capacity. Starting with avulsion cycle 5, σ and δS were allowed to change to a constant, non-zero value corresponding to each model run.

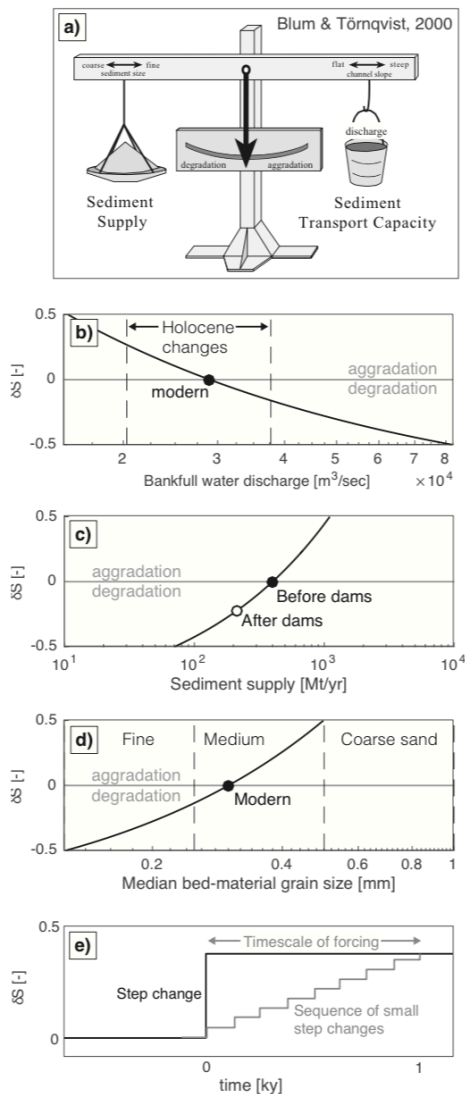


Fig. 3.4: a) Conceptualization of balance between sediment supply and transport capacity (Blum and Törnqvist 2000b). Decreasing water discharge, increasing sediment supply, and/or increasing sediment size causes sediment supply to exceed capacity, resulting in aggradation. Conversely, increasing water discharge, decreasing sediment supply, and/or decreasing sediment size causes sediment transport capacity to exceed sediment supply, resulting in degradation. Aggradation and degradation are associated with increasing and decreasing equilibrium transport slopes, respectively. b) Fractional change in equilibrium transport slope δS due to changing water discharge, computed using a Darcy-Weisbach normal-flow relation and modern values on the Mississippi River as an example (Jerolmack and Mohrig 2007; Milliman and Syvitski 1992). Vertical dashed lines indicate the domain of $\pm 30\%$ change in bankfull water discharge over the Holocene (Knox 2000). c) Computed fractional change in δS due to changing sediment supply. Black and white points indicate estimates for the Mississippi river before and after the construction of major dams in the 20th century (Milliman and Syvitski 1992). d) Computed fractional change in δS due to changing sediment grain-size. Vertical dashed lines define fine sand, medium sand, and coarse sand. e) Schematic diagram illustrating how long-term, gradual changes in equilibrium transport slope δS can be approximated by a series of small step-changes.

3.3.3 Changing flood regimes

Following previous work, we approximated flood regimes using a log-normal distribution (Stedinger 1993; LeBoutillier and Waylen 1993), uniquely defined by a bankfull exceedance probability F_{bf} , which describes the frequency of overbank floods, and a coefficient of variation CV , which describes the magnitude of large floods relative to low flows (Fig. 3.5). The distribution was discretized into twenty logarithmically spaced bins, with each bin i being described by normal flow depth $H_{n,i}$ and probability F_i . We sampled the flood distribution at a normalized flow event duration $T_e^* = \frac{T_e \bar{Q}_s}{H_c L_b B}$, where T_e is dimensional flood duration. Sediment supply was varied with each flow event such that the equilibrium transport slope remained unchanged ($\delta S = 0$), allowing us to isolate the effects of flood regime. Using a reasonable value of $T_e = 1$ month, we find $F_{bf} \sim 1 - 10\%$, $CV \sim 0.1 - 0.7$, and $T_e^* \sim 10^{-4} - 10^{-1}$ for many lowland river deltas (Table 1). We also consider the avulsion threshold H^* in Eq. (3.6) a flood regime parameter. On lowland deltas H^* varies in the range $0.2 - 1$, with lower H^* associated with higher values of CV (Ganti et al., 2014).

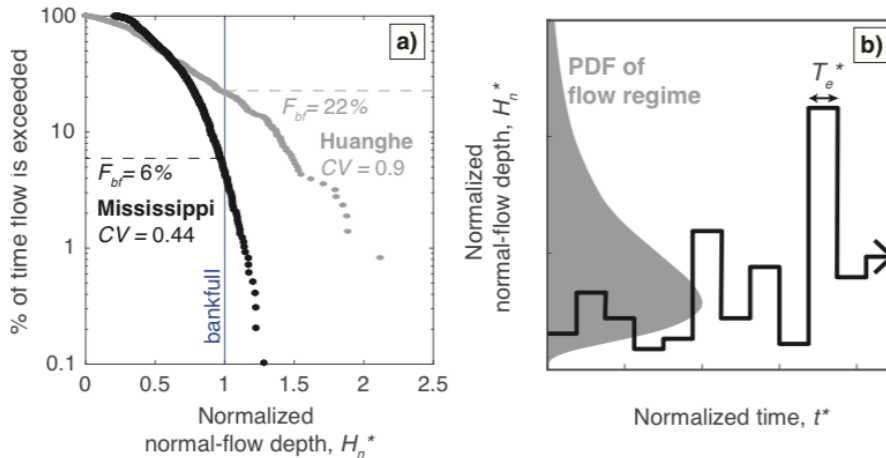


Fig. 3.5: a) Exceedance probability of normal-flow depth normalized by bankfull depth for the Mississippi and Huanghe (Ganti et al. 2014), illustrating how bankfull exceedance probability (F_{bf}) and the coefficient of variation (CV) were estimated in Table 1. Steeper trends of exceedance probability correspond to lower values of CV . b) Schematic time-series of modelled normal-flow depth after non-dimensionalization, showing how input flow depth is determined by randomly sampling a log-normal distribution for fixed flow events of duration T_e^* .

Timescales of riverbed adjustment to different flood regimes are relatively short, being comparable to the timescale of a single avulsion (Chatanantavet, Lamb, and Nittrouer 2012; Chatanantavet and Lamb 2014). For simplicity we ignore effects of transient adjustment between flood regimes, and instead explore the effects of different flood regimes on delta avulsion location and frequency over many avulsion cycles.

3.3.4 Base-case climate and climate-change model runs

To provide reference to climate-change scenarios, we considered a base-case climate scenario. The base case corresponds to a stable sea level downstream, balanced sediment supply and capacity at the upstream end, and a moderate flow regime which is necessary for realistic backwater-scaled avulsion nodes (Table 2) (Chatanantavet, Lamb, and Nittrouer 2012; Ganti, Chadwick, Hassenruck-Gudipati, Fuller, et al. 2016; Chadwick et al. 2019). Under the base-case climate scenario we characterized trends and variability in avulsion location and frequency. We then systematically changed individual climate parameters, holding all other climate parameters constant and equal to base-case values. Results for avulsion location and frequency for climate-change runs were compared to those of the base case.

3.4. RESULTS

3.4.1 Avulsions under a base-case climate scenario

In order to identify trends and inherent variability in avulsion dynamics under constant climate conditions, we first considered a model run under steady sea level, transport capacity, and sediment supply ($\sigma^* = 0, \delta S = 0$) and a moderate flow regime typical of lowland rivers ($CV = 0.53, F_{bf} = 0.05, T_e^* = 0.001, H^* = 0.5$).

Over the nine avulsion cycles considered, we observed a preferential avulsion node with an avulsion length approximately equal to the backwater length-scale (Fig. 3.6). Consistent with previous studies, low flows enhanced deposition due to spatial deceleration through the backwater zone and high flows eroded the downstream-most reach, resulting in a spatial peak in time-averaged deposition rate midway through the backwater zone (Lamb et al. 2012; Chatanantavet, Lamb, and

Nittrouer 2012; Ganti, Chadwick, Hassenruck-Gudipati, Fuller, et al. 2016). Avulsions occurred at the site of maximum deposition rate, and in most cycles only a short reach ($< 0.4 L_b$) was within 10% of the threshold at times of avulsion. The frequency of avulsion events was comparable to the rate of bed adjustment ($f_A^* = \frac{T_{adj}}{T_A} = 0.1 - 0.7$), consistent with existing field data and models (Jerolmack and Mohrig 2007; Ganti et al. 2014).

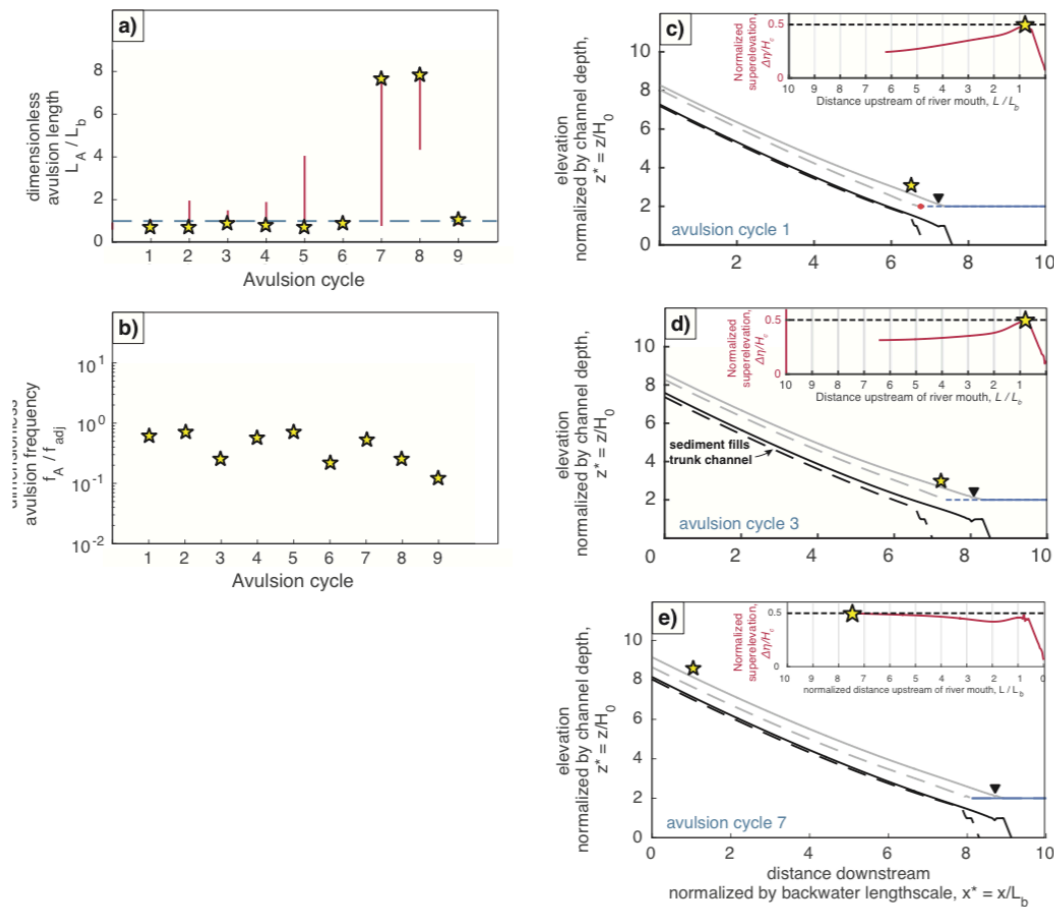


Fig. 3.6: Model results for dimensionless avulsion length (a) and frequency (b) under a stable, base-case climate for 10 avulsion cycles. c) An example of a lateral avulsion cycle, which occurred during cycles 5, 6, 8, and 9. d) An example of a trunk-filling avulsion cycle, which occurred during cycles 7, 10, and 13. e) An example of an upstream avulsion, which occurred during cycles 11 and 12. In c-e), black lines are riverbed profile at start (dashed) and end (solid) of an avulsion cycle. Floodplain profiles of active lobe (gray solid line) and lowest inactive lobe (gray dashed line) are used to calculate superelevation (see inset). Black triangles are river mouth at end of the avulsion cycle. Yellow stars show avulsion location.

Despite constant climate conditions, we observed inherent variability in avulsion location and timing due to periodic sedimentation of the trunk channel. Most avulsion cycles avulsed laterally

among self-similar delta lobes with negligible sedimentation in the trunk channel, which we refer to as lateral avulsion cycles. During lateral avulsions, avulsions occurred at the backwater-scaled node ($L_A^* \sim 1$) at a frequency $f_A^* = 0.2 - 0.7$. In contrast, some avulsion cycles featured significant sedimentation upstream of the avulsion node in the trunk channel, systematically lower avulsion frequency ($f_A^* = 0.1 - 0.2$) and greater distances of lobe progradation (Fig. 3.6). Progradation was accompanied by downstream translation of the avulsion node in order to maintain a constant avulsion length ($L_A^* \sim 1$).

Deltas alternated between lateral and trunk-filling avulsion cycles because because aggradation to the avulsion threshold was measured relative to inactive delta lobes (Eqs. (3.6 – 7)). During lateral avulsion cycles (cycles 1, 2, 4, and 5) the active lobe was activated with an elevation comparable to inactive delta lobes, and reached the avulsion threshold after depositing a thickness of $\sim H^*$. However, once all but one lobe had experienced an avulsion, the remaining lobe initiated with an elevation $\sim H^*$ lower than the inactive lobes. The active lobe then deposited $\sim 2H^*$ during one cycle, in order to level itself with inactive lobes and then superelevate itself to the threshold of avulsion. Greater deposit thickness was achieved through enhanced progradation of the river mouth, and the trunk channel was filled to maintain alluvial grade. Due to our assumed number of four delta lobes, trunk-filling avulsion cycles occurred once every three cycles (cycles 3, 6, and 9).

During avulsion cycles 7 and 8, avulsions occurred far upstream of the backwater zone ($L_A^* > 2$), and without a prominent peak in superelevation (Fig. 3.6). These avulsion cycles were caused by transient, nearly uniform deposition rate in the trunk channel during its adjustment towards alluvial grade, which in these cases persisted slightly after the trunk-filling avulsion cycle. Occasional avulsions far upstream of a backwater-mediated node have been interpreted in Mississippi River deposits (Chamberlain et al. 2018). In our model, upstream avulsions were uncommon in our model runs because the trunk channel usually filled and achieved grade within one avulsion cycle.

3.4.2 Avulsions during changes in sea level

Next, we considered model runs identical to the base-case but with relative sea-level rise and fall (Table 2). As described in recent work (Chadwick et al., *in review*), increasing the relative sea-

level rise rate in our model caused more frequent avulsions at a persistent avulsion node (Fig. 3.7). More frequent avulsions in the domain $0.1 < \sigma^* < 1$ reflected a regime where sea-level rise was the dominant control on aggradation rate. In contrast, for $\sigma^* < 0.1$ aggradation was primarily caused by progradation, and for $\sigma^* > 1$ sediment supply limited aggradation rates.

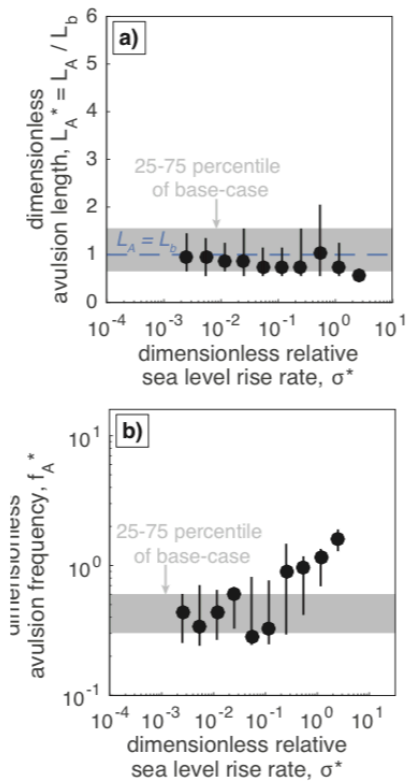


Fig. 3.7: Model results for dimensionless avulsion length (a) and avulsion frequency (b) under changing sea level rise rate. Black circles show average and 25-75 percentile range of avulsion location and frequency. Gray shaded regions denote the 25-75 percentile range for a stable climate in the base-case simulation. Blue dashed line indicates where $L_A = L_b$.

Avulsion length was insensitive to relative sea-level rise rate. For $\sigma^* < 1$, backwater effects continued to drive a spatial maximum in sedimentation at the onset of the backwater zone, similar to the base case. For $\sigma^* > 1$, backfilling driven by sea-level rise overwhelmed backwater effects, and avulsions occurred at the inactive-lobe shoreline. However, because the distance between actives and inactive-lobe shorelines was comparable to the backwater length-scale, avulsion length was only slightly smaller than the base case (Fig. 3.7). Previous work has illustrated sea-level backfilling can cause backwater-scaled avulsion locations even under conditions of constant discharge (Chadwick et al. 2019).

Because avulsion length was relatively constant, delta progradation and retreat due to sea-level rise were associated with avulsion node migration (Fig. 3.8). For example, constant sea-level allowed for steady delta progradation, and the avulsion node followed the shoreline downstream, consistent with field observations on the Yellow River delta (Ganti et al. 2014) and scaled laboratory experiments (Ganti, Chadwick, Hassenruck-Gudipati, Fuller, et al. 2016). Sea-level rise reduced progradation rates, stabilizing both the shoreline and avulsion node location. There was not sufficient time in our ten-cycle simulation to observe a full onset of delta autoretreat, but progradation rates slowed over time consistent with the early stages of autoretreat shoreline trajectories (Tetsuji Muto and Steel 2002). At sufficiently high rise rates, the delta drowned, the shoreline retreat, and the avulsion node migrated upstream with a constant avulsion length. While shoreline progradation and retreat took place gradually in our simulations, avulsion node translation occurred in discrete pulses associated with trunk-filling avulsion cycles (Fig. 3.8).

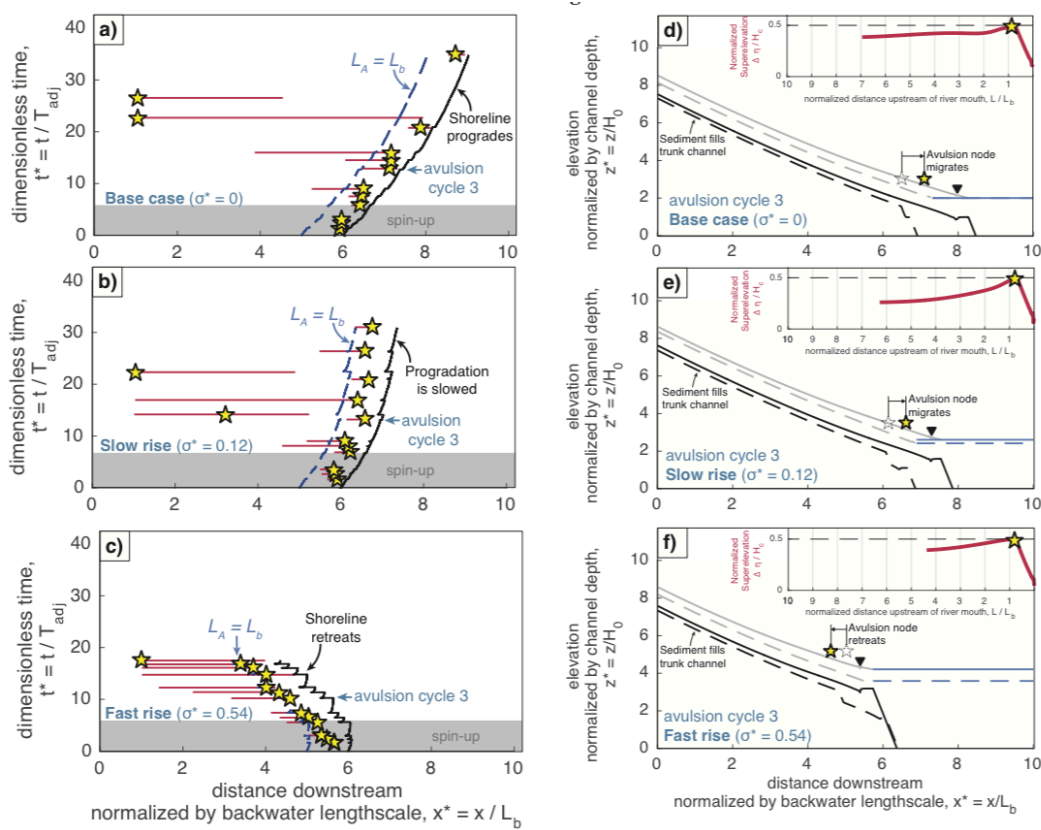


Fig. 3.8: Model results for constant sea level (a), slow sea-level rise (b), and fast sea-level rise (c) during an example lateral avulsion cycle. Black lines are shoreline trajectories, blue dashed lines show where $L_A = L_b$, yellow stars are avulsions, and red error bar indicate the reach within 10% of the avulsion threshold at time of avulsion. Grey shaded regions indicate the model spin-up period, during which avulsion location was affected by initial conditions (Chadwick et al. 2019). Examples of trunk-filling avulsions and associated migration of the avulsion node for each rise scenario are shown in panels d-f).

3.4.3 Avulsions during changing sediment supply and transport capacity

Next we considered runs where we systematically changed the balance between sediment supply and transport capacity at the upstream end, expressed in terms of change in the equilibrium transport slope. All other parameters were held constant and equal to base case values.

In model runs where transport capacity exceeded sediment supply ($\delta S < 0$) we observed transient long-profile adjustment to a shallower transport slope, which was achieved through degradation of the trunk channel. (Fig. 3.9). Degradation occurred during the first avulsion cycle on each of the four lobes. After cycle 4 the trunk channel resumed intermittent aggradation, similar to

the base case, and the spatially averaged riverbed slope was approximately constant. Aggradation and avulsions continued to occur in the backwater zone throughout the simulation, similar to the base case ($L_A^* \sim 1$) (Fig. 3.6c). In contrast to the base-case, however, degradation caused entrenchment of the trunk channel, thereby preventing outlier avulsions farther upstream. Furthermore, avulsion frequency was enhanced as high as $f_A^* = 2.5$ during the first four avulsion cycles, because sediment sourced during degradation contributed to aggradation of the backwater zone. After the trunk channel resumed aggradation in cycle 5, we observed avulsion frequency values similar to the base case ($f_A^* = 0.1 - 1$).

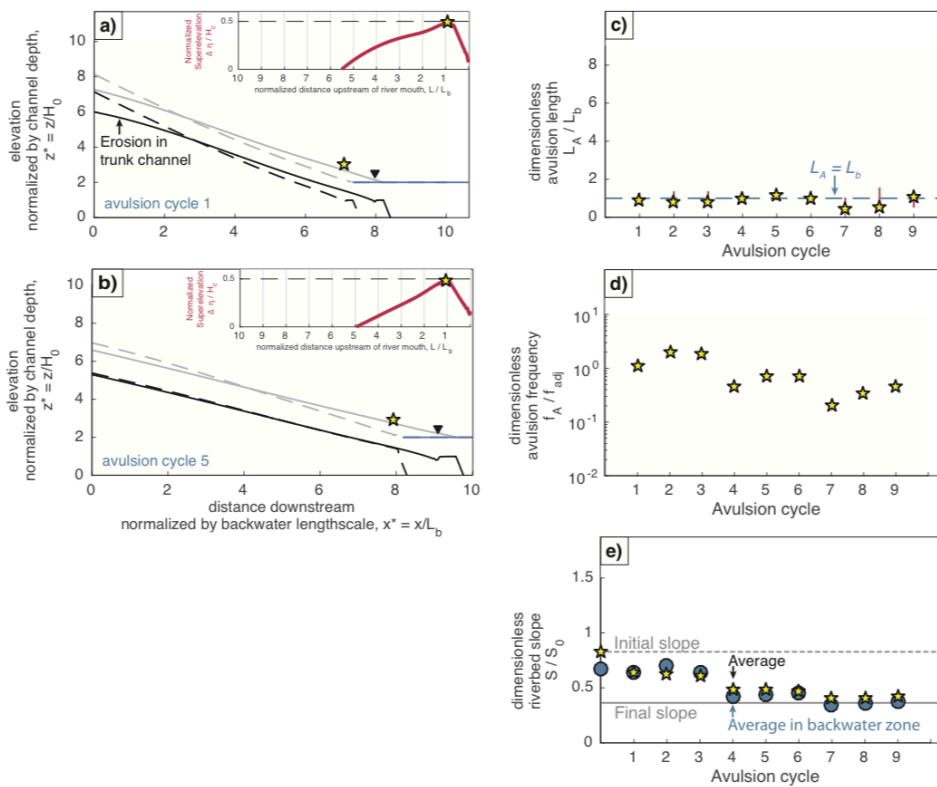


Fig. 3.9: Model results for a 40% reduction in equilibrium transport slope, associated with decreased sediment supply and/or grain-size at the upstream end. Panel a) is an example of a lateral avulsion cycle during transient adjustment, and b) is an example after equilibrium has been reached. c-e) Dimensionless avulsion length, frequency, and slope over ten avulsion cycles. Slope is averaged over the entire fluvial reach (yellow stars) and averaged over the backwater zone (blue circles) at times of avulsion. Gray lines show initial (dashed) and final (solid) values of the equilibrium transport slope.

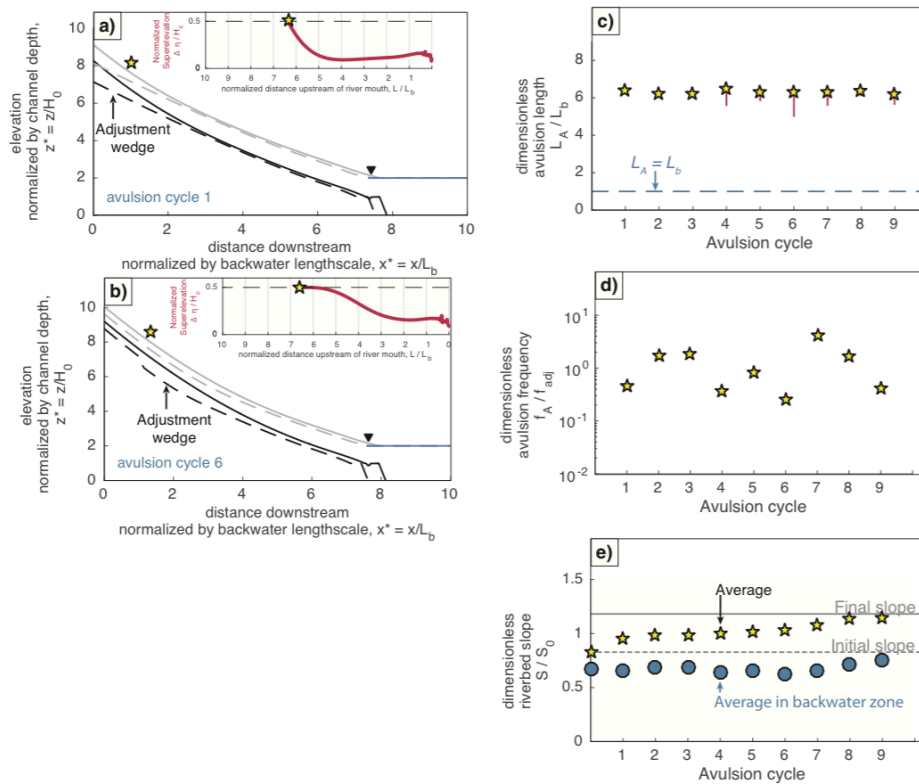


Fig. 3.10: Model results for a 40% increase in equilibrium transport slope, associated with increased sediment supply and/or grain-size at the upstream end. Panels a) and b) show long-profile evolution during cycles 1 and 6, respectively. c-e) Dimensionless avulsion length, frequency, and slope over ten avulsion cycles. Slope is averaged over the entire fluvial reach (yellow stars) and averaged over the backwater zone (blue circles) at times of avulsion. Gray lines show initial (dashed) and final (solid) values of the equilibrium transport slope.

In model runs where sediment supply exceeded transport capacity ($\delta S > 0$), we observed long-profile adjustment towards a steeper transport slope, which was achieved through aggradation of the trunk channel (Fig. 3.10). In contrast to the $\delta S < 0$ model runs, long-profile adjustment often continued beyond avulsion cycle 4. Adjustment was prolonged when trunk-channel aggradation caused avulsions, interrupting downstream migration of the downfilling wedge. Avulsion frequency was statistically similar to the base-case scenario, but avulsion location was sensitive to the magnitude of δS . For $\delta S > 0.1$, the backwater-scaled avulsion node was shut down (Fig. 3.10). Instead, avulsions occurred repeatedly as far upstream as allowed by the model ($x^* = 1$). Avulsions occurred only at the upstream end because trunk-channel aggradation during adjustment outpaced the aggradation rate of the backwater-scaled avulsion node. Model runs with $0.01 < \delta S < 0.1$ featured slower trunk-channel aggradation rates in comparison, at a pace similar to those of the

backwater-scaled avulsion node (Fig. 3.11). As a result, avulsion locations alternated randomly between the backwater-scaled node ($L_A^* = 1$) and the upstream boundary ($x^* = 1$).

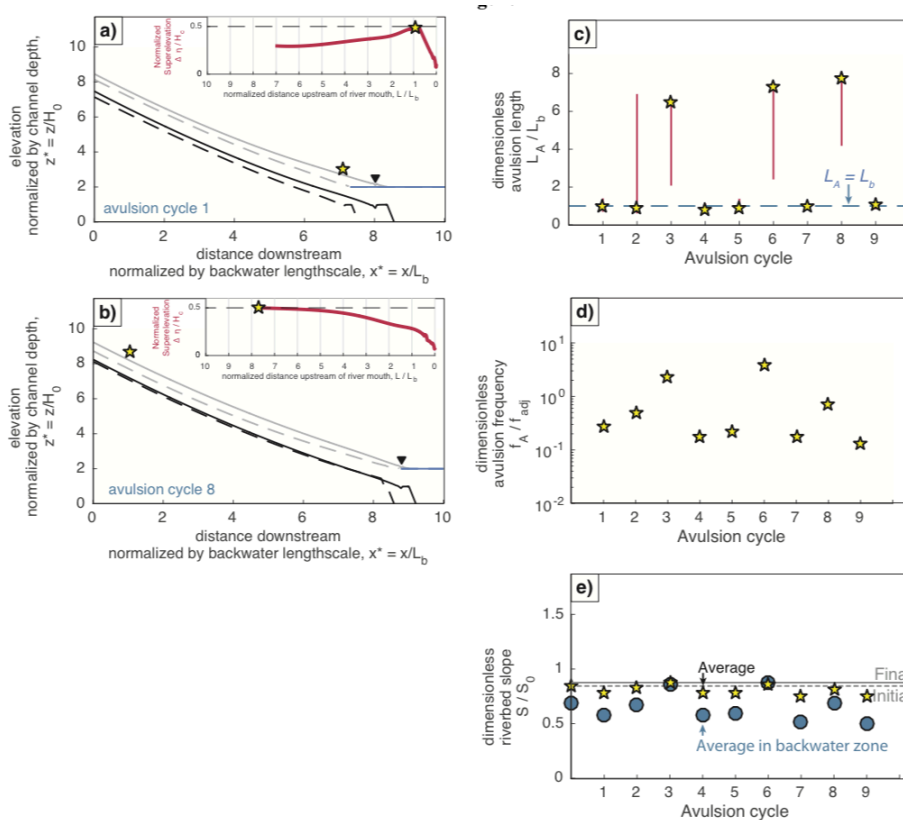


Fig. 3.11: Model results for a 2.5% increase in equilibrium transport slope, associated with increased sediment supply and/or grain-size at the upstream end. Panels a) and b) show long-profile evolution during cycles 1 and 8, respectively. c-e) Dimensionless avulsion length, frequency, and slope over ten avulsion cycles. Slope is averaged over the entire fluvial reach (yellow stars) and averaged over the backwater zone (blue circles) at times of avulsion. Gray lines show initial (dashed) and final (solid) values of the equilibrium transport slope.

Fig. 3.12 provides a summary of model results for avulsion location and frequency during adjustment to a new equilibrium transport slope. When imbalances in sediment supply and transport capacity provoked a change in transport slope less than 1% ($-0.01 < \delta S < 0.01$), the long-profile adjusted before any avulsions took place. Avulsion frequency was relatively unaffected by changes in sediment supply and transport capacity, except for when $\delta S \leq 0.4$ and sediment mined during trunk-channel degradation contributes to accelerate delta aggradation. For $\delta S > 0.01$, avulsions sometimes occurred upstream of the backwater zone due to enhanced trunk-channel aggradation. For $\delta S > 0.1$, all 9 avulsions in our simulation occurred at the upstream boundary.

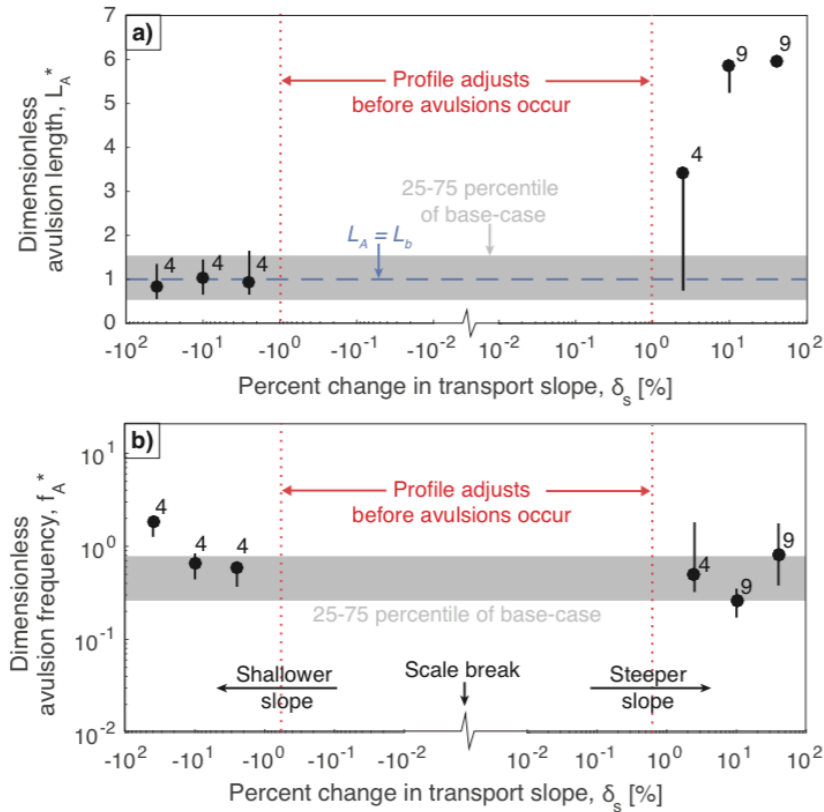


Fig. 3.12: Summary of model results for dimensionless avulsion length (a) and frequency (b) during transient adjustment of the equilibrium transport slope. Circles show average and 25-75 percentile range of avulsion location and frequency, and numbers beside each circle indicate the number of avulsions during adjustment. For simulations where the profile adjusted before 9 avulsions occurred, avulsions after adjustment were statistically similar to the base-case scenario, which is indicated by the gray shaded region (25-75 percentile range). Blue dashed line indicates where $L_A = L_b$.

3.4.4 Avulsions during different flood regimes

Next, we considered a suite of model runs where we systematically varied each climate parameter associated with flood regime (F_{bf} , CV , T_e^* , H^*), holding other parameters constant and equal to base case values ($F_{bf} = 0.05$, $CV = 0.53$, $T_e^* = 0.001$, $H^* = 0.5$) (Table 2). During these model runs sea level was stable ($\sigma^* = 0$) and sediment supply was equal to transport capacity ($\delta S = 0$).

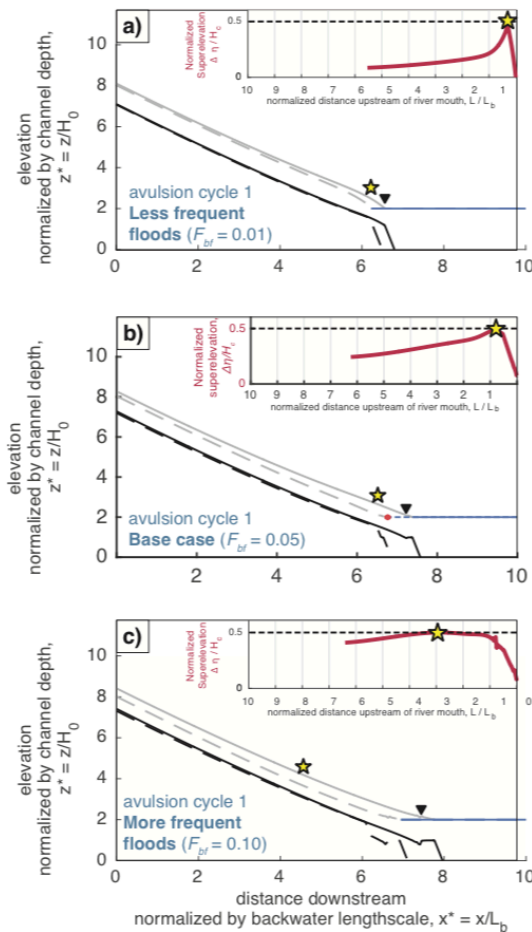


Fig. 3.13: Examples of model results under different flow regimes, including a) lower bankfull exceedance probability $F_{bf} = 0.01$, b) base-case $F_{bf} = 0.05$, and c) higher bankfull exceedance probability $F_{bf} = 0.10$. Black lines are riverbed profile at start (dashed) and end (solid) of an avulsion cycle. Floodplain profiles of active lobe (gray solid line) and lowest inactive lobe (gray dashed line) are used to calculate superelevation (see inset). Black triangles are river mouth at end of the avulsion cycle. Yellow stars show avulsion location.

In our model, increasing flood frequency (F_{bf}) caused avulsions to occur farther upstream (Fig. 3.13). This is because more frequent flooding was accompanied by restricted low-flow deposition. Low flows play an important role in backwater zones by partially filling the scours cut by large flood events, and over many flood events set the spatial maximum in sedimentation coinciding with the avulsion node (Lamb et al. 2012; Chatanantavet, Lamb, and Nittrouer 2012). When floods occurred more frequently in our model, low-flow deposition occurred over shorter intervals and is restricted to the upper reach of the backwater zone, resulting in an avulsion node farther upstream. Model runs with very frequent floods ($F_{bf} > 0.05$) lacked a backwater-

scaled avulsion node entirely because low-flow filling was insignificant, and the riverbed adjusted to normal-flow conditions associated with large floods.

Systematic changes the avulsion node location also indirectly reduced avulsion frequency (Fig. 3.14). When frequent floods pushed the avulsion node farther upstream, avulsion lengths increased. Consequently, delta lobe topsets were larger and required more sediment, and thus more time, to aggrade to avulsion. This is consistent with geometric mass-balance modeling of avulsion frequency under different avulsion lengths (Chadwick et al., *in review*), but until now has not been linked to changes in flood frequency.

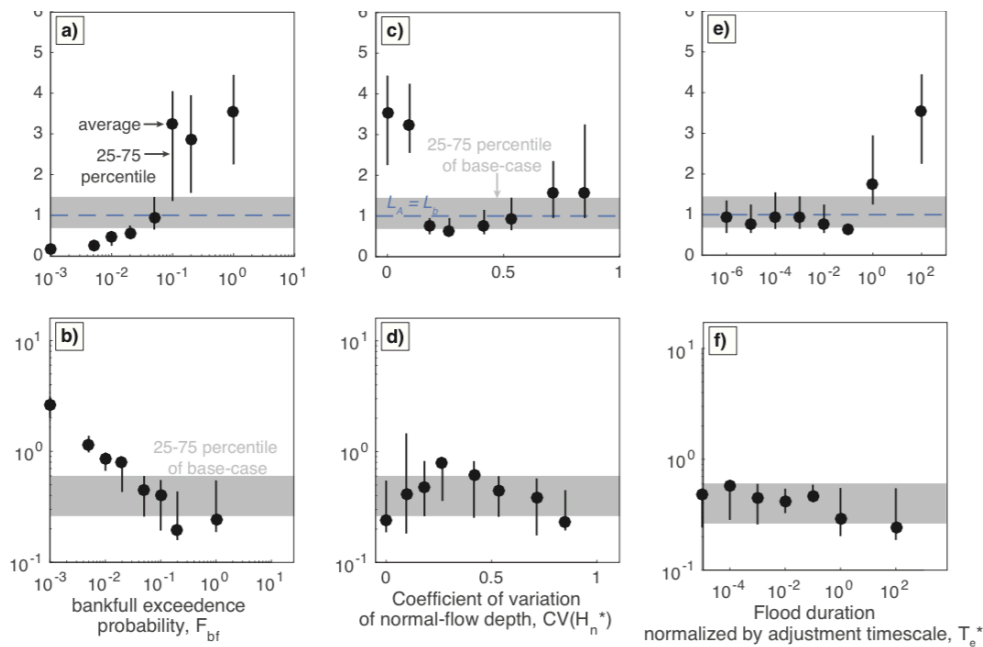


Fig. 3.14: Model results for dimensionless avulsion length and avulsion frequency under changing bankfull exceedance probabilities (a-b), coefficients of variation of normal-flow depth (c-d), and normalized flood durations (e-f). Black circles show average and 25-75 percentile range of avulsion location and frequency. Gray shaded regions denote the 25-75 percentile range for a stable climate in the base-case simulation. Blue dashed line indicates where $L_A = L_B$.

Under most climate scenarios, changes to coefficient of variation of stage height (CV) or flood duration (T_e^*) did not yield avulsion locations or frequencies significantly different than the base-case distribution (Fig. 3.14). However, extreme values of CV and T_e^* were capable of destabilizing the avulsion node, as documented in previous work (Chadwick et al. 2019). Under very low discharge variability ($CV < 0.2$) and long flood durations ($T_e^* \geq 1$), the backwater-mediated

avulsion node was abandoned and avulsions occurred with similar likelihood throughout the river profile, because the riverbed adjusted to normal flow conditions associated with low flows. Cases with extremely high discharge variability (CV) also abandoned the avulsion node, because the riverbed adjusted to normal flow conditions associated with large floods.

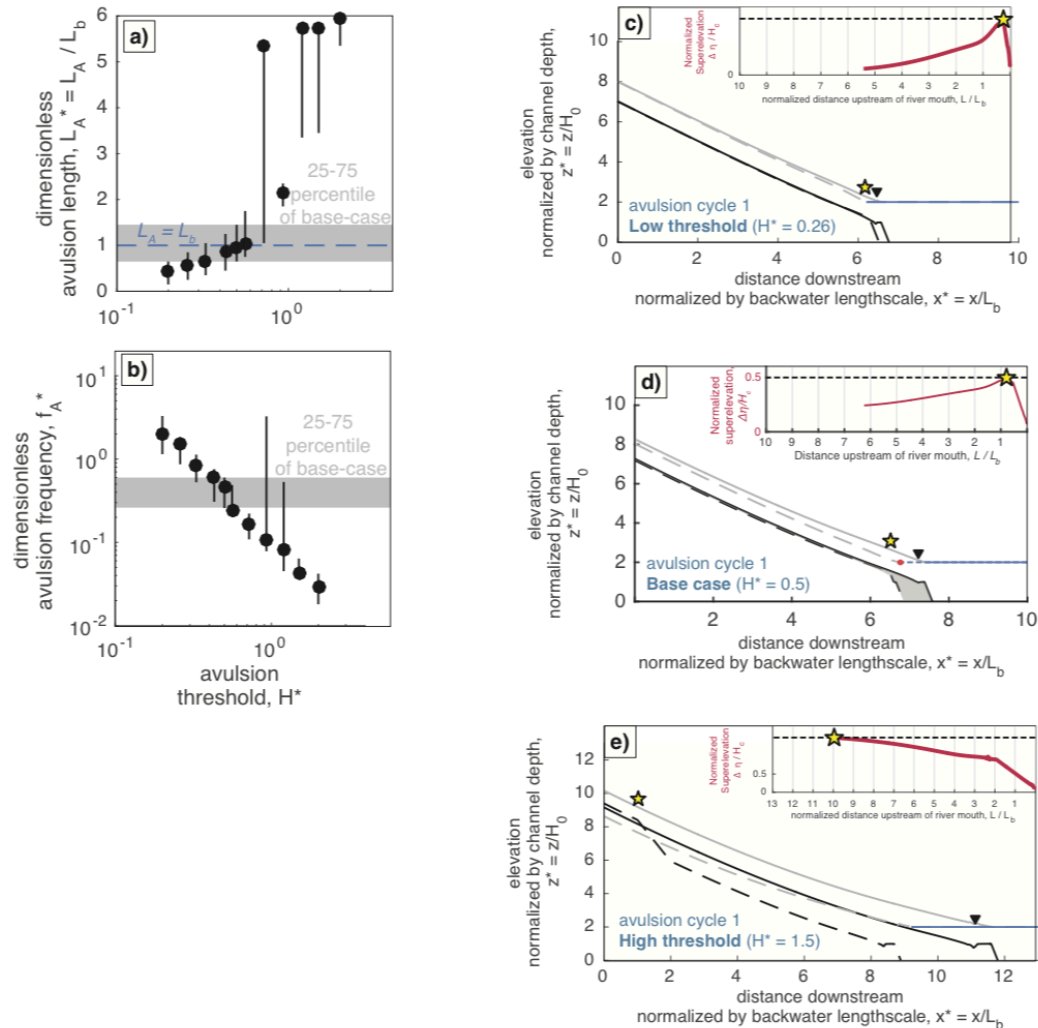


Fig. 3.15: Model results for dimensionless avulsion length (a) and avulsion frequency (b) under changing avulsion threshold, which is associated with discharge variability (Ganti et al. 2014). Black circles show average and 25-75 percentile range of avulsion location and frequency. Gray shaded regions denote the 25-75 percentile range for a stable climate in the base-case simulation. Blue dashed line indicates where $L_A = L_b$. Examples of long-profile evolution during a lateral avulsion cycle are shown in panels c-e).

Increasing flow variability has been associated with reduced avulsion thresholds (Ganti et al. 2014). In our simulations, we found reduced avulsion thresholds lead to shorter avulsion lengths and higher avulsion frequencies (Fig. 3.15). Avulsion frequency is directly enhanced because less aggradation is necessary to superelevate the channel to lower H^* values (Eq. 1). Less aggradation necessitated less progradation, and as a result lobe progradation distance was also reduced (Fig. 3.5c-e). Shorter progradation distances allow backwater-mediated avulsions to occur closer to the river mouth, because superelevation is greatly reduced downstream of the initial shoreline where the levee profile must converge to sea level (Katherine Murray Ratliff 2017; Chadwick et al. 2019). We observed the effect of reduced superelevation downstream of the initial shoreline is minor for the common scenario that $H^* < 1$. However, if $H^* > 1$, then the entire backwater zone is relegated downstream of the initial shoreline, where avulsion is unlikely, and thus avulsions are denodalized (Fig. 3.15).

3.4.5 Inherent variability in avulsion dynamics across climate scenarios

All simulations featured lateral avulsion cycles, trunk-filling avulsion cycles, and upstream avulsion cycles, which differed in frequency and location (Fig. 3.16). Lateral avulsions were the most common (55% of avulsions), and featured $L_A^* = 0.5 - 2$ and $f_A^* = 0.2 - 1$. Trunk-filling avulsions occurred periodically (33% of all avulsions) and exhibited characteristically longer setup times due to additional time required to fill the trunk channel ($f_A^* = 0.1 - 0.2$). Outlier avulsions were the least common (12% of all avulsions), and occurred significantly upstream of the backwater-scaled avulsion node ($L_A^* \gg 1$). Despite their differences, all avulsion types show an inverse correlation between avulsion frequency and length. This is because reduced avulsion lengths resulted in smaller lobes, which required less sediment, and thus less time, to aggrade to the necessary superelevation for avulsion, consistent with geometric mass-balance modeling (Chadwick et al., *in review*).

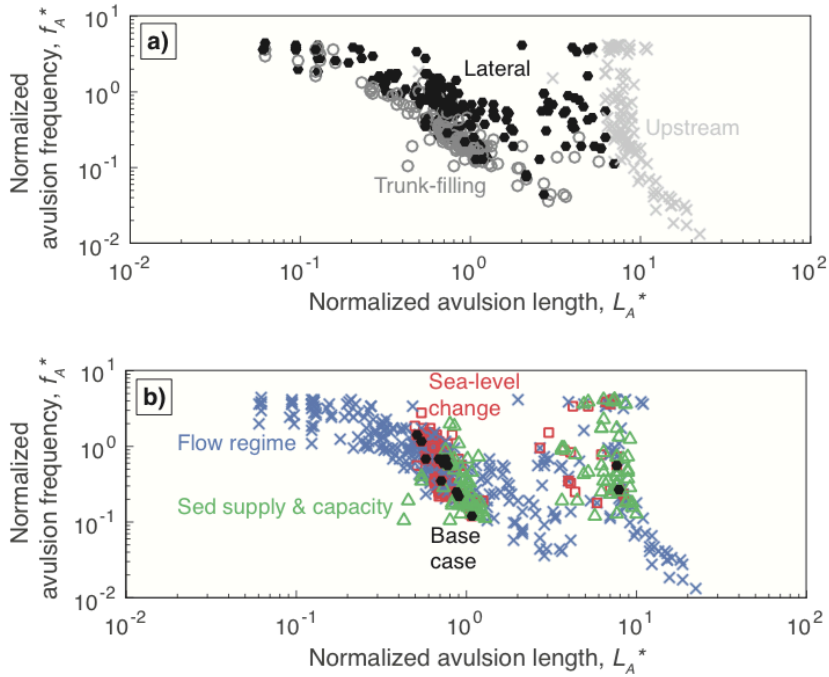


Fig. 3.16: The distribution of avulsion lengths and frequencies across all climate regimes considered in this study. In panel a), data are color-coded depending on whether avulsions were lateral (black), trunk-filling (dark gray), or occurring at the upstream end of the model domain (light gray). Panel b) shows the same data, now color-coded by model runs: base-case climate model run (black), sea-level change runs (red), changing sediment supply and transport capacity runs (green), and changing flow regime runs (blue).

Under some climate forcings, inherent variability between lateral, trunk, and upstream avulsions overwhelmed trends due to climate (Fig. 3.16). We observed no significant trend in avulsion node location across all sea-level rise rates (σ^*) and sediment supply and transport imbalances (δS) considered. In these model runs, lateral and trunk-filling avulsions were always clustered about $L_A^* = 0.5 - 2$ regardless of climate values, and the only differences were due to upstream avulsions where $L_A^* \sim 10$. In addition, flow regime changes only shifted the avulsion frequency in the range $f_A^* = 0.05 - 5$, which is not substantially greater than the difference between trunk-filling avulsions and lateral avulsions under our constant, base-case climate scenario ($f_A^* = 0.1 - 0.2$ and $f_A^* = 0.2 - 1$ for trunk-filling and lateral avulsions, respectively).

3.5. DISCUSSION

3.5.1 Comparison to avulsions during Holocene climate change

Our results provide quantitative relationships between avulsion frequency, avulsion location, and climate forcings that can explain field observations during Holocene climate change. For example, our model captures the response of enhanced aggradation and more frequent avulsions during accelerated sea-level rise, consistent with Holocene records on the Rhine-Meuse delta (Stouthamer and Berendsen 2001; Törnqvist 1994), highlighting that this response occurs when sea level rises at rates comparable to the sediment supply ($0.1 < \sigma^* < 1$; Fig. 3.7). Importantly, avulsion frequency in our model is less sensitive to sea-level rise if rise rate is very low or high compared to the sediment supply ($\sigma^* < 0.1$ or $\sigma^* > 1$), which can reconcile observations on the Mitchell River delta (Lane et al. 2017) and Holocene modeling of the Trinity River (Moran et al. 2017). Under these conditions, avulsion frequency instead varies as a result of intermittent filling in the trunk channel (Fig. 3.6), and is sensitive to basin geometry (Chadwick et al., *in review*). Results indicate avulsion frequency is less sensitive to upstream changes (Fig. 3.12, Fig. 3.14), but that stormier climates can indirectly cause more frequent avulsions by reducing the avulsion threshold (Fig. 3.15), consistent with field data (Ganti et al. 2014).

Unlike existing models and experiments of delta response, our model shows the avulsion node at the delta apex is mobile and sensitive to climate forcings. Avulsion nodes in our model moved in tandem with shoreline progradation such that the avulsion length remained constant, similar to natural deltas built during the late Holocene stillstand (Chatanantavet, Lamb, and Nittrouer 2012) but in this case manifesting across a wide range of sea-level rise rates (Fig. 3.7). Importantly, avulsion nodes also migrated upstream during shoreline retreat, a phenomenon that has not yet been documented in nature but could have disastrous consequences on densely populated deltas experiencing relative sea-level rise in the coming century (Chadwick et al., *in review*). While our simulations did not cover timescales long enough to capture avulsions during delta autoretreat (Tetsuji Muto and Steel 2002), results suggest the onset of autoretreat would be associated with autogenic retreat of the avulsion node to maintain a constant avulsion length during shoreline retreat (Fig. 3.8). With regards to upstream climate controls, our model supports field observations on the

Tacuari megafan (Makaske et al. 2012) and in New Zealand catchments (Korup 2004) that increased sediment supply can cause avulsions far upstream of deltas, and highlights that these avulsions arise when aggradation during slope-adjustment outpaces rates of backwater sedimentation ($\delta S > 1\%$ in our model).

We reason that, similar to these historic examples, Holocene avulsions far upstream of the Mississippi delta (Saucier 1994; Chamberlain et al. 2018) could also be explained by an increase in sediment supply. However, without a history of Holocene sediment supply we cannot rule out the possibility that upstream avulsions simply represent autogenic variability, which in our model caused avulsions far upstream during intermittent filling of the trunk channel. According to our model, climatic changes in flood regime during this period (Knox 2000) were insufficient to have significantly affected avulsion location. We observed a preferential avulsion length scaled with the backwater length-scale ($0.5 < L_A^* < 2$) except for rivers with a constant discharge, or with discharges exceeding bankfull extremely often (Fig. 3.14), at which point avulsions became denodalized as documented by Chadwick et al. (2019).

3.5.2 Implications for avulsions during anthropogenic climate change

Anthropogenic climate change has the potential to affect avulsion hazards on modern deltas. Global sea levels are rising at an accelerating pace (Pachauri et al. 2014; Bintanja, van de Wal, and Oerlemans 2005), and our model predicts accelerated rise will be associated with more frequent avulsion hazards at a relatively stable avulsion node (Fig. 3.7). Accelerated rise rates anticipated over the next century may also instigate supply-limited conditions on some deltas, whereby avulsion frequency reaches a maximum value and avulsion nodes migrate upstream with shoreline retreat (Fig. 3.8) (Chadwick et al., *review*). This dangerous threshold in delta response is especially important when considering large lowland, densely populated deltas, which are extensively dammed and require more sediment to sustain their topset areas (Livio Giosan 2014).

Modern sea level change is occurring simultaneously with reductions in sediment supply and flow variability due to land management (Zhou et al. 2015; Liviu Giosan et al. 2005). Our model suggests that reduction in transport slope ($\delta S < 0$), while causing scour in the trunk channel, should have minimal effect on the location and frequency of backwater-scaled avulsions (Fig. 3.12).

However, reduced bankfull exceedance probability (F_{bf}) promotes avulsions farther downstream (Fig. 3.14), potentially shifting the immediate dangers of avulsion towards downstream communities. At the same time, reduced flow variability due to dams have the potential to counteract land loss in the face of relative sea-level rise. According to our model, lower bankfull exceedance caused avulsions to occur farther downstream and with greater frequency (Fig. 3.14), which should focus land-building into a smaller and more easily sustained delta area. Thus, we view discharge modulation by dams as an opportunity to influence avulsion locations without directly cutting levees, allowing for cost-effective efforts to build land and restore wetlands in targeted zones.

Predicting future avulsions requires identifying climate controls, but also depends on inherent differences between lateral avulsions, trunk-filling avulsions, and upstream avulsions. While lateral avulsions are the most common, trunk-filling and upstream avulsions occurred across all climate scenarios and were associated with order-of-magnitude excursions in avulsion frequency and avulsion location, respectively (Fig. 3.6). Differences between lateral, trunk-filling, and outlier avulsions under one climate scenario were sometimes more prominent than changes in lateral avulsions caused by climate change (Fig. 3.12). Hiatuses in avulsion due to trunk-channel filling may be particularly important to identify in the field, as they are not uncommon in our simulations (33% of all avulsions), and should temporarily reduce both avulsion hazards and land-building potential for 10—1000 years until the trunk channel has adjusted. We reason it is possible to diagnose trunk-filling avulsion cycles currently underway in the field: deltas undergoing trunk-filling avulsion cycles should exhibit comparable aggradation rates between the trunk channel and delta, compared to lateral avulsion cycles where aggradation rates are much lower in the trunk channel. Furthermore, trunk-filling avulsion cycles are associated with relatively low-elevation active lobes compared to abandoned delta lobes, which can be identified using digital terrain models.

3.5.3 Implications for interpreting ancient climates from avulsions in deltaic deposits

While changes in sea-level rise and sediment supply have a similar effect on delta stratigraphy (T Muto and Steel 1997; Liang, Van Dyk, and Passalacqua 2016b), our model results suggest trunk-channel stratigraphy can be used to differentiate between these sea-level and sediment supply changes. In our simulations, higher sediment supplies caused avulsions in the trunk channel

to become more common (Fig. 3.10-11), and reduced sediment supplies prevented avulsions in the trunk channel due to entrenchment (Fig. 3.9). Based on these results, we reason that trunk-channel deposits recording changing sediment supply should exhibit up-section changes in the prevalence of avulsion-induced unconformities, which exhibit diagnostic vertical spacing and horizontal length-scales (Ganti, Lamb, and Chadwick 2019; Trower et al. 2018). In contrast, for delta deposits recording changes in sea level rise rate under constant sediment supply, we reason trunk channel deposits feature a more uniform distribution of avulsion-induced unconformities. This diagnostic would offer another means to disentangle changes in sediment supply and sea level, which is difficult in pre-Quaternary deposits because stream terraces and other upstream indicators are not typically preserved (Blum and Törnqvist 2000b).

Our results also suggest the organization of avulsion nodes in Martian deltaic deposits may record information regarding the planet's climate history. On Mars, good preservation of sand bodies allows identification of avulsion nodes from satellite imagery (DiBiase et al. 2013). Avulsion length remains constant during sea level rise and fall (Fig. 3.10-11), so multiple avulsion nodes in a deltaic deposit can be used to infer shoreline progradation and retreat, even if fine-grained shoreline deposits have not been preserved. Furthermore, the presence of avulsion nodes on unconfined plains is indicative of an intermediate degree flow variability on Earth (Fig. 3.4c; $CV = 0.1 - 0.6$), and could be used to infer runoff variability in ancient Martian environments. For example, a Martian deltaic deposit with an avulsion node that is not tied to a canyon or crater rim likely featured flows with a flood regime comparable to those on Earth.

3.6. CONCLUSIONS

In this manuscript, we developed a generic model for avulsion location and frequency that depends on climate change. We then explored model behavior under systematic isolation of important climate variables, namely sea-level change, Changing sediment supply and transport capacity, and changing flow regime. Model results indicate that

- 1) Increasing sea level rise rate (σ^*) in the range $0.1 < \sigma^* < 1$ caused more frequent avulsions at a constant avulsion length. Because avulsion length was constant, shoreline progradation and retreat were associated with downstream and upstream migration of the avulsion node.

- 2) If sediment supply exceeds transport capacity ($\delta S > 0$) the delta transiently responds by avulsing far upstream of the backwater zone, because the sediment wedge associated with long-profile adjustment aggrades at a rate greater than or equal to that of the backwater-scaled avulsion node. After the long profile has fully adjusted, usually after ~ 4 avulsion cycles, avulsions location and timing is indistinguishable from pre-adjustment conditions.
- 3) A variable flood regime is important for maintaining a backwater-scaled avulsion node, but avulsion location and frequency is relatively insensitive to the degree of variability. However, if the flow regime's variability is diminished or exacerbated beyond of a typical range of $0.2 < CV < 0.7$ and $T_e^* < 1$, then avulsions become denodalized and occur randomly throughout the river profile. Increased variability is also indirectly associated with a reduced avulsion threshold H^* , resulting in avulsions that occur more frequently and closer to the shoreline.
- 4) Under a stable climate scenario, avulsion length naturally varies between $0.5 - 2L_b$ and avulsion frequency naturally varies between $f_A^* = 0.2 - 1$. Deltas intermittently fill their trunk channel in order to prograde or keep pace with sea level rise, and during trunk-filling avulsion cycles avulsions may take twice as long as usual, or occur far upstream of the backwater zone. Trunk-filling and upstream avulsions occurred in all our model runs, regardless of climate change, suggesting in nature they may potentially distort climate signals recorded by avulsions.
- 5) Model results point to future changes in avulsion location and timing on modern deltas where sea levels are rising and dams reduce water discharge and sediment loads. In addition, the organization of preserved avulsion nodes in deltaic deposits may record changes in sea level rise, sediment supply, and flow variability.

3.7. REFERENCES

- Baker, Victor R, and Margarida Maria Penteado-Orellana. 1977. "Adjustment to Quaternary Climatic Change by the Colorado River in Central Texas." *The Journal of Geology* 85 (4): 395–422.
- Begin, Ze'ev B. 1988. "Application of a Diffusion-Erosion Model to Alluvial Channels Which Degrade Due to Base-Level Lowering." *Earth Surface Processes and Landforms* 13 (6): 487–500.
- Bianchi, Thomas S, and Mead A Allison. 2009. "Large-River Delta-Front Estuaries as Natural 'Recorders' of Global Environmental Change." *Proceedings of the National Academy of Sciences* 106 (20): 8085–92.
- Bintanja, Richard, Roderik S W van de Wal, and Johannes Oerlemans. 2005. "Modelled Atmospheric Temperatures and Global Sea Levels over the Past Million Years." *Nature* 437 (7055): 125.
- Blum, Michael D. 1990. "Climatic and Eustatic Controls on Gulf Coastal Plain Fluvial Sedimentation: An Example from the Late Quaternary of the Colorado River, Texas." In *Sequence Stratigraphy as an Exploration Tool: Concepts and Practices in the Gulf Coast*. Gulf Coast Section SEPM Foundation, *Proceedings of the 11th Annual Research Conference*, 71–83.
- Blum, Michael D., and Torbjörn E. Törnqvist. 2000a. "Fluvial Responses to Climate and Sea-Level Change: A Review and Look Forward." *Sedimentology* 47 (SUPPL. 1): 2–48. <https://doi.org/10.1046/j.1365-3091.2000.00008.x>.
- Blum, Michael D, M J Guccione, D A Wysocki, P C Robnett, and E M Rutledge. 2000. "Late Pleistocene Evolution of the Lower Mississippi River Valley, Southern Missouri to Arkansas." *Geological Society of America Bulletin* 112 (2): 221–35.
- Blum, Michael D, and David M Price. 1998. "Quaternary Alluvial Plain Construction in Response to Glacio-Eustatic and Climatic Controls, Texas Gulf Coastal Plain."
- Blum, Michael D, and Harry H Roberts. 2009. "Drowning of the Mississippi Delta Due to Insufficient Sediment Supply and Global Sea-Level Rise." *Nature Geoscience* 2 (7): 488.
- Blum, Michael D, and Torbjörn E Törnqvist. 2000b. "Fluvial Responses to Climate and Sea-Level Change: A Review and Look Forward." *Sedimentology* 47: 2–48.
- Blum, Michael D, and Salvatore Valastro Jr. 1994. "Late Quaternary Sedimentation, Lower Colorado River, Gulf Coastal Plain of Texas." *Geological Society of America Bulletin* 106 (8): 1002–16.
- Bufe, Aaron, Jens M Turowski, Douglas W Burbank, Chris Paola, Andrew D Wickert, and Stefanie Tofelde. 2019. "Controls on the Lateral Channel-Migration Rate of Braided Channel Systems in Coarse Non-Cohesive Sediment." *Earth Surface Processes and Landforms*.
- Burgess, Peter M, and Niels Hovius. 1998. "Rates of Delta Progradation during Highstands: Consequences for Timing of Deposition in Deep-Marine Systems." *Journal of the Geological Society* 155 (2): 217–22.
- Busschers, F S, C Kasse, R T Van Balen, J Vandenberghe, K M Cohen, H J T Weerts, J Wallinga, C Johns, P Cleveringa, and F P M Bunnik. 2007. "Late Pleistocene Evolution of the Rhine-Meuse System in the Southern North Sea Basin: Imprints of Climate Change, Sea-Level Oscillation and Glacio-Isostasy." *Quaternary Science Reviews* 26 (25–28): 3216–48.
- Chadwick, A J, M P Lamb, A J Moodie, G Parker, and J A Nittrouer. 2019. "Origin of a Preferential Avulsion Node on Lowland River Deltas." *Geophysical Research Letters* 46 (8): 4267–77.
- Chamberlain, Elizabeth L., Torbjörn E. Törnqvist, Zhixiong Shen, Barbara Mauz, and Jakob Wallinga. 2018. "Anatomy of Mississippi Delta Growth and Its Implications for Coastal Restoration." *Science Advances* 4 (4): 1–10. <https://doi.org/10.1126/sciadv.aar4740>.
- Chatanantavet, Phairot, and Michael P. Lamb. 2014. "Sediment Transport and Topographic Evolution of a Coupled River and River Plume System: An Experimental and Numerical Study," no. Figure 1: 1–20. <https://doi.org/10.1002/2013JF002810>.Received.
- Chatanantavet, Phairot, Michael P. Lamb, and Jeffrey a. Nittrouer. 2012. "Backwater Controls of Avulsion Location on Deltas." *Geophysical Research Letters* 39 (1). <https://doi.org/10.1029/2011GL050197>.

- Church, M, and R I Ferguson. 2015. "Morphodynamics: Rivers beyond Steady State." *Water Resources Research* 51 (4): 1883–97.
- Davis, William M. 1902. "Baselevel, Grade and Peneplain." *The Journal of Geology* 10 (1): 77–111.
- DiBiase, Roman a., Ajay B. Limaye, Joel S. Scheingross, Woodward W. Fischer, and Michael P. Lamb. 2013. "Deltaic Deposits at Aeolis Dorsa: Sedimentary Evidence for a Standing Body of Water on the Northern Plains of Mars." *Journal of Geophysical Research: Planets* 118 (6): 1285–1302. <https://doi.org/10.1002/jgre.20100>.
- Dunne, Thomas, José Antonio Constantine, and M Singer. 2010. "The Role of Sediment Transport and Sediment Supply in the Evolution of River Channel and Floodplain Complexit." *Transactions, Japanese Geomorphological Union* 31 (2): 155–70.
- Edmonds, Douglas A., David C Hoyal, Ben A. Sheets, and Rudy L. Slingerland. 2009. "Predicting Delta Avulsions: Implications for Coastal Wetland Restoration." *Geology* 37 (8): 759–62. <https://doi.org/10.1130/G25743A.1>.
- Einstein, H A. 1950. "The Bed-Load Function for Sediment Transportation." In *Open Channel Flow Technical Bulletin*, 1026. U.S. Department of Agriculture, Washington, D.C.
- Ely, Lisa L. 1997. "Response of Extreme Floods in the Southwestern United States to Climatic Variations in the Late Holocene." *Geomorphology* 19 (3–4): 175–201.
- Engelund, Frank, and Eggert Hansen. 1967. "A Monograph on Sediment Transport in Alluvial Streams." *Technical University of Denmark Ostervoldgade 10, Copenhagen K*.
- Fisk, Harold Norman, and others. 1945. "Geological Investigation of the Alluvial Valley of the Lower Mississippi River."
- Gagliano, Sherwood M, Klaus J Meyer-Arendt, and Karen M Wicker. 1981. "Land Loss in the Mississippi River Deltaic Plain." *GCAGS Transactions* 31: 295–300.
- Galloway, William E. 1975. "Process Framework for Describing the Morphologic and Stratigraphic Evolution of Deltaic Depositional Systems."
- Ganti, Vamsi, Austin J Chadwick, Hima J Hassenruck-Gudipati, Brian M Fuller, and Michael P Lamb. 2016. "Experimental River Delta Size Set by Multiple Floods and Backwater Hydrodynamics." *Science Advances* 2 (5): e1501768.
- Ganti, Vamsi, Austin J Chadwick, Hima J Hassenruck-Gudipati, and Michael P Lamb. 2016. "Avulsion Cycles and Their Stratigraphic Signature on an Experimental Backwater-Controlled Delta." *Journal of Geophysical Research: Earth Surface* 121 (9): 1651–75.
- Ganti, Vamsi, Zhongxin Chu, Michael P. Lamb, Jeffrey A. Nittrouer, and Gary Parker. 2014. "Testing Morphodynamic Controls on the Location and Frequency of River Avulsions on Fans versus Deltas: Huanghe (Yellow River), China." *Geophysical Research Letters* 41: 7882–90. <https://doi.org/10.1002/2014GL061918>.
- Ganti, Vamsi, Michael P. Lamb, and Austin J Chadwick. 2019. "Autogenic Erosional Surfaces in Fluvio-Deltaic Stratigraphy from Floods, Avulsions, and Backwater Hydrodynamics." *Journal of Sedimentary Research*.
- Gilbert, G K. 1877. "Report on the Geology of the Henry Mountains: Washington." *DC, Government Printing Office*.
- Giosan, Livio. 2014. "Protect the World's Deltas." *Nature* 516: 5–7.
- Giosan, Liviu, Jeffrey P Donnelly, Emil Vespremeanu, Janok P Bhattacharya, Cornel Olariu, and Frank S Buonaiuto. 2005. "River Delta Morphodynamics: Examples from the Danube Delta." *SEPM Special Publication* 83: 393–412. <https://doi.org/10.2110/pec.05.83.0393>.
- Gleick, Peter H. 2003. "Global Freshwater Resources: Soft-Path Solutions for the 21st Century." *Science (New York, N.Y.)* 302 (2003): 1524–28. <https://doi.org/10.1126/science.1089967>.
- Hajek, E.A., and D.A. Edmonds. 2014. "Is River Avulsion Style Controlled by Floodplain Morphodynamics?" *Geology* 42 (3): 199–202. <https://doi.org/10.1130/G35045.1>.

- Hajek, Elizabeth a., and Kyle M. Straub. 2017. "Autogenic Sedimentation in Clastic Stratigraphy." *Annual Review of Earth and Planetary Sciences* 45 (1): 681–709. <https://doi.org/10.1146/annurev-earth-063016-015935>.
- Hajek, Elizabeth A., and Matthew A. Wolinsky. 2012. "Simplified Process Modeling of River Avulsion and Alluvial Architecture: Connecting Models and Field Data." *Sedimentary Geology* 257–260 (June): 1–30. <https://doi.org/10.1016/j.sedgeo.2011.09.005>.
- Hallet, Bernard, Lewis Hunter, and Jim Bogen. 1996. "Rates of Erosion and Sediment Evacuation by Glaciers: A Review of Field Data and Their Implications." *Global and Planetary Change* 12 (1–4): 213–35.
- Heller, Paul L, and Chris Paola. 1996. "Downstream Changes in Alluvial Architecture; an Exploration of Controls on Channel-Stacking Patterns." *Journal of Sedimentary Research* 66 (2): 297–306.
- Hoover Mackin, J. 1948. "Concept of the Graded River." *Geological Society of America Bulletin* 59 (5): 463–512.
- Howard, Alan D. 1982. "Equilibrium and Time Scales in Geomorphology: Application to Sand-Bed Alluvial Streams." *Earth Surface Processes and Landforms* 7 (4): 303–25.
- Howard, Alan D, Jeffrey M Moore, and Rossman P Irwin III. 2005. "An Intense Terminal Epoch of Widespread Fluvial Activity on Early Mars: 1. Valley Network Incision and Associated Deposits." *Journal of Geophysical Research: Planets* 110 (E12).
- Jerolmack, Douglas J. 2009. "Conceptual Framework for Assessing the Response of Delta Channel Networks to Holocene Sea Level Rise." *Quaternary Science Reviews* 28 (17–18): 1786–1800. <https://doi.org/10.1016/j.quascirev.2009.02.015>.
- Jerolmack, Douglas J., and David Mohrig. 2007. "Conditions for Branching in Depositional Rivers." *Geology* 35 (5): 463. <https://doi.org/10.1130/G23308A.1>.
- Jerolmack, Douglas J., and John B. Swenson. 2007. "Scaling Relationships and Evolution of Distributary Networks on Wave-Influenced Deltas." *Geophysical Research Letters* 34 (23). <https://doi.org/10.1029/2007GL031823>.
- Jerolmack, Douglas J, and Chris Paola. 2007. "Complexity in a Cellular Model of River Avulsion." *Geomorphology* 91 (3–4): 259–70.
- . 2010. "Shredding of Environmental Signals by Sediment Transport." *Geophysical Research Letters* 37 (19).
- Kasse, C, Jef Vandenberghe, and S J P Bohncke. 1995. "Climatic Change and Fluvial Dynamics of the Maas during the Late Weichselian and Early Holocene." In *European River Activity and Climatic Change during the Lateglacial and Early Holocene: Paläoklimaforschung/Palaeoclimate Research, Vol. 14, Special Issue: ESF Project "European Palaeoclimate and Man" 9*, 123–50.
- Khan, Imran A, John S Bridge, John Kappelman, and Regan Wilson. 1997. "Evolution of Miocene Fluvial Environments, Eastern Potwar Plateau, Northern Pakistan." *Sedimentology* 44 (2): 221–51.
- Kidder, Tristram R., and Haiwang Liu. 2017. "Bridging Theoretical Gaps in Geoarchaeology: Archaeology, Geoarchaeology, and History in the Yellow River Valley, China." *Archaeological and Anthropological Sciences* 9 (8): 1585–1602. <https://doi.org/10.1007/s12520-014-0184-5>.
- Knox, James C. 1993. "Large Increases in Flood Magnitude in Response to Modest Changes in Climate." *Nature* 361 (6411): 430.
- . 2000. "Sensitivity of Modern and Holocene Floods to Climate Change." *Quaternary Science Reviews* 19 (1–5): 439–57.
- Knox, James C, and H E Wright. 1983. "Responses of River Systems to Holocene Climates." *Late Quaternary Environments of the United States* 2: 26–41.
- Kostic, Svetlana, and Gary Parker. 2003. "Progradational Sand-Mud Deltas in Lakes and Reservoirs. Part 1. Theory and Numerical Modeling." *Journal of Hydraulic Research* 41 (2): 127–40.
- Lamb, Michael P., Jeffrey a. Nittrouer, David Mohrig, and John Shaw. 2012. "Backwater and River Plume Controls on Scour Upstream of River Mouths: Implications for Fluvio-Deltaic Morphodynamics." *Journal of Geophysical Research* 117 (F1): F01002. <https://doi.org/10.1029/2011JF002079>.

- Lambeck, Kurt, and John Chappell. 2001. "Sea Level Change through the Last Glacial Cycle." *Science* 292 (5517): 679–86.
- Lane, T I, R A Nanson, B K Vakarelov, R B Ainsworth, and S E Dashtgard. 2017. "Evolution and Architectural Styles of a Forced-Regressive Holocene Delta and Megafan, Mitchell River, Gulf of Carpentaria, Australia." *Geological Society, London, Special Publications* 444 (1): 305–34.
- Langbein, Walter B, and Stanley A Schumm. 1958. "Yield of Sediment in Relation to Mean Annual Precipitation." *Eos, Transactions American Geophysical Union* 39 (6): 1076–84.
- LeBoutillier, David W, and Peter R Waylen. 1993. "A Stochastic Model of Flow Duration Curves." *Water Resources Research* 29 (10): 3535–41.
- Leeder, M R, and M D Stewart. 1996. "Fluvial Incision and Sequence Stratigraphy: Alluvial Responses to Relative Sea-Level Fall and Their Detection in the Geological Record." *Geological Society, London, Special Publications* 103 (1): 25–39.
- Leeder, Mike R, Tracey Harris, and Mike J Kirkby. 1998. "Sediment Supply and Climate Change: Implications for Basin Stratigraphy." *Basin Research* 10 (1): 7–18.
- Li, Qi, Lizhu Yu, and Kyle M Straub. 2016. "Storage Thresholds for Relative Sea-Level Signals in the Stratigraphic Record." *Geology* 44 (3): 179–82.
- Liang, Man, Corey Van Dyk, and Paola Passalacqua. 2016. "Quantifying the Patterns and Dynamics of River Deltas under Conditions of Steady Forcing and Relative Sea Level Rise." *Journal of Geophysical Research: Earth Surface* 121 (2): 465–96. <https://doi.org/10.1002/2015JF003653>.
- MacNaughton, Robert B., Robert W. Dalrymple, and Guy M. Narbonne. 1997. "Early Cambrian Braid-Delta Deposits, MacKenzie Mountains, North-Western Canada." *Sedimentology* 44 (4): 587–609.
- Malatesta, Luca C, Jeffrey P Prancevic, and Jean-Philippe Avouac. 2017. "Autogenic Entrenchment Patterns and Terraces Due to Coupling with Lateral Erosion in Incising Alluvial Channels." *Journal of Geophysical Research: Earth Surface* 122 (1): 335–55.
- Martin, John, Ben Sheets, Chris Paola, and David Hoyal. 2009. "Influence of Steady Base-Level Rise on Channel Mobility, Shoreline Migration, and Scaling Properties of a Cohesive Experimental Delta." *Journal of Geophysical Research: Earth Surface* 114 (F3).
- McLennan, Scott M, John P Grotzinger, Joel A Hurowitz, and Nicholas J Tosca. 2019. "The Sedimentary Cycle on Early Mars." *Annual Review of Earth and Planetary Sciences* 47: 91–118.
- Meade, Robert H, Ted R Yuzyk, and Terry J Day. 1990. "Movement and Storage of Sediment in Rivers of the United States and Canada." *IN: Surface Water Hydrology. Geological Society of America, Boulder, Colorado. 1990. p 255-280, 21 Fig, 3 Tab, 185 Ref.*
- Members, Cohmap. 1988. "Climatic Changes of the Last 18,000 Years: Observations and Model Simulations." *Science*, 1043–52.
- Milliman, John D., and James P. M. Syvitski. 1992. "Geomorphic/Tectonic Control of Sediment Discharge to the Ocean: The Importance of Small Mountainous Rivers." *The Journal of Geology* 100 (5): 525–44. <https://doi.org/10.1086/629606>.
- Mohrig, David, Paul L Heller, and William J Lyons. 2000. "Interpreting Avulsion Process from Ancient Alluvial Sequences : Guadalupe-Matarranya System (Northern Spain) and Wasatch Formation (Western Colorado)," no. 12: 1787–1803.
- Moran, Kaitlin E, Jeffrey A Nittrouer, Mauricio M Perillo, Jorge Lorenzo-Trueba, and John B Anderson. 2017. "Morphodynamic Modeling of Fluvial Channel Fill and Avulsion Time Scales during Early Holocene Transgression, as Substantiated by the Incised Valley Stratigraphy of the Trinity River, Texas." *Journal of Geophysical Research: Earth Surface* 122 (1): 215–34.
- Muto, T., R. J. Steel, and J. B. Swenson. 2007. "Autostratigraphy: A Framework Norm for Genetic Stratigraphy." *Journal of Sedimentary Research* 77 (1): 2–12. <https://doi.org/10.2110/jsr.2007.005>.
- Muto, T, and R J Steel. 1997. "Principles of Regression and Transgression: The Nature of the Interplay between Accommodation and Sediment Supply." *Journal of Sedimentary Research* 67 (6, B): 994–1000. <https://doi.org/10.1306/D42686A8-2B26-11D7-8648000102C1865D>.

- Nicholas, A P, R E Aalto, G H Sambrook Smith, and A C Schwendel. 2018. "Hydrodynamic Controls on Alluvial Ridge Construction and Avulsion Likelihood in Meandering River Floodplains." *Geology* 46 (7): 639–42.
- Nittrouer, Jeffrey A, John Shaw, Michael P Lamb, and David Mohrig. 2012. "Spatial and Temporal Trends for Water-Flow Velocity and Bed-Material Sediment Transport in the Lower Mississippi River." *Bulletin* 124 (3–4): 400–414.
- Nummedal, D, and G W Riley. 1993. "High-Resolution Sequence Architecture: A Chronostratigraphic Model Based on Equilibrium Profile Studies." *Sequence Stratigraphy and Facies Associations* 18: 55–58.
- Oeschger, Hans, J Beer, Urs Siegenthaler, B Stauffer, Willy Dansgaard, and C C Langway. 1983. "Late-Glacial Climate History from Ice Cores." In *Palaeoclimatic Research and Models*, 95–107. Springer.
- Olson, David M, and Eric Dinerstein. 1998. "The Global 200: A Representation Approach to Conserving the Earth's Most Biologically Valuable Ecoregions." *Conservation Biology* 12 (3): 502–15.
- Opperman, Jeffrey J, Ryan Luster, Bruce A McKenney, Michael Roberts, and Amanda Wrona Meadows. 2010. "Ecologically Functional Floodplains: Connectivity, Flow Regime, and Scale 1." *JAWRA Journal of the American Water Resources Association* 46 (2): 211–26.
- Pachauri, R K, L Meyer, G K Plattner, and T Stocker. 2014. "IPCC, 2014: Climate Change 2014: Synthesis Report." *IPCC, Geneva, Switzerland*.
- Paola, Chris. 2000a. "Quantitative Models of Sedimentary Basin Filling." doi:10.1046/j.1365-3091.2000.00006.X." *Sedimentology* 47 (s1): 121–78. <http://www.blackwell-synergy.com/doi/abs/10.1046/j.1365-3091.2000.00006.x>.
- . 2000b. "Quantitative Models of Sedimentary Basin Filling." *Sedimentology* 47: 121–78.
- Paola, Chris, Paul L Heller, and Charles L Angevine. 1992. "The Large-Scale Dynamics of Grain-Size Variation in Alluvial Basins, 1: Theory." *Basin Research* 4 (2): 73–90.
- Paola, Chris, and David Mohrig. 1996. "Palaeohydraulics Revisited: Palaeoslope Estimation in Coarse-Grained Braided Rivers." *Basin Research* 8 (3): 243–54. <https://doi.org/10.1046/j.1365-2117.1996.00253.x>.
- Parker, Gary. 1979. "Hydraulic Geometry of Active Gravel Rivers." In *ASCE J Hydraul Div*, 105:1185–1201.
- . 2004. "1D Sediment Transport Morphodynamics with Applications to Rivers and Turbidity Currents." *E-Book Available from Http://Vtchl. Uiuc. Edu/People/Parkerg/Morphodynamics_e-Book. Htm (Last Accessed 23 February 2010)*.
- Parker, Gary, Tetsuji Muto, Yoshihisa Akamatsu, William E. Dietrich, and J. Wesley Lauer. 2008. "Unravelling the Conundrum of River Response to Rising Sea-Level from Laboratory to Field. Part I: Laboratory Experiments." *Sedimentology* 55 (6): 1643–55. <https://doi.org/10.1111/j.1365-3091.2008.00961.x>.
- Parker, Gary, Tetsuji Muto, Yoshihisa Akamatsu, William E. Dietrich, and J. Wesley Lauer. 2008. "Unravelling the Conundrum of River Response to Rising Sea-Level from Laboratory to Field. Part II. The Fly-Strickland River System, Papua New Guinea." *Sedimentology* 55 (6): 1657–86. <https://doi.org/10.1111/j.1365-3091.2008.00962.x>.
- Poff, N LeRoy, J David Allan, Mark B Bain, James R Karr, Karen L Prestegard, Brian D Richter, Richard E Sparks, and Julie C Stromberg. 1997. "The Natural Flow Regime." *BioScience* 47 (11): 769–84.
- Posamentier, H W, M T Jervey, and P R Vail. 1988. "Eustatic Controls on Clastic Deposition I—Conceptual Framework."
- Powell, John Wesley. 1875. *Exploration of the Colorado River of the West and Its Tributaries*.
- Probst, J L. 1989. "Hydroclimatic Fluctuations of Some European Rivers since 1800." *Historical Change of Large Alluvial Rivers: Western Europe*, 41–55.
- Pufahl, Peir K, Franco Pirajno, and Eric E Hiatt. 2013. "Riverine Mixing and Fluvial Iron Formation: A New Type of Precambrian Biochemical Sediment." *Geology* 41 (12): 1235–38.

- Ratliff, Katherine M, Eric H W Hutton, and A Brad Murray. 2018. "Exploring Wave and Sea-Level Rise Effects on Delta Morphodynamics With a Coupled River-Ocean Model." *Journal of Geophysical Research: Earth Surface* 123 (11): 2887–2900.
- Ratliff, Katherine Murray. 2017. "From the River to the Sea: Modeling Coastal River, Wetland, and Shoreline Dynamics." Duke University.
- Reitz, Meredith D., and Douglas J. Jerolmack. 2012. "Experimental Alluvial Fan Evolution: Channel Dynamics, Slope Controls, and Shoreline Growth." *Journal of Geophysical Research* 117 (F2): F02021. <https://doi.org/10.1029/2011JF002261>.
- Richards, Keith, James Brasington, and Francine Hughes. 2002. "Geomorphic Dynamics of Floodplains: Ecological Implications and a Potential Modelling Strategy." *Freshwater Biology* 47 (4): 559–79.
- Saucier, Roger T. 1994. "Geomorphology and Quaternary Geologic History of the Lower Mississippi Valley. Mississippi River Commission." *US Army Corps of Engineers, Vicksburg* 2: 363.
- . 1996. "A Contemporary Appraisal of Some Key Fiskian Concepts with Emphasis on Holocene Meander Belt Formation and Morphology." *Engineering Geology* 45 (1–4): 67–86.
- Schumm, S A. 1993. "River Response to Baselevel Change: Implications for Sequence Stratigraphy." *The Journal of Geology* 101 (2): 279–94.
- Sellers, William D. 1969. "A Global Climatic Model Based on the Energy Balance of the Earth-Atmosphere System." *Journal of Applied Meteorology* 8 (3): 392–400.
- Shanley, K W, P J McCabe, S S Flint, and I D Bryant. 1993. "Alluvial Architecture in a Sequence Stratigraphic Framework: A Case History from the Upper Cretaceous of Southern Utah, USA." In *The Geological Modelling of Hydrocarbon Reservoirs and Outcrop Analogues*, 15:21–56. International Association of Sedimentologists.
- Slingerland, Rudy, and Norman D. Smith. 2004. "River Avulsions and Their Deposits." *Annual Review of Earth and Planetary Sciences* 32 (1): 257–85. <https://doi.org/10.1146/annurev.earth.32.101802.120201>.
- Soong, Ta Wei, and Yean Zhao. 1994. "The Flood and Sediment Characteristics of the Lower Yellow River in China." *Water International* 19 (3): 129–37.
- Stanley, Daniel J, and Andrew G Warne. 1997. "Holocene Sea-Level Change and Early Human Utilization of Deltas." *GSA Today*.
- Stanley, Daniel Jean, and Andrew G Warne. 1994. "Worldwide Initiation of Holocene Marine Deltas by Deceleration of Sea-Level Rise." *Science* 265 (5169): 228–31.
- Stedinger, J R. 1993. "Frequency Analysis of Extreme Events." In *Handbook of Hydrology*.
- Stouthamer, E, and H J a Berendsen. 2001. "Avulsion Frequency, Avulsion Duration, and Interavulsion Period of Holocene Channel Belts in the Rhine-Meuse Delta, The Netherlands." *Journal of Sedimentary Research* 71 (4): 589–98. <https://doi.org/10.1306/112100710589>.
- Straub, K. M., C. Paola, D. Mohrig, M. A. Wolinsky, and T. George. 2009. "Compensational Stacking of Channelized Sedimentary Deposits." *Journal of Sedimentary Research* 79 (9): 673–88. <https://doi.org/10.2110/jsr.2009.070>.
- Swenson, J.B., V.R. Voller, C. Paola, G. Parker, and J.G. Marr. 2000a. "Fluvio-Deltaic Sedimentation: A Generalized Stefan Problem." *European Journal of Applied Mathematics* 11 (5): 433–52.
- Swenson, J B, V R Voller, C Paola, Gary Parker, and J G Marr. 2000b. "Fluvio-Deltaic Sedimentation: A Generalized Stefan Problem." *European Journal of Applied Mathematics* 11 (5): 433–52.
- Syvitski, James P M. 2008. "Deltas at Risk." *Sustainability Science* 3 (1): 23–32.
- Syvitski, James P M, and Yoshiki Saito. 2007. "Morphodynamics of Deltas under the Influence of Humans." *Global and Planetary Change* 57 (3–4): 261–82. <https://doi.org/10.1016/j.gloplacha.2006.12.001>.
- Syvitski, James P M, Charles J Vörösmarty, Albert J Kettner, and Pamela Green. 2005. "Impact of Humans on the Flux of Terrestrial Sediment to the Global Coastal Ocean." *Science* 308 (5720): 376–80.
- Toomey III, Rickard S, Michael D Blum, and Salvatore Valastro Jr. 1993. "Late Quaternary Climates and Environments of the Edwards Plateau, Texas." *Global and Planetary Change* 7 (4): 299–320.

- Törnqvist, Torbjörn E. 1998. "Longitudinal Profile Evolution of the Rhine-Meuse System during the Last Déglaciation: Interplay of Climate Change and Glacioeustasy?" *Terra Nova* 10 (1): 11–15. <https://doi.org/10.1046/j.1365-3121.1998.00159.x>.
- Törnqvist, Torbjörn E., Santina R. Wortman, Zenon Richard P. Mateo, Glenn a. Milne, and John B. Swenson. 2006. "Did the Last Sea Level Lowstand Always Lead to Cross-Shelf Valley Formation and Source-to-Sink Sediment Flux?" *Journal of Geophysical Research* 111 (F4): F04002. <https://doi.org/10.1029/2005JF000425>.
- Törnqvist, Torbjörn E. 1994. "Middle and Late Holocene Avulsion History of the River Rhine (Rhine-Meuse Delta, Netherlands)." *Geology* 22 (8): 711–14.
- Törnqvist, Torbjörn E., Juan L González, Lee A Newsom, Klaas der Borg, Arie F M De Jong, and Charles W Kurnik. 2004. "Deciphering Holocene Sea-Level History on the US Gulf Coast: A High-Resolution Record from the Mississippi Delta." *Geological Society of America Bulletin* 116 (7–8): 1026–39.
- Törnqvist, Torbjörn E., and Marc P Hijma. 2012. "Links between Early Holocene Ice-Sheet Decay, Sea-Level Rise and Abrupt Climate Change." *Nature Geoscience* 5 (9): 601.
- Törnqvist, Torbjörn E., Jakob Wallinga, Andrew S Murray, Hein De Wolf, Piet Cleveringa, and Wim De Gans. 2000. "Response of the Rhine--Meuse System (West-Central Netherlands) to the Last Quaternary Glacio-Eustatic Cycles: A First Assessment." *Global and Planetary Change* 27 (1–4): 89–111.
- Trower, Elizabeth J, Vamsi Ganti, Woodward W Fischer, and Michael P Lamb. 2018. "Erosional Surfaces in the Upper Cretaceous Castlegate Sandstone (Utah, USA): Sequence Boundaries or Autogenic Scour from Backwater Hydrodynamics?" *Geology* 46 (8): 707–10.
- Vandenbergh, Jef, B Frenzel, J Vandenbergh, C Kasse, S Bohncke, and B Gläser. 1995. "Postglacial River Activity and Climate: State-of-the-Art and Future Prospects." *Paläoklimaforschung* 14.
- Veldkamp, A, and M W den Berg. 1993. "Three-Dimensional Modelling of Quaternary Fluvial Dynamics in a Climo-Tectonic Dependent System. A Case Study of the Maas Record (Maastricht, The Netherlands)." *Global and Planetary Change* 8 (4): 203–18.
- Vörösmarty, Charles J, James Syvitski, John Day, Alex de Sherbinin, Liviu Giosan, and Chris Paola. 2009. "Battling to Save the World's River Deltas." *Bulletin of the Atomic Scientists* 65 (2): 31–43. <https://doi.org/10.2968/065002005>.
- Walling, D E, and B W Webb. 1996. "Erosion and Sediment Yield: A Global Overview." *IAHS Publications-Series of Proceedings and Reports-Intern Assoc Hydrological Sciences* 236: 3–20.
- Wickert, Andrew D., John M. Martin, Michal Tal, Wonsuck Kim, Ben Sheets, and Chris Paola. 2013. "River Channel Lateral Mobility: Metrics, Time Scales, and Controls." *Journal of Geophysical Research: Earth Surface* 118 (2): 396–412. <https://doi.org/10.1029/2012JF002386>.
- Wood, L J, F G Ethridge, and S A Schumm. 1993. "The Effects of Rate of Base-Level Fluctuation on Coastal-Plain, Shelf and Slope Depositional Systems: An Experimental Approach." *Sequence Stratigraphy and Facies Associations* 18: 43–53.
- Zhang, Zhouliang, Keqin Sun, and Jarun Yin. 1997. "Sedimentology and Sequence Stratigraphy of the Shanxi Formation (Lower Permian) in the Northwestern Ordos Basin, China: An Alternative Sequence Model for Fluvial Strata." *Sedimentary Geology* 112 (1–2): 123–36.
- Zhou, Yuanyuan, He Qing Huang, Gerald C Nanson, Chong Huang, and Gaohuan Liu. 2015. "Progradation of the Yellow (Huanghe) River Delta in Response to the Implementation of a Basin-Scale Water Regulation Program." *Geomorphology* 243: 65–74.
- Zong, Yongqiang, Z Wang, J B Innes, and Z Chen. 2012. "Holocene Environmental Change and Neolithic Rice Agriculture in the Lower Yangtze Region of China: A Review." *The Holocene* 22 (6): 623–35

*Chapter 4***EFFECT OF SEA-LEVEL RISE
ON AN EXPERIMENTAL LOWLAND RIVER DELTA**

A.J. Chadwick^{a,1}, M.P. Lamb^a, S. Steele^a, J. Silvestre^b,

^aDivision of Geological and Planetary Sciences, California Institute of Technology, Pasadena, CA
91125

^bDepartment of Earth and Environmental Sciences, Tulane University, New Orleans, Louisiana,
USA

4.0. ABSTRACT

River deltas are densely populated landscapes in danger of drowning due to anthropogenic relative sea-level rise in the coming century. Delta response to sea-level rise is commonly forecasted using radially averaged models based on sustainability of the entire delta; however, deposition and land loss can vary spatially because river avulsions periodically and abruptly shift the river course, changing the distribution of sediment. Here, we present results from an experimental delta with low Froude numbers and variable discharge floods, which are needed to produce backwater-scaled avulsions similar to lowland deltas, with systematic changes in sea-level rise and fall rate. Avulsions repeatedly occurred at a spatial node located midway through the backwater zone and migrated basinward in tandem with delta progradation, similar to previous backwater-controlled experiments conducted with steady sea level, but unlike previous work the avulsion node in our experiment migrated landward when sea-level rise caused river-mouth retreat. River avulsions were more frequent as sea-level rise accelerated, up until the point the delta was drowned and avulsions were not allowed. Avulsions resumed during moderate rates of sea-level fall, so long as progradation was sufficient to drive net channel aggradation. Avulsions occurred more frequently than predicted by radially averaged models, but show good agreement with recent lobe-averaged models that account for discrete lobes with a constant length set by backwater hydrodynamics. Delta land area in our experiments was also significantly less than predicted by radially averaged models, on account of transient land loss on abandoned delta lobes that were starved of sediment between avulsion events. Results imply anthropogenic relative sea-level rise on lowland deltas may cause more land loss than previously estimated, and that drowning of the coastal plain will be accompanied by avulsion hazards that occur more frequently and shift farther landward.

4.1. INTRODUCTION

River deltas are ecologically diverse, socioeconomically valuable, and host over half a billion of the Earth's population (Gleick, 2003; Olson & Dinerstein, 1998; Vörösmarty et al., 2009). Many deltas develop a triangular-shaped planform morphology through repeated changes in channel course to the shoreline, known as river avulsions, that occur every 10 – 1000 years (Allen, 1965; Slingerland & Smith, 2004). Channel avulsions pose a hazard to human life and property (Sinha, 2009; Syvitski & Brakenridge, 2013), and have been responsible some of the deadliest flood disasters in human history (Kidder & Liu, 2017; Soong & Zhao, 1994). At the same time, avulsions counter land lost to sea-level rise and coastal subsidence by nourishing wetlands with sediment (Edmonds et al., 2009; Richards et al., 2002). Today, engineered avulsions are important parts of billion-dollar coastal restoration plans (Brakenridge et al., 2017; Coastal Protection and Restoration Authority of Louisiana, 2007). Predictive models of channel avulsion and land loss will be crucial for the success of such plans and for sustaining coastal cities and ecosystems, because anthropogenic interference and greenhouse effects are causing unprecedented rates of relative sea-level rise across the globe (Pachauri et al., 2014).

One approach to predict river avulsion and delta response to sea-level rise is through simplified models of delta geometry and growth. The most common approach is to assume deposition and erosion are dictated by radially averaged sediment mass-balance,

$$Q_s = \frac{\partial}{\partial t}(AH_b) = A\sigma + H_b \frac{\partial A}{\partial t} \quad (4.1)$$

where Q_s is volumetric sediment supplied per unit time, A is the planform delta area, H_b is the basin depth offshore, and $\sigma = \frac{\partial H_b}{\partial t}$ is the relative sea-level rise rate (sea level rise + uniform

subsidence) (Jerolmack, 2009; W. Kim et al., 2009; Wonsuck Kim et al., 2006; Paola et al., 2011). In Eq. (4.1), the first term on the right-hand-side describes deposition on the delta topset, and the second term describes foreset progradation. Radially averaged models do not resolve channels or avulsion processes, but nevertheless provide quantitative predictions for delta land area. Relative sea-level rise causes land loss and a reduction in delta area A until the sediment supply is sufficient to keep pace with sea level. Stable coastlines correspond to the steady-state condition $v_a = \frac{Q_s}{A} = \sigma$, where v_a is the aggradation rate, which is used for assessment of sediment budgets and land loss predictions (Giosan, 2014).

In contrast to radially averaged models, deposition on deltas varies spatially and, at the largest scale, spatial patterns are set by river avulsions that reroute sediment amongst active and inactive lobes (Coleman et al., 1998; Jerolmack & Swenson, 2007; Pang & Si, 1979) (Fig. 4.1). Global compilations of lowland deltas (e.g., Fig. 4.1) show that avulsions preferentially occur at a distance upstream of the shoreline that scales with the backwater length-scale,

$$L_A \sim L_b = H_c/S \quad (4.2)$$

where L_A is the avulsion length measured along the channel from the river mouth to the avulsion location and L_b is the backwater length-scale, defined as the ratio channel depth H to average bed slope S (Chatanantavet et al., 2012; Jerolmack, 2009; Jerolmack & Swenson, 2007). The backwater length approximates the distance that sea level influences river flow upstream, and can extend for hundreds of kilometers for large, low-sloping rivers (Lamb et al., 2012; Paola & Mohrig, 1996). The frequency of lobe-switching events, f_A , scales with the rate the riverbed aggrades to a height comparable to the channel depth,

$$f_A \sim \frac{v_a}{H^*H_c} \quad (4.3)$$

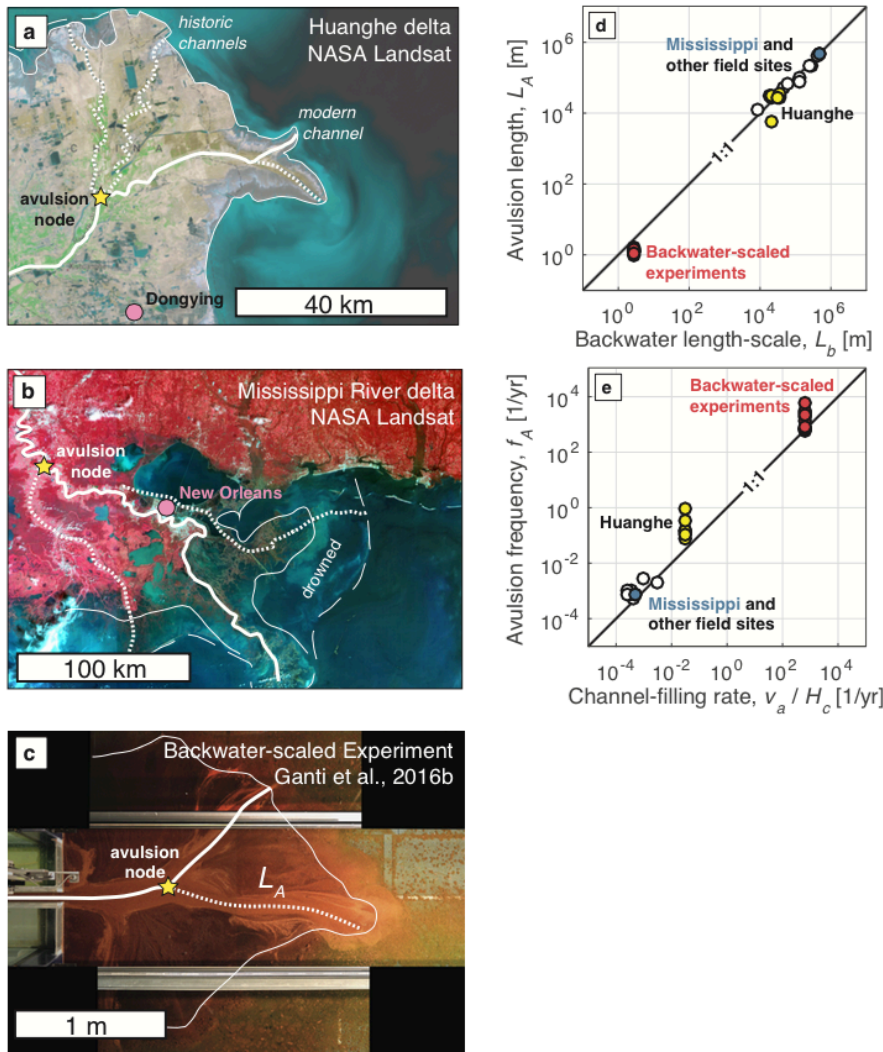


Fig. 4.1: a) Huanghe delta, China, illustrating modern (solid line) and abandoned (dotted line) channel pathways and avulsion node (yellow star). Pink circle denotes city of Dongying. b) Mississippi River delta, USA. Thin dashed line indicates approximate shoreline in 1900 A.D. (Gagliano, Meyer-Arendt, and Wicker 1981). Pink circle denotes New Orleans. c) Backwater-scaled delta experiment conducted under variable river discharge (Ganti et al., 2016b). d) Correlation between measured avulsion length and computed backwater length-scale, which approximates the distance upstream of the shoreline where sea-level causes gradually-varied flow (Chatanantavet, Lamb, and Nittrouer 2012; Ganti et al. 2014; Ganti, Chadwick, Hassenruck-Gudipati, Fuller, et al. 2016). e) Correlation between measured avulsion frequency and the rate at which riverbed aggradation fills the channel-depth (Jerolmack and Mohrig 2007; Ganti et al. 2014; Ganti, Chadwick, Hassenruck-Gudipati, Fuller, et al. 2016).

where v_a is the vertical aggradation rate and H^* is the avulsion threshold, a dimensionless constant of order unity (Bryant et al., 1995; Ganti et al., 2014; Mohrig et al., 2000) (Fig. 4.1). Chatanantavet et al. (2012) hypothesized that avulsion nodes on lowland deltas originate from a spatial maximum in v_a midway through the backwater zone due to non-uniform flow dynamics and floods of variable discharge (Eq. 4.3). Using a morphodynamic model of the Mississippi River, they observed that low flows (less than bankfull) tended to deposit sediment in the upper part of the backwater zone, whereas high flows (greater than bankfull) caused scour in the lower part of the backwater zone. Alternation between low flows and high flows led to the site of maximum v_a that drove preferential avulsions at $L_A \sim L_b$, whereas model scenarios with constant discharge floods did not produce a preferred avulsion location. Although the hypothesis of Chatanantavet et al. (2012) was supported by later numerical models (Chadwick et al., 2019; Moodie et al., 2019) and field evidence of deposition and scour on the Lower Mississippi River (Lamb et al., 2012; J. A. Nittrouer et al., 2011; J. a. Nittrouer et al., 2011), few direct measurements of natural avulsions exist to test these models.

Channel-resolving 2-D and 3-D models have provided valuable insight into avulsion processes and delta response during sea-level change (Caldwell & Edmonds, 2014; Edmonds et al., 2010; Gao et al., 2019; Geleynse et al., 2011a; Van De Lageweg & Slangen, 2017). DeltaRCM models reproduce deltas with smaller topset areas and higher avulsion frequencies during sea-level rise, consistent with radially averaged models (Liang, Geleynse, et al., 2015; Liang, Kim, et al., 2016; Liang, Van Dyk, et al., 2016a; Liang, Voller, et al., 2015). In contrast, similar modeling using Delft3D showed evidence for persistent avulsions during sea-level fall, which is not captured in radially averaged models (Nijhuis et al., 2015). While such models include the physics that result in backwater-scaled delta lobes (Eq. 4.2), simulations have yet to

be evaluated in terms of lobe size or avulsion location (Geleynse et al., 2011b; Nijhuis et al., 2015; Van De Lageweg & Slangen, 2017). Delta lobes and avulsion location have been evaluated using simpler 1-D morphodynamic models, but these models are tuned to specific case studies (Chatanantavet et al., 2012; Moran et al., 2017) and yielded opposite trends for avulsion frequency response during sea-level rise. A 2-D reduced complexity model found that avulsion frequency was insensitive to sea-level rise for low rise rates due to progradation (Ratliff et al., 2018). However, this model did not include backwater hydrodynamics or a model spin-up phase that is needed to avoid bias associated with the assumed initial condition of the riverbed and land-surface elevation profiles (Chadwick et al., 2019).

The most recent models that produce backwater-scaled avulsion nodes (Eq. 4.2) include quasi-2D non-uniform flow, a variable flood regime that maintains backwater effects, and a spin-up phase to avoid issues associated with initial conditions (Chadwick et al., 2019; Moodie et al., 2019). Chadwick et al. (*in review*) used such a model to show avulsion frequency during sea-level rise depends on the dominant cause of aggradation: whether due to basinward progradation, relative sea-level rise, or limited by sediment supply. In their model, avulsion frequency increased with sea-level rise under rise-dominated conditions, corresponding to when sea-level rise rate is comparable to the maximum possible rate of radially averaged delta aggradation. However, avulsion frequency became insensitive to sea-level at lower rise rates, when aggradation is instead set by progradation. Avulsion frequency was also insensitive to rise rate during rapid sea level rise, when aggradation became limited by the sediment supply. Importantly, previous work incorporating backwater hydrodynamics did not explore the effect of sea-level rise on avulsion location or delta area, and model validation was limited to existing field data, which are scarce because river avulsions occur infrequently and are difficult to

observe safely in nature. In this regard, physical laboratory experiments provide an opportunity to compensate for limited field data and contribute substantially to our understanding.

Experimental studies have documented lobe-scale avulsions in relatively steep flume experiments, and generally support radially-averaged models (Hajek et al., 2010; Wonsuck Kim et al., 2006; Muto et al., 2016; Muto & Steel, 2004a; Reitz & Jerolmack, 2012; Reitz et al., 2010; Wickert et al., 2013). These experiments featured high Froude numbers, which prevented backwater effects, and high sedimentation rates that caused channel braiding, making these experiments closer analogs to alluvial fans or fan deltas than lowland deltas (Ganti, Chadwick, Hassenruck-Gudipati, Fuller, et al., 2016; Ganti et al., 2014). Hoyal & Sheets (2009) produced a delta with lower surface slopes and single-thread channels, in which they observed channel backfilling during progradation as the primary driver for avulsions. Subsequent experiments varied sea-level rise in a similar experimental set up (Li et al., 2016; Martin et al., 2009; Yu et al., 2017), and found good agreement with radially averaged model predictions of delta area and avulsion frequency. However, despite their low slopes these experiments featured an avulsion node tied to the basin inlet and a constant river discharge that prevented backwater-scaled avulsions (Chatanantavet et al., 2012; Ganti, Chadwick, Hassenruck-Gudipati, Fuller, et al., 2016). Chatanantavet & Lamb (2014) used a physical model to verify that deposition and erosion in the backwater zone is controlled by variable discharge floods, but their setup did not allow for lobe-scale avulsions or changes in sea level. The first backwater-scaled delta with avulsions was that of Ganti et al. (2016a; 2016b; 2019), and was conducted under constant sea-level, variable-discharge floods, and low Froude numbers (Fig. 4.1). In their experiment, single-thread rivers avulsed among multiple lobes with a characteristic avulsion length set by half the backwater

length-scale ($L_A = 0.5L_b$). The avulsion site was coincident with the site of maximum in-channel sedimentation in between avulsions, as a result of competition between low-flow deposition throughout the backwater zone and high-flow scour closer to the river mouth, consistent with previous work by Chatanantavet et al. (2012). At the avulsion node, avulsions were observed to occur when the channel had aggraded to $\sim 30\%$ of the flow depth ($H^* = 0.3 \pm 0.13$) at a frequency $f_A = 0.17 \text{ hr}^{-1}$.

Here we build on the experiment presented by Ganti et al. (2016a; 2016b; 2019) by conducting a similar backwater-scaled experiment with variable flood discharges, but instead of constant sea level, we systematically varied sea-level rise and fall rates. We sought to address how relative sea-level rise and fall affect delta growth and avulsion. We present results for delta land area, channel hydrodynamics and sedimentation, and avulsion location and frequency from this experiment. We compared results to existing radially-averaged model predictions, theory for backwater-influenced deltas, and past experiments of backwater-influenced delta formation conducted under constant sea-level conditions. Lastly, we discuss implications for predicting future avulsion and land-loss hazards in the face of anthropogenic climate change.

4.2. METHODS

4.2.1 *Experimental setup*

We performed scaled physical experiments to grow a delta and observe its dynamics under conditions of persistent backwater effects and changing sea levels. The experiments were designed to isolate the effect of sea-level rise and fall on backwater-influenced delta growth and avulsion in the simplest way possible. To this end, we excluded from this experiment a number of other processes that can affect natural deltas, including: waves, tides, oceanic storms, water

density gradients, strongly cohesive sediment, vegetation, and differential subsidence (Caldwell & Edmonds, 2014; Hoyal & Sheets, 2009; Jerolmack, 2009; Nienhuis et al., 2015; Reitz et al., 2015). While we ignored differential subsidence, we note that delta response to uniform subsidence is mechanically similar to that of sea-level rise (González & Tornqvist, 2006; Jerolmack, 2009; Reitz et al., 2015).

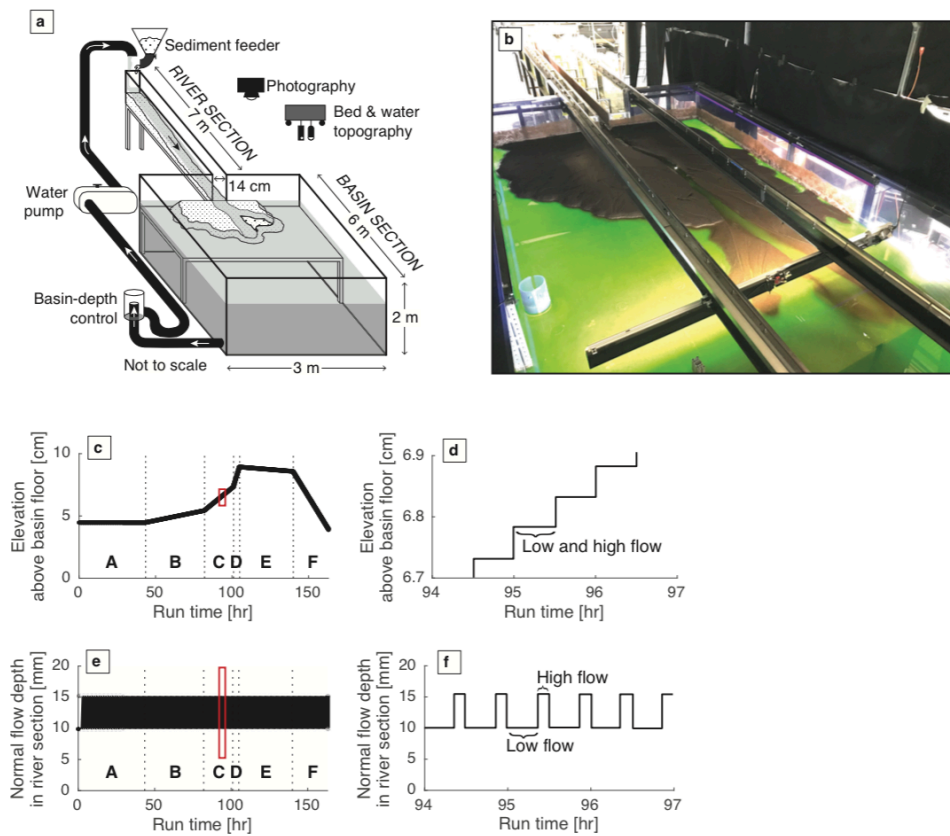


Fig. 4.2: a) Schematic of the experimental facility. b) Photograph of the delta experiment taken at the termination of the experiment, at run time of 163.5 hr. c) Sea level as a function of run time over the course of the experiment. Dashed lines indicate the boundaries of experimental phases A through F, each of which featured a different rate of sea-level change. Red box shows area of zoom in panel d). d) A zoomed-in view of experimental sea level through time, showing sea-level rise was implemented in discrete steps at the end of high flow events. e) Normal flow depth in the confined river section as a function of run time over the course of the experiment. Red box indicates area of zoom in panel f). f) A zoomed-in view of normal flow depth over time, showing flow was alternated between a low flow event (22-minute duration) and a high-flow event (8-minute duration).

Experiments were conducted in the same facility as past constant-sea-level experiments of backwater-scaled delta growth (Ganti, Chadwick, Hassenruck-Gudipati, Fuller, et al., 2016; Ganti, Chadwick, Hassenruck-Gudipati, & Lamb, 2016b; Ganti et al., 2019a), which was modified to simulate and characterize the effects of changing sea levels. The experimental flume consisted of a 7-m-long, 14-cm-wide fixed-width alluvial river that flowed into a 5-m-long, 3-m-wide unconfined ocean basin (Fig. 4.2). Sea level was controlled using a programmable stand pipe at the downstream end, which was incrementally adjustable in 0.1-mm increments. Sea level rise rates were selected such that the balance of relative sea-level rise and sediment supply was similar to that of natural deltas. The dimensionless relative sea-level rise rate σ^* describes this balance, and is defined by the parameter σ^* , defined as

$$\sigma^* = \frac{\sigma n L_b B}{Q_s / (1 - \lambda_p)} \quad (4.4)$$

where σ is the rate of relative sea-level rise (uniform subsidence + sea level rise), L_b is the backwater length-scale, Q_s is the volumetric sediment supply, λ_p is the sediment porosity, B is the lobe width, and $n = (N + 1)/2$ is the number of avulsions before a given lobe is reoccupied and N is the average number of delta lobes. On modern deltas, σ^* typically falls within the range of $10^{-3} - 10^0$ (Chadwick et al., *in review*). Pleistocene glacial-interglacial cycles induced rise and fall of global sea levels at the scale of $\sim 120\text{m}$ over $\sim 10^5$ years (Bintanja et al., 2005), corresponding to σ^* in the range -10^0 to $+10^0$ using modern values of sediment supply (Milliman & Syvitski, 1992).

We observed delta evolution under natural ranges of σ^* , broken into six phases each with a different rate of sea-level change (Table 4.1; Fig. 4.2). Sediment supply was held constant and equal to $0.0019 \text{ m}^3/\text{hr}$ during all phases. During the first phase, Phase A, we allowed the delta

to grow under constant sea-level conditions similar to previous experiments (Ganti et al. 2016a; 2016b; 2019). During Phase B, sea level rose at a constant rate of $\sigma = 0.25$ mm/hr, corresponding to $\sigma^* = 0.097$. Sea level rise accelerated during Phase C ($\sigma = 1$ mm/hr, $\sigma^* = 0.39$) and Phase D ($\sigma = 4$ mm/hr, $\sigma^* = 1.55$), eventually drowning the delta and restricting deposition to the narrow river section. During Phase E, we lowered sea level at a rate of $\sigma = 0.1$ mm/hr ($\sigma^* = -0.04$). Sea level fall was accelerated during phase F ($\sigma = -2$ mm/hr, $\sigma^* = -0.77$). Each phase was allowed to continue until the delta produced several (≥ 10) avulsions, or in cases where no avulsions occurred until the delta drowned (Phase D) or the delta shoreline prograded to the end of the basin (Phase F).

| | Phase A. | Phase B. | Phase C. | Phase D. | Phase E. | Phase F. |
|--|-------------|-------------|-------------|-------------|-------------|-------------|
| Sea-level rise rate, σ $\left[\frac{\text{mm}}{\text{hr}}\right]$ | 0 | 0.25 | 1 | 4 | -0.1 | -2 |
| Experimental duration, Δt [hr] | 25 | 38.5 | 19 | 4 | 35 | 23.5 |
| Dimensionless sea-level rise rate, σ^* [-] | 0 | 0.10 | 0.39 | 1.55 | -0.04 | -0.77 |
| Number of observed avulsions [-] | 10 | 22 | 16 | 0 | 20 | 0 |

Table 4.1: Sea-level-change conditions systematically varied during each phase of the experiment

We conducted experiments under subcritical flow conditions ($Fr \cong 0.5$) allowing for backwater hydrodynamics, and used crushed, non-cohesive walnut shells of uniform grain size ($\rho_s = 1300$ kg/m³, $D = 0.7$ mm) to allow gentle laboratory-scale flows to transport sediment at low slopes (Table 4.2). Sediment was transported primarily as bedload with intermittent suspension ($\tau^* \cong 0.2 - 0.3$). In order to maintain persistent backwater effects and a backwater-scaled avulsion node, we alternated water discharge between a 22-minute low flow and an 8-

minute high flow for a total of 300 flow cycles. Discharges were scaled roughly as 2-yr and 30-yr recurrence interval floods following the technique of Ganti et al. (2016a). Sediment supply was adjusted in tandem with water discharge to maintain a constant equilibrium transport slope in the normal flow reach ($S = 3.8 \times 10^{-3}$). This ensured that patterns of deposition and erosion were due to backwater effects and relative sea-level rise, and not imbalances in water and sediment supply (Blum & Törnqvist, 2000; Paola, 2000; Paola et al., 1992). The duration of low and high flows was chosen to be short compared to the channel adjustment timescale ($T_{adj} \sim H_c B_c L_b / Q_s$) (Chatanantavet & Lamb, 2014b). This ensured that the riverbed was in a perpetual state of morphodynamic adjustment, which was shown to be necessary for backwater-scaled avulsion nodes in previous experiments and models (Chadwick et al., 2019; Chatanantavet & Lamb, 2014b; Chatanantavet et al., 2012; Ganti, Chadwick, Hassenruck-Gudipati, Fuller, et al., 2016). The water and sediment discharge were also chosen such that the transport slope S yielded a backwater length during low flow of 2.6 m and a drawdown length during high flow of 1.3 m (Table 4.2), fitting within the confines of the 5 m x 3 m basin. Backwater length and drawdown length were calculated according to the Bresse solution, which accounts for Fr and the magnitude of each flow event (Lamb et al., 2012). The river section of the flume was long enough such that normal-flow conditions and a constant bed slope could be observed upstream of backwater effects throughout the entirety of the experiment.

A constant rate of sea-level rise during each phase was approximated by discrete 0.1-mm vertical adjustments in the programmable standpipe every 30 minutes of experimental run time. For Phase E, sea-level fall rate was so slow that vertical adjustments were limited to once every hour in 0.1-mm increments.

| | Low flow | High flow |
|--|----------|-----------|
| Flow duration [min] | 22 | 8 |
| Water discharge Q_w [liters/min] | 14.4 | 20.4 |
| Sediment feed, Q_s [g/min] | 30.42 | 69.42 |
| Normal-flow depth, H_n [mm] | 9.9 | 15.2 |
| Normal-flow transport slope, S_n [-] | 3.8E-3 | 3.8E-3 |
| Backwater length-scale, H_n/S_n [m] | 2.6 | – |
| Drawdown length-scale* [m] | – | 1.3 |
| Froude number, Fr [-] | 0.56 | 0.42 |
| Shields number, τ^* [-] | 0.18 | 0.28 |
| Friction coefficient, C_f | 0.012 | 0.022 |

*Drawdown length-scale was approximated using the Bresse solution following Lamb et al. (2012).

Table 4.2: Upstream conditions of the variable-discharge regime used through the entire experiment.

4.2.2 Data collection

The water was dyed using a fluorescent green dye, which allowed for visual distinction between subaerial and submerged surfaces even for shallow (~ 1 cm) water depths under ultraviolet light fixtures. Before starting a flow event, we inserted ~ 0.5 gallons of dye into the end tank and ran the flow using a very low discharge ($Q = 0.002$ L/min) with no sediment feed, which allowed the dye to disperse evenly through the tank over the course of ~ 12 hours of standby without mobilizing sediment or disturbing the delta. Overhead images of delta evolution were collected every minute for the entire duration of the experiment using six mounted cameras that bordered the experimental facility. Photos from each camera were concatenated to ensure a wide field of view that extended beneath railings in the facility. A single camera was devoted to recording a 30-second video at the start of each flow event, which was coordinated simultaneously with a concentrated dye pulse injection at the upstream end to characterize channel flow velocity.

An ultrasound distance meter (Massa) and laser triangulation sensor (Keyence) measured water surface elevation at 1-mm vertical resolution and bed topography at 0.1-mm resolution, respectively. Before each flow event we validated that basin sea level followed the experimental sea level curve (Fig. 4.2) within 0.1 mm by scanning a thin piece of floating wax paper at the downstream end using the laser sensor. At the beginning of each flow event we collected water surface elevation data, and after each event we switched off the flow and measured bed surface elevation. Topographic scans included a long profile through the river and basin section along the flume centerline at 3-mm horizontal resolution, as well as a series of cross sections in the basin section perpendicular to the flume axis (3-mm resolution in the cross-stream resolution, spaced every 15 cm in the downstream direction). The basin water level was maintained during bed topography scans, and data for the submerged parts of the delta were corrected for the refraction index of the Keyence laser beam through still water. The green color of the fluorescent dye in the basin ensured transmission of the red laser signal. Summed errors associated with vertical measurements from the instrument itself and the refraction-index correction were ± 0.1 mm. Raw data from topographic scans were denoised using a median filter of kernel size 1.5 cm.

4.2.3 Data analysis

Concatenated overhead images were used to identify channel avulsion events, shoreline evolution, and land building and land loss during the experiment. Following previous work, we defined avulsions as the establishment of a new channel (the daughter channel) that captured the majority of flow through consecutive flow events, and the old channel (the parent channel) was partially or completely abandoned (Ganti et al., 2016b). Avulsion location and time were

determined as the location and time when the levee breach in the parent channel initiated.

Manual identification of avulsions involved a degree of subjectivity, but our measurements for avulsion location have an uncertainty of less than a channel width and much less than a backwater length-scale, and measurements for avulsion time have an uncertainty of less than one minute (Ganti 2016a; 2016b). Avulsion length (L_A) was computed as the distance along the parent channel from the river mouth to the avulsion location. Avulsion frequency was calculated using $f_A = 1/T_A$, where T_A is the time between the current avulsion event and the previous avulsion event. Land building and land loss were characterized through repeated mapping of the delta shoreline, which was manually identified by the boundary of fluorescent green water and the brown sediment surface. We also independently mapped the location of the topset-foreset break visually; during sea-level rise we observed the shoreline retreated upstream from the topset-foreset break, especially on abandoned delta lobes.

We computed channel aggradation and erosion using topographic scans at the end of each flow event. In the upstream river section with imposed channel width, we computed aggradation using the difference in channel bed elevation along the channel centerline. On the delta topset the channel formed its own single-thread channel. Preliminary experiments were used to determine the wall spacing in the fixed-width river section that match the self-formed channel width on the delta top, thereby eliminating non-uniformity in the channel across this transition that occurred in previous experiments (Chatanantavet 2014; Ganti 2016a; 2016b). In the self-formed channel, we calculated a cross-sectionally averaged bed elevation by subtracting the width-averaged channel depth from the mean levee height,

$$\eta_b = \eta_{levee} - H_c \quad (4.5)$$

where η_{levee} is the mean elevation of the levees on either bank, $H_c = A_c/B_c$ is the width-averaged channel depth, B_c is the channel top width, and A_c is the computed cross-sectional area of the channel. Levees were identified in topographic scans using overhead images as a guide.

4.2.4 Predictions from radially averaged and lobe-averaged models

Using the radially averaged model (Eq. 4.1), we predicted changes in delta area over the course of the experiment. A central assumption of the radial model is that the avulsion location remains geographically fixed, defining the delta apex (Jerolmack, 2009; Paola et al., 2011). We computed model predictions for avulsion frequency using Eq. (4.3) under approximately steady-state delta area, corresponding to aggradation at the pace of sea-level rise ($v_a = \sigma$).

We also compared experimental results for avulsion location and frequency to the analytical model presented by Chadwick et al. (*in review*). This model accounts for sediment-mass partitioning between delta-lobe topset and foreset during sea-level rise, incorporating a constant avulsion length scaled by the backwater length (Eq. 4.2). Compared to the radially averaged model, the lobe-averaged approach of Chadwick et al. (*in review*) requires additional input parameters that we measured in the experiment: the avulsion threshold H^* , the average lobe width B , and the number of delta lobes N comprising the delta surface. Following Ganti et al. (2016b), we measured the avulsion threshold by measuring in-channel aggradation at avulsion from topographic scans, and dividing the aggradation thickness by the characteristic channel depth of 9.9 mm. We used a characteristic value of $N = 3$ delta lobes, because active channels typically visited 1/3 of the delta surface between avulsions. Lobe width was estimated by dividing the lobe area by the avulsion length ($B = \frac{A_{lobe}}{L_A}$, where $A_{lobe} = A/N$ is the delta lobe area). For simplicity, surface slopes on the lobe topset and foreset are approximated as constant,

allowing for an analytical solution. This analytical approach shows good agreement with numerical simulations that allow for variable slopes and autogenic avulsion locations arising from variable flood discharges.

4.3. RESULTS

4.3.1 Phase A

After an initial 18-hr period of sheet flow similar to that documented by Ganti et al. (2016b), flow channelized on the delta topset and the experimental delta grew through repeated avulsion cycles under constant sea level for the following 26 hr. Fig. 4.3 shows experimental data for dry-land area over time in the experiment. We also include area of the entire delta, the sum of both dry and drowned zones, which is measured to the distalmost topset-foreset break. During Phase A, the dry land area increased at a rate of $0.084 \text{ m}^2/\text{hr}$. Dry land area was equal to total land area because sea level was stable and no land was drowned.

During Phase A, we observed 10 channel avulsions. Fig. 4.4a shows avulsion locations and shorelines over time overlain on a photograph captured at the end of Phase A. Avulsions occurred between 30-50cm downstream of the basin inlet, moving downstream over time, maintaining a mean avulsion length of 1.3m with a standard error of 0.06m, a minimum length of 0.9m, and a maximum length of 1.7m ($L_A = 1.3 \pm 0.1 [0.9 - 1.7] \text{ m}$). Channel avulsions occurred at a frequency of $f_A = 0.4 \text{ hr}^{-1}$, with a standard error of 0.1 hr^{-1} , a minimum of 0.19 hr^{-1} , and a maximum of 1.1 hr^{-1} ($f_A = 0.4 \pm 0.1 [0.19 - 1.1] \text{ hr}^{-1}$) (Fig. 4.3). Lateral migration was not pronounced and was limited to 2-3 times the channel width between avulsions, potentially due to backwater effects which are thought to reduce migration rates on the Mississippi (Hudson & Kesel, 2000; J. A. Nittrouer et al., 2012). In our experiments, reduced

lateral migration led to the development of distinct lobes with each avulsion (Fig. 4.4a), similar to previous backwater-scaled experiments (Ganti, Chadwick, Hassenruck-Gudipati, & Lamb, 2016b). During Phase A, progradation of the delta caused the land area to increase from 0.75 m^2 to 2.75 m^2 . Progradation, in turn, caused aggradation of the active channel riverbed by a total of $\sim 1 \text{ cm}$, with an average in-channel aggradation rate of 0.38 mm/hr (Fig. 4.4b).

Aggradation was caused by basinward progradation of the delta, which maintained a constant riverbed slope of $S = 3.8 \times 10^{-3}$. While the quantitative results differ slightly from the previous experiment due to slightly different input parameters, Phase A was qualitatively consistent with Ganti et al. (2016) experiment with variable discharge floods.

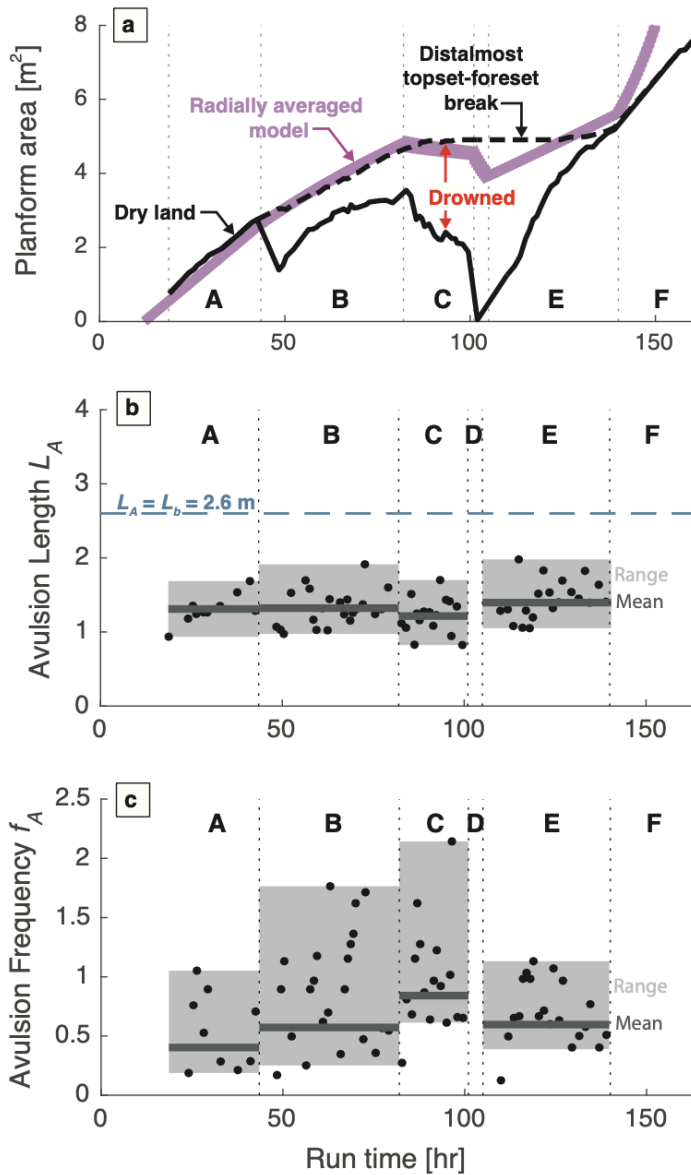


Fig. 4.3: a) Planform area as a function of run time in the experiment, showing dry land area (black line), sum of dry and drowned areas within the distalmost topset-foreset break (black dashed line), and predictions according to the radially averaged model of Eq. (4.1). The area of drowned topset is annotated in red. Dashed vertical lines indicate the boundaries of experimental phases A through F. Lower panels show avulsion length (b) and avulsion frequency (c) measured over the course of the experiment. Dashed lines indicate boundaries of experimental phases A through F. Black points indicate individual avulsions. Mean (dark gray line), and range (light gray area) of values for each experimental phase are shown. No avulsions were observed during Phase D, Phase F, or the initial sheet-flow period of the experiment before run time of 18 hr.

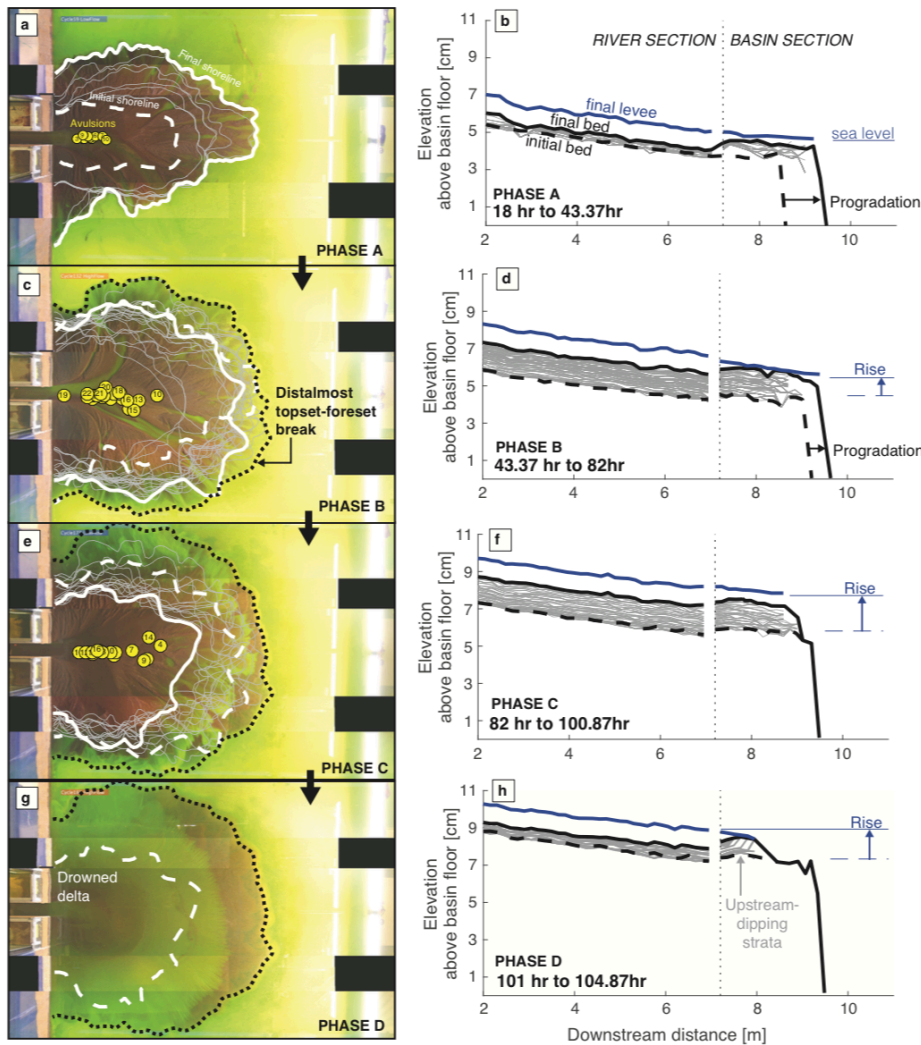


Fig. 4.4: a) Photograph of the experimental delta during Phase A, overlain with avulsion sites (yellow circles) and shorelines (gray lines) through time. Initial shoreline (white dashed line) and final shoreline (white solid line) for the phase are also shown. Numbers on avulsion sites indicate their chronological order. b) Long-profile evolution of the main channel of the experimental delta during Phase A. Bed topography (black) is shown for the start (dashed line) and end (solid line) of the phase, with synthetic stratigraphy shown in gray. Blue solid line shows end of phase levee-topography (in the basin section) and low flow water surface (in the river section), which were approximately equal. Sea level is shown in a thin blue horizontal line. c-h) same as a and b, but for experimental phases B, C, and D.

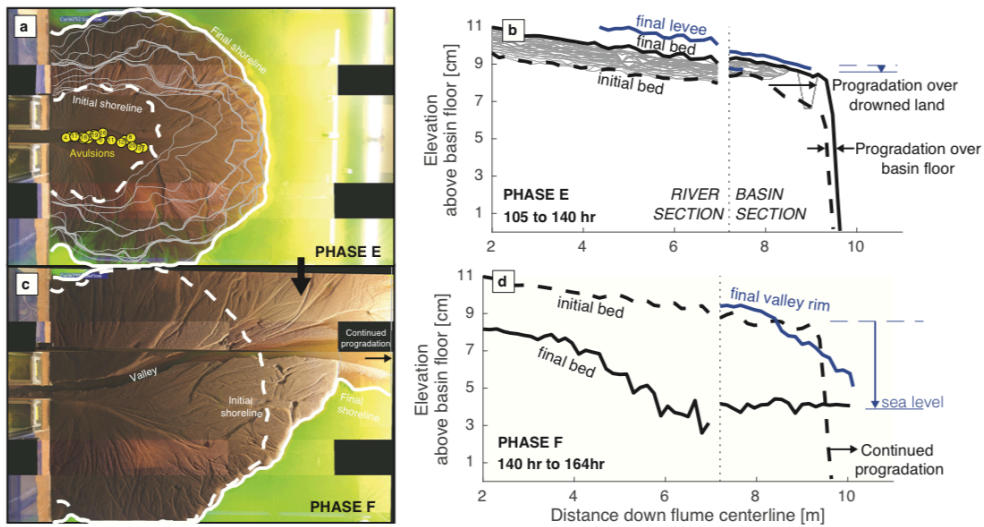


Fig. 4.5: Same as Fig. 4.4, but here shown for experimental phases E and F.

Fig. 4.6 provides an example of a typical avulsion cycle during each experimental phase, with the exception of Phases D and F when no avulsions occurred. Under constant sea-level conditions (Phase A), river-mouth progradation drove delta topset aggradation similar to previous backwater-scaled experiments (Fig. 4.6a-b) (Ganti, Chadwick, Hassenruck-Gudipati, Fuller, et al., 2016; Ganti, Chadwick, Hassenruck-Gudipati, & Lamb, 2016b). Aggradation rate and depositional thickness were maximized midway through the backwater zone corresponding to $L_A = 0.5L_b$. Avulsions occurred when the site of maximum aggradation reached a threshold thickness of $\sim 38\%$ of the channel depth ($H^* = \frac{H_{fill}}{H_c} = 0.38 \pm 0.13$, where \pm indicates a standard deviation), which is within error the same avulsion threshold observed in constant-sea level experiments of backwater-scaled deltas (Ganti, Chadwick, Hassenruck-Gudipati, & Lamb, 2016b). We observed convex-up bed topography within one backwater-length of the shoreline, which is associated with backwater-scaled avulsion nodes driven by variable discharges (Chadwick et al., 2019).

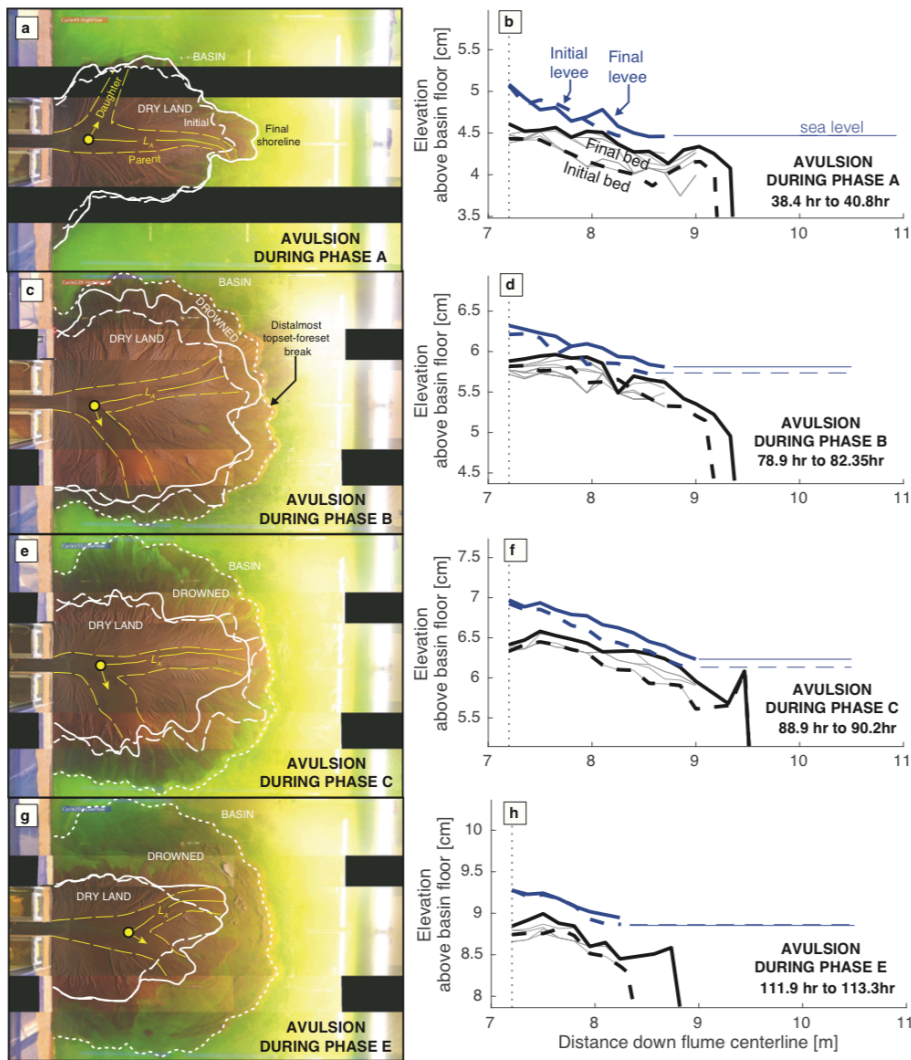


Fig. 4.6: a) Photograph of the experimental delta during a representative avulsion cycle during Phase A, overlain with avulsion site (yellow circle), initial shoreline (white dashed line) and final shoreline (white solid line). Parent channel, daughter channel, and measured avulsion length are annotated. Numbers on avulsion sites indicate their chronological order. b) Long-profile evolution of the main channel during the same representative avulsion cycle in Phase A. Bed topography (black) is shown for the start (dashed line) and end (solid line) of the cycle, with synthetic stratigraphy shown in gray. Initial levee (blue dashed line) and final levee (blue solid line) are also shown. Sea level is shown in a thin blue horizontal line. c-h) same as a and b, but for experimental phases B, C, and E.

4.3.2 Phase B

Starting at 43.3 hours of experimental run time, Phase B began and sea level rose at a rate of 0.25 mm/hr for the next 38.6 hr. Land-building continued during sea-level rise in Phase B, albeit at a slower pace of 0.057 m²/hr (Fig. 4.3). Furthermore, sea-level rise caused temporary drowning of inactive lobes such that, at a given time, roughly 1 m² of the land area was submerged. Active deltas periodically replenished zones with sediment, and also prograded the distal-most topset-foreset break basinward.

During this time, we observed 22 avulsion events, which occurred ~50% more frequently compared to stable sea-level conditions ($f_A = 0.57 \pm 0.1$ [0.17 – 1.8] hr⁻¹) due to higher aggradation rates (Fig. 4.3). Avulsions maintained an approximately constant avulsion length during Phase B ($L_A = 1.3 \pm 0.1$ [1.0 – 1.9] m) which was statistically similar to Phase A. Despite a constant avulsion length, avulsion locations were geographically more variable, within a domain 0.1 – 1m downstream of the tank inlet (Fig. 4.3). Variable avulsion locations were accompanied by decimeter-scale fluctuations in the shoreline position; the shoreline moved basinward near the active channel mouth due to progradation, but moved landward on inactive delta lobes, similar to the Mississippi (Fig. 4.1). Although the total area of delta topset increased from 2.75 m² to 4.68 m² due to net progradation during Phase B, roughly ~1m² of delta topset was submerged at any given time. In long profile, the combination of progradation and 0.96 cm of sea-level rise induced approximately 1.64 cm of channel-bed aggradation (Fig. 4.4d), both on the delta topset and in the river section. Progradation was less than in Phase A (Fig. 4.4d) because that sediment was sequestered on the delta top at an aggradation rate of 0.43 mm/hr, which was ~10% greater than in Phase A. Higher aggradation rates caused avulsions to occur

more frequently at a similar avulsion threshold compared to Phase A (Fig. 4.3) ($H^* = 0.26 \pm 0.14$).

4.3.3 Phase C

Phase C initiated at 82 hours of experimental run time and was associated with an increase in sea-level rise rate to 1 mm/hr. Increased sea-level rise caused a decrease in dry land area over time (Fig. 4.3). An actively avulsing main channel continued to distribute sediment among drowning zones, similar to Phase B, but unlike Phase B the active lobe was no longer able to prograde to the distal-most topset-foreset break, and so over time the distal-most zones stopped receiving sediment. The active channel in Phase C never prograded beyond the distal-most topset-foreset break built during earlier phases (Fig. 4.4f). Furthermore, much of the old topset was drowned by sea-level rise, and the dry-land area decreased from $\sim 3.5 \text{ m}^2$ to $\sim 1.9 \text{ m}^2$. Sea level rose by a total of 1.9 cm during this phase, and was accompanied by a comparable amount of aggradation (1.6 cm) in the main topset channel and river section (Fig. 4.4f).

We observed 16 avulsions over the 18.9-hr duration of this phase. Avulsions occurred $\sim 50\%$ more frequently than in Phase B, and more than twice as frequently compared to stable sea-level conditions in Phase A ($f_A = 0.84 \pm 0.11 [0.61 - 2.2] \text{ hr}^{-1}$) (Fig. 4.3). Avulsions occurred when the channel had aggraded to an avulsion threshold of $H^* = 0.24 \pm 0.7$, comparable to that of Phases A and B (Fig. 4.3). Also similar to Phases A and B, we observed a constant avulsion length ($L_A = 1.2 \pm 0.06 [0.83 - 1.7] \text{ m}$) and a wide geographical spread of avulsion locations driven by intermittent advance and retreat of the shoreline.

4.3.4 Phase D

We initiated Phase D at 100.87 hr of experimental run time, and sea level was raised at 4 mm/hr for the subsequent 4 hours. Rapid sea-level rise completely drowned the delta within the first hour, and dry land area was reduced to zero. Unlike all earlier phases, no avulsions occurred (Fig. 4.4g). Sediment deposition was mostly restricted to the confined river section where avulsions were not allowed (Fig. 4.4h). Sea level rose by a total height of 1.6 cm during Phase D, but the channel bed only aggraded by ~ 0.69 cm at a rate limited by the sediment supply. River mouth retreat was associated with a series of upstream-dipping mouth bar deposits (Fig. 4.4h).

4.3.5 Phase E

Starting at 105 hrs of experimental run time, we commenced Phase E and lowered sea level at a rate of $\sigma = -0.1$ mm/hr for 35 hours. Sea-level fall allowed for a resumption of delta growth (Fig. 4.3; Fig. 4.5). During the first period of Phase E (run time 105 hr to 128.5 hr), the delta prograded across the drowned delta topset from Phases C and D. Because water depths were shallow over drowned zones, progradation was rapid and dry land area increased rapidly, at over twice the rate compared to Phase A (0.17 m²/hr). Land growth slowed down upon reaching the distalmost topset-foreset break starting at 128.5 hr of run time, because the river resumed progradation into comparatively deep water on the experimental basin floor.

Despite sea level fall during Phase E, we observed rapid delta growth and aggradation for 20 avulsion cycles. Avulsion locations translated downstream over time in tandem with shoreline progradation, maintaining a constant avulsion length of $L_A = 1.3 \pm 0.1$ [1.1 – 2.0] m, comparable to that of Phases A – C (Fig. 4.3). Avulsions occurred at a frequency of $f_A = 0.57 \pm$

0.10 [0.12 – 1.13] hr^{-1} (Fig. 4.3). Similar to earlier phases, avulsion was associated with a spatial maximum in channel aggradation and a convex-up bed topography in the backwater zone (Fig. 4.6). We found avulsions occurred when the site of maximum aggradation reached $\sim 18\%$ of the channel depth ($H^* = 0.18 \pm 0.08$), which is less than the avulsion threshold observed during Phases A – C.

We observed changes in delta growth and avulsion midway during Phase E. During the first part of Phase E, from run times of 105 – 128.5 hr, land area grew rapidly (4.2 m^2 in 23.5 hr). Growth was rapid because the active channel was building land into shallow water ($\sim 1.6 \text{ cm}$ water depth) over the drowned delta topset from Phases C and D (Fig. 4.5b). During the second part of Phase E (128.5 hr to 140 hr), land building was significantly slower (1 m^2 in 11.5 hr) because the active channel overtook the distal-most topset-foreset break, and resumed progradation into deep water over the sediment-free basin floor ($\sim 8.6 \text{ cm}$ water depth). Avulsions were more frequent during the initial period of delta growth ($f_A = 0.6 \pm 0.6$ [0.13 – 1.13] hr^{-1}) compared to the subsequent period of reduced progradation ($f_A = 0.52 \pm 0.06$ [0.40 – 0.77] hr^{-1}) (Fig. 4.3). Over the entire duration of Phase E, the main channel aggraded by $\sim 1.4 \text{ cm}$ (rate) despite 0.35 cm of sea-level fall due to progradation (Fig. 4.5b)

4.3.6 Phase F

The final experimental phase, Phase F, began at 140 hours of run time and was associated with accelerated sea-level fall at a rate of 2 mm/hr for 23.5 hr. During this time, rapid sea-level fall and associated shallowing of the offshore basin depth allowed for accelerated land-building at $0.12 \text{ m}^2/\text{hr}$. No channel avulsions occurred (Fig. 4.5c). Instead, the channel carved a valley

into underlying delta deposits to a depth of 5.16 cm, roughly 5 times the channel depth (Fig. 4.5d). The delta rapidly prograded during this phase, building 2.46 m² of dry land downstream of the previous shoreline at the valley mouth. Progradation during sea-level fall was accompanied by a sequence of autogenic terrace development, similar to that documented in fan delta experiments during sea-level fall (Muto & Steel, 2004b). The experiment was concluded at 163.5 hr of experimental run time, when the river mouth had prograded to the downstream end of the ocean basin.

4.3.7 Predictions from radially averaged and lobe-averaged models

We compared experimental results for avulsion frequency against predictions using a radially averaged model (Eq. 4.1) and predictions using a lobe-averaged model (Chadwick et al., *in review*) of delta-sediment mass balance. We found that using the radially averaged model consistently underpredicted observations of avulsion frequency, consistent with recent modeling by Chadwick et al. (*in review*) (Fig. 4.7). This is because radially averaged models, which assume $v_a = \sigma$, do not account for the additional aggradation contributed by progradation. In contrast, the lobe-averaged model provides a reliable prediction of the observed avulsion frequencies within a factor of 2. The lobe-averaged model accounts for aggradation caused by progradation and sea-level rise, and shows that higher avulsion frequency during Phases B and C were due to higher sea-level rise rates. Avulsions are also expected in Phase D during drowning of the delta, but we did not observe this in our experiment because avulsions were not possible in the confined-width section. The lobe-averaged model also correctly predicts avulsions were prevented during rapid sea-level fall in Phase F, but continued to occur during slow sea-level fall in Phase E. Avulsion frequency was higher during Phase E compared to constant sea-level

conditions (Phase A) because of a reduced avulsion threshold, which is consistent with lobe-averaged model predictions.

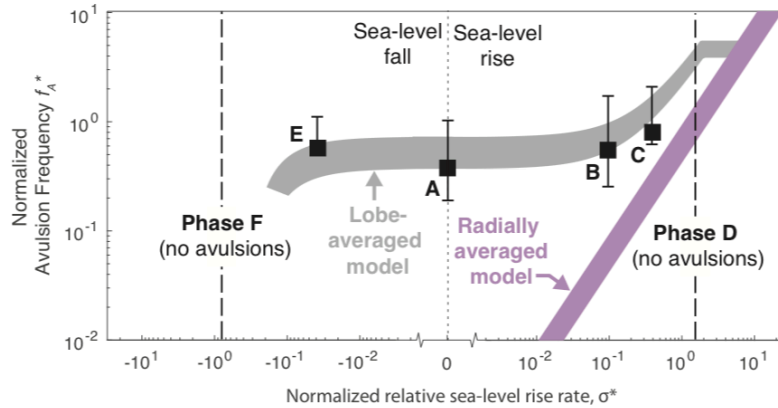


Fig. 4.7: Normalized avulsion frequency f_A^* as a function of normalized relative sea-level rise rate σ^* , showing mean and range of experimental observations (black squares with error bars), radially-averaged model predictions (pink area; Eq. 4.1) and lobe-averaged model predictions (Gray shaded area; Chadwick et al., *in review*).

We also compared our results for dry land area and total land area against radially averaged model predictions of Eq. (4.1). Although radially averaged models are commonly used to estimate changes in dry land area on natural deltas (Giosan, 2014; W. Kim et al., 2009; Paola et al., 2011), we found that Eq. (4.1) more closely followed the total land area, that is, the sum of dry land and drowned land (Fig. 4.3). This is because the radially averaged model assumes sediment supply is distributed evenly and instantaneously across the delta top. Thus, contrary to observations in our experiments and on natural deltas (Fig. 4.1), Eq. (4.1) assumes all delta lobes are active at a given time and no land is temporarily lost on abandoned delta lobes.

The radially averaged model also overpredicted the growth of total delta topset area during rapid sea-level fall in experimental Phase F. This is because Eq. (4.1) assumes that, during sea level fall, the entire delta topset area is eroded uniformly, and furthermore that eroded sediment is redistributed towards foreset progradation. However, in our experiment the channel

carved a valley along the flume centerline and abandoned the rest of the delta topset (Fig. 4.5), and so only a small portion of earlier deposits were repurposed towards progradation.

4.4. DISCUSSION

4.4.1 *Comparison to previous experiments and field observations*

Our study provides the first documentation of a backwater-scaled experimental delta subjected to sea-level changes. Similar to previous experiments of low-sloping deltas, aggradation under constant sea-level conditions was set by back-filling due to progradation (Hoyal & Sheets, 2009). Sea-level rise enhanced delta top aggradation, resulting in more frequent avulsions, consistent with experiments (Li et al., 2016; Martin et al., 2009; Yu et al., 2017) and field observations on the Rhine-Meuse delta (Stouthamer & Berendsen, 2001; Törnqvist, 1994). Importantly, back-filling due to progradation did not control the avulsion location in our experiment (Hoyal & Sheets, 2009; Zheng et al., 2019). Instead, avulsions occurred at a constant distance upstream of the shoreline scaled by the backwater-length (Eq. 4.2) because our experiment incorporated subcritical Froude numbers and variable flood discharges, consistent with the findings of Ganti et al. (2016a; 2016b). Thus, our results support the notion that backwater-scaled avulsion nodes originate from the competition between variable flood discharges in the backwater zone (Chadwick et al., 2019; Chatanantavet et al., 2012), even on deltas where back-filling is present such as the Yellow River delta (Moodie et al., 2019; Zheng et al., 2019).

The avulsion node in our experiment translated downstream with shoreline progradation to maintain a constant avulsion length, similar to the backwater-controlled experiment of Ganti et al. (2016b) conducted under constant sea level, and consistent with field observations of the

Yellow River Delta (Ganti et al., 2014). Importantly, avulsion lengths in our experiment remained constant across a wide range of sea-level rise and fall rates, and the avulsion node migrated landward during shoreline transgression, which has not previously been documented in field or experimental studies. This new finding contrasts sharply to previous experiments of alluvial fans and fan-deltas, where avulsion location was geographically fixed by a tank inlet boundary condition (Hajek et al., 2010; W. Kim, 2006; Muto et al., 2016; Reitz & Jerolmack, 2012; Reitz et al., 2010). While fan deltas and alluvial fans are known to respond to sea-level rise by shrinking in size following the radially averaged model (Eq. 4.1), our experimental results suggest lowland deltas respond fundamentally differently, maintaining a constant size scaled with the backwater length during sea-level change, because the avulsion node migrates basinward and landward in tandem with the shoreline.

4.4.2 Comparison to existing models

Our experimental results reproduce backwater-scaled avulsion nodes originating from variable floods in the backwater zone, showing support for recently developed models that incorporate backwater hydrodynamics into processes of delta lobe construction and avulsion (Chadwick et al., 2019; Moodie et al., 2019; Chadwick et al., *in review*). The model of Chadwick et al. (*in review*) accurately estimates avulsion frequency in our experiment within a factor of 2 across a wide range of sea-level rise rates, and also correctly predicts when avulsions continue or halt under conditions of sea-level fall. Based on reliable performance in the prediction of avulsions, we advocate future application of such models for forecasting avulsion hazards on deltas, as well as for the development similar models in the future to apply to land-loss problems.

Results also illustrate the limitations of radially averaged models (Eq. 4.1). At the crux of the radially averaged approach is the assumption that the avulsion node is geographically fixed, setting the delta apex (Jerolmack, 2009; Paola et al., 2011). As a result, the radially averaged model predicts deltas respond to sea-level rise by shrinking the topset area until aggradation matches pace with sea-level rise ($v_a = \sigma$), which combined with Eq. (4.3) results in a linear increase in avulsion frequency with sea-level rise rate ($f_A = \sigma/H^*H_c$). While this behavior adequately describes alluvial fans and fan deltas, our results indicate it is inadequate for lowland deltas, which are characterized by a constant delta size set by the backwater-scaled avulsion length (Eq. 4.2) (Chatanantavet et al., 2012; Ganti, Chadwick, Hassenruck-Gudipati, Fuller, et al., 2016; Ganti et al., 2014). In our experiment, avulsion length remained constant during sea-level rise and fall, and so aggradation rate and avulsion frequency were not set by changes in delta area, but instead by the competition between progradation, sea-level rise, and the sediment supply, consistent with the lobe-averaged approach of Chadwick et al. (*in review*) (Fig. 4.7). Although radially averaged models are typically applied to estimate dry land growth and loss on lowland deltas (W. Kim et al., 2009; Paola et al., 2011), in our experiment the radially averaged model more closely tracked the sum of both dry land and drowned areas. The area of drowned land is significant in our experimental data (Fig. 4.3) and in nature (Fig. 4.1), on account of low surface-slopes. However, this limitation of the radially averaged model has not been characterized in previous experiments, perhaps because steep slopes in early experiments minimize land loss for an incremental increase in sea-level.

Our experimental results show agreement with recent Delft3D modeling of the Goose River delta (Nijhuis et al., 2015), showing avulsions may continue to occur during sea-level fall. Interestingly, higher sea-level fall rates led to more frequent avulsions in Delft3D simulations, a

trend that is not observed in our experiments or in existing lobe-averaged models (Chadwick et al., *in review*) (Fig. 4.7). However, our experiments do show evidence for reduced avulsion thresholds during sea-level fall, which could conceivably cause more frequent avulsions if aggradation rate was relatively steady (Eq. 4.3) (Moodie et al., 2019). We reason that, in our experiments, the reduced avulsion threshold may be attributed to increased superelevation of the channel during sea-level fall: as sea level falls, all paths to the shoreline become steeper, and thus overbank flows may be capable of triggering avulsions more easily.

In contrast to our experiments, many sophisticated 2-D and 3-D numerical modeling studies exhibit a geographically fixed avulsion node (Caldwell & Edmonds, 2014; Edmonds et al., 2010; Gao et al., 2019; Geleynse et al., 2011a; Liang, Geleynse, et al., 2015; Liang, Kim, et al., 2016; Liang, Van Dyk, et al., 2016b; Liang, Voller, et al., 2015; Van De Lageweg & Slangen, 2017). Although these models contain the relevant physics to produce backwater hydrodynamics, they are often conducted under constant discharges that preclude the emergence of backwater-scaled avulsion nodes (Chadwick et al., 2019; Ganti, Chadwick, Hassenruck-Gudipati, Fuller, et al., 2016). Furthermore, such modeling studies have generally been focused on deltaic processes at spatial scales much less than the backwater length scale, such as mouth-bar bifurcation (Edmonds & Slingerland, 2007; Salter et al., 2018), and so model domains are typically smaller than the backwater length-scale. Importantly, if a delta has not grown to a size comparable to its backwater length-scale, then backwater-scaled avulsions are not possible and avulsions will be tied to the upstream boundary condition, as documented in the early stages of a backwater-controlled delta experiment (Ganti, Chadwick, Hassenruck-Gudipati, & Lamb, 2016a). In order to resolve the effect of sea-level rise on avulsion location in Delft3D and similar

models, future work should incorporate variable flood discharges and a model domain that is larger than the backwater length.

4.4.3 Implications for predicting avulsion hazards

Our results provide support for the expectation that the most-likely site of future avulsion hazards is the location of maximum channel-bed aggradation within the backwater zone (Fig. 4.6), consistent with the hypothesis of Chatanantavet et al. (2012). A constant avulsion length was observed across a wide range of sea-level rise and fall conditions in our experiment, and was found to be equal to the avulsion length under stable sea level ($L_A = 0.5L_b$). This suggests previous avulsion lengths observed on natural deltas are a good indicator of future avulsion lengths, even though relative-sea level conditions are changing dramatically due to anthropogenic greenhouse effects and coastal subsidence. Importantly, shoreline fluctuations during sea-level rise have the potential to spread avulsion locations over a broader zone, even though L_A may remain constant (Fig. 4.3). This suggests avulsion hazard mitigation on natural deltas may need to be expanded into new reaches upstream and downstream that were not previously in danger of avulsion. Because the distance between the shoreline and the avulsion location is expected to remain constant, expansion of mitigation efforts should be prioritized in zones where shoreline change is rapid.

Our results also warn of increased frequency of avulsion hazards in the face of relative sea-level rise, consistent with recent modeling work (Chadwick et al., *in review*). As rates increase, sea-level rise enhances aggradation rates and causes channels to reach the avulsion threshold more quickly (Fig. 4.3; Fig 7). However, this effect is expected to become less pronounced at very extreme rise rates ($\sigma^* \geq 1$), where aggradation rates are limited by the

sediment input. This scenario also introduces new hazards associated with upstream translation of the avulsion node and drowning of the coastal plain.

Experimental results suggest cycles of lobe-building and avulsion also mediate natural hazards relating to coastal land loss during sea-level rise. Similar to observations on the Mississippi (Fig. 4.1) (Gagliano et al., 1981), the majority of land loss observed in our experiments was focused on abandoned delta lobes, which were starved of sediment between avulsions. Drowning on abandoned lobes was periodically counteracted when avulsions rerouted the channel to drowned zones. During Phase B, we observed a consistent land area ($\sim 1\text{m}^2$) was drowned at a given time, even though the delta was on average progradational (Fig. 4.3). This implies that even deltas with ample sediment supply are susceptible to land loss, especially on managed deltas where man-made infrastructure inhibits avulsion. Furthermore, results indicate that identifying where to reroute sediment in man-made diversions may be more crucial than the size of the diversion itself. Because lobes on large lowland deltas can be abandoned for hundreds to thousands of years, transient land loss is effectively permanent for the purposes of human settlement and infrastructure. We reason future work should be focused on characterizing the rates and scales of transient drowning on lowland river deltas.

4.5. CONCLUSIONS

We conducted a delta experiment scaled to incorporate backwater hydrodynamics and investigated delta evolution across a range of relative sea-level rise and fall rates. We present results for delta land area, channel hydrodynamics and sedimentation, and avulsion location and frequency from this experiment, and compare results to model predictions using radially-averaged and lobe-averaged approaches. Results indicate that

1. Channel avulsions occurred at a persistent spatial node corresponding to an avulsion length of $L_A = 0.5L_b$ regardless of sea-level rise or fall and similar to previous constant sea-level experiments (Ganti, Chadwick, Hassenruck-Gudipati, Fuller, et al., 2016). To maintain a constant avulsion length, the avulsion node translated downstream in tandem with shoreline progradation and migrated upstream in tandem with shoreline retreat. Furthermore, avulsions occurred across a wider range of locations when sea-level rise caused transient shoreline advance and retreat.
2. Channel avulsions occurred more frequently at higher sea-level rise rates (Phases *A – C*), up to a limit where delta retreat restricted deposition to within the river section where the channel was artificially embanked and avulsion was impossible (Phase *D*). Avulsions resumed during moderate sea-level fall (Phase *E*) and were caused by river mouth progradation, but avulsions were prevented during rapid sea-level fall (Phase *F*) because the river incised a valley with a relief of ~ 5 channel depths. Avulsion frequency is consistently underestimated by radially averaged sediment mass balance (Eq. 4.1), but well-predicted using a lobe-averaged approach according to Chadwick et al., (*in review*).
3. The amount of dry land in our experiment was less than predicted by radially averaged models, suggesting that natural deltas may be in more danger than previously estimated. This deficit arose because abandoned delta lobes were starved of sediment between avulsions, and as a result experienced transient drowning due to sea-level rise, similar to the Mississippi (Fig. 4.1). The radially-averaged model more closely followed the evolution of the distalmost topset-foreset break, including drowned zones.

4.6. REFERENCES

- Allen, John R L. 1965. "A Review of the Origin and Characteristics of Recent Alluvial Sediments." *Sedimentology* 5 (2): 89–191.
- Bianchi, Thomas S, and Mead A Allison. 2009. "Large-River Delta-Front Estuaries as Natural 'Recorders' of Global Environmental Change." *Proceedings of the National Academy of Sciences* 106 (20): 8085–92.
- Bintanja, Richard, Roderik S W van de Wal, and Johannes Oerlemans. 2005. "Modelled Atmospheric Temperatures and Global Sea Levels over the Past Million Years." *Nature* 437 (7055): 125.
- Blum, M., J. Martin, K. Milliken, and M. Garvin. 2013. "Paleovalley Systems: Insights from Quaternary Analogs and Experiments." *Earth-Science Reviews* 116: 128–69. <https://doi.org/10.1016/j.earscirev.2012.09.003>.
- Blum, Michael D. 1990. "Climatic and Eustatic Controls on Gulf Coastal Plain Fluvial Sedimentation: An Example from the Late Quaternary of the Colorado River, Texas." In *Sequence Stratigraphy as an Exploration Tool: Concepts and Practices in the Gulf Coast*. Gulf Coast Section SEPM Foundation, *Proceedings of the 11th Annual Research Conference*, 71–83.
- Blum, Michael D., and Torbjörn E. Törnqvist. 2000a. "Fluvial Responses to Climate and Sea-Level Change: A Review and Look Forward." *Sedimentology* 47 (SUPPL. 1): 2–48. <https://doi.org/10.1046/j.1365-3091.2000.00008.x>.
- Blum, Michael D, M J Guccione, D A Wysocki, P C Robnett, and E M Rutledge. 2000. "Late Pleistocene Evolution of the Lower Mississippi River Valley, Southern Missouri to Arkansas." *Geological Society of America Bulletin* 112 (2): 221–35.
- Blum, Michael D, and Torbjörn E Törnqvist. 2000b. "Fluvial Responses to Climate and Sea-Level Change: A Review and Look Forward." *Sedimentology* 47: 2–48.
- Brakenridge, G R, J P M Syvitski, E Niebuhr, I Overeem, S A Higgins, A J Kettner, and L Prades. 2017. "Design with Nature: Causation and Avoidance of Catastrophic Flooding, Myanmar." *Earth-Science Reviews* 165: 81–109.
- Bryant, Madeline, Peter Falk, and Chris Paola. 1995. "Experimental Study of Avulsion Frequency and Rate of Deposition." *Geology* 23 (4): 365. [https://doi.org/10.1130/0091-7613\(1995\)023<0365:ESOFAFA>2.3.CO;2](https://doi.org/10.1130/0091-7613(1995)023<0365:ESOFAFA>2.3.CO;2).
- Caldwell, Rebecca L, and Douglas A Edmonds. 2014. "The Effects of Sediment Properties on Deltaic Processes and Morphologies: A Numerical Modeling Study." *Journal of Geophysical Research: Earth Surface*, 961–82. <https://doi.org/10.1002/2013JF002965>. Received.
- Chadwick, A J, M P Lamb, A J Moodie, G Parker, and J A Nittrouer. 2019. "Origin of a Preferential Avulsion Node on Lowland River Deltas." *Geophysical Research Letters* 46 (8): 4267–77.
- Chatanantavet, Phairot, and Michael P. Lamb. 2014. "Sediment Transport and Topographic Evolution of a Coupled River and River Plume System: An Experimental and Numerical Study," no. Figure 1: 1–20. <https://doi.org/10.1002/2013JF002810>. Received.
- Chatanantavet, Phairot, Michael P. Lamb, and Jeffrey a. Nittrouer. 2012. "Backwater Controls of Avulsion Location on Deltas." *Geophysical Research Letters* 39 (1). <https://doi.org/10.1029/2011GL050197>.
- Christie-Blick, Nicholas, Ian A Dyson, and C C Von Der Borch. 1995. "Sequence Stratigraphy and the Interpretation of Neoproterozoic Earth History." *Precambrian Research* 73 (1–4): 3–26.
- Coastal Protection and Restoration Authority of Louisiana (CPRA). 2007. "Integrated Ecosystem Restoration and Hurricane Protection: Louisiana's Comprehensive Master Plan for a Sustainable Coast."
- DiBiase, Roman A, Ajay B Limaye, Joel S Scheingross, Woodward W Fischer, and Michael P Lamb. 2013. "Deltaic Deposits at Aeolis Dorsa: Sedimentary Evidence for a Standing Body of Water on the Northern Plains of Mars." *Journal of Geophysical Research: Planets* 118 (6): 1285–1302.

- Edmonds, D. A., D.C.J.D. Hoyal, B. A. Sheets, and R. L. Slingerland. 2009. "Predicting Delta Avulsions: Implications for Coastal Wetland Restoration." *Geology* 37 (8): 759–62. <https://doi.org/10.1130/G25743A.1>.
- Edmonds, D. A., R. L. Slingerland, J. Best, D. Parsons, and N. Smith. 2010. "Response of River-Dominated Delta Channel Networks to Permanent Changes in River Discharge." *Geophysical Research Letters* 37 (12). <https://doi.org/10.1029/2010GL043269>.
- Edwards, Kacey L, Jayaram Veeramony, David Wang, K Todd Holland, and Y L Hsu. 2009. "Sensitivity of Delft3D to Input Conditions." In *OCEANS 2009*, 1–8.
- Flemings, Peter B, and John P Grotzinger. 1996. "STRATA: Freeware for Analyzing Classic Stratigraphic Problems." *GSA Today* 6 (12): 1–7.
- Gagliano, Sherwood M, Klaus J Meyer-Arendt, and Karen M Wicker. 1981. "Land Loss in the Mississippi River Deltaic Plain." *GCAGS Transactions* 31: 295–300.
- Ganti, Vamsi, Austin J Chadwick, Hima J Hassenruck-Gudipati, Brian M Fuller, and Michael P Lamb. 2016. "Experimental River Delta Size Set by Multiple Floods and Backwater Hydrodynamics." *Science Advances* 2 (5): e1501768.
- Ganti, Vamsi, Austin J Chadwick, Hima J Hassenruck-Gudipati, and Michael P Lamb. 2016. "Avulsion Cycles and Their Stratigraphic Signature on an Experimental Backwater-Controlled Delta Vamsi," 1–25. <https://doi.org/10.1002/2016JF003915>. Received.
- Ganti, Vamsi, Zhongxin Chu, Michael P. Lamb, Jeffrey A. Nittrouer, and Gary Parker. 2014. "Testing Morphodynamic Controls on the Location and Frequency of River Avulsions on Fans versus Deltas: Huanghe (Yellow River), China." *Geophysical Research Letters* 41: 7882–90. <https://doi.org/10.1002/2014GL061918>.
- Ganti, Vamsi, Michael P. Lamb, and Austin J Chadwick. 2019. "Autogenic Erosional Surfaces in Fluvio-Deltaic Stratigraphy from Floods, Avulsions, and Backwater Hydrodynamics." *Journal of Sedimentary Research*.
- Gao, Weilun, Dongdong Shao, Zheng Bing Wang, William Nardin, Prateek Rajput, Wei Yang, Tao Sun, and Baoshan Cui. 2019. "Long-Term Cumulative Effects of Intra-Annual Variability of Unsteady River Discharge on the Progradation of Delta Lobes: A Modeling Perspective." *Journal of Geophysical Research: Earth Surface* 124 (4): 960–73.
- Geleynse, Nathanaël, Joep E.a. Storms, Dirk-Jan R. Walstra, H.R. Albert Jagers, Zheng B. Wang, and Marcel J.F. Stive. 2011. "Controls on River Delta Formation; Insights from Numerical Modelling." *Earth and Planetary Science Letters* 302 (1–2): 217–26. <https://doi.org/10.1016/j.epsl.2010.12.013>.
- Giosan, Livio. 2014. "Protect the World's Deltas." *Nature* 516: 5–7.
- Gleick, Peter H. 2003. "Global Freshwater Resources: Soft-Path Solutions for the 21st Century." *Science (New York, N.Y.)* 302 (2003): 1524–28. <https://doi.org/10.1126/science.1089967>.
- González, Juan L, and Torbjörn E Tornqvist. 2006. "Coastal Louisiana in Crisis: Subsidence or Sea Level Rise?" *Eos, Transactions American Geophysical Union* 87 (45): 493–98.
- Hartley, Adrian J, Gary S Weissmann, and Louis Scuderi. 2017. "Controls on the Apex Location of Large Deltas." *Journal of the Geological Society* 174 (1): 10–13.
- Hoyal, D., and B. A. Sheets. 2009. "Morphodynamic Evolution of Experimental Cohesive Deltas." *Journal of Geophysical Research* 114 (F2): F02009. <https://doi.org/10.1029/2007JF000882>.
- Hudson, Paul F, and Richard H Kesel. 2000. "Channel Migration and Meander-Bend Curvature in the Lower Mississippi River Prior to Major Human Modification." *Geology* 28 (6): 531–34.
- Irwin, Rossman P., Alan D. Howard, Robert a. Craddock, and Jeffrey M. Moore. 2005. "An Intense Terminal Epoch of Widespread Fluvial Activity on Early Mars: 2. Increased Runoff and Paleolake Development." *Journal of Geophysical Research E: Planets* 110: 1–38. <https://doi.org/10.1029/2005JE002460>.

- Jerolmack, Douglas J. 2009. "Conceptual Framework for Assessing the Response of Delta Channel Networks to Holocene Sea Level Rise." *Quaternary Science Reviews* 28 (17–18): 1786–1800. <https://doi.org/10.1016/j.quascirev.2009.02.015>.
- Jerolmack, Douglas J., and David Mohrig. 2007. "Conditions for Branching in Depositional Rivers." *Geology* 35 (5): 463. <https://doi.org/10.1130/G23308A.1>.
- Jerolmack, Douglas J., and John B. Swenson. 2007. "Scaling Relationships and Evolution of Distributary Networks on Wave-Influenced Deltas." *Geophysical Research Letters* 34 (23). <https://doi.org/10.1029/2007GL031823>.
- Jerolmack, Douglas J., and Chris Paola. 2010. "Shredding of Environmental Signals by Sediment Transport." *Geophysical Research Letters* 37 (19).
- Jones, L S, and S A Schumm. 1999. "Causes of Avulsion: An Overview." In *Fluvial Sedimentology VI*, 28:171–78. Wiley Online Library.
- Kidder, Tristram R., and Haiwang Liu. 2017. "Bridging Theoretical Gaps in Geoarchaeology: Archaeology, Geoarchaeology, and History in the Yellow River Valley, China." *Archaeological and Anthropological Sciences* 9 (8): 1585–1602. <https://doi.org/10.1007/s12520-014-0184-5>.
- Kim, W., D. Mohrig, Robert R. Twilley, C. Paola, and G. Parker. 2009. "Is It Feasible to Build New Land in the Mississippi River Delta?" *Eos Transactions, AGU* 90 (42): 373–74. http://www.agu.org/pubs/eos-news/supplements/2009/kim_90_42.shtml.
- Kim, Wonsuck, Chris Paola, Vaughan R Voller, and John B Swenson. 2006. "Experimental Measurement of the Relative Importance of Controls on Shoreline Migration." *Journal of Sedimentary Research* 76 (2): 270–83.
- Lageweg, Wietse Van De, and Aimée Slangen. 2017. "Predicting Dynamic Coastal Delta Change in Response to Sea-Level Rise." *Journal of Marine Science and Engineering* 5 (2): 24. <https://doi.org/10.3390/jmse5020024>.
- Lamb, Michael P., Jeffrey a. Nittrouer, David Mohrig, and John Shaw. 2012. "Backwater and River Plume Controls on Scour Upstream of River Mouths: Implications for Fluvio-Deltaic Morphodynamics." *Journal of Geophysical Research* 117 (F1): F01002. <https://doi.org/10.1029/2011JF002079>.
- Lambeck, Kurt, and John Chappell. 2001. "Sea Level Change through the Last Glacial Cycle." *Science* 292 (5517): 679–86.
- Lane, T I, R A Nanson, B K Vakarelov, R B Ainsworth, and S E Dashtgard. 2017. "Evolution and Architectural Styles of a Forced-Regressive Holocene Delta and Megafan, Mitchell River, Gulf of Carpentaria, Australia." *Geological Society, London, Special Publications* 444 (1): 305–34.
- Lesser, Giles R, J A v Roelvink, JATM Van Kester, and G S Stelling. 2004. "Development and Validation of a Three-Dimensional Morphological Model." *Coastal Engineering* 51 (8–9): 883–915.
- Li, Qi, Lizhu Yu, and Kyle M Straub. 2016. "Storage Thresholds for Relative Sea-Level Signals in the Stratigraphic Record." *Geology* 44 (3): 179–82.
- Martin, John, Ben Sheets, Chris Paola, and David Hoyal. 2009. "Influence of Steady Base-Level Rise on Channel Mobility, Shoreline Migration, and Scaling Properties of a Cohesive Experimental Delta." *Journal of Geophysical Research: Earth Surface* 114 (F3).
- Mattheus, Christopher R, Antonio B Rodriguez, D Lawrence Greene, Alexander R Simms, and John B Anderson. 2007. "Control of Upstream Variables on Incised-Valley Dimension." *Journal of Sedimentary Research* 77 (3): 213–24.
- McLennan, Scott M, John P Grotzinger, Joel A Hurowitz, and Nicholas J Tosca. 2019. "The Sedimentary Cycle on Early Mars." *Annual Review of Earth and Planetary Sciences* 47: 91–118.
- Milliman, John D., and James P. M. Syvitski. 1992. "Geomorphic/Tectonic Control of Sediment Discharge to the Ocean: The Importance of Small Mountainous Rivers." *The Journal of Geology* 100 (5): 525–44. <https://doi.org/10.1086/629606>.

- Mohrig, David, Paul L Heller, and William J Lyons. 2000. "Interpreting Avulsion Process from Ancient Alluvial Sequences : Guadalupe-Matarranya System (Northern Spain) and Wasatch Formation (Western Colorado)," no. 12: 1787–1803.
- Moodie, Andrew, Jeffrey Nittrouer, Hongbo Ma, Brandee Carlson, Austin Chadwick, Michael Lamb, and Gary Parker. n.d. "Modeling Deltaic Lobe-Building Cycles and Channel Avulsions for the Yellow River Delta, China." *Journal of Geophysical Research: Earth Surface*.
- Moran, Kaitlin E., Jeffrey a. Nittrouer, Mauricio M. Perillo, Jorge Lorenzo-Trueba, and John B. Anderson. 2017. "Morphodynamic Modeling of Fluvial Channel Fill and Avulsion Time Scales during Early Holocene Transgression, as Substantiated by the Incised Valley Stratigraphy of the Trinity River, Texas." *Journal of Geophysical Research: Earth Surface* 122 (1): 215–34. <https://doi.org/10.1002/2015JF003778>.
- Mosselman, E. 2005. "Basic Equations for Sediment Transport in CFD for Fluvial Morphodynamics." *Computational Fluid Dynamics*, 71–89.
- Muto, Tetsuji, and Ron J. Steel. 2004. "Autogenic Response of Fluvial Deltas to Steady Sea-Level Fall: Implications from Flume-Tank Experiments." *Geology* 32 (5): 401–4. <https://doi.org/10.1130/G20269.1>.
- Nienhuis, Jaap H, Andrew D Ashton, and Liviu Giosan. 2015. "What Makes a Delta Wave-Dominated?" *Geology* 43 (6): 511–14.
- Nijhuis, A G, D A Edmonds, R L Caldwell, J A Cederberg, R L Slingerland, James Leonard Best, D R Parsons, and R A J Robinson. 2015. "Fluvio-Deltaic Avulsions during Relative Sea-Level Fall." *Geology* 43 (8): 719–22.
- Nittrouer, J. a., J. Shaw, M. P. Lamb, and D. Mohrig. 2011. "Spatial and Temporal Trends for Water-Flow Velocity and Bed-Material Sediment Transport in the Lower Mississippi River." *Geological Society of America Bulletin* 124 (3–4): 400–414. <https://doi.org/10.1130/B30497.1>.
- Nittrouer, Jeffrey A, David Mohrig, Mead A Allison, and AYMERIC-PIERRE B PEYRET. 2011. "The Lowermost Mississippi River: A Mixed Bedrock-Alluvial Channel." *Sedimentology* 58 (7): 1914–34.
- Nittrouer, Jeffrey A, John Shaw, Michael P Lamb, and David Mohrig. 2012. "Spatial and Temporal Trends for Water-Flow Velocity and Bed-Material Sediment Transport in the Lower Mississippi River." *Bulletin* 124 (3–4): 400–414.
- Olson, David M, and Eric Dinerstein. 1998. "The Global 200: A Representation Approach to Conserving the Earth's Most Biologically Valuable Ecoregions." *Conservation Biology* 12 (3): 502–15.
- Pachauri, R K, L Meyer, G K Plattner, and T Stocker. 2014. "IPCC, 2014: Climate Change 2014: Synthesis Report." *IPCC, Geneva, Switzerland*.
- Paola, Chris. 2000. "Quantitative Models of Sedimentary Basin Filling." *Sedimentology* 47: 121–78.
- Paola, Chris, Paul L Heller, and Charles L Angevine. 1992. "The Large-Scale Dynamics of Grain-Size Variation in Alluvial Basins, 1: Theory." *Basin Research* 4 (2): 73–90.
- Paola, Chris, and David Mohrig. 1996. "Palaeohydraulics Revisited: Palaeoslope Estimation in Coarse-Grained Braided Rivers." *Basin Research* 8 (3): 243–54. <https://doi.org/10.1046/j.1365-2117.1996.00253.x>.
- Paola, Chris, Robert R. Twilley, Douglas a. Edmonds, Wonsuck Kim, David Mohrig, Gary Parker, Enrica Viparelli, and Vaughan R. Voller. 2011. "Natural Processes in Delta Restoration: Application to the Mississippi Delta." *Annual Review of Marine Science* 3 (1): 67–91. <https://doi.org/10.1146/annurev-marine-120709-142856>.
- Posamentier, H W, M T Jervey, and P R Vail. 1988. "Eustatic Controls on Clastic Deposition I—Conceptual Framework."
- Posamentier, H W, and P R Vail. 1988. "Eustatic Controls on Clastic Deposition II—Sequence and Systems Tract Models."

- Ratliff, Katherine M., Eric H.W. Hutton, and A. Brad Murray. 2018. "Exploring Wave and Sea-Level Rise Effects on Delta Morphodynamics With a Coupled River-Ocean Model." *Journal of Geophysical Research: Earth Surface* 123 (11): 2887–2900. <https://doi.org/10.1029/2018JF004757>.
- Reitz, Meredith D., Jennifer L. Pickering, Steven L. Goodbred, Chris Paola, Michael S. Steckler, Leonardo Seeber, and Syed H. Akhter. 2015. "Effects of Tectonic Deformation and Sea Level on River Path Selection: Theory and Application to the Ganges-Brahmaputra-Meghna River Delta." *Journal of Geophysical Research: Earth Surface*. <https://doi.org/10.1002/2014JF003202>.
- Richards, Keith, James Brasington, and Francine Hughes. 2002. "Geomorphic Dynamics of Floodplains: Ecological Implications and a Potential Modelling Strategy." *Freshwater Biology* 47 (4): 559–79.
- Roberts, Harry H. 1997. "Dynamic Changes of the Holocene Mississippi River Delta Plain: The Delta Cycle." *Journal of Coastal Research*, 605–27.
- Shaw, John B., David Mohrig, and Spencer K. Whitman. 2013. "The Morphology and Evolution of Channels on the Wax Lake Delta, Louisiana, USA." *Journal of Geophysical Research: Earth Surface* 118 (3): 1562–84. <https://doi.org/10.1002/jgrf.20123>.
- Sinha, Rajiv. 2009. "The Great Avulsion of Kosi on 18 August 2008." *Current Science*, 429–33.
- Slingerland, Rudy, and Norman D. Smith. 2004. "River Avulsions and Their Deposits." *Annual Review of Earth and Planetary Sciences* 32 (1): 257–85. <https://doi.org/10.1146/annurev.earth.32.101802.120201>.
- Soong, Ta Wei, and Yean Zhao. 1994. "The Flood and Sediment Characteristics of the Lower Yellow River in China." *Water International* 19 (3): 129–37.
- Stouthamer, E, and H J a Berendsen. 2001. "Avulsion Frequency, Avulsion Duration, and Interavulsion Period of Holocene Channel Belts in the Rhine-Meuse Delta, The Netherlands." *Journal of Sedimentary Research* 71 (4): 589–98. <https://doi.org/10.1306/112100710589>.
- Straub, Kyle M, Vamsi Ganti, Chris Paola, and Efi Foufoula-Georgiou. 2012. "Prevalence of Exponential Bed Thickness Distributions in the Stratigraphic Record: Experiments and Theory." *Journal of Geophysical Research: Earth Surface* 117 (F2).
- Syvitski, James P M, and G Robert Brakenridge. 2013. "Causation and Avoidance of Catastrophic Flooding along the Indus River, Pakistan." *GSA Today* 23 (1): 4–10.
- Törnqvist, Torbjörn E. 1994. "Middle and Late Holocene Avulsion History of the River Rhine (Rhine-Meuse Delta, Netherlands)." *Geology* 22 (8): 711–14.
- Trower, Elizabeth J, Vamsi Ganti, Woodward W Fischer, and Michael P Lamb. 2018. "Erosional Surfaces in the Upper Cretaceous Castlegate Sandstone (Utah, USA): Sequence Boundaries or Autogenic Scour from Backwater Hydrodynamics?" *Geology* 46 (8): 707–10.
- Vörösmarty, Charles J, James Syvitski, John Day, Alex de Sherbinin, Liviu Giosan, and Chris Paola. 2009. "Battling to Save the World's River Deltas." *Bulletin of the Atomic Scientists* 65 (2): 31–43. <https://doi.org/10.2968/065002005>.